Polymer-Templated Functional Organic-Inorganic Nanocomposites for Lithium Ion Batteries, Capacitors and Ferroelectric Devices

A Dissertation
Presented to
The Academic Faculty

by

Beibei Jiang

In Partial Fulfillment
of the Requirements for the Degree
Doctor of Philosophy in the
School of Materials Science and Engineering

Georgia Institute of Technology
December, 2016

Polymer-Templated Functional Organic-Inorganic Nanocomposites for Lithium Ion Batteries, Capacitors and Ferroelectric Devices

To be approved by:

Dr. Zhiqun Lin, Advisor
School of Materials Science and Engineering
Georgia Institute of Technology

Dr. Nazanin Bassiri-Gharb
School of Mechanical Engineering & Materials Science and Engineering
Georgia Institute of Technology

Dr. Meilin Liu
School of Materials Science and Engineering
Georgia Institute of Technology

Dr. Vladimir V. Tsukruk
School of Materials Science and Engineering
Georgia Institute of Technology

Dr. Zhong Lin Wang
School of Materials Science and Engineering
Georgia Institute of Technology

Dr. Gleb Yushin
School of Materials Science and Engineering
Georgia Institute of Technology

Date Approved: Sept. 29, 2016

Dedicated to my loving family

ACKNOWLEDGEMENTS

I would like to express my sincere appreciation to my academic advisor Dr. Zhiqun Lin for his constant support and guidance of my Ph.D study, for his patience, motivation, and immense knowledge, for the opportunities he provided me with, and for the trust in me. I would also like to thank all my thesis committee: Dr. Nazanin Bassiri-Gharb, Dr. Vladimir V. Tsukruk, Dr. Zhong Lin Wang, Dr. Gleb Yushin, and Dr. Meilin Liu, who devoted their precious time to serve in my PhD proposal and defense committees, and provided tremendous support to my ongoing research activity by sharing their expertise, insights, and instruments.

I would also like to thank all NanoFM group members, who have contributed to the excellent working environment and the perfect collaboration in our group, and inspire me greatly with their passion, intelligence, talent, and patience. Particularly, I would like to thank Dr. Ming He, Dr. Hui Xu, Dr. Cuiping Han, Dr. Chaowei Feng, Yanjie He, James Iocozzia, Prof. Yingkui Yang, Prof. Yupeng Yuan, Shiqiang Zhao, Young Jun Yoon, Zewei Wang, Dr. Yijie Tao and Yihuang Chen for their helpful discussion at different stages of my research. Special thanks go to Dr. Xinchang Pang who mentored me to initiate the lab work in this study.

Lastly, I would like to thank my family who sacrifice their time, and support me with their love and encouragement in all my pursuits. For my loving, supportive, encouraging, and patient husband Dr. Bo Li whose faithful support and continuous encouragement makes my Ph.D experience full of joy and enthusiasm.

TABLE OF CONTENTS

LIST OF TABLES

LIST OF FIGURES

SUMMARY

Functional hybrid organic-inorganic nanocomposites, formed by integrating two or more materials at the nanoscale with complementary properties, offer the potential to achieve performance, functionality and architecture far beyond those of each constituent. Despite this, we lack a versatile approach to design hybrid nanocomposites with desired functions and properties while having a good control over the size, shape, and architecture of the resulting nanocomposites. In this thesis, we developed a versatile and robust polymer-templated approach for synthesizing organic-inorganic nanocomposites with controllable size, shape, morphology, and functionality. This viable polymer-templated approach enables the *in-situ* synthesis of inorganic nanocrystals with well-controlled size, shape, and functionality in the presence of some rationally designed polymer template by utilizing the interplay between the functional groups of polymer templates and the inorganic precursors.

Two main targeted applications, namely, functional nanocomposites as electrodes for Lithium ion batteries (LIBs) and as dielectric materials for capacitors guide the polymer-templated strategy when designing the polymer templates and crafting hybrid organic-inorganic nanocomposites. The major achievements can be summarized as follows:

First, a viable and robust *in-situ* synthesis of poly(vinylidene fluoride) (PVDF)-$BaTiO_3$ nanocomposites composed of monodisperse ferroelectric $BaTiO_3$ nanoparticles with tunable diameter directly and stably connected with ferroelectric PVDF was initiated

by exploiting both the ability to synthesizing amphiphilic star-like poly(acrylic acid)-*block*-poly(vinylidene fluoride) (PAA-*b*-PVDF) diblock copolymers with well-defined molecular weight of each block as nanoreactors, and the strong coordination interaction between the precursors and hydrophilic PAA blocks. The resulting PVDF-$BaTiO_3$ nanocomposites, with tunable PVDF/$BaTiO_3$ volume ratio, displayed high dielectric constant and low dielectric loss, which is promising for applications in high energy density capacitors. In addition, these PVDF-functionalized $BaTiO_3$ nanoparticles exhibited the ferroelectric tetragonal structure.

Second, we extended this amphiphilic star-like diblock copolymer nanoreactor strategy to bottlebrush-like diblock copolymer and crafted ferroelectric PVDF-$BaTiO_3$ nanocomposites composed of ferroelectric $BaTiO_3$ nanorods with tunable diameter, length and aspect ratio stably connected with ferroelectric PVDF. The capability of systematically varying the size of $BaTiO_3$ nanocrystals offers the potential to investigate the size and shape effects on the ferroelectric and dielectric properties of $BaTiO_3$-based nanocomposites, thereby providing insight into the rational design of ferroelectric PVDF-$BaTiO_3$ nanocomposites for practical applications.

Third, we developed a facile and effective strategy for *in-situ* crafting $ZnFe_2O_4$/carbon nanocomposites comprising small-sized $ZnFe_2O_4$ nanoparticles embedded within the continuous carbon network through the pyrolysis of $ZnFe_2O_4$ precursors-containing polymer template PS@PAA core@shell nanospheres. The advantages of this strategy are threefold. First, the PS@PAA nanosphere template is synthesized by emulsion polymerization in one-step. Second, the pyrolysis leads to the formation of $ZnFe_2O_4$ nanoparticles. Third, in the meantime the pyrolysis also induced

the carbonization of PS@PAA, forming continuous carbon network that encapsulates the formed $ZnFe_2O_4$ nanoparticles. The synergy of nanoscopic $ZnFe_2O_4$ particles and their hybridization with a continuous conductive carbon network contributes to excellent rate performance and prolonged cycling stability over several hundred cycles when the $ZnFe_2O_4$ (79.3 wt%)/carbon nanocomposites are investigated as anodes for lithium ion batteries (LIBs). We envision that this synthetic strategy is simple and robust, and can be readily extended for the preparation of other carbon hybridized electrode materials for high-performance LIBs.

Finally, we crafted corn-like SnO_2 nanocrystals, composed of hundreds of SnO_2 nanoparticles (~5 nm) decorated along the cob with a large number of pores between SnO_2 nanoparticles, using judiciously designed bottlebrush-like hydroxypropyl cellulose-*graft*-poly (acrylic acid) (HPC-*g*-PAA) as template and coated the corn-like SnO_2 with a thin layer of protective polydopamine (PDA). The synergy of the corn-like nanostructures and the protective PDA coating enabled the excellent electrochemical performance for the PDA-coated corn-like SnO_2 electrode, including the superior long-term cycling stability, high $Sn \rightarrow SnO_2$ reversibility, and excellent rate capability. We envisage that the bottlebrush-like polymer templating strategy is facile and robust, and can be readily extended to create a rich variety of other functional metal oxides and metal sulfides for high-performance LIBs.

The bottom-up crafting of functional hybrid organic-inorganic nanocomposites offers new levels of tailorability to nanostructured materials and promises new opportunities for achieving exquisite control over the surface chemistry and properties of

nanocomposites with engineered functionality for diverse applications in energy conversion and storage, catalysis, electronics, nanotechnology, and biotechnology.

Chapter 1 Introduction

1.1 Background of hybrid nanocomposites

Hybrid nanocomposites obtained by integrating two or more materials at the nanoscale with complementary properties offer the potential to achieve performance, function and hierarchical architecture far beyond those of each constituent.[20] Usually, the properties of hybrid nanocomposites are not simply the sum of the individual contributions, but are dominated by the interplay of the inherent properties of each constituent, the hierarchical structure and the inner interfaces.[1] The research into functional hybrid nanocomposites has become a mushrooming field of investigation, yielding innovative advanced materials with high added value. Various types of organic-inorganic hybrid nanocomposites have been investigated for achieving improved or unusual features that could allow myriad innovations, such as new generation of catalysts and electrolyte membranes for fuel cells, [21-22] new generation of photovoltaic devices, [23-24] smart microelectronic devices, [25-26] next generation lithium ion batteries (LIBs),[27-28] high energy density capacitors, [5, 29] etc. In this chapter, the background of hybrid nanocomposites will be introduced by reviewing the general strategies for designing functional hybrid nanocomposites, the basics of two common hybrid organic-inorganic nanocomposites (i.e. polymer-ceramic nanocomposites and electrochemically active-inactive nanocomposites), the general approaches for preparing polymer-ceramic nanocomposites and active-inactive nanocomposites, and finally the chemistry of polymer-templated approach for preparing hybrid nanocomposites. The advantages and challenges of polymer-templated approach for preparing hybrid nanocomposites are also briefly discussed.

1.1.1 General strategies for designing functional hybrid nanocomposites

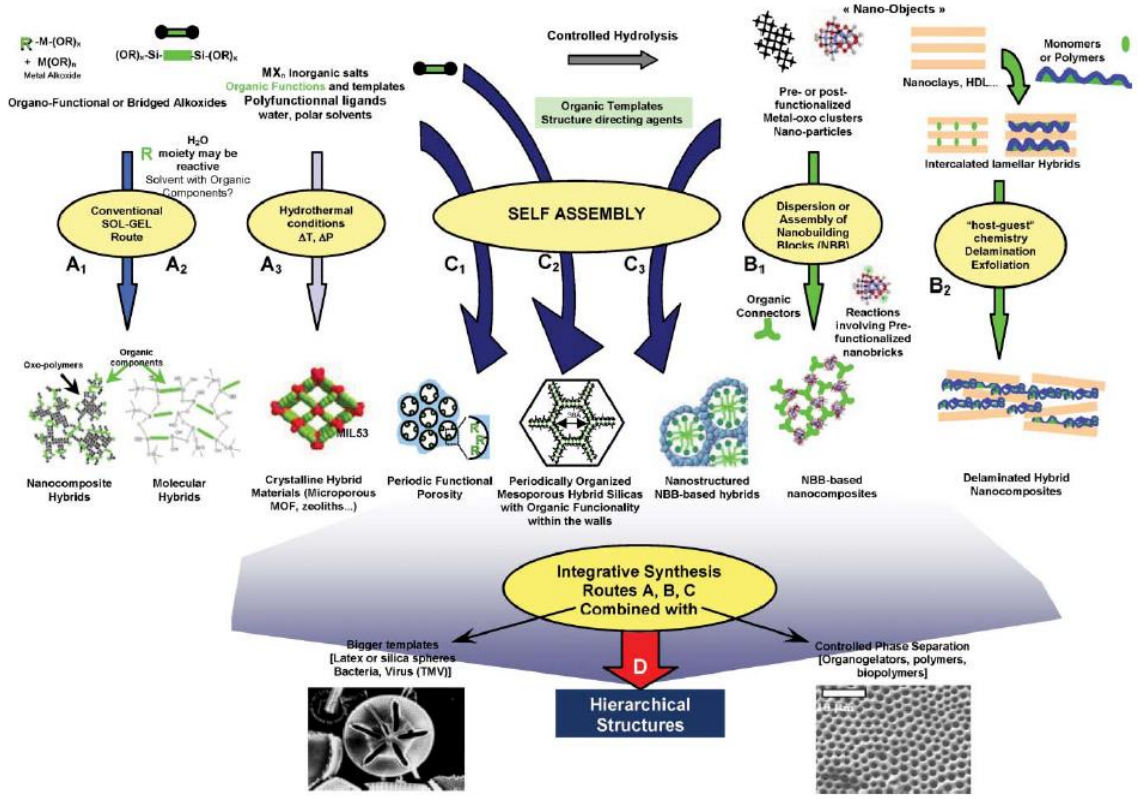

Figure 1.1 Scheme of the main chemical routes for the synthesis of organic-inorganic hybrid nanocomposites. [1] Copyright © The Royal Society of Chemistry 2005

The easiest way to prepare hybrid organic-inorganic nanocomposites is physically mixing the components together. However, due to the interfacial incompatibility and high surface energy of inorganic nanoparticles, [29-30] serious problems such as phase separation and the agglomeration of nanoparticles will be created.[5, 30] To this end, many chemical pathways have been implemented for tailoring the organic/inorganic interface of a given hybrid material. According to the nature of the interfacial bonding, hybrid nanocomposites can be divided into two distinct classes. In class I materials, the organic and inorganic components are embedded and only week bonds (such as hydrogen bonding, van der Walls or ionic bonds) give the cohesion to the whole structure. In class

II materials, strong chemical bonds (e.g. covalent or ionic-covalent bonds) are existed in the interface for linking different components together. [31] The main chemical routes for all types of organic-inorganic hybrid nanocomposites are schematically illustrated in **Figure 1.1**. Path A corresponds to the conventional soft chemistry based routes, including conventional sol-gel pathways as shown in route A_1, the use of specific bridged precursor or polyfunctional precursors (route A_2) and hydrothermal synthesis (route A_3). Some of the chemical routes will be discussed in details in this chapter.

For route A_1, hybrid nanocomposites can be processed via the encapsulation of organic components (such as organic molecules, oligomers, macromonomers, and biocomponents) within sol-gel derived siloxane-oxide matrices or metal oxide-based networks just by mixing organic components with metal alkoxides or/and organosilanes in a common solvent. During the hydrolysis and condensation reactions of metal alkoxides or/and organosilanes, the organic components may become crosslinked, or they can interact or get trapped within the inorganic components through a large set of fuzzy interactions (H-bonds, π-π interations, van der Waals).[1] Despite the simplicity and low cost of this strategy, route A_1 usually yield amorphous hybrid nanocomposite materials and the inorganic components are generally polydisperse in size and locally heterogeneous in chemical composition, and thus requires more understanding and better control of the local and semi-local structure in order to achieve higher degree of organization and homogeneity in the yielded hybrid organic-inorganic nanocomposites.[1]

The strategy listed in route A_2 is based on the same sol-gel chemistry as route A1 but usually use specific bridged precursors such as silsesquioxanes $X_3Si\text{-}R'\text{-}SiX_3$ (where R' is an organic group covalently bound to n groups of $-SiX_3$, X=Cl, Br, OR) for constructing hybrid organic-inorganic nanocomposites. In the beginning, the hydrolysis/polycondensation of precursors occur, forming a short-range ordered organization of 3-D organized structures controlled by the van der Walls interactions

between the organic units. In the following step, the short-range order extends to larger domains due to the formation and redistribution of Si-O-Si bonds by hydrolysis/polycondensation of Si-OR groups, leading to the formation of homogeneous molecular silicon-based hybrid organic-inorganic nanocomposites having a better degree of local organization.[1, 32] In recent work, some modifications have been made by incorporating urea functional group to the bridged silsesquioxanes precursors for realizing targeted morphologies. The organo-bridged precursors bearing urea groups first self-assembly into designed supramolecular architectures through the strong hydrogen bonding between urea groups, then through judiciously hydrolyzing the precursors, highly crystalline organic-inorganic hybrids with variable morphologies (fibers, spheres and tubes, and sheets) can be created.[33-36] The uniqueness of path A_1 and path A_2 is that they can mix the organic and inorganic components at the molecular level due to the use of organic bridged inorganics containing precursors.

Route A_3 introduces the hydrothermal/solvothermal synthesis in polar solvents (water, formamide, etc.) in the presence of organic templates for creating hybrid nanocomposites. A new generation of hybrid materials that have been created through route A_3 is highly microporous Metal Organic Frameworks (MOF) which usually exhibit very high surface areas. They possess magnetic or electronic properties, which are promising for an extensive number of applications.[37-40]

Path B corresponds to the assembling or the dispersion of well-defined functional nanobuilding blocks (NBBs) that are generally capped with polymerizable ligands and can be connected through organic spacers or surface-driven condensation reactions or as a reservoir of inorganic matter that can be delivered at the hybrid interface to build an extended inorganic network or connected through organic spacers.[41] These NBBs are quite diverse in nature, structure, and functionality, including clusters, organically functionalized nanoparticles, or layered compounds that are able to intercalate organic

components. Such flexibility and diversity in the choices of NBBs together with the use of organic templates that can self-assemble allows one to create an amazing range of hierarchical architectures and interfaces with tunable functionalities.[1, 41]

Path C describes another self-assembling procedure for constructing organic-inorganic hybrid nanocomposites. They can be achieved through the organization or the texturation of growing inorganic components or hybrid networks with organic surfactants as template, as described in route C_1. This approach is also able to build a whole continuous range of nanocomposites, from ordered dispersions of inorganics in a hybrid matrix to highly controllable nano-segregation of organic polymers within inorganic matrices.[42] The hybrid nanocomposites can also be achieved through the templated growth of mesoporous hybrids by using bridged silsesquioxanes as precursors in the present of surfactants (route C_2).[43] Route C_3, which combines nanobuilding block approaches with the use of organic templates that can self-assemble and allows the control of the assembling step, is another promising strategy for realizing hybrid nanocomposites with tunable functionalities.[44-45]

1.1.2 Functional hybrid nanocomposites for energy storage applications

With the rapid development of global economy, the depletion of fossil fuels and the environmental contamination are driving scientists and engineers to develop environmental friendly, renewable, and highly efficient methods of creating and storing energy. New clean energy sources such as solar energy, mechanical energy, thermal energy, biochemical and chemical energy have been widely studied. This also motivates the development of high-performance energy storage systems. Better electrical energy storage devices in terms of more energy stored and maximum power as well as size and weight, cost, lifetime, etc. are also under rapid development driven by their applications.[46] Functional hybrid nanocomposites for energy storage applications have

been created by selecting appropriate components with desired properties, designing the interface and functionality, and controlling the connectivity of the multiphase nanocomposites in a controlled manner, as the energy storage performance of these devices depends crucially on the properties of these hybrid nanocomposites.

Well-developed energy storage devices, such as capacitors, are highly desirable for energy pulse and power conditioning applications. However, traditional dielectric ceramics in capacitors cannot store enough energy in the available volume and weight, due to the intrinsic dielectric properties of large permittivity but relative small breakdown strength of ceramic materials. Large electric energy storage in capacitor devices requires the dielectric materials to exhibit both large permittivity and high breakdown strength, since the electric energy density that can be stored in a dielectric material is limited to $\varepsilon E_b^2/2$, where ε and E_b are the dielectric constant and breakdown strength of the material, respectively.[47-48] It is thus not surprising that ceramic-polymer nanocomposites combining polymers of high breakdown strength with ceramic nanoparticles of high permittivity would enhance greatly the electric energy density of the resulting capacitors.[49-50] The approach of combining the advantages of both components in the ceramic-polymer nanocomposites is appealing for two reasons. First, there are large interfacial areas in polymer-ceramic nanocomposites, which could promote interfacial exchange coupling through a dipolar interface layer and lead to enhanced polarization and polarizability in polymer matrix near the interface. As a result, enhanced permittivity can be expected in the polymer matrix near the interface.[51] Second, the nanoscale ceramic materials also make it possible to reduce the thickness of polymer matrix film to nanoscale, since the electrical breakdown strength increases when decreasing the sample thickness, [52] the already high breakdown strength of polymer matrix can be further enhanced by avoiding avalanche effects in the resulting nanocomposites.[53] Both effects are beneficial for enhancing electric energy density. Other advantages of the polymer-

ceramic nanocomposites include the facile solution processibility, mechanical flexibility, and reduced weight for device scalability. The capacitors based on polymer-ceramic nanocomposites are promising to possess energy density values close to or higher than that of linear dielectric capacitors.

Another rapidly developed new energy storage technology is rechargeable lithium batteries (e.g. lithium ion batteries (LIBs)), which stores electrical energy through storing Li ions in the electrochemically active materials. For example, graphite, which is the widely used commercialized anode material, stores energy through the reversible intercalation of Li ions between graphite layers with up to one Li atoms intercalated per six C atoms under ambient conditions (i.e. forming LiC_6).[54] However, the strong desire of enhancing energy density and power density of LIBs requires the electrode materials to store more Li ions within a shorter time period. As a result, a variety of rationally designed electrochemically active-inactive hybrid nanocomposites composed of electrochemically active material which can react with lithium and inactive material which cannot react with lithium but usually has other useful functions have been widely exploited as advanced electrode materials for LIBs.[55] In such active-inactive hybrid nanocomposites, the electrochemically active materials are capable of storing much more Li ions than graphite, while the inactive materials usually serve for multifold functions, including capable of conducting charges quickly for enhancing the power rate, capable of protecting the structural stability of active materials for achieving long cycle life, to name a few. Therefore, active-inactive nanocomposites are emerging as promising electrode materials for significantly enhancing the energy density and power density of the corresponding LIBs.

1.2 Polymer-ceramic nanocomposites as dielectric materials for capacitors

1.2.1 Connection types of binary polymer-ceramic nanocomposites

Constructing composites by combining multiphase materials together means not only choosing component phases with the desired properties, but also coupling them in the best manner. Connectivity of a composite material describes the manner how each phase is self-connected and coupled with other phases, i.e. the interspatial relationships in a multiphase material. It is well known that the connectivity between phases in the multiphase composite materials is very important in achieving the designed properties, since physical properties can change by many orders of magnitude depending on the manner in which connections are made. [56] Connectivity pattern of the polymer-ceramic nanocomposites controls their mechanical, electrical, thermal, dielectric, ferroelectric properties, to name a few. [56-59]

The connectivity of one phase in the composite material is defined by how many dimensions the phase is self-connected. For example, if a phase is self-connected in three dimensions, its connectivity is termed as 3. If a phase is self-connected in two dimensions, its connectivity is termed as 2, and so on. Considering a two-phase composite material, its connectivity is defined by combination of terms m-n, where m presents the connectivity of the active phase (filler) while n represents the connectivity of the inactive phase (matrix). [2] There are ten connectivities for a two-phase composite material: 0-0, 0-1, 1-1, 0-2, 1-2, 2-2, 0-3, 1-3, 2-3, and 3-3, depending on how each phase is self-connected. [2, 60] The ten connectivities of a two-phase composite material is illustrated in **Figure 1.2**, in which two kinds of cubes, shaded and unshaded, are used to represent the

basic building block of the two different phases. [2] For 1-2 connectivity pattern, one phase is self-connected in two-dimensions, and the other phase is self-connected in one dimensional chains or fibers. In the 1-3 connectivity pattern, the shaded phase is three-dimensionally connected and the unshaded phase is one-dimensionally connected. The 2-2 patterned composite is made up of alternating layers of the two phases, and both phases are self-connected in the lateral X and Y directions but not connected perpendicular to the layers along Z. 3-3 patterned connectivity, in which two phases form interpenetrating three-dimensional networks, is the most complicated pattern. Patterns of this type often occur in living systems such as coral where organic tissue and an inorganic skeleton interpenetrate one another. [60]

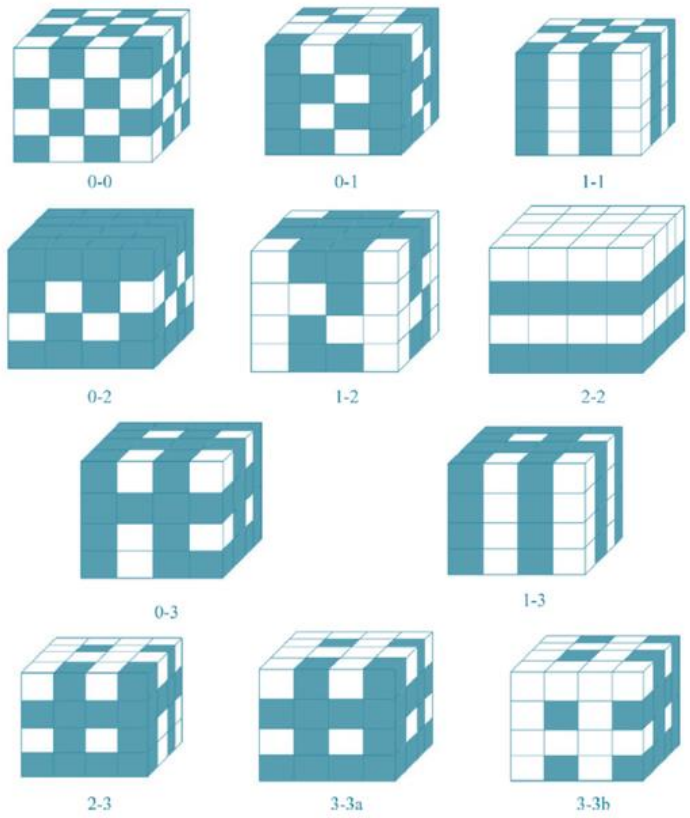

Figure 1.2 Ten connectivity patterns for two-phase composite materials. Each phase has zero-, one, two or three dimensional connectivity to itself.[2] Copyright © 2011Elsevier Ltd

0-3 patterned polymer-ceramic composites, in which a three-dimensionally connected polymer phase is loaded with isolated ceramic particles, are the most attractive form the application point of view. In 0-3 patterned polymer-ceramic composites, the two phases are homogeneously mixed without any phase segregation, resulting in excellent dielectric properties with high dielectric constant and high breakdown strength.[61] Composites of 0-3 connectivity enable flexible forms and very different shapes with very inexpensive fabrication methods including mechanical mixing, solution mixing, and molding. [56] Interfacial effects can occur between the ceramic grains and the polymer matrix, leading to large dielectric relaxations normally at low frequencies (called Maxwell–Wagner relaxations). [62]

1.2.2 Theoretical models of dielectric properties of polymer-ceramic nanocomposites

A number of models have been proposed for predicting the dielectric properties of the polymer-ceramic composites composed of high dielectric constant ceramic fillers and high breakdown strength polymer matrix. Depending on the loading amount of the ceramic fillers and the connectivity pattern of the polymer-ceramic hybrid composites, three common models are most accepted and they are Maxwell-Garnett equation, Bruggeman self-consistent effective medium approximation, and Jaysundere-smith equation.

1.2.2.1 Maxwell-Garnett equation

Considering the mixing condition when ceramic particles of permittivity k_f (volume fraction is $\emptyset_f$) are mixed into an isotropic polymer matrix of dielectric

permittivity k_m(volume fraction is $\emptyset_m$, $\emptyset_m$=1-$\emptyset_f$). The permittivity of the two-phase ceramic-polymer composite (k_c) lies between a lower permittivity ($k_{c,min}$) and an upper permittivity ($k_{c,max}$) value ($k_{c,min} \leq k_c \leq k_{c,max}$), and the two limiting values are described by the following equations: [2]

$$k_{c,min} = \frac{k_m k_f}{k_m \emptyset_f + k_f \emptyset_m} \qquad (1.1)$$

$$k_{c,max} = k_m \emptyset_m + k_f \emptyset_f \qquad (1.2)$$

The lower permittivity ($k_{c,min}$) describes a series model in which both phases are self-connected in two dimensions (2-2 type connectivity), forming a layer parallel to the electrode films deposited on the surface, as shown in **Figure 1.3a**. The upper permittivity ($k_{c,max}$) corresponds to the parallel model as shown in **Figure 1.3b**, in which each phase is self-connected in two dimensions, while the layer formed is perpendicular to the electrode film. [2] The practical two-phase composites are described by the mixing model as shown in **Figure 1.3c.**

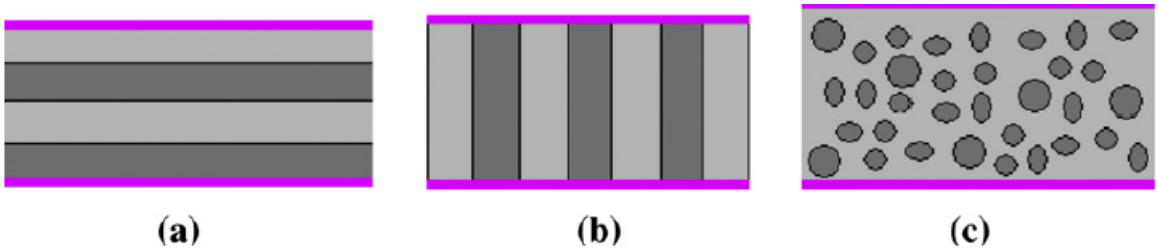

Figure 1.3 Ideal connection types of two-phase ceramic-polymer composites, (a) series model, (b) parallel model, and (c) a mixing model for the practical composites. The pink lines stand for electrodes. [2] Copyright © 2011 Elsevier Ltd

Further efforts in modeling the dielectric properties of two-phase composites have achieved a more accurate equation (the Maxwell-Garnett equation) for predicting the

dielectric properties of composites. The Maxwell-Garnett equation is valid for lower concentration of ceramic filler and is as described by equation 1.3: [2, 63]

$$k_c = k_m[1 + \frac{3\emptyset_f(k_f - k_m)}{(1-\emptyset_f)(k_f - k_m)+3k_m}] \qquad (1.3)$$

For more general situations when the ceramic particles are not spherical in shape, the modified Maxwell-Garnett equation, which takes into account of the geometry of the dispersed particles in the polymer matrix, is more accurate in predicting the dielectric properties of the two-phase composites. The more general Maxwell-Garnett equation considering the geometry of dispersed particles is in the following form as described equation 1.4, [2] where the parameter A is the depolarization factor and A=1/3 for spherical particles.

$$k_c = k_m[1 + \frac{\emptyset_f(k_f - k_m)}{A(1-\emptyset_f)(k_f - k_m)+k_m}], \quad \text{for } \emptyset_f < 0.1 \qquad (1.4)$$

As described above, the Maxwell-Garnett equation is reasonable for composites consisting of a continuum polymer matrix with low amount of embedded inclusions. [64]

1.2.2.2 Bruggeman self-consistent effective medium approximation

In contrast to the Maxwell-Garnett equation, the Bruggeman self-consistent effective medium approximation treats each phase equally, assuming all components are randomly mixed together. [64-65] This theory has been widely used to predict the dielectric and optical properties of composite materials, and provided more valid predictions at a much higher content of spherical filler (up to 0.5). The final Bruggeman's formula is described as in equation 1.5: [2]

$$\frac{k_f - k_c}{k_c^{1/3}} = \frac{(1-\emptyset_f)(k_f - k_m)}{k_m^{1/3}} \quad (\emptyset_f \ll 0.5) \qquad (1.5)$$

1.2.2.3 Jaysundere-smith equation

In the situation when a low concentration ($\emptyset_f < 0.1$) of filler is present in the composite, as shown in **Figure 1.4a**, the interaction between filler particles is too weak due to a large distance between filler particles and is often neglected. Therefore, the Maxwell-Garnett equation is valid in the course of theoretical prediction for dielectric properties. However, at higher concentration of fillers when the particles are closely located, as described by **Figure 1.4b**, the interaction between fillers is becoming significant and the electrical field arising from the distribution of dipole moment is no more negligible when calculating overall field locally experienced in the matrix. Taking into consideration of both the two factors, the Jaysundere-smith equation is described as follows in equation 1.6: [2]

$$k_c = \frac{k_m \emptyset_m + k_f \emptyset_f \frac{3k_m}{(2k_m + k_f)}\left[1 + 3\emptyset_f \frac{k_f - k_m}{2k_m + k_f}\right]}{\emptyset_m + \emptyset_f \frac{3k_m}{(2k_m + k_f)}\left[1 + 3\emptyset_f \frac{k_f - k_m}{2k_m + k_f}\right]} \qquad (1.6)$$

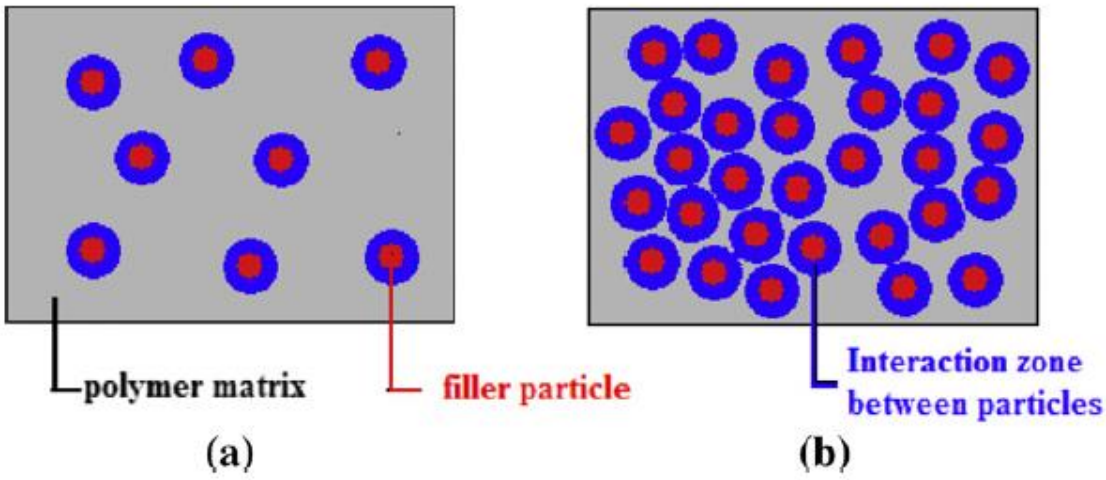

Figure 1.4 A schematic showing the distribution of filler particles in a polymer matrix at (a) low concentration of fillers and (b) high concentration of fillers. [2] Copyright © 2011 Elsevier Ltd

1.2.3 General strategies for preparing polymer-ceramic nanocomposites

The energy density stored in dielectric materials is proportional to the dielectric constant and electric field (E) according to the equation 1.7:

$$U = \frac{1}{2}\varepsilon_0\varepsilon_r E^2 \qquad (1.7)$$

where ε_0 is the dielectric permittivity of vacuum, ε_r is the relative permittivity of the dielectric materials, and E is the applied electric field. Therefore, the maximum energy density depends on both the dielectric permittivity and electric breakdown strength (E_b) of the dielectric material. [66-67] Polymer-ceramic nanocomposites composed of high permittivity ceramic nanoparticles and high dielectric strength polymer matrix are currently of considerable interest, as they can be solution processed on large and flexible substrate at low temperatures and ambient pressures, and have been successfully

demonstrated as high-quality dielectric nanocomposites for electronic applications such as embedded capacitors, multilayer capacitors, high-energy-density capacitors, and gate insulators in organic field effect transistors. [68-70] To obtain polymer-ceramic nanocomposites with both high permittivity and high dielectric strength suitable for practical applications as high energy density dielectric materials, large volume fraction (＞30%) of ceramic nanoparticles are needed but this usually leads to problems such as nanoparticles agglomeration and phase separation from the polymer host matrix due to the high specific surface area and high surface energy of ceramic nanoparticles. [68] As a result, poor processability, high defect density, large leakage currents and low breakdown strength are expected for the yielded polymer-ceramic nanocomposites dielectric materials. To avoid these problems, especially at high volume fractions of ceramic nanoparticles, synthetic approaches that enable a homogeneous distribution of each constituent in the nanocomposites and a well-defined interface between them are of great importance.[71]

Surface modification of ceramic nanoparticles with functional ligands has emerged as an effective strategy to mitigating these problems. Surface modification of ceramic nanoparticles produces excellent integration and improves the interfacial interactions between ceramic nanoparticles and the polymer matrix, and hence enhances the homogeneity of the nanocomposites. The dispersion behavior of surface modified ceramic nanoparticles in a polymer matrix is described in **Figure 1.5**. [3] As shown in **Figure 1.5a**, the bare ligand-free nanoparticles tend to aggregate together, leading to phase separations in the nanocomposites. However, the aggregated nanoparticles become further separated after grafting with some macromolecular chain (**Figure 1.5b**), and the

polymer-grafted nanoparticles have much better miscibility with the polymer matrix due to increased hydrophobicity. [72]

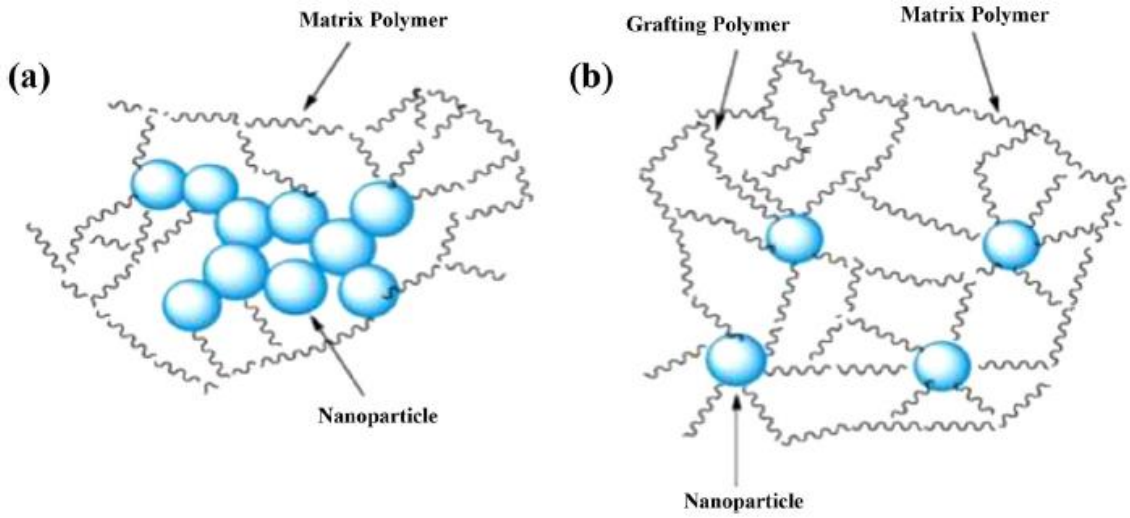

Figure 1.5 Schematics of :(a) agglomerated nanoparticles in the matrix polymer in the case without polymer and (b) separation of particles due to the grafting polymer. [3] Copyright © 2013 Elsevier Ltd

Different surface modification techniques lead to different interfacial interactions between ceramic nanoparticles and polymer matrix. The ideal features of well-controlled polymer-ceramic interface would be (a) robust, stable, and physically thick insulating layers to prevent direct particle-particle contact, (b) a shielded and buried polar or charged interface between the ceramic nanoparticles and the polymer matrix, and (c) increased dispersibility of the modified ceramic nanoparticles by matching the solubility parameters of the outer surface of the nanoparticles with polymer matrix.[5] Covalent attachment of organic molecules or polymer chains to the surface of ceramic nanoparticles provides a stable and passivated interface that is of key importance to realizing homogenous distribution of the modified ceramic nanoparticles to polymer matrix. Surface passivation through covalently attaching ligands to a surface have been

accomplished by two main strategies, that is, "grafting-to" (chemically binding end-functionalized small molecules, oligomers or preformed polymers to the nanoparticle surface through charged or polar-polar interaction) [5, 70, 73-74] and "grafting-from" (initiating the controlled polymerization from the nanoparticle surface functionalized with an initiator).[30, 75] The schematic representations of the "grafting-to" and "grafting-from" methods are shown in **Figure 1.6**. Each strategy will be discussed in detail in the following part, as the appropriate surface modification agent is essential in fabricating ceramic-polymer nanocomposites of excellent energy storage properties. In-situ synthesis of ceramic nanoparticles in the presence of polymer better at tailoring the interface interactions will also be introduced.

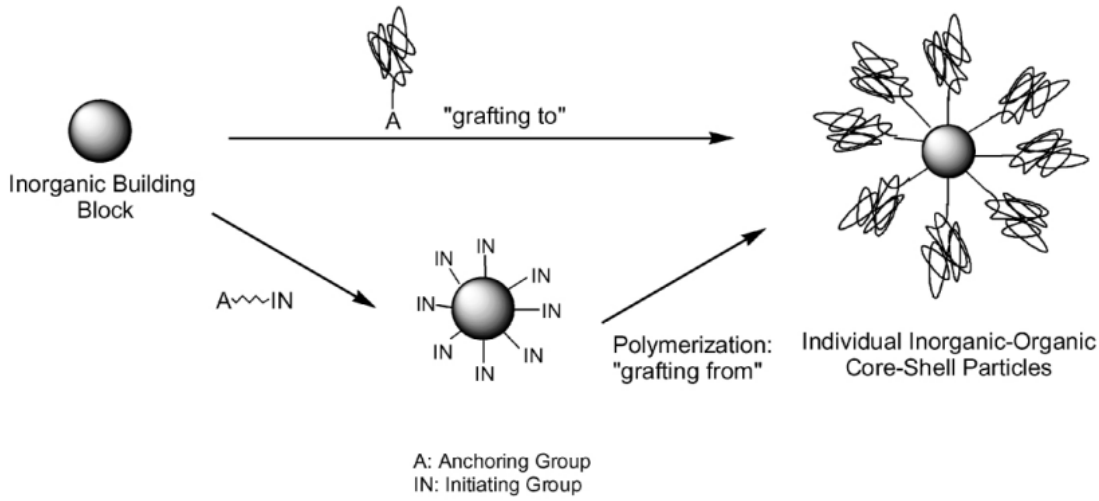

Figure 1.6 Schematic description of grafting-to and grafting-from approaches for the synthesis of inorganic-organic core-shell nanoparticles. [4] Copyright © 2002 Elsevier Science Ltd

1.2.3.1 "Grafting-to" approach to modify the surface of ceramic nanoparticle

Various ligands have been demonstrated to be able to functionalize the surface of nanoparticles when they are grafted to nanoparticles surface, and improved interfacial compatibility and better dispersion of modified ceramic nanoparticles in various host polymer matrics have been achieved. [29, 68, 70] For example, researchers have demonstrated that phosphonic acids can form a robust and functional organic shell on the surface of perovskite-type metal oxide nanoparticles (e.g. Barium Titanate ($BaTiO_3$)) by a simple solution-processing technique of mixing nanoparticles with the polymer ligand bearing the phosphonic acid functional group in an ethanol/water solution. [29, 70] Such modification of metal oxide nanoparticles surface is thought to be rendered either by heterocondensation of phosphonic acid with surface hydroxyl groups or coordination to metal ions on the surface. [70] They further showed that the phosphonic acid-modified $BaTiO_3$ nanoparticles with high surface coverage can be homogeneously incorporated into poly(vinylidene fluoride-cohexafluoropropylene) (P(VDF-HFP)) polymer matrix and the resulting $BaTiO_3$-polymer nanocomposite films exhibit good phase stability, high film quality, and large maximum energy storage density at optimized volume fraction of $BaTiO_3$ nanoparticles.[29, 68, 70]

Polyvinylprrolidone (PVP) has also been demonstrated as a good surface modification agent for $BaTiO_3$ nanoparticles in fabricating polymer-ceramic nanocomposites, as PVP can interact strongly with surface hydroxyl groups of $BaTiO_3$ nanoparticles and be coated on the surface of $BaTiO_3$ nanoparticles. [66, 76-77] By mixing PVP with $BaTiO_3$ nanoparticles in ethanol and sonicating the solution for enough time, a complete coating of PVP on the surface of $BaTiO_3$ nanoparticles can be achieved, which

makes the PVP-modified $BaTiO_3$ nanoparticles soluble in some organic solvents (e.g. N, N-dimethylformamide(DMF)). [66] Besides, the PVP-functionalized $BaTiO_3$ nanoparticles have very high compatibility in PVDF polymer matrix due to the strong specific dipolar interaction between the PVP's carbonyl group(C=O) and the PVDF's fluorine group (C=F2), leading to a high homogeneity in the PVP-modified $BaTiO_3$-PVDF nanocomposites.[78] The resulting nanocomposites exhibit greatly enhanced dielectric permittivity, electric breakdown strength and energy density, which can be attributed to the improvement of the homogeneity of the nanocomposites after PVP surface modification. [66]

Diblock copolymer polystyrene-*b*-poly (styrene-co-vinylbenzylchloride) (PS-*b*-PSVBC) has also been reported as a good surface modifier and passivation layer for realizing good dispersibility of $BaTiO_3$ nanoparticles in a nonpolar polystyrene matrix. As shown in **Figure 1.7a**, a two-step process was implemented to fabricate the core-shell structured polymer-coated $BaTiO_3$ nanoparticles, where PS-*b*-PSVBC was introduced as the stable polymer shell for the complete wrapping of $BaTiO_3$ nanoparticlse. In the first step, the chloromethyl group in PS-b-PSVBC was reacted with an oxy anion on the surface of $BaTiO_3$ nanoparticles, forming an organic layer consisted of covalently bonded PS-*b*-PSVBC and a weakly absorbed second layer surrounding the $BaTiO_3$ nanoparticles. In the second step, the nonpolar chloromethyl functional blocks of the unstably absorbed PS-*b*-PSVBC was transformed *in situ* into the polar ammonium blocks through triethylamine treatment process, which form a polar inner layer and interact strongly with the $BaTiO_3$ nanoparticles surface. As a result, the nonpolar polystyrene block outer layer and the polar ammonium-containing block inner layer self-assembled to form the stable,

layered and dense polymer shell. This surface polymer shell was directly observed by TEM as shown in **Figure 1.7b**, exhibiting a uniform thickness of 5-7 nm without any noncovered sites. The PS-*b*-PSVBC modified $BaTiO_3$ nanoparticles demonstrated good dispersibility into polystyrene matrix even at a high volume fraction of 33 vol %, resulting in homogeneous ($BaTiO_3$/PS-*b*-PSVBC)/polystyrene nanocomposites film with low leakage current, high dielectric permittivity (ε_r=44 at 10kHz), large breakdown strength (222±14V/μm) and high energy density (9.7 J/cm^3).[5]

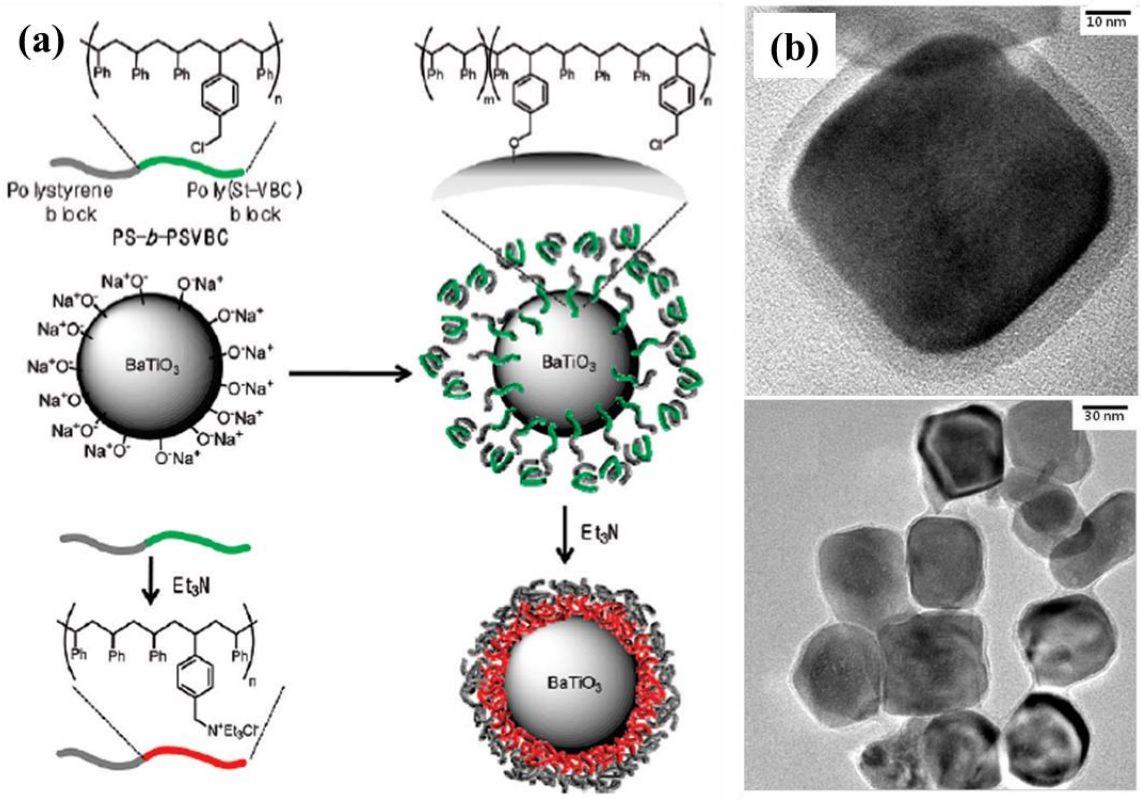

Figure 1.7 (a) Schematic illustration of the formation of $BaTiO_3$ nanoparticles with the polymer shell (PS-b-PSVBC). (b) TEM images of $BaTiO_3$ nanoparticles coated with PS-b-PSVBC after amine treatment. The 5-7 nm thickness PS-*b*-PSVBC layers were clearly shown on the $BaTiO_3$ nanoparticles, and these layers were intact and stable after dispersion in THF or toluene. [5] Copyright © 2009 American Chemical Society

Despite various successful demonstrations of surface modification by “grafting-to” method, there are still many problems existed with this surface modification approach. For example, incomplete surface coverage or insufficient interaction between the surface modifier and polymer matrix may occur, therefore, the interface between the ceramic nanoparticles and the polymer matrix is relatively loose, and an abrupt decrease of the dielectric breakdown strength can be observed when relatively large amount of nanoparticles are present in the polymer-ceramic nanocomposites.[30, 79] A reversible interaction between the organic surface modifiers and the ceramic surface may also occur which usually interferes with the formation of a robust polymer shell and results in increased current leakage and lower breakdown voltage when the composite ratio of the ceramic nanoparticles in the polymer matrix is very high. [5] Meanwhile, many other surface modification approaches better at tailoring the interface are widely investigated to prepare high performance nanocomposites with the universally desirable properties of dielectric materials for use in energy storage devices.

1.2.3.2 "Grafting-from” approach to modify the surface of ceramic nanoparticle

A higher percentage of successful grafts in polymer-modified nanoparticles with a higher polymer grafting density can be obtained by the “grafting-from” approach. The “grafting-from” polymerization process, which may include radical, anionic and cationic polymerization methods, involves propagation of the grafted polymers from the surface of the ceramic nanoparticle.[3, 80] Such methods afford control over the molecular weight, the distribution of molecular weight, and structure of the resulting polymers. So far, the application of controlled “living” polymerization technique to the synthesis of ceramic-

polymer nanocomposite is widely explored. For instance, Guo *et al*. prepared a series of high dielectric constant polyolefin-metal oxide nanocomposites by *in situ* polymerization of olefin on the surface of metal oxide nanoparticles which were coated with methylaluminoxane (MAO). [81] The obtained polymer-metal oxide nanocomposites exhibited respectable permittivities and high breakdown strengths at low particle loadings. However, the nanocomposites at a high particle loading (7 vol%) showed significantly increased leakage current density. More recently, Marks *et al*. implemented *in situ* polymerization of propylene by catalysts anchored on the Al_2O_3-coated $BaTiO_3$ and ZrO_2 nanoparticles surface, yielding homogeneously dispersed nanoparticles in a polyolefin matrix. The nanocomposites, with high permittivity, small dielectric loss, are attractive for large energy storage capacities. [75]

The method of surface-initiated reversible addition fragmentation chain transfer (RAFT) polymerization was carried out by Yang *et al*. to prepare a series of fluoro-polymer-coated $BaTiO_3$ nanoparticles for tailoring the interface between $BaTiO_3$ nanoparticles and polymer matrix (**Figure 1.8a**).[6] TEM images in **Figure 1.8b** show that a stable and dense polymer shell without any noncovered sites was directly coated on the surface of $BaTiO_3$ nanoparticles. In addition, the insulating fluoro-polymer shell structures and thicknesses can be rationally adjusted during the RAFT polymerization process so that the interface between $BaTiO_3$ nanoparticles and the polymer matrix can be modulated. The fluoro-polymer modified $BaTiO_3$ nanoparticles demonstrated excellent compatibility when they were mixed with ferroelectric polymer poly (vinylidene fluoride-co-hexafluoro popylene) (P(VDF-HFP)), as the fluoro-polymer shells have similar chemical structure and surface energy to P(VDF-HFP) matrix,

therefore, strong interfacial adhesion between $BaTiO_3$ nanoparticles and the ferroelectric polymer matrix is obtained. The fluoro-polymer modified $BaTiO_3$ nanocomposites demonstrated good dispersity in the polymer marix and no agglomeration could be found (**Figure 1.8 c**). The resulting P(VDF-HFP)–$BaTiO_3$ nanocomposites by the dispersion of thick fluoro-polymer-coated $BaTiO_3$ nanoparticles in P(VDF-HFP) matrix exhibited significantly enhanced energy storage capability and low dielectric loss. Moreover, the energy storage density for the nanocomposites could be tailored by adjusting the structure and thickness of the fluoro-polymer shell. [6]

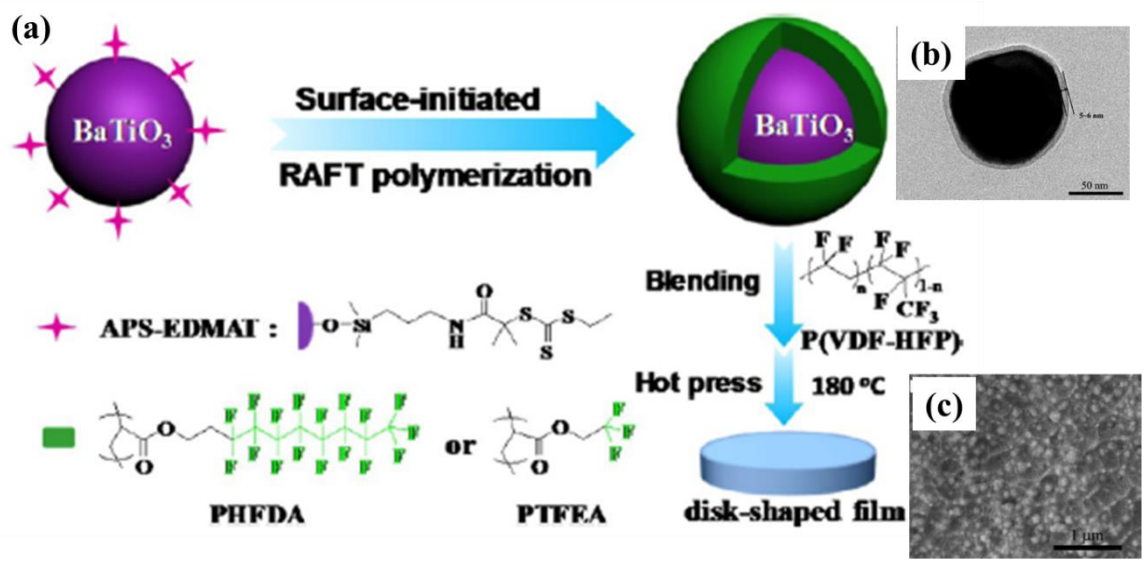

Figure 1.8 (a) Schematic illustration for the preparation of fluoro-polymer coated $BaTiO_3$ nanoparticles and (P(VDF-HFP)) nanocomposite films. (b) TEM images of a fluoro-polymer coated $BaTiO_3$ nanoparticle, the fluoro-polymer shell is clearly seen with a thickness of 5-6 nm. (c) SEI images of the resulting P(VDF-HFP)–$BaTiO_3$ nanocomposites. [6] Copyright 2013 American Chemical Society.

Controlled *in situ* atom transfer radical polymerization (ATRP) has been widely used to grow polymers from a variety of nanocrystal surface, including silica, [82-83] gold, [84] nanotubes, [85-86] and graphene oxide. [87] The "grafting-from" method, ATRP, can graft various kinds of polymers and can achieve a higher graft density and a higher

capping efficiency, allowing accurate tailoring of the thickness and composition of the polymer layer.[88] A broad range of monomers have been polymerized by *in situ* ATRP method to modify the surface of ceramic nanoparticles for creating ceramic-polymer nanocomposites with enhanced energy storage performance. For example, Marder *et al*. reported the grafting of polystyrene and poly (methyl methacrylate) (PMMA) polymer on $BaTiO_3$ nanoparticles through ATRP with a phosphonic acid as surface initiator, and the one-component PMMA-$BaTiO_3$ nanocomposites achieved a maximum extractable energy density of 2 J/cm^3 at a field strength of ~220 V/ μm. [89] Poly (di(ethylene glycol) methyl ether methacrylate) was also successfully grafted from the surface of TiO_2 nanoparticles by ATRP, yielding the core-shell structured TiO_2-polymer nanocomposites with elevated value of dielectric permittivity and low loss tangent. [90] Recently, high performance core-shell structured $BaTiO_3$-PMMA nanocomposites was demonstrated by in situ ATRP approach.[87] As shown in **Figure 1.9a**, the surface of $BaTiO_3$ nanoparticles was functionalized with reactive hydroxyl (-OH) groups for further conversion into brominated $BaTiO_3$ nanoparticles, which introduced a sufficient quantity of initiating sites for ATRP reaction. The following *in situ* ATRP of methyl methacrylate (MMA) monomer under an oxygen-free atmosphere successfully grafted PMMA onto the surface of $BaTiO_3$ nanoparticles, yielding the core-shell $BaTiO_3$-PMMA. The PMMA polymer layer is directly observed on the surface of $BaTiO_3$ nanoparticles, and the polymer shell thickness can be controlled by the feed ratio of monomer to $BaTiO_3$ nanoparticles (**Figure 1.9b**). The highly filled $BaTiO_3$-PMMA nanocomposites with $BaTiO_3$ nanoparticles embedded in the PMMA shell polymer matrix demonstrated excellent homogeneity free of voids and pores, as observed in the SEM images of their fractured

surface in **Figure 1.9c**. The $BaTiO_3$ nanoparticles are well isolated from each other by the polymer shell, and there is no evidence of particle-matrix debonding, indicating very strong interfacial bonding and excellent dispersion of the $BaTiO_3$ nanoparticles, forming high quality $BaTiO_3$-PMMA nanocomposites. Broadband dielectric analysis of the $BaTiO_3$-PMMA nanocomposites indicated excellent dielectric properties, with high dielectric constants and low dielectric loss in a wide range of frequencies and temperatures, demonstrating that in situ ATRP could be a promising method to fabricate high quality dielectric nanocomposites for high energy density storage.

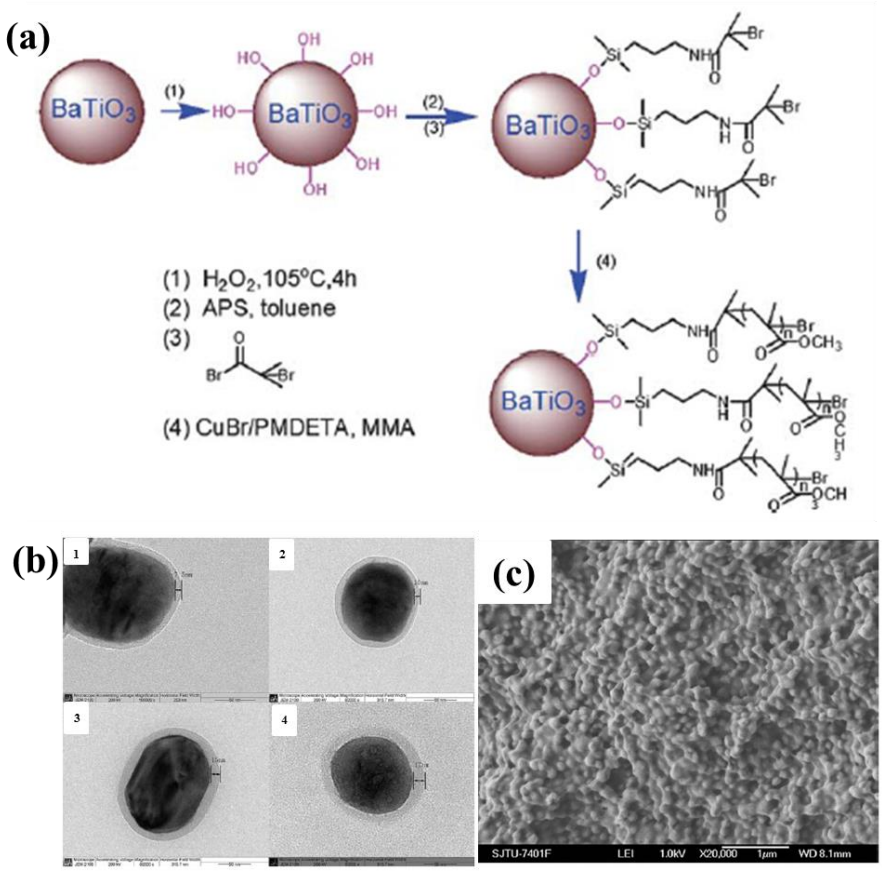

Figure 1.9 (a) Schematic diagram illustrating the process of ATRP from the surface of $BaTiO_3$ nanoparticles. (b) TEM images of core-shell $BaTiO_3$-PMMA with different polymer shell thickness, from 1 to 4, the PMMA polymer thickness increases from 7.5 nm to 17 nm. (c) SEM image of the cross-sectional images of the $BaTiO_3$-PMMA nanocomposite films with polymer shell thickness of 10 nm. [7] Copyright © The Royal Society of Chemistry 2011

The "grafting-from" strategy relies on the *in-situ* polymerization of monomers from the surface of initiator-functionalized nanoparticle and requires the introduction of a sufficient quantity of initiating sites on the nanoparticle surfaces, therefore, this method may be plagued by the low initiation efficiency, and thus low grafting density and yield. [91] In addition, the percentage of grafting and grafting efficiency is highly dependent on the choice of initiator during the radical polymerization. [92] As a result, other surface modification approaches better at controlling the interfacial interaction between the ceramic nanoparticles and the polymer matrix than the "grafting-to" and "grafting-from" approaches are of becoming increasingly important and useful. This is one of the goals of this study.

1.2.3.3 Polymer-assisted in-situ synthesis of inorganic nanocrystals

The above mentioned "grafting-to" and "grafting-from" approaches created the inorganic nanocrystals through some *ex-situ* synthesis method, which offer limited control on the size, shape, and size distribution of the inorganic nanocrystals. On the contrary, *in-situ* synthesis of inorganic nanoparticles in the presence of polymer matrix has been demonstrated to be a simple and cost-effective means of modifying the surface of nanoparticles for achieving a uniform dispersion of nanoparticles in the polymer matrix, while having a versatile control over the size, morphology and uniformity of the inorganic nanocrystals.[8, 93] Typically, a microdomain is formed by the polymer which contains or is functionalized with some polar groups. These functional groups show strong chemical affinity to the inorganic precursors added, and then the ceramic nanocrystals form selectively upon reduction of the precursor within the precursor-loaded

polymer domains, yielding ceramic nanocrystals with polymer grafted on the surface. [93] For example, Lee *etc*. reported an *in-situ* synthesis approach of forming poly (vinylidene fluoride)-graft-poly(2-hydroxyethylmethacrylate) (PVDF-g-HEMA)/Barium Titanate ($BaTiO_3$) nanocomposites without any catalyst or initiator. [8] The mechanism of *in-situ* synthesis of $BaTiO_3$ nanoparticle in the presence of PVDF-*g*-HEMA is shown in **Figure 1.10**. Briefly, the PVDF was first treated by electron beam radiation to create active sites of PVDF capable of reacting with HEMA monomers (**Figure 1.10a**), further propagation of the added monomer lead to the formation of macroradicals. After the grafting reaction was completed, the macroradicals was converted into the product PVDF-g-HEMA (**Figure 1.10c**). In the following step (**Figure 1.10d**), the $BaTiO_3$ precursor solution was added into PVDF-g-HEMA solution and the reaction was carried out at 100 °C for 2 h. The $BaTiO_3$ nanoparticles obtained through *in-situ* co-precipitation method contained the OH group on the surface, and were well dispersed and bonded strongly with PVDF-g-HEMA based on the covalent bonding of -OH group of PVDF-g-HEMA and OH group of $BaTiO_3$. The resulting PVDF-g-HEMA/$BaTiO_3$ nanocomposites via the novel *in-situ* synthesis method exhibit highest dielectric constant reaching up to 333, and a dielectric loss of 0.73 at 30 wt% $BaTiO_3$ at 1kHz, which may be attributed to the inclusion of nanosized $BaTiO_3$, higher polarizability of the grafted polymer matrix, and reduction of amorphous/crystalline interfaces.

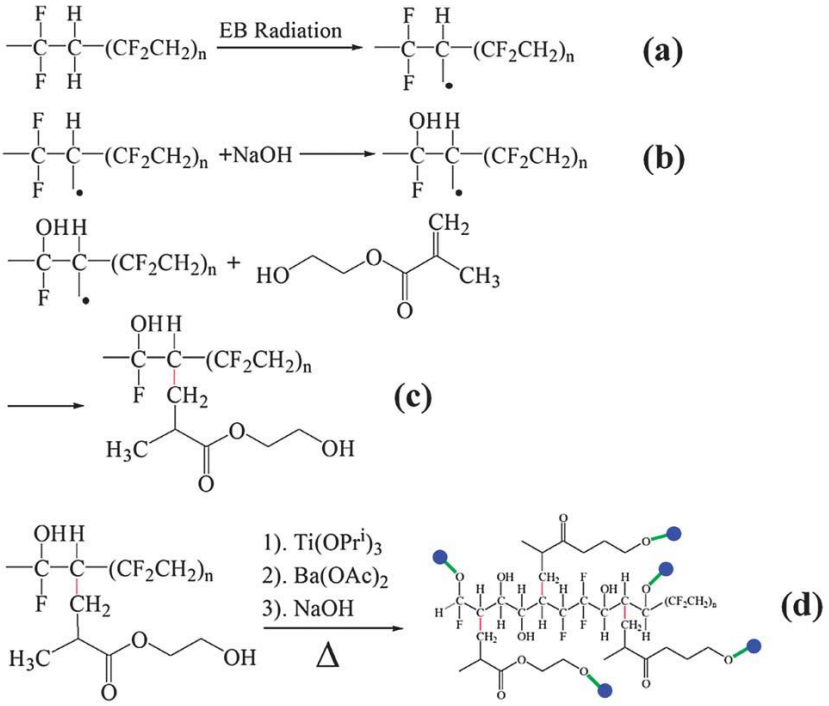

Figure 1.10 Mechanism for in-situ synthesis of PVDF-g-HEMA/$BaTiO_3$. (a) Chain initiation, (b) dehydrofluorination with an alkaline solution, (c) chain termination and (d) binding of PVDF-g-HEMA on the $BaTiO_3$ nanoparticle surface. [8] Copyright © The Royal Society of Chemistry 2013

However, current polymer-assisted *in-situ* synthesis approach is still limited in controlling the size, shape and uniformity of the ceramic nanocrystals, because the *in-situ* synthesis is affected by the complicated interplay of loaded precursor homogeneity, nucleation and growth process, and the stabilization of particle surfaces by the surrounding polymer matrix. Therefore, this approach has limited applications in those areas that require precise control over the particle size, shape, and architecture. [93-95] Clearly, it is highly desirable to construct intimate and stable ceramic-polymer nanocomposites with size controllable, monodisperse ceramic nanoparticle and well-defined polymer/ceramic interface. In our study, the robust and versatile polymer-templated approach for the *in-situ* crafting of inorganic nanocrystals by capitalizing some

rationally designed polymer as nanoreactors is able to satisfy all these requirements. The chemistry of the polymer-templated approach will be discussed in detail in section 1.4.

1.3 Active-inactive nanocomposites as electrodes for Lithium ion batteries (LIBs)

1.3.1 Introduction to the main challenges of LIBs

As the leading battery technology, LIBs have been widely used in consumer electronics due to their superior energy density, flexible and lightweight design, good cycle life and good power performances.[96] They are the technology of choice for future hybrid electric vehicles, which are central to the reduction of CO_2 emissions arising from transportation.[46]

The commercialized LIBs are typically comprised of a graphite negative electrode (anode), a non-aqueous liquid electrolyte containing lithium salts dissolved in an organic carbonate solution which enables the ion transfer between the two electrodes, and a positive electrode (cathode) formed from layered $LiCoO_2$ (**Figure 1.11**). The storage capacity of a LIB is given by the amount of lithium that can be stored reversibly in the two electrodes. On charging, lithium ions are extracted from the layered $LiCoO_2$ intercalation host, pass through the electrolyte, and are intercalated between the graphite layers in the anode, while at the same time, the electrons pass around the external circuit in the same direction. During discharging process, the lithium ions are reversibly extracted from the anode and inserted into the positive electrode. [9, 46]

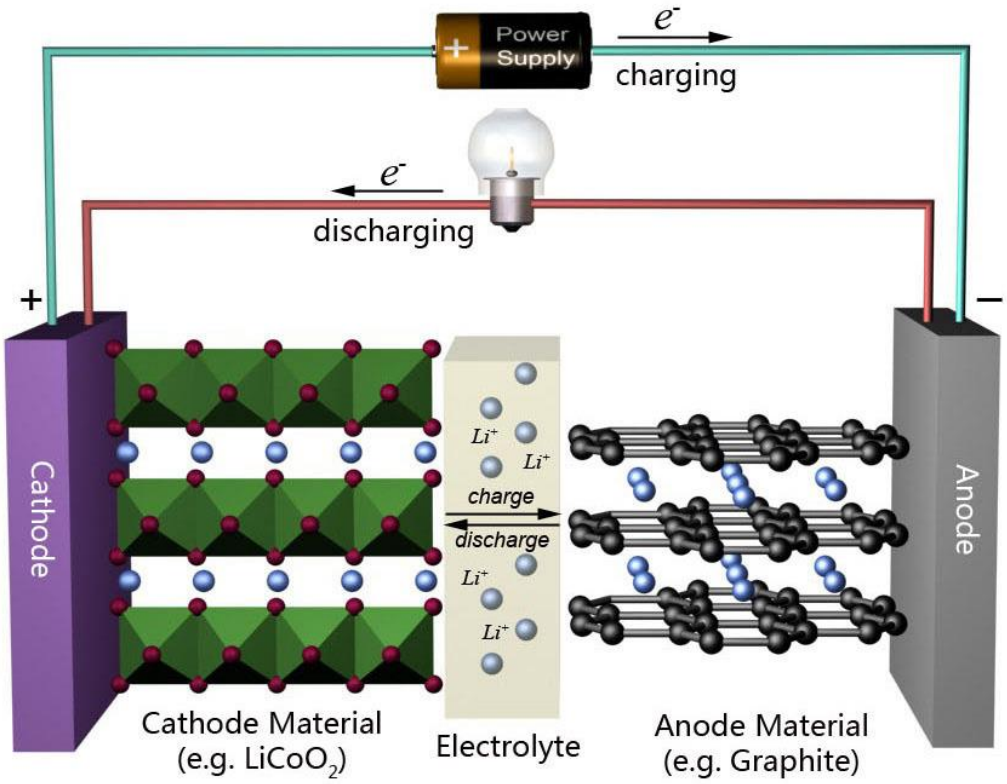

Figure 1.11 Schematic representation of typical commercial Li-ion battery comprising a negative electrode (graphite), a positive electrode ($LiCoO_2$), separated by a nonaqueous liquid electrolyte, showcasing the charge-discharge mechanism. [9] Copyright © The Royal Society of Chemistry 2011

Most commonly researched anode materials include graphite, silicon, tin, titanium dioxide, transition metal oxide, to name a few, [97-100] while typically researched cathode materials include $LiCoO_2$, $LiFePO_4$, $LiMn_2O_4$, etc. [101-104] The energy storage capacity of these electrode materials is rated by their specific capacity (mA h g^{-1}), which highlights how much charge can be stored in a given mass of material before the potential exceeds its electrochemically reversible window.

The enormous spectrum of applications of LIBs, particularly in electric vehicles (EVs), hybrid EVs and electric grids, invokes essential requirements on their energy and

power densities, as well as cycle life. However, the most common commercial graphite anode material still exhibits a relatively low theoretical specific capacity of 372 mA h g^{-1}, which cannot meet the demand of the high-energy applications noted above. [97] In this context, considerable efforts have been devoted to the development of advanced electrodes with high energy density and power density as well as long cycle life and low cost. [105] To date, a wide variety of anode materials with much higher lithium storage capacity are under extensively investigation for replacing the graphite anode material. For example, silicon, which electrochemically form alloys with lithium, has emerged as one of the most promising high-energy electrode materials, as it offers an appropriate low voltage as an anode and a high theoretical specific capacity of ~4200 mA h g^{-1}, ten times higher than that of traditional graphite anode.[98] Metal oxides (M_xO_y, where M is Fe, Co, Ni, Cu, Sn, Mn, etc.) are also widely studied as promising alternatives to graphite owing to their attractive higher theoretical capacities ($>$ 600 mA h g^{-1}), low cost, environmental friendliness and wide availability containing earth-abundant elements.[11, 97, 106] Other metal oxides also deliver much higher capacity than graphite, such as MnO_2 (1233 mA h g^{-1}), SnO_2 (790 mA h g^{-1}), Fe_2O_3 (1005 mA h g^{-1}), CoO (715 mA h g^{-1}), Co_3O_4 (890 mA h g^{-1}), to name but a few, making them attractive as advanced anode materials for high energy density Li-ion batteries. [107-108]

Despite the intriguing features described above, these high-capacity electrode materials have not yet been implemented for practical applications. This is due to their capacity decay over cycling which originates primarily from the huge volume change during the repeated insertion and extraction of lithium ions.[109-110] The volumetric change and the large mechanical strain rapidly leads to the deterioration of electrode (cracking,

crumbling, or eventually pulverization) and causes a substantial loss in capacity, as well as a shortened lifetime of only a few charge–discharge cycles.[111] The problem is especially a big issue for silicon-based and metal oxide-based anodes, as silicon expands volumetrically by up to 400% on fully lithium insertion, and metal oxide totally disrupted their original structure after lithiation. In addition, the large volume change can easily break the solid-electrolyte interface (SEI) layer formed in the lithiated expanded state and repeatedly expose the fresh surface of active materials to electrolyte, leading to the continual growth of SEI layer and gradual depletion of electrolyte over cycling. All these factors contribute to the severe capacity fading observed for these high-capacity electrode materials. Another challenging issue is the poor electrical conductivity of electrode materials (e.g. TiO_2 (10^{-10} S cm^{-1}), SnO_2 (10^{-3} S cm^{-1}), and Fe_3O_4 (10^2 S cm^{-1})), which limits the attainable lithium storage capacity at high charge/discharge rate, and cannot satisfy the requirement of high power density for future large-scale applications in electric or hybrid vehicles.[11, 112-115]

Many research efforts have been directed to construct nanostructured electrode materials for alleviating these issues and improving battery performances, which can be attributed to the multiply functions enabled by the nanometer scale dimension. Firstly, the reduced dimensions of active electrode materials can significantly shorten the transport length for both electrons and lithium ions. According to Fick's Law, the characteristic time constant for diffusion is given by $t = L^2/D$, where L is the diffusion length and D is the diffusion constant, as can be seen, the time t for intercalation decreases with the square of the particle size on replacing micrometer with nanometer particles. [116] Therefore, lithium ions can be quickly inserted and extracted with active particles,

rendering fast charging/discharging. [117-118]. Secondly, the reduced dimension leads to high surface/volume ratio and high electrode/electrolyte contact area, which are favorable for improving the lithium reaction rate.[116, 119]. Thirdly, the nanostructured materials can better withstand the volume change and the induced stress than bulk materials, as the absolute volume changes in the local environment for nanostructured materials are still very small.[120-121] Thirdly, by reducing the active materials to nanometer scale, the degradation to the SEI stability and the original structures could be reduced.[55] By now, nanostructured electrode materials in various morphologies such as nanoparticles,[11, 122-123] nanotubes,[124] nanorods/nanowires,[125-127] nanospindles,[128] nanosheets,[129] etc. have been demonstrated to offer opportunities in achieving superior electrochemical performance. For example, Park *et. al*. reported that by using Si nanotubes as anodes, a very high reversible capacity of 3247 mA h g^{-1} with Coulombic efficiency of 89% had been achieved. Besides, the nanostructuring strategy also increased the cycle life up to a few hundred cycles with 80% capacity retention.[130] However, by constructing nanoscale electrode materials is not enough in significantly enhancing the battery performance, as the conductivity of nanostructured electrode materials is still very low. Besides, other new problems, such as undesirable electrode/electrolyte reactions, may arise for nanostructured electrode materials as a result of the high surface-to-volume ratio and the large surface energy of nanostructured materials.[116] Hence these high capacity nanostructured electrode materials should be rationally designed in order to improve the electrochemical performance for practical applications.

Active-inactive nanocomposites composed of electrochemically active nanomaterial and inactive material have also been demonstrated as an effective strategy

for enhancing the energy density and power density of LIBs. The energy storage performance is highly dependent on the choices of the active and inactive materials, the amount of each component and their architectures. In addition, the way in which the inactive component is interacted with the active component, e.g. homogenous integration or inhomogeneous mixing, would strongly affect the interfacial interaction between them and strongly influence the physical, mechanical, electrical, and thermal properties of the composite materials when they are used as electrodes for LIBs. The most widely investigated inactive materials are those more electrically conductive carbons and elastic polymers.

1.3.2 Active-inactive nanocomposites as advanced electrodes for LIBs

1.3.2.1 Methods for integrating active materials with carbons

Carbon-based nanocomposites by integrating carbons (including graphite, graphene, mesoporous carbon, carbon nanotubes (CNTs), carbon nanofibers (CNFs), [131-138]) with those high capacity active electrode materials are the most widely studied active-inactive nanocomposites. The typical textures of graphite, activated carbon, ordered mesoporous carbons, and CNTs are shown in the SEM images in **Figure 1.12**. The carbons, in such complex hierarchical structure, are usually acting as structuring agents for reducing the adverse effects of these pure active materials. In addition, carbon materials possess good electronic conductivity, which is favorable for realizing the fast electron transport between active materials and the current collector and hence for achieving good rate performance.[139-140]. In addition, due to the high chemical stability of carbon, they can protect the electrolyte from decomposition by catalytic reactions with the electrodes.

Moreover, carbons, if are homogenously dispersed around nanostructured active materials, have the capability of accommodating the mechanical stresses/strains experienced by the active materials, preserving the structural integrity of active materials and composite electrode during the alloying/dealloying processes, [55] preserving the structural stability of SEI layer, and thereby enabling enhanced cyclability and rate capacity in the resulting hybrid composites.[141] Benefited by the manifold morphology of carbons, and their unique mechanical and physical properties, the macroscopic connectivity between carbons and the active materials can be designed to have desirable transport routes within the storage medium. [10] One important issue to consider when forming carbon-based nanocomposites is to find an appropriate compromise between a high packing density of those high capacity active materials for delivering high lithium storage capacity and sufficient space to buffer the volume variation. [142]

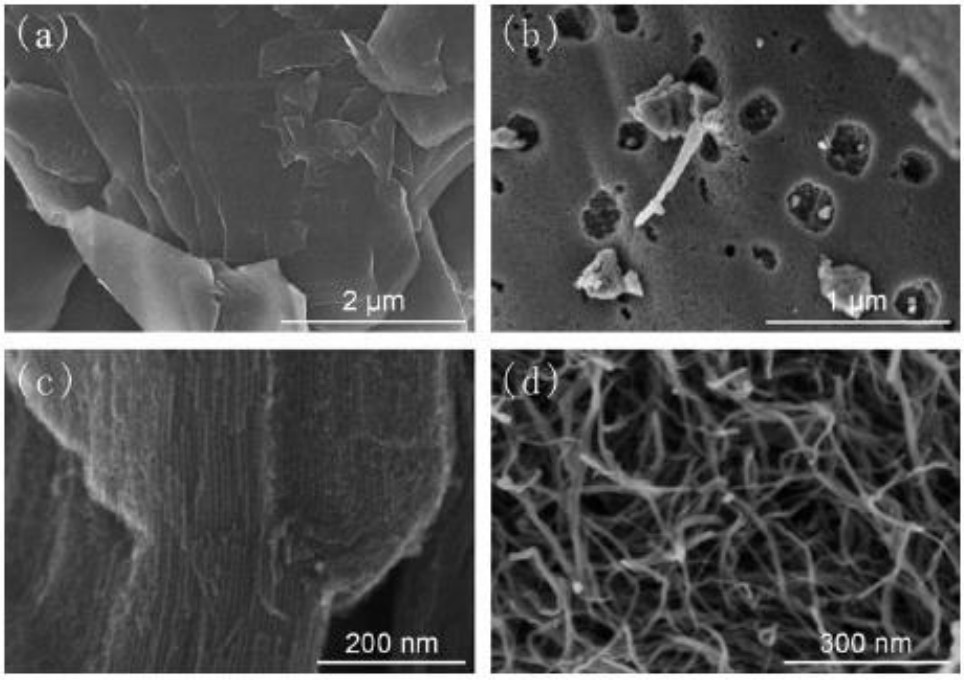

Figure 1.12 SEM images of several carbon materials commonly used for electrochemical energy storage. (a) graphite (b) activated carbon. (c) ordered mesoporous carbon. (d) CNTs. [10] Copyright ©2010 Wiley-VCH Verlag GmbH& Co. KGaA, Weinheim

Due to the flexibility of the structural units of carbons, a diversity of modifications with carbon materials have been exploited, such as surface carbon coating,[11, 143-146] graphene as substrate with active nanomaterials decorating, growing or anchoring on the surface,[147-150] graphene/carbon encapsulated active materials,[11, 110, 151] mechanically mixing graphene with active materials,[152] graphene nanosheets wrapped active material particles,[153] sandwich-like graphene/active material/graphene structures,[154] layered structures with active materials alternating with graphene sheets,[155] etc. The most common and simple approach of forming carbon-based nanocomposites is to coat a carbon layer on the active materials surface, which will provide sufficient mechanical strength to buffer the volume changes of active materials during repetitive charging and discharging. The carbon coating layer can be in various forms, and the uniformity of the carbon coatings play an important role in improving the capacity and cycle lifetime of battery with the carbon-based nanocomposites as electrodes. For instance, uniform and continuous carbon layers have been coated on various nanocrystal surfaces (e.g. Fe_3O_4,[128] $ZnFe_2O_4$,[143]), forming core-shell structure, and the results give clear evidence of the uniform carbon coatings in improving the electrochemical performance of nanostructured transition metal oxides. The carbon shell plays multiply roles when improving the electrochemical performance: (1) maintain the integrity of the active nanocrystals, (2) increase the electronic conductivity of the electrodes, and (3) stabilize the as-formed SEI films. [128]

Two-dimensional (2D) carbon network with active nanomaterials encapsulated inside is another widely studied morphology for achieving high rate electrode materials. For example, He *et al*. [11] constructed an advanced architecture in which carbon-

encapsulated Fe_3O_4 nanoparticles (~18.2 nm) were homogeneously embedded in 2D porous graphitic carbon nanosheets (PGC) with a thickness of less than 30 nm (**Figure 1.13**). In this architecture, the thin carbon shells can effectively avoid the direct exposure of Fe_3O_4 nanoparticles to the electrolyte and preserve the structural and interfacial stabilization of Fe_3O_4. Meanwhile, the flexible and conductive 2D PGC nanosheets can accommodate the mechanical stress induced by the volume change of the embedded Fe_3O_4 nanoparticles, as well as inhibit the aggregation of Fe_3O_4 nanoparticles and thus maintain the structural and electrical integrity of such morphology during the repeated charge and discharge process.

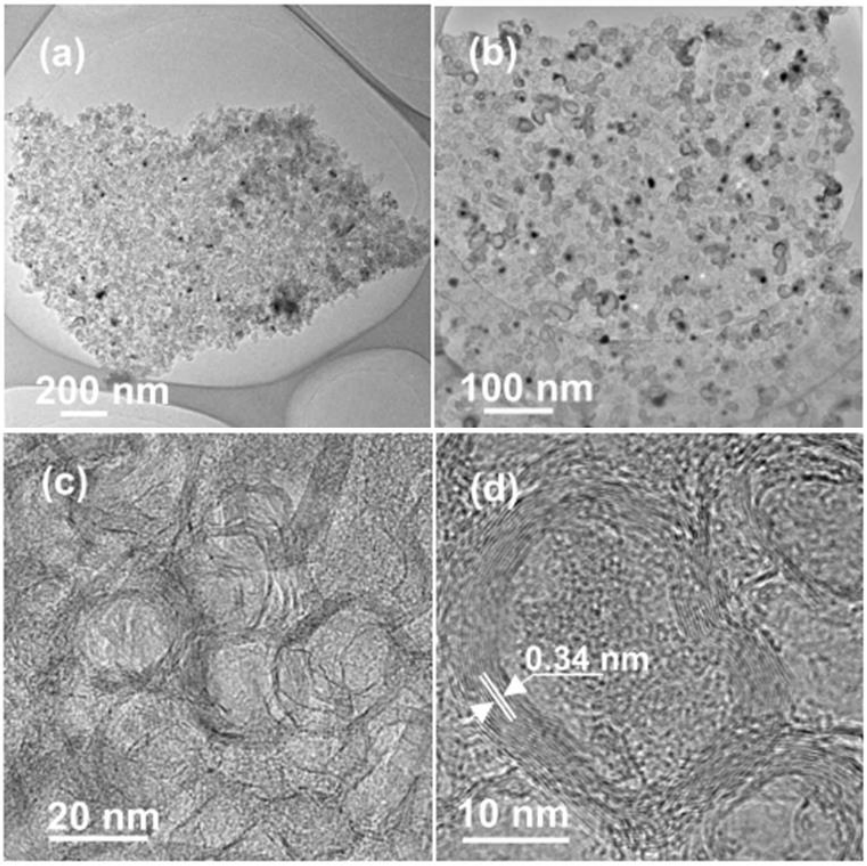

Figure 1.13 (a-c) Low-magnification TEM images, and (d) high-magnificaiton TEM images of 2D Fe_3O_4@C@PGC nanosheets clearly reveal that the Fe_3O_4 nanoparticles (5-25 nm) are perfectly encapsulated by thin and well-graphitized onion-like carbon shells within the nanosheets. [11]

Nanocomposites composed of flexible and electrically conductive graphene sheets anchored with nanostructured active materials are also widely investigated. Such architecture is capable of maximizing the utilization of electrochemically active materials due to the synergetic effect of the hybrids. The ultrathin flexible graphene layers with good electrical conductivity, high surface area, mechanical flexibility, and good electrochemical performance play multiple roles: (1) to provide a mechanical support for anchoring well-dispersed nanoparticles; [148] (2) to provide a continuous and conductive matrix for transporting electrons and hence to achieve good rate capability; (3) to immobilize the nanoparticles through a strong bonding and prevent the aggregation of nanoparticles during charge/discharge process. Meanwhile, the anchoring of nanoparticles on graphene can effectively reduce the degree of restacking of graphene sheets and consequently keep their high active surface are, and to some extent, increase the lithium storage capacity and cycling performance of graphene-based material. [156] By now, graphene anchored with Co_3O_4 nanoparticles, [156] $ZnFe_2O_4$ nanoparticles, [148] graphene shell-coated Sn nanoparticles, [157] Sulfur nanoparticles, [158]etc. have demonstrated enhanced electrochemical performance.

1.3.2.2 Methods for integrating active materials with polymers

Various kinds of polymers have also been introduced as inactive components for constructing active-inactive nanocomposites to improve the electrochemical performance of the nanocomposites electrodes. The polymers introduced usually play different roles, including serving as conductive matrix for improving the electrical conductivity, [159-160] acting as soft polymer matrix/coating for relaxing the internal stress of the active

materials that suffer from severe volume change during charge-discharge cycles, [161] or serving as the carbon source, etc.

Conductive polymers such as polypyrrole (PPy) and polyaniline (PANi) are the most widely studied polymer additives for the formation of active-inactive nanocomposites electrodes owing to their inherent high electrical conductivity (~100-10000 S m^{-1}), intrinsic flexibility, and high stability in electrochemical environments. [162-166] They themselves have been demonstrated as promising cathode materials capable of lithium storage, however, access of ions to the polymer structure and structural instability still remain as big issues, inhibiting their practical applications.[167] Therefore, many efforts are focused on incorporating PPy and PANi with active nanomaterials for using the advantages of both components and maximizing the performance of the resulting batteries. For example, SnO_2-PPy hybrid nanowires with SnO_2 nanoparticles incorporated inside the PPy nanowire was synthesized in a one-step process by a simple electrochemical method and was evaluated for their use as high performance anode materials for LIBs. The hybrid SnO_2-PPy hybrid nanowires showed superior cyclic performance and a high capacity for over 200 cycles, mostly likely because the PPy matrix effectively prevented the agglomeration of the SnO_2 nanoparticles and acted as an elastic buffer to mitigate the volumetric change in the nanoparticles that occurs during cycling.[168] Another work of fabricating core-shell structured hollow SnO_2-PPy nanocomposites was realized by a hydrothermal method followed by an *in-situ* chemical polymerization route. The hollow SnO_2-PPy nanocomposites electrode exhibited significantly enhanced cycling performance and excellent Coulombic efficiency compared to the hollow SnO_2 spheres without PPy coating, attributing to the PPy coating

which was able to prevent the possible pulverization of the hollow SnO_2 spheres, alleviate the volume changes of SnO_2 nanoparticles, and prevent the agglomeration of generated Sn particles during the lithium insertion-extration process.[169] Wang et al. prepared a series of PPy-coated $LiFePO_4$ nanocomposites as cathode, which delivered better cyclability and increased reversible capacity compared with that of bare-$LiFePO_4$ electrodes. [160]

Wu et al. reported a Si-PANi hydrogel composite by *in-situ* polymerization and crosslinking of aniline in the presence of Si nanoparticles, resulting in the hierarchical 3D porous conductive foam-like polymer framework with the conformally PANi-coated Si nanoparticles embedded inside, in intimate contact with the conductive polymer hydrogel matrix at both the microscopic and molecular level (see **Figure 1.14**). [12] Such a hierarchical hydrogel framework combines multiple advantageous features, including fast electronic and ionic transfer channels due to the continuous electrically conductive PANi network, as well as sufficient empty space for the large volume expansion of Si nanoparticles during lithium insertion. As a result, the composite anode demonstrated superior electrochemical performance with over 90% capacity retention at a current density of 6.0 A g^{-1} for over 5000 cycles.

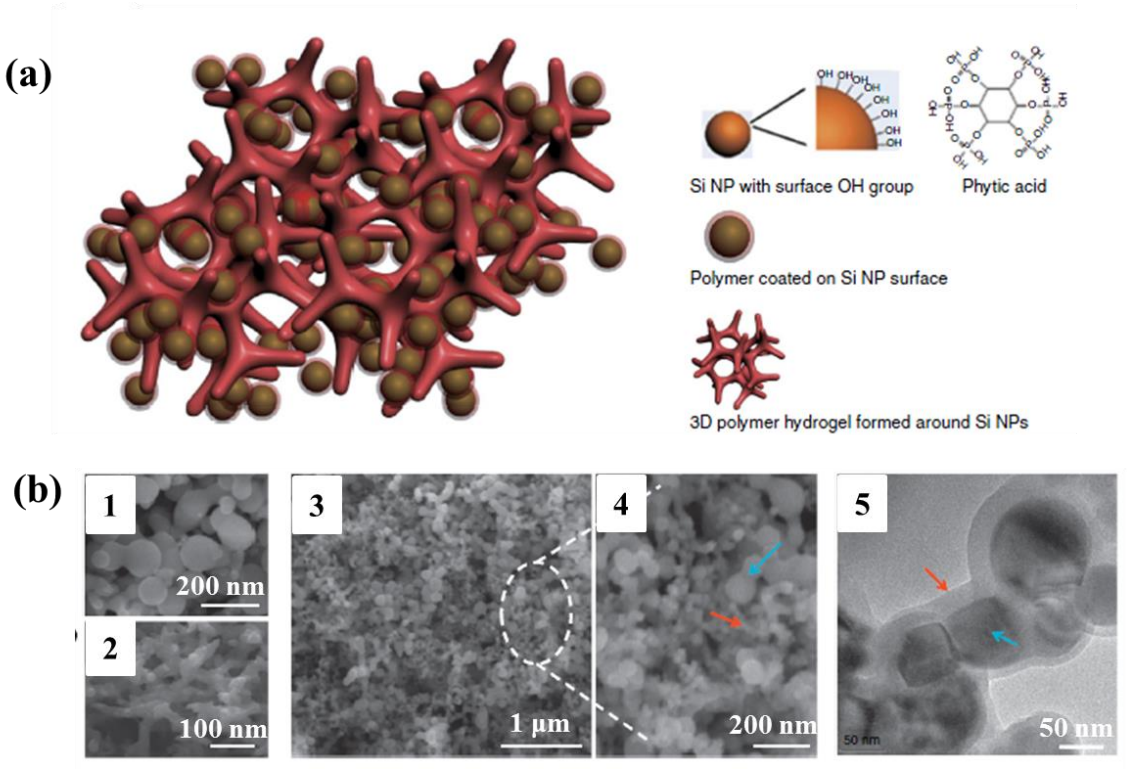

Figure 1.14 (a) Schematic illustration of 3D porous Si-PANi hydrogel composite electrodes. Each Si nanoparticle is uniformly coated with conductive PANi and is further connected to the highly porous hydrogel framework. (b) Microstructure of the Si-PANi composite electrode: 1) SEM image of pure Si nanoparticles. 2) SEM image of the PANi hydrogel sample. 3, 4) SEM images of a Si-PANi composite electrode at lower and higher magnification, respectively. 5) TEM image for uniformly PANi-coated Si nanoparticles. [12] Copyright © 2013 Macmillan Publishers Limited

The conducting polymer can also be used as carbon source for converting the polymer-based nanocomposites into carbon-based nanocomposites. Especially, the carbonization of heteroatom-containing polymers (e.g. Polyacrylonitrile (PAN), [170] polydopamine, sulfonated poly(divinylbenzene)),[171] poly(1,3,5-tris(thienyl)benzene) (PTTB), [172] PPy, have been widely applied in preparing heteroatom (such as nitrogen, sulfur, and phosphorous) doped carbon materials with improved electrochemical properties. The degree of disorder of the obtained carbon is dependent on the polymeric carbon source, pyrolysis temperature, *etc*. For example, Zhang *et al*. prepared silicon-

polyparaphenylene (Si-PPP) and silicon-polyvinylchloride (Si-PVC) nanocomposites with Si nanoparticles coated by the polymers by using mechanical milling method. The following *in-situ* pyrolysis of PPP and PVC under argon atmosphere produced disordered carbon layers coated on Si nanoparticle surfaces, and the coatings formed by PVC-based carbon appeared to be more uniform than those by PPP-based carbon, offering better accommodation of the silicon volume change, and increasing capacity and cycle life. [173] Si-C nanocomposites with similar morphology was also prepared by *in situ* chemical polymerization of 3,4-ethylenedioxythiophene (EDOT) with Si nanoparticles in a poly(styrenesulfonate) (PSS) aqueous solution and subsequent carbonization of Si/PEDOT:PSS, respectively. The heteroatom sulfur in PSS caused a 2.66 wt% sulfur doping amount in the resulting disordered carbon matrix, which exhibited a favorable effect on improving the electrochemical performance of the Si-C composite electrode. [174]

Polydopamine has been widely demonstrated as a green and cost-effective carbon source, since polydopamine has a strong tendency to form coatings on various substrates and nanostructures, allowing facile functionalization of electrochemically active nanomaterials as electrode materials for Li-ion batteries. [175] Besides, the thickness of polydopamine coatings can be conveniently controlled. Moreover, polydopamine-induced carbons have high electrical conductivities comparable to those of multi-layered graphene, which may be attributed to the altered molecular charge-transfe behavior induced by the N-type doping by nitrogen and effective π-π stacking. TEM images (**Figure 1.15**) for polydopamine-induced carbon coating on SnO_2 nanoparticles indicated that the polydopamine coating had a stacked-layer structure with a mean inter-layer spacing of about 0.4 nm. The layered structure was well retained after the carbonization

and the induced carbon coating had a slightly smaller mean interlayer spacing of 0.37 nm. [13] Hence, polydopamine-induced carbons are usually regarded as multilayered graphene doped with heteroatom. [176] Various unique morphologies have been obtained when converting polydopamine to carbon for preparing the carbon-based composite electrodes. For example, a yolk-shell structured Si-Carbon composites with silicon nanoparticle (~100 nm) as the "yolk" and amorphous carbon (5-10 nm thick) as the "shell" was prepared by carbonizing the polydopamine-coated Si-SiO_2 core-shell nanoparticles, followed by removing the SiO_2 sacrifical layer from the obtained Si@SiO_2@C composites. High capacity (~2800 mAh g^{-1} at C/10), long cycle life (1000 cycles with 74% capacity retention), and high Coulombic efficiency (99.84%) were realized in this yolk-shell structured Si-C electrode, attributed to the following advantages of such yolk-shell structure: a) the self-supportive carbon shell together with the well-controlled void space provided enough flexibility for the volume expansion of Si nanoparticles without breaking the carbon shell; b) the uniform and pinhole-free carbon shell prevented the direct contact of Si with electrolyte, inhibiting the continuous growth of SEI films formed on the carbon shell, and thus improved cycling stability; c) the highly electronically and ionically conducting carbon shells allowed good kinetics and hence improved rate capability. [177]

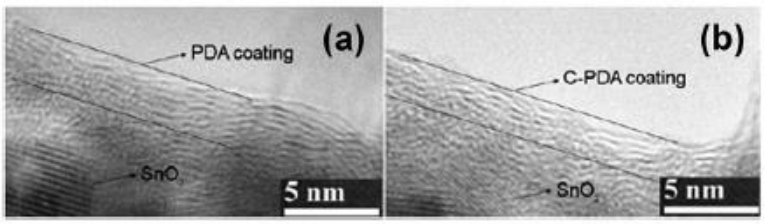

Figure 1.15 TEM images of (a) the polydopamine coating, and (b) the polydopamine-induced carbon coating on SnO_2 nanoparticles, showing the layered structure. [13] Copyright © The Royal Society of Chemistry 2012

1.4 Polymer-templated approach for designing hybrid nanocomposites

As introduced in section 1.2, polymer-templated approach for *in-situ* synthesis of inorganic nanocrystals in the presence of rationally-designed polymers as nanoreactors, different with "grafting-to" and "grafting-from" approaches, is able to control the size, shape, morphology and uniformity of the created inorganic nanocrystals in the resulting hybrid nanocomposites. Inorganic reagents can be loaded into the domains formed by polymers through interacting with the functional groups of the polymer. The nanoscale domains formed by the polymers provide space for the nucleation and crystallization of the inorganic nanocrystals, while the block copolymer architecture can facilitate both the modification of the nanoparticle surface and the long-range positioning of the inorganic nanocrystals. [178] However, due to the complicated interplay of loaded precursor homogeneity within the polymer domains, nucleation and growth process of inorganic nanocrystals within polymer domains, and the stabilization of particle surfaces by the surrounding polymer matrix, the effect of polymers on the size, morphology and uniformity of the resulting nanocomposites depends strongly on the selection of polymers, the synthesis temperature of the inorganic nanocrystals, as well as the thermodynamic quality of the system. [179] It was found that the molecular weight of the polymer used can greatly influences the average size of the inorganic nanocrystals, as well as their size distribution and stability against aggregation. [93-95]

The polymer molecules in this polymer-templated approach serve as two main roles: they serve as nanoreactors, proving confined medium for the nucleation and crystallization of inorganic nanocrystals, and thereby controlling the size, shape and size

distribution of the generated inorganic nanocrystals. Furthermore, they stabilize and isolate the generated inorganic nanoparticles, thus preventing their aggregation. [179]

Up to date, many organic molecules, surfactants, polymers and dendrimers have been used as polymer nanoreactors for the preparation of inorganic nanocrystals. [180-182] For example, Bao *et al*. synthesized the Au nanoparticles by reduction of $HAuCl_4$ with sodium borohydride ($NaBH_4$) in the presence of generation 1.5 poly(amidoamine) dendrimers with hydroxyl as terminal groups (OH-PAMAM-1.5). Due to the electrostatic attraction between charged OH-PAMAM-1.5 and oppositely charged Au ions, the added Au ions was immediately coordinated to the nitrogens of the OH-PAMAM-1.5, forming a salt between protonized tertiary nitrogen of OH-PAMAM-1.5 and Au anions. By reducing the Au ions with $NaBH_4$, Au nanoparticles were created *in-situ*, with uniform size distribution, and were surrounded and stabilized by the OH-PAMAM-1.5. [180]

Poly (ethylene oxide) (PEO)-containing polymers have been widely used for templating the *in-situ* synthesis of metal nanoparticles (e.g. Au, Ag, Pd) of a variety of morphologies, including spheres, plates, prisms, etc. [181-184] It has been demonstrated that in PEO-containing polymers, the Au precursor $AuCl_4^-$ ions were bound to pseudocrown ether structures (cavities) that were formed from PEO coils, in which several oxygen atoms of the PEO chains interacted with one metal ion. The strength of the attraction between PEO and $AuCl_4^-$ ions depends on the length of the PEO chains. [178, 182] Then the bound $AuCl_4^-$ ions were reduced via the oxidation of PEO by the metal center. The resulting Au species then migrates to other cavities where the equilibrium $3\,Au\ (\mathrm{I}) \leftrightarrow 2Au + Au(\mathrm{III})$ occured. Finally, the Au atoms coalesced to form clusters, which then grew to yield Au nanoparticles. The efficiency of particle formation process,

the size and uniformity of the produced Au nanoparticles were dependent on the composition of PEO containing polymer, molecular mass, and concentration. A single-step synthesis of Au nanoparticles from hydrogen tetrachloroaureate(III) hydrate ($HAuCl_4 \cdot 3H_2O$) has been achieved in the presence of poly (ethylene oxide)–poly(propylene oxide)–poly(ethylene oxide) (PEO–PPO–PEO) block copolymers but not with any other reducing agent. [181] This synthesis proceeded fast to completion (in less than 2 h), and is environmentally benign and economical since it involves only water and non-toxic, commercially available polymers. It was proposed that Au nanoparticles formation in the aqueous solutions of PEO-PPO-PEO comprises three main steps: (1) initial reduction of metal ions by the PEO block in crown-ether-like domains formed by the PEO-containing block copolymer in solution, (2) absorption of block copolymer on the gold clusters initially formed because of the amphiphilic character of the block copolymer, and localized reduction of metal ions on the surface of these gold clusters to increase their size (3) growth of metal particles to a certain size and shape that are dictated by the block copolymers that stabilize them. Therefore, an increase in the PEO chain length (molecular mass) favors the reduction of the gold precursor $HAuCl_4$ and the formation of Au nanoparticles. [181-182]

Amine-containing polymers, such as poly (2-vinylpyridine), poly (ethylenimine), have also been utilized as polymer nanoreactors for the *in-situ* synthesis of inorganic nanocrystals, because the amino group has strong coordination ability with metals. [182, 185-187] For example, Antonietti *et al*. reported that a double-hydrophilic polyethyleneoxide-polyethyleneimine block copolymer (PEO-b-PEI), where the amino group in the PEI block was able to coordinate with the metal compound ($AuCl_3$) would

result in the formation of micellar core for loading the Au precursors, while the other block PEO provides good solubility and stabilization of the produced Au nanoparticles.[187] Nagasaki et al. prepared monodispersed gold nanoparticles by the simple addition of a ligand installed R-biotinyl-PEG-*block*-poly[2-(*N*,*N*-dimethylamino) ethyl methacrylate] (biotinyl-PEG/PAMA) in $HAuCl_4$ aqueous solution at room temperature without using any additional reducing reagent. The ligand-installed PEG layer locating on the outer surface of the obtained gold nanoparticles substantially contributed to sterically stabilize them even under very high salt concentration. Furthermore, biotin as the ligand molecule installed at the end of tethered PEG chain showed specific recognition of streptavidin under physiological salt concentration indicating the high utility of these ligand-installed PEG/PAMA-gold nanoparticles as colloidal biosensor systems. [185]

Carboxylic acid-containing polymers, such as Poly (acrylic acid) (PAA), have been used as nanoreactors for *in-situ* growth of inorganic nanocrystals. Carboxylic (-COOH) group present in PAA chain allows many types of bond formation, such as hydrogen, ionic, covalent and coordination.[188] These bonding have been used to make hydrogels, clelating agents, esters and complex nanoparticles.[189] Metal oxides have been obtained through PAA-assisted *in-situ* synthesis approach through the strong coordination bonds formed between oxygen atoms of $–COO^-$ groups and metal moiety of the inorganic precursors. The electrostatic attraction between positively charged metal ions and $–COO^-$ groups resulted in the absorption of metal ions onto the domain formed by PAA chains. Recently, rationally designed PAA-containing block copolymers were designed as polymer nanoreactors to synthesize monodisperse colloidal nanocrystals

possessing controlled size, shape and functionality. [14, 190-192] This method, developed by our group, is one of the most advanced *in-situ* synthesis methods to fabricate inorganic nanocrystals, permitting exquisite control over the particle size, size uniformity, hydrophilicity, and morphology. Moreover, this method frequently dictates a well-ordered spatial arrangement of the generated nanocrystals. The templates used were a series of star-like diblock copolymers prepared by sequential ATRP and click reactions. The templates include diblock copolymer poly (acrylic acid)-*block*-polystyrene (PAA-*b*-PS), poly (acrylic acid)-*block*-poly (ethylene oxide) (PAA-*b*-PEO) for preparing solid spherical nanoparticles, and polystyrene-*block*-poly (acrylic acid)-*block*-polystyrene (PS-*b*-PAA-*b*-PS) and polystyrene-block-poly(acrylic acid)-block-poly (ethylene oxide) (PS-*b*-PAA-*b*-PEO) triblock copolymers for preparing spherical hollow nanoparticles.

The schematic representation of synthetic strategies for the rationally designed diblock copolymers and triblock copolymers and the templated *in-situ* synthesis of spherical solid and hollow nanoparticles are shown in **Figure 1.16a, b,** respectively. These block copolymers, prepared by a series of ATRP and click reactions, form thermodynamically stable unimolecular micelles, the size and shape of which can be tuned by chemical synthesis. They acted as nanoreactors for the *in-situ* synthesis of inorganic materials. The inner PAA block in the unimolecular micelles is hydrophilic and imparts the preferential incorporation of precursors into the interior space occupied by 21 PAA blocks *via* a strong coordination bonding between the metal moiety of the precursors and the functional groups of PAA (–COOH). It is important to note that there was no such coordination with the outer hydrophobic PS blocks. Subsequent hydrolysis and condensation of appropriate precursors in the mixed solvents of dimethylformamide

(DMF) and benzyl alcohol formed the desired nanoparticles with the PAA blocks encapsulated inside, while the surface of the nanoparticles was intimately and permanently connected with hydrophobic PS blocks **(Figure 1.16a)**. Similarly, hollow nanoparticles capped with PS blocks were obtained by using triblock copolymer PS-*b*-PAA-*b*-PS as nanoreactor (**Figure 1.16b**).

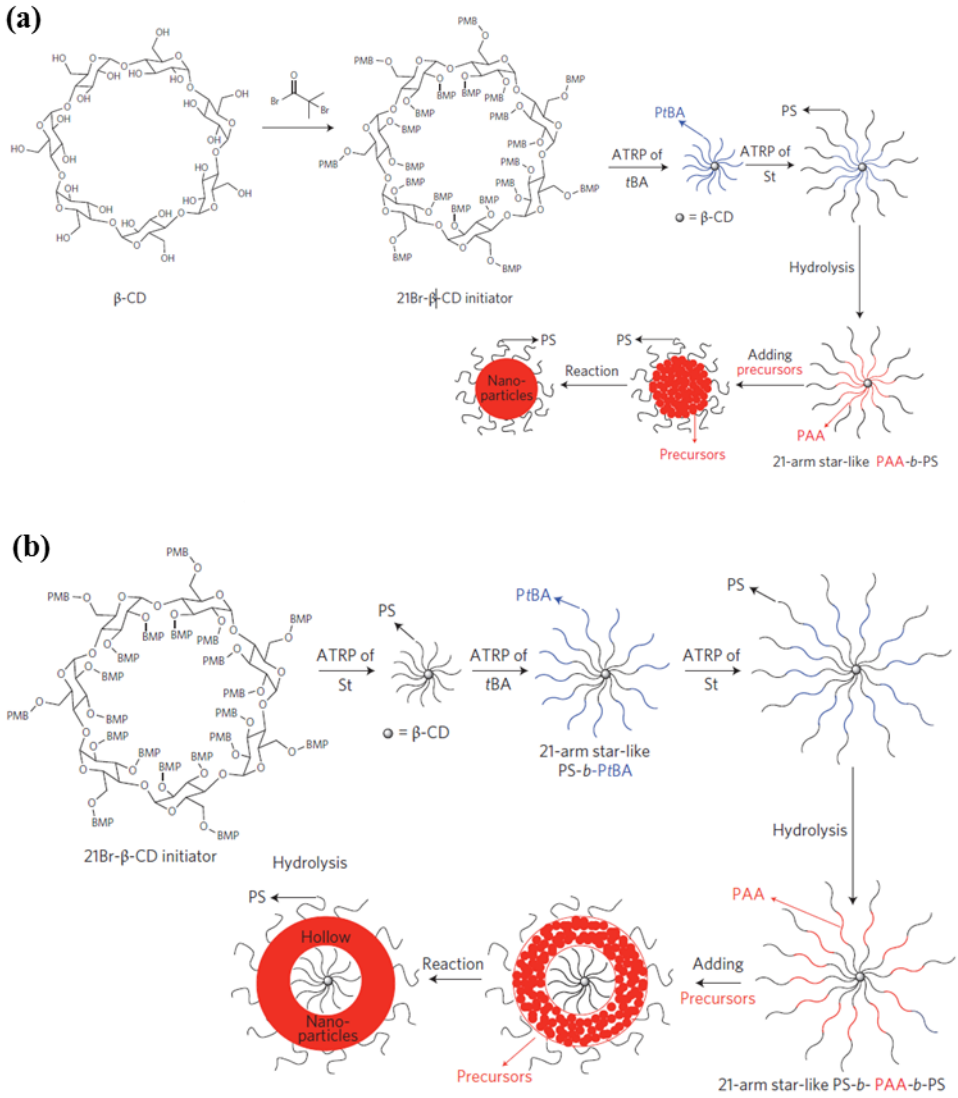

Figure 1.16 Schematic representation of synthetic strategies for nanoparticles with different architectures (plain, hollow) using amphiphilic star-like block co-polymers as nanoreactors. (a) Formation of plain nanoparticles, and (b) hollow nanoparticles. [14]

The unimolecular polymer-templated strategy by using rationally designed PAA-containing block copolymers as nanoreactors enables the synthesis of nearly monodisperse nanoparticles with precisely controllable size and surface chemistry. The permanent connection between the inorganic nanoparticles and the respective hydrophobic or hydrophilic polymer chains renders them soluble in many organic solvents, and provides the ability of homogeneous incorporation of the polymer-capped inorganic nanoparticles in respective polymer matrix (i.e. forming 0-3 patterned polymer-ceramic nanocomposites). In addition, the polymer-templated approach is quite versatile and can be readily extended to nearly all the transition or main-group metal ions and organometallic ions, thus, enabling the creation of a wide variety of metal oxides with rationally designed composition and stoichiometric ratio.

Chapter 2 Research Goals, Objectives, and Overview

2.1 Goals

The goal of this study is to (1) develop a versatile polymer-templated approach for *in-situ* synthesis of inorganic nanocrystals in the presence of polymer templates, forming functional hybrid organic-inorganic nanocomposites with well-controlled size, shape, architecture, crystallinity, interface, and functionality; (2) craft ceramic-polymer nanocomposites with excellent dielectric properties using the polymer-templated approach for use as dielectric materials in ultrasmall size high energy density capacitors, (3) design active-inactive nanocomposites with excellent electrochemical performance by employing the polymer-templated approach for use as advanced anode materials in lithium ion batteries (LIBs). The overarching goal is to design and synthesize a series of rationally designed block copolymers, which can be used to template the *in-situ* synthesis of a wide variety of inorganic nanocrystals with well-controlled size, shape, crystallinity and functionality, forming functional hybrid nanocomposites for various applications. The design of the polymer templates, including their morphology, the molecular weight, the functional groups, and the roles the polymers played in templating the growth of inorganic nanocrystals are highly dependent on the applications of the resulting hybrid organic-inorganic nanocompsites.

Thus, in order to make the polymer-templated approach versatile and practical, the mechanisms of how the functional groups and the morphology of the polymers work in templating the growth of various inorganic nanocrystals will be proposed and

systematically explored. Four kinds of polymer templates designed according to the proposed mechanism will be utilized to craft inorganic nanocrystals for demonstrating the generality of this polymer-templated approach. The polymer templates are also designed based on the requirements imposed by the potential applications of the resulting hybrid nanocomposites in LIBs, as dielectric materials in capacitors and as ferroelectric materials in nanoscale ferroelectric memory devices. The general principle of how to design the polymer template is discussed by understanding how the polymer template works.

The polymer-templated approach for designing hybrid nanocomposites will bring uniqueness to the resulting hybrid nanocomposites, such as extreme uniformity in morphology, nanometer scale dimension, well-designed interface, excellent homogeneity between different phases, one-step approach, cost-effective, etc. The precise control over the dimension, morphology, and homogeneity of the resulting hybrid nanocomposites will make it possible to study very basic science questions, such as the size and shape effects on dielectric and ferroelectric materials. In order to demonstrate the advantages of the polymer-templated approach, the resulting hybrid nanocomposites will be characterized as dielectric materials in capacitors, as ferroelectric materials in ferroelectric memory devices, and as advanced anode materials in LIBs.

2.2 Objectives

To realize the goal noted above, the following specific research objectives will be pursued and summarized in **Figure 2.1**. The specific tasks are described as follows.

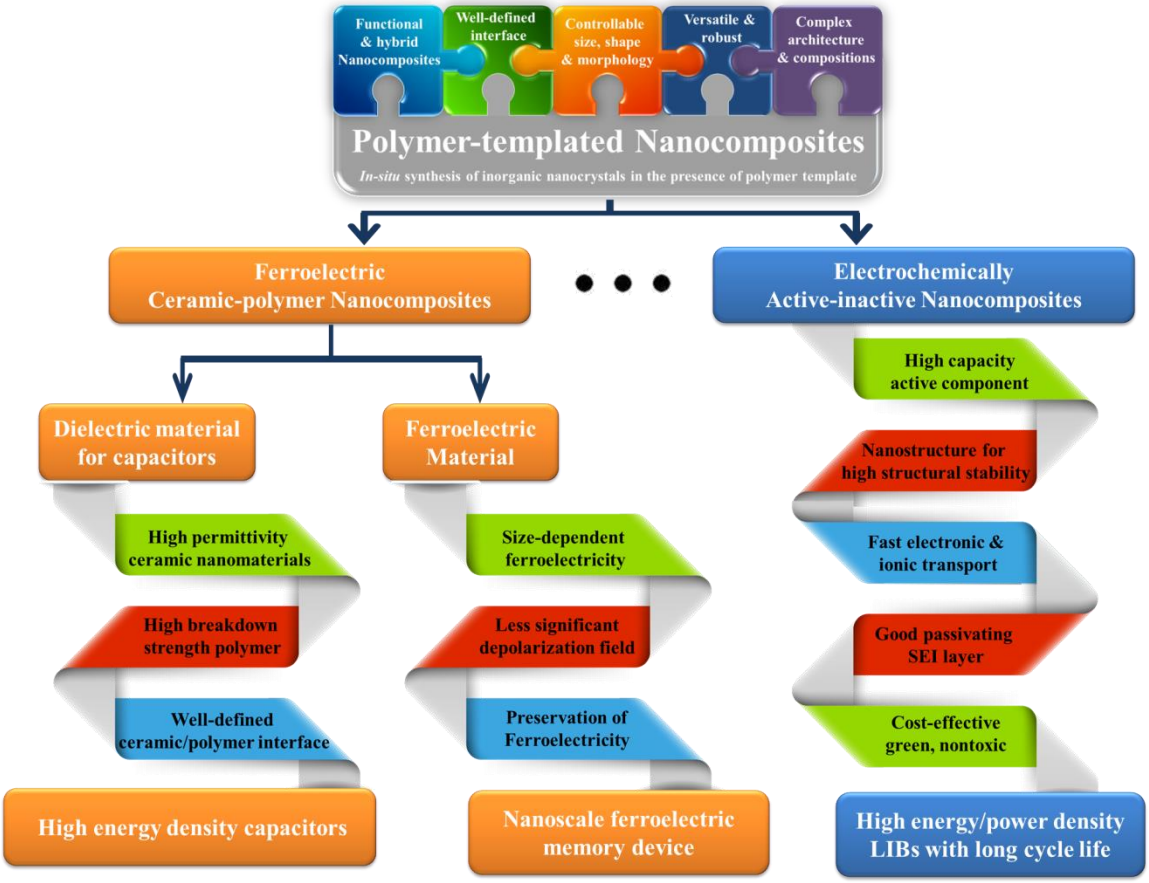

Figure 2.1 Illustration of research goals and technical objectives.

Task one: Polymer-templated ferroelectric PVDF-$BaTiO_3$ nanocomposites

(a). Designing and synthesizing star-like and bottlebrush-like diblock copolymers poly(acrylic acid)-*block*-poly(vinylidene fluoride) (PAA-*b*-PVDF) as nanoreactors to craft *in-situ* monodisperse inorganic nanocrystals with tunable sizes that are intimately

and permanently connected to PVDF chains. The morphology of the star-like and bottlebrush-like diblock PAA-*b*-PVDF copolymers, including the length of inner PAA block and outer PVDF block, the length of the bottlebrush-like diblock copolymer, and the polydispersity of the polymer nanoreactors will be well-controlled and rationally designed to precisely control the size and shape of the inorganic nanocrystals.

(b). *In-situ* synthesis of spherical and rod-like PVDF-capped $BaTiO_3$ nanocrystals (i.e. PVDF-$BaTiO_3$ nanocomposites) by utilizing the rationally designed star-like and bottlebrush-like diblock copolymers (PAA-*b*-PVDF) as nanoreactors, respectively.

(c). Scrutinizing the dielectric and ferroelectric properties of PVDF-$BaTiO_3$ nanocomposites. The dependence of dielectric permittivity and dielectric strength on size, and volume fraction of $BaTiO_3$ nanocrystals will be scrutinized and understood for the purpose of rationally crafting $BaTiO_3$-based nanocomposite materials with controlled dielectric permittivity and maximized energy storage density for capacitors in various portable electronic and communication devices.

Task two: Polymer-templated electrochemically active-inactive nanocomposites

(a). Designing and synthesizing bottlebrush-like PAA-containing polymer with rationally designed size and morphology for use as polymer template which can interact with the formed metal oxide (SnO_2) nanoparticles and bind them to the backbone of the polymeric template, forming a corn-like SnO_2 nanocrystals.

(b). Designing and synthesizing a core-shell structured PAA-containing polymer with rationally designed size and morphology for use as polymer template for loading the

inorganic precursors within the PAA shell region and creating a network-structured $ZnFe_2O_4$-carbon nanocomposites.

(c). Investigate and optimize the electrochemical performance of the polymer-templated hybrid nanocomposites as anodes in LIBs.

2.3 Organization and composition of dissertation.

Chapter 1 is a general review of the polymer-templated approaches for designing ceramic-polymer nanocomposites and electrochemically active-inactive nanocomposites. These nanocomposites exhibit excellent properties due to the integration of two components with complementary properties. In the beginning, the connection types of the two-component ceramic-polymer nanocomposites are discussed and the corresponding theoretical models for predicting their dielectric properties are introduced. Later, the general strategies for preparing both the polymer-ceramic nanocomposites and active-inactive/carbon nanocomposites are reviewed. The advantages and disadvantages of these traditional strategies are listed and compared with the polymer-templated approach. Finally, we introduced the polymer-templated approach for the *in-situ* synthesis of inorganic nanocrystals in the presence of polymer template.

Chapter 2 describes the scientific goals and technical objectives of the work discussed in this dissertation, which are polymer-templated *in-situ* synthesis of inorganic nanocrystals in the presence of polymer templates for the construction of functional

hybrid nanocomposites for applications as dielectric materials in capacitors, as ferroelectric materials in ferroelectric devices, and as anodes in LIBs.

Chapter 3 introduces the experimental techniques that critically support the studies presented in this dissertation. It includes material synthesis (polymer synthesis, inorganic materials synthesis), material characterization, Sample/device preparation, and device characterization. Materials synthesis techniques include esterification, fractional precipitation, atom transfer radical polymerization (ATRP), emulsion polymerization, click reaction, hydrolysis, wet-chemistry method, hydrothermal method. Sample/device preparation includes the assembly of LIBs based on the active-inactive nanocomposites as electrodes, and hot-pressing of the polymer-ceramic nanocomposites into disk-like dielectric materials. Materials characterization techniques include transmission electron microscopy (TEM), scanning electron microscopy (SEM), atomic force microscopy (AFM), Raman spectroscopy, X-ray diffraction (XRD), gel permeation chromatography (GPC), fourier transform infrared spectroscopy (FTIR). Device characterization includes galvanostatic charging-discharging, cyclic voltammetry, electrochemical impedance spectroscopy (EIS), and LCR meter.

Chapter 4 reports the polymer-templated *in-situ* synthesis of intimate ferroelectric organic-inorganic nanocomposites (PVDF-$BaTiO_3$) with well-controlled dimensions and compositions by exploiting both the ability to synthesize amphiphilic star-like PAA-*b*-PVDF diblock copolymers with well-defined molecular weight of each block as nanoreactors, and the strong coordination interaction between the precursors and hydrophilic PAA blocks of the star-like PAA-*b*-PVDF nanoreactor. Notably, the unimolecular nanoreactor strategy renders the crafting of functional nanocomposites with

a well-defined size and shape, precisely controllable PVDF/$BaTiO_3$ ratio, and superior long-term stability. PVDF-$BaTiO_3$ nanocomposites displayed high dielectric constant and low dielectric loss. As such, they offer promising potential for applications in energy storage, such as high energy density capacitors. In addition, these PVDF-functionalized $BaTiO_3$ nanoparticles exhibited the ferroelectric tetragonal structure, and the ferroelectricity is further substantiated by the PFM study.

Chapter 5 reports the polymer-templated approach for designing active-inactive nanocomposites (i.e. $ZnFe_2O_4$/carbon nanocomposites) composed of $ZnFe_2O_4$ nanoparticles with an average size of 16±5 nm encapsulated within the continuous carbon network as anode materials for LIBs. Such intriguing nanocomposites were yielded *in-situ via* the pyrolysis-induced carbonization of polystyrene@poly(acrylic acid) (PS@PAA) core@shell nanospheres in conjunction with the formation of $ZnFe_2O_4$ nanoparticles through the thermal decomposition of $ZnFe_2O_4$ precursors incorporated within the PS@PAA nanospheres. The $ZnFe_2O_4$/C nanocomposites containing 79.3 wt% $ZnFe_2O_4$ exhibited excellent rate performance and cycling performance.

Chapter 6 reports the polymer-templated formation of corn-on-the-cob-like SnO_2 nanocrystals composed of hundreds of SnO_2 nanoparticles decorated along the cob by capitalizing on rationally designed hydrophilic bottlebrush-like hydroxypropyl cellulose-*graft*-poly (acrylic acid) (HPC-*g*-PAA) as template. The corn-like SnO_2 was further coated with a thin layer of polydopamine (PDA) for obtaining a good passivating solid-electrolyte-interface (SEI), yielding the PDA-coated corn-like SnO_2 while maintaining the structural and morphological integrity of as-prepared corn-like SnO_2 (i.e., uncoated sample). The PDA-coated corn-like SnO_2 electrode exhibited the excellent rate capability,

the superior long-term stability for over 300 cycles, and the high $Sn \rightarrow SnO_2$ reversibility with capacities approaching the theoretical capacity of 1494 mA h g^{-1} at low current density of 160 mA g^{-1}, attributing to the synergistic effect of corn-like nanostructure and the protective PDA coating.

Chapter 7 presents the general discussion of the overall research. Three aspects of broader impacts of the polymer-templated approach for constructing functional hybrid nanocomposites are discussed: a) investigating the fundamental study of size and shape effect on the dielectric and ferroelectric properties of $BaTiO_3$-based nanocomposites owing to the capability of the polymer-template approach in precisely controlling the size and shape of the resulting $BaTiO_3$ nanocrystals, b) extending the polymer-templated approach to craft many other organic-inorganic nanocomposites with well-defined interface for various applications, and extending the polymer-templated approach to design diverse rationally designed block copolymers for constructing nanocomposites with complex architectures for different applications.

Chapter 3 Experimental Methods

3.1 Synthesis of Polymer templates

3.1.1 Synthesis of macroinitiator (cellulose-Br, HPC-Br)

Cellulose-based macroinitiator (cellulose-Br) was prepared by the homogeneous esterification procedure. Before esterification process, the cellulose powder (5 g) was vacuum-dried at 80 °C for 24h, followed by the azeotropic distillation in 100ml of dry toluene to further remove water. Then 50 g AMIMCL ionic liquid was added and the mixture was heated to 80 °C under stirring to disperse cellulose powder, the mixture turned to a viscous transparent solution when cellulose was completely dissolved. Subsequently, a mixed solution of DMF (30 ml) and NMP (30 ml) was added to dilute the solution and to absorb HBr generated in the following esterification reaction. The temperature was then reduced to 40 °C for obtaining an appropriate esterification reaction rate while achieving good solution mobility for homogeneous esterification reaction. Then 28ml 2-Bromoisobutyryl bromide (the molar ratio of 2-bromoisobutyl bromide to hydroxyl groups of cellulose=2:1) was added dropwise to the cellulose solution under stirring, and the esterification reaction was allowed to continue at 40 °C for 24h. The resulting dark brownish solution was poured into 200 ml water to precipitate the product. The precipitated product was filtered and dried under vacuum at 60 °C, and then re-dissolved in acetone and precipitated in water for purification. The dissolution-precipitation purification process was repeated three times, and the final product was vacuum dried at 60 °C for 24h. Hydroxypropyl cellulose-based macroinitiator (HPC-Br)

was prepared by similar esterification procedure but was conducted in the mixed solution of dimethylformamide (DMF) and N-Methyl-2-pyrrolidone (NMP) mixed solution.

3.1.2 Fractional precipitation of macroinitiator

The length of PVDF-capped $BaTiO_3$ nanorods, and corn-like SnO_2 nanocrystals templated by bottlebrush-like PAA-*b*-PVDF and HPC-*g*-PAA, respectively, are determined by the molecular weight of the macroinitiators. Fractional precipitation was used to separate crude cellulose-Br and HPC-Br into a series of monodisperse macroinitiators with very low molecular weight distribution (polydispersity < 1.2) with aceton as solvent and DI water precipitator. Specifically, 10 g of prepared macroinitiators were dissolved into 400 ml acetone, and then water as precipitator was added to the solvent dropwise until the transparent solution started to become opaque and precipitant started to appear. The precipitant was collected by filtration, dried in vacuum and then dissolved in THF for checking the molecular weight and polydispersity. This fractional precipitation process was repeated for several times. Each time was slightly different regarding the precipitator amount until the desired molecular weight was obtained.

3.1.3 Grafting P*t*BA block via Atom Transfer Radical Polymerization (ATRP)

In the typical process of preparing star-like P*t*BA-*b*-PVDF diblock copolymer, the poly(*tert*-butyl acrylate) (P*t*BA) side chain was prepared by ATRP of *tert*-butyl acrylate (*t*BA) monomer in methyl ethyl ketone (MEK), with 21Br-β-CD as the macroinitiator and CuBr/PMDETA as the cocatalyst. Typically, an ampule charged with CuBr (0.0707 g), PMDETA (0.1707 g), 21Br-β-CD (0.1 g), *t*BA (45 mL), and 45 mL of MEK was

vacuumed by three freeze-thaw cycles in liquid nitrogen, then sealed, and placed in an oil bath at 60 °C. The ampule was taken out from the oil bath and dipped in ice bath at different desired times to terminate the polymerization. The solution was then diluted with acetone, passed through a neutral alumina column to remove the catalyst, and precipitated in the mixed solvents of methanol/water (v/v = 1/1). After filtration, the product was purified by dissolution/precipitation twice with acetone and methanol/water and dried at 40 °C in vacuum for 2 days. The bottlebrush-like block copolymers with P*t*BA as side chains were prepared in the same method by replacing 21Br-β-CD with cellulose-Br and HPC-Br as macroinitiators, respectively.

3.1.4 Grafting PVDF block via click reaction

In the typical process of preparing star-like P*t*BA-*b*-PVDF diblock copolymer, the PVDF block was produced by click reaction between P*t*BA-N_3 and linear PVDF—≡. Specifically, star-like P*t*BA−N_3 and PVDF—≡ were dissolved in DMF (10 mL) in a dry ampule. CuBr and PMDETA were added, and the reaction mixture (PVDF—≡ : star-like P*t*BA−N_3 : copper bromide : PMDETA = 1.5 : 1 : 10 : 10; molar ratio) was degassed by three freeze-pump-thaw cycles in liquid nitrogen. The ampoule was first immersed in an oil bath at 90 °C for 24 h, and then taken out of the oil bath and placed in liquid nitrogen to terminate the polymerization. The mixture was diluted with DMF and passed through the alumina column to remove the copper salt. The product was precipitated in cold methanol and dried in vacuum oven at 40 °C for 4 h, yielding multi-arm, star-like P*t*BA-*b*-PVDF diblock copolymer.

3.1.5 Hydrolysis of P*t*BA block into PAA block

Amphiphilic star-like and bottlebrush-like PAA-*b*-PVDF diblock copolymers were yielded by the hydrolysis of *tert*-butyl ester groups of P*t*BA block into PAA block. In the typical process of preparing star-like PAA-*b*-PVDF, star-like P*t*BA-*b*-PVDF (0.5 g) was dissolved in 50 mL THF, and 10 mL trifluoroacetic acid (TFA) was then added. The reaction mixture was stirred at room temperature for 24 h. After the hydrolysis, the resulting star-like PAA-*b*-PVDF diblock copolymer was gradually precipitated in THF. The final product star-like PAA-*b*-PVDF diblock copolymer was purified, washed with THF, and thoroughly dried under vacuum at 40 °C overnight.

3.1.6 PS@PAA core-shell structured template *via* emulsion Polymerization

PS@PAA core-shell nanospheres were prepared by emulsion polymerization of the mixture of styrene and acrylic acid in aqueous solution. Typically, 2.176 g of acrylic acid was dissolved in 150 ml DI water to form a homogeneous solution. 10.4 g of styrene were then added to the above solution to form uniform oil-in-water droplets by stirring at 450 rpm for 30 min at room temperature, followed by the addition of 0.54 g $K_2S_2O_8$. Subsequently, the mixture was degassed under argon purge for 1 h. The polymerization was then performed by reacting at 80 °C for 24 h under vigorous magnetic stirring.

3.1.7 Synthesis of inorganic nanocrystals by the polymer-templated approach

The polymer-templated *in-situ* synthesis of inorganic nanocrystals was conducted *via* a wet chemistry approach by capitalizing on rationally designed block copolymers as templates. In a typical process of synthesizing PVDF-functionalized $BaTiO_3$

nanoparticles by using PAA-*b*-PVDF as templates, 10 mg star-like PAA-*b*-PVDF was dissolved in the mixed solvents containing N,N-Dimethylformamide (DMF) and benzyl alcohol (BA) at DMF : BA = 5 : 5 by volume at room temperature, followed by the addition of an appropriate amount of precursors (0.244 g $BaCl_2 \cdot 2H_2O$ + 0.24 g NaOH + 0.11 ml $TiCl_4$) that were selectively incorporated into the space occupied by the inner PAA blocks through the strong coordination bonding between the carboxyl groups of PAA and the metal ions of precursors as there were no active functional groups in the outer PVDF blocks to coordinate with the precursors. The solution was then refluxed at 180 °C under argon for 2 h, yielding ferroelectric $BaTiO_3$ nanoparticles intimately and permanently capped with ferroelectric PVDF. The solution was then purified by ultracentrifugation with MEK as solvent and ethonal as precipitant for several times to remove unreacted precursors and mixed solvents. The PVDF-functionalized $BaTiO_3$ nanorods were prepared in the same method by replacing star-like PAA-*b*-PVDF with bottlebrush-like PAA-*b*-PVDF.

In the typical process of crafting $ZnFe_2O_4$/carbon nanocomposites by using PS@PAA as template, the precursor solution, prepared by dissolving $Zn(NO_3)_2 \cdot 6H_2O$ and $Fe(NO_3)_3 \cdot 9H_2O$ in DI water and adjusting the pH value to 2, was added dropwise into the PS@PAA template solution under strong magnetic stirring and then stirred at 80°C for 6 h to ensure the complete coordination between the carboxyl groups of PAA and the metal moieties of precursors. The precursors-loaded PS@PAA powder was obtained by centrifugation and then dried at 65 °C in vacuum oven. The precursors-loaded PS@PAA powder was first grinded by mortar and pestle and then heated at

1°C/min to 600 °C for 2 h in a tubular furnace (MTI) under argon atmospher0e, yielding the $ZnFe_2O_4$/carbon nanocomposites.

In the typical process of crafting corn-like SnO_2 nanocrystals by using HPC-*g*-PAA as templates, 20 mg polymer template HPC-*g*-PAA was dispersed into 50 ml mixed solution of ethanol and H_2O ($V_{ethanol}/V_{H2O}$ = 1/2) by ultrasonication until HPC-*g*-PAA was completely dissolved, forming a transparent colorless solution. After that, 0.75 g urea and 0.2 g $Na_2SnO_3 \cdot 3H_2O$ were added into the solution and sonicated for 15 mins, forming an opaque solution. The solution was then transferred to 60 ml polytetrafl uoroethylene (Teflon)-lined stainless-steel autoclave and kept in an electric oven at 180 °C for 12h. The autoclave was then taken out from the oven and left to cool to room temperature. The white precipitate was collected by centrifuge, washed thoroughly with ethanol and H_2O, and then re-dispersed in a Tris buffer aqueous solution (33 ml, 10 mM; pH=8.5) by continuously stirring for the following treatment.

3.2 Characterization

3.2.1 Gel permeation chromatography (GPC)

The molecular weight of polymers was measured by gel permeation chromatography (GPC), equipped with an Agilent1100 with a G1310A pump, a G1362A refractive detector, and a G1314A variable wavelength detector. THF was used as eluent at 35 °C at 1.0 mL/min. One 5μm LP gel column (500 Å, molecular range: 500-2 $\times 10^4$ g/mol) and two 5μm LP gel mixed bed columns (molecular range: 200-3$\times 10^6$ g/mol) were calibrated with PS standard samples.

3.2.2 Proton NMR (^{1}H NMR)

^{1}H NMR spectra were obtained by a Varian VXR-300 spectroscope, in which CDC_{l3} DMSO-d_6, DMF-d_7 were used as solvents. The efficiency of esterification of hydroxyl groups of cellulose can be calculated based on the ^{1}H-NMR spectrum by the equation: $E_T = \frac{A_b}{18A_a}$, where E_T is the esterification efficiency of hydroxyl groups of cellulose; A_b and A_a are the integral areas of the methyl protons of cellulose and protons of cellulose, respectively.

3.2.3 Fourier transform infrared spectroscopy (FTIR)

FTIR studies were conducted over a wavenumber range of 400-4400 cm^{-1} (Shimadzu Japan) to confirm the successful loading of precursors within the PS@PAA polymer shell, and to confirm the coating of polydopamine on corn-like SnO_2 nanocrystals.

3.2.4 Transmission electron microscopy (TEM)

The morphology of PVDF-capped $BaTiO_3$ nanocrystals, polydopamine-coated and uncoated corn-like SnO_2 nanocrystals, and $ZnFe_2O_4$/carbon nanocomposites were examined by TEM (JEOL 100; operated at 100kv) and HRTEM (FEI Tecnai F30; operated at 300kV).

3.2.5 Scanning electron microscopy (SEM)

The structure and morphology for the electrodes before and after cycling were characterized using a field-emission scanning electron microscope (FESEM; FEI Quanta 250 operating at 10 kV in high vacuum).

3.2.6 X-ray diffraction (XRD)

The crystal structures of inorganic nanocrystals were characterized by XRD on an Alpha-1 (Cu-Kα, λ=0.154nm). The crystal size of the nanocrystals was calculated based on the Scherrer's equation($d = k\lambda\beta^{-1}cos\theta^{-1}$; where k = 0.89, λ is the X-ray wavelength, θ is the Bragg angle, and β is the real half-peak width in radians after corrections for the instrument broadening).

3.2.7 Raman Spectroscopy

The nature of the carbon network encapsulating the $ZnFe_2O_4$ nanoparticles was confirmed by Raman spectroscopy using a Renishaw InVia Raman Spectrometer equipped with a 785 nm laser.

3.2.8 Piezoresponse force microscopy (PFM)

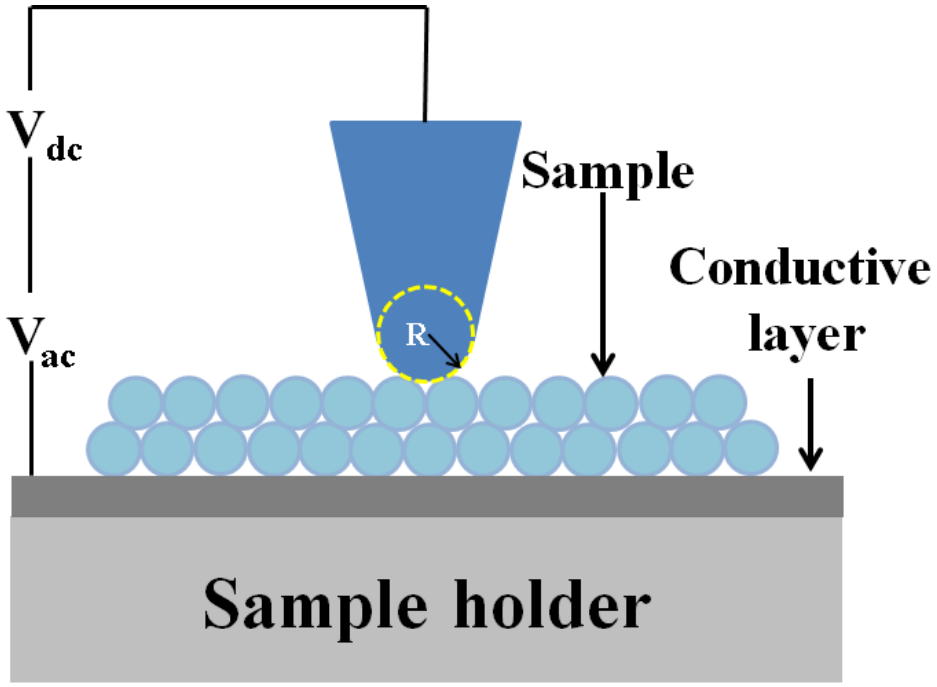

Figure 3.1 Schematic illustration of the bias condition in piezoforce microscropy measurement (PFM; vertical mode)

Ferroelectricity of a single PVDF-functionalized $BaTiO_3$ nanoparticle was measured by atomic force microscopy (Bruker Dimension Icon) in piezoelectric force microscopy (PFM) mode. As shown in **Figure 3.1**, the DC bias was applied through the AFM tip, and the AC bias was applied to the bottom electrode. The Pt/Ti-coated conductive AFM probes have a nominal force constant of 0.4 N/m. The applied AC bias had 2 V peak-to-peak amplitude and a frequency of 15 KHz. The nanocomposites films were prepared by spin-coating the solution on the ITO glass. Well-dispersed single PVDF-functionalized $BaTiO_3$ nanoparticle was obtained by simply drop-casting the solution onto the carbon-coated copper TEM grid as the TEM grid is conductive and can thus serve as the substrate for the PFM measurement.

3.2.9 LCR meter

The frequency dependent capacitance and loss tangent using a parallel equivalent circuit were measured using an Agilent E4980A LCR meter in the frequency range 100 Hz-2 MHz at $1V_{rms}$ (root mean square voltage) in open/short-circuit-correction mode to eliminate the residual capacitance from the cables connected between the meter and the probe station. Permittivity values were calculated using the formula $\varepsilon_r = \frac{C_{P\times t}}{A\times\varepsilon_0}$ from the measured capacitance (C_p) and thickness of each capacitor (t) for which the area (A) was known.

3.2.10 Electrochemical characterization

Electrochemical performance of electrodes was examined by galvanostatic testing of CR 2032-type coin cells assembled in argon filled glove box (MBraun). The coin cells used the $ZnFe_2O_4$/carbon nanocomposites as cathode, lithium foil as anode, and polypropylene (Celgard 2500, Celgard Inc., USA) as separator. The cathode was composed of 80 wt% of $ZnFe_2O_4$/C nanocomposites as active material, 10 wt% of acetylene black as conductive agent, and 10 wt% of polyvinylidene fluoride (PVDF) as binder. The electrolyte purchased was a 1M $LiPF_6$ solution in the mixed solvents of ethylene carbonate (EC), diethyl carbonate (DEC) and ethyl methyl carbonate (EMC) (volume ratio = 1:1:1, 1M $LiPF_6$/EC+DEC+EMC). The assembled cells were galvanostatically cycled between 0.005 V and 3 V (Arbin battery testing system, BT2043) at room temperature. The cyclic voltammograms (CVs) were recorded using an IM6ex electrochemical workstation at a scan rate of 0.1 mV s^{-1} over the voltage window of

0.005 V-3.0 V. The electrochemical impedance spectroscopy (EIS) measurements were also performed on the IM6ex electrochemical workstation over a frequency range of 10^{-2}-10^{5} Hz. A perturbation of 0.005 V was applied. After the cycling performance test, the fully charged coin cells were dissembled in glove box for further examination. The $ZnFe_2O_4$/carbon nanocomposites electrodes were rinsed using dimethyl carbonate (DMC) to remove the organic solvents and dissolved salts, and dried in the glove box prior to examination.

Similarly, the coin cells used the PDA-coated and uncoated corn-like SnO_2 electrodes as cathode, lithium foil as anode, and polypropylene (Celgard 2500, Celgard Inc., USA) as separator. The cathode was composed of 70 wt% of active material, 15 wt% of acetylene black as conductive agent, and 15 wt% of sodium alginate as binder. The other parameters are the same with $ZnFe_2O_4$/C nanocomposites-based electrodes.

Chapter 4 Polymer-templated Isotropic $BaTiO_3$-PVDF Nanocomposites

Related publication: B. Jiang, X. Pang, B. Li, and Z. Lin, "Organic-inorganic nanocomposites via placing monodisperse ferroelectric nanocrystals in direct and permanent connect with ferroelectric polymers", ***Journal of the American Chemical Society***. **137**, 11760 (2015)

4.1 Introduction

Polymer-ceramic nanocomposites composed of high permittivity ceramic nanoparticles and high dielectric strength polymer matrices possess the enhanced dielectric properties inherited from the ceramic nanoparticles and the facile solution processibility, high breakdown strength, flexibility, and light weight for device scalability originated from the polymer matrix.[66, 81] They have found wide applications as high permittivity and low dielectric loss materials in the fields of embedded capacitors,[193] gate insulators in organic transistors,[194-195] and power-storage devices.[70, 79] Among various polymer-ceramic nanocomposites, ferroelectric poly (vinylidene fluoride)-barium titanate (PVDF-$BaTiO_3$) nanocomposites exhibit many interesting properties, such as nonzero switchable remnant polarization, and excellent dielectric properties.[74, 196]

PVDF is a semicrystalline polymer with pyro-, piezo- and ferro-electric properties.[196] The relatively high breakdown strength and large dielectric constant (~10 at 1 kHz) of PVDF make it a potential polymeric material as polymer matric for dielectric

nanocomposites.[30, 126] It is interesting to note that PVDF can crystallize in five crystalline phases (α, β, γ, δ, ε), in which β, γ and δ phases are the polar phases and possess a net dipole moment, and α and ε phases are non-polar phases.[197] The α phase is the most common and stable form, while β phase is the most important and widely studied phase due to its excellent piezoelectric and pyroelectric properties.[198] The ferroelectricity of PVDF originates from a permanent dipole moment in monomeric unit, configuration, conformation, morphology and packing of polymeric chains or crystallites in a manner that individual dipole moment is not compensated.

$BaTiO_3$ is one of the most extensively studied ceramic nanofillers for dielectric nanocomposites due to its excellent dielectric and ferroelectric properties. $BaTiO_3$ material is currently utilized in a wide variety of fields including multilayer capacitors,[199-201] transducers,[202-206], actuators,[206-208] electro-optical devices,[209-211] electromechanical devices,[212-215] dynamic random-access memory,[216-219] field-effect transistors,[220-223] and thermistors,[224-227] among others. $BaTiO_3$ primarily exists in four crystallographic forms including cubic, tetragonal, orthorhombic, and rhombohedral crystal structures (**Figure 4.1**). [15] At high temperatures (T >120 °C), it possesses the classic perovskite cubic phase with a face centered cubic (FCC)-derivative structure in which the larger cation Ba^{2+} and O^{2-} together form FCC lattice, and the smaller cation Ti^{4+} occupies the octahedral interstitial sites in the FCC array. Due to the structural symmetry, the cubic phase is paraelectric. As temperature is lowered, $BaTiO_3$ successively phase-transitions into the three different ferroelectric phases with each involving small distortions from the cubic symmetry. It undergoes a paraelectric-to-ferroelectric transition to the tetragonal phase as T drops below the curie temperature (T_C)

of 120 °C (**Figure 4.1**). The tetragonal structure (space group P4mm) can be regarded as the movement of Ti^{4+} ion off-center along a Ti-O bond, causing the positive and negative ions to be separated, thereby resulting in a polarization of around 26 $\mu C/cm^2$ along the <001> direction. Each unit cell of the crystals holds a reversible dipole moment, which is spontaneously aligned parallel to the direction of the dipole moments of neighboring unit cells, creating a net dipole moment. With further cooling, the orthorhombic phase occurs at T between 5°C and -90°C. Lastly, onset of the rhombohedral phase occurs at T <-90°C. Each of these distortions can be regarded as elongations of the cubic unit cell in some directions, such as along an edge ([001]; tetragonal), along a face diagonal ([011]; orthorhombic), or along a body diagonal ([111]; rhombohedral), respectively (Figure 1). [15] Distortions along these directions result in a net displacement of the cation center with respect to anion center, resulting in spontaneous polarization in the ferroelectric phases.

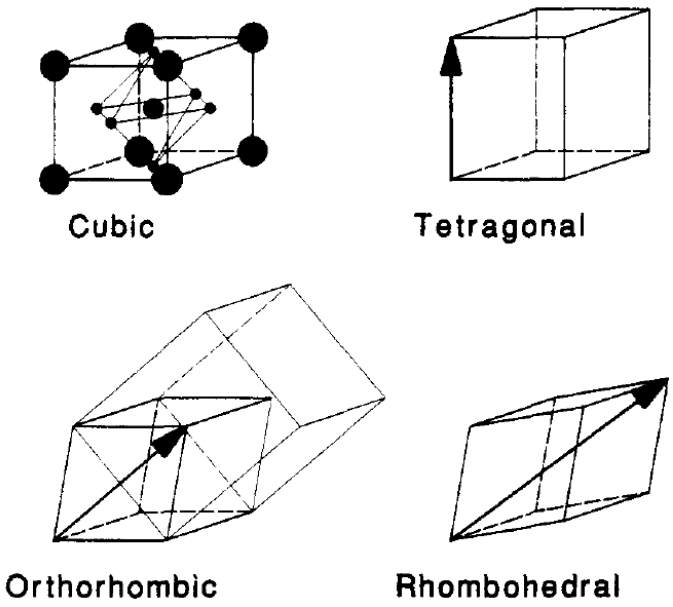

Figure 4.1 Schematic representations of the different phases of $BaTiO_3$. The tetragonal, orthorhombic and rhombohedral phases are ferroelectric. [15] Copyright 1993, American Chemical Society.

A reduction of system size into the nanoscale regime typically enhances the effect of microstructure, composition, stress, defect concentration and surface composition on the type and the intensity of ferroelectric diploes. Nanoscale $BaTiO_3$ behaves differently from both their bulk counterparts and the atomic species from which they are derived. For example, the dielectric property of $BaTiO_3$ has been found to depend heavily on their crystal size (i.e., size effect),[16, 228-230] with the permittivity first increases as the $BaTiO_3$ particle size is reduced, reaches through a maximum value, and ultimately decrease with further reducing the particle size. The ferroelectric property, on the other hand, would disappear when the $BaTiO_3$ particle size is reduced to below some critical value. In this context, understanding and ultimately manipulating the dielectric properties through structure or phase design at the nanoscale is of prime importance for the practical application of this interesting material in various types of new generation micro-devices and nano-devices that rely on dielectric materials. Various strategies are proposed for controlling and obtaining desirable dielectric properties. Among them, changing the size and modifying the surface of $BaTiO_3$ nanocrystals stand out as the most effective and widely studied strategies.

4.1.1 Size effect

Size effects of the dielectric properties of polycrystalline $BaTiO_3$ were first reported over 50 years ago by Kniepkamp and Heywang.[231-232] The size effect is generally defined as follows: as the grain size or particle size is reduced, the dielectric constant at room temperature is found to first increase to a maximum value at a certain grain or particle size and then decrease (**Figure 4.2 a-b**). In addition to the size-

dependent permittivity, another change accompanying the grain/particle size decrease is a progressive reduction in the Curie temperature (T_C, the temperature above which $BaTiO_3$ transforms from the tetragonal to the cubic phase). As a result, the room-temperature tetragonal distortion (i.e., c/a, where c and a are the unit cell lattice constant of $BaTiO_3$) gradually disappears and thus the ferroelectricity of $BaTiO_3$ particles decreases with decreasing particle size at room temperature. It has been noted that below a certain critical size, ferroelectricity of $BaTiO_3$ particles disappears due to the transformation from tetragonal to cubic phase.[229] To date, a number of factors have been found to influence the specific critical size within this range in addition to the size effect, including the microstructure, composition, stress, defect concentration and interfacial effects among others. [16, 228-230, 233] However, it is difficult to separate the intrinsic size effect from these other factors. Furthermore, many of these factors are likely interrelated with each other, making the isolation of individual effects very challenging. As a result, various models have been developed to explain the size effect, [234-235] though no agreement of accepted models exists. The only widely accepted point is that the size effect not only originates from the intrinsic structure, *i.e.*, related to the changes in atomic polarization at small scales, but is also determined by the extrinsic nature of the material which is strongly related to processing history and the crystallinity of NCs.[229]

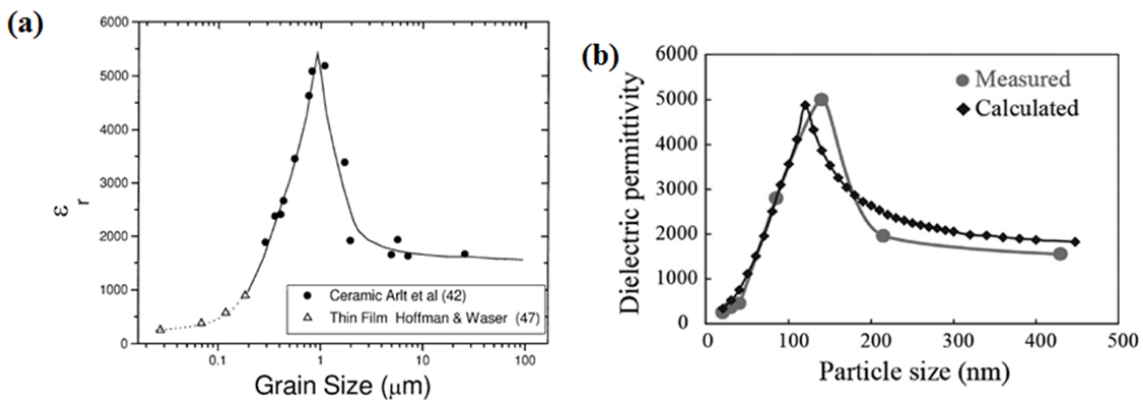

Figure 4.2 (a) Grain size dependence of the permittivity of $BaTiO_3$ ceramics and polycrystalline thin films. Reproduced with permission.[16] Copyright 2000, Annual Reviews. (b) Particle size dependence of the permittivity of $BaTiO_3$ nanoparticles (experimental measurements and calculation results are compared). [17] Copyright 2009, IEEE Ultrasonics, Ferroelectrics, and Frequency Control Society.

Theoretically, the size-dependent ferroelectricity and the disappearance of ferroelectricity at lower dimensions can be well explained by the depolarization effect. Depolarization fields in ferroelectric materials arise from incomplete compensations for the ferroelectric polarization charges.[236] For a ferroelectric material with polarization P, a total surface charge density (σ) of $\sigma = \rho \cdot n$ is induced (where p is the polarization vector and n is the unit normal to the surface) due to the polarization discontinuities in the vicinity of the surface.[237] Such surface charges produce a depolarization field inside the ferroelectric material oriented in the opposite direction with respect to the spontaneous polarization P. [238] However, the surface charges are unstable if they are not compensated. In the case when the ferroelectric material is sandwiched between two metallic electrodes, the surface charges are completely compensated, so there is no depolarization field. On the other hand, if the surface charges are not fully compensated, a depolarization field E_{dep} develops and can be described by the following equation[236]: $E_{dep} =$

$-\frac{P}{\varepsilon_F}\left(\frac{2\varepsilon_F/l}{2\varepsilon_F/l+\varepsilon_e/l_s}\right)$, where ε_F denotes the dielectric constant of the ferrroelectric material, ε_e is the dielectric constant of the screening electrode, l_s is the screening length that characterizes the space-charge extent in the electrode, and l is the thickness of the ferroelectric film. It is clear from the equation that, in the limit when $l\rightarrow\infty$ or $l_s\rightarrow 0$, the depolarization field vanishes. However, for extremely small dimension when $l\rightarrow 0$ and at relatively large screening lengths, a significant depolarization field will build up, resulting in the disappearance of ferroelectricity at small dimensions.

4.1.2 Surface effects

The size-dependent dielectric, ferroelectric and structural properties are mainly attributed to the large surface/volume ratio and the increased surface energy of nanoscale $BaTiO_3$ crystals compared to those in micrometer scale. Depending on the preparation methods, the surface of as-prepared $BaTiO_3$ NCs can be covered with different molecular adsorbates, such as hydroxyl groups (OH) from sol-gel and hydrothermal techniques, or carbonaceous species from various precursor routes. [239] Recently, it has been shown that atomic and molecular adsorbates such as OH and carbonates are more effective than metals in stabilizing the ferroelectricity of $BaTiO_3$ nanoscale domains. [240] In this regard, the controlled surface modification of $BaTiO_3$ NC is clearly an effective method for tailoring the surface chemistry as well as improving their dielectric and ferroelectric properties. To date, surface modification has been widely achieved through chemical bonding with surface ligands[70, 239]and coatings.[241] For example, n-hexylphosphonic acid (HPA)-functionalized $BaTiO_3$ NCs have been found to

possess improved dielectric properties as compared to un-modified NCs. [239] This is reflected by the decreased sensitivity to temperature and frequency of both the dielectric constant and dielectric loss. In addition, surface coating has also emerged as an effective method in increasing the tetragonality and thus preserving the ferroelectric property at extremely small particle/domain sizes by affecting the chemical features near the grain boundaries. A representative example is that $BaTiO_3$ nanoparticles (D=40 nm) coated with a manganese (Mn) layer adopt a pure tetragonal ferroelectric phase, while the uncoated $BaTiO_3$ nanopowders adopt the cubic paraelectric phase, [241] and that can be attributed to the induced strain in the samples due to Mn coating, which led to increased tetragonality and the preservation of ferroelectricity below the critical size of unmodified particles.[17, 242]

4.2 Experiments, results, and discussion

4.2.1 Synthesizing star-like PAA-*b*-PVDF diblock copolymer

In this study, we will synthesize a 21-arm star-like PAA-*b*-PVDF diblock copolymer by a series of living polymerization and click reactions. These nonlinear PAA-*b*-PVDF diblock copolymers will be used as nanoreactors to template the growth of $BaTiO_3$ nanoparticles intimately capped with PVDF.

Amphiphilic unimolecular star-like PAA-*b*-PVDF diblock copolymer was first synthesized by a combination of atom transfer radical polymerization (ATRP) and click reaction, followed by hydrolysis, as illustrated in **Figure 4.3**. Briefly, β-cyclodextrin (β-CD), a cyclic oligosaccharide possessing 21 hydroxyl groups was esterified by reacting

the surface hydroxyl groups with 2-bromoisobutryryl bromide, yielding star-like macroinitiator (denoted 21-Br-β-CD; upper second panel in **Figure 4.3**).[14, 190-191] Subsequently, it was employed to conduct ATRP of tert-butyl acrylate (*t*BA) monomers (upper third panel in **Figure 4.3**) in methyl ethyl ketone (MEK), using 21Br-β-CD as the macroinitiator and CuBr/PMDETA as the cocatalyst (upper third panel in **Figure 4.3**). The resulting star-like poly (tert-butyl acrylate) (P*t*BA) was then transformed into star-like azide-functionalized P*t*BA (i.e., P*t*BA-N_3; upper fourth panel in **Figure 4.3**) by reacting with sodium azide (NaN_3).

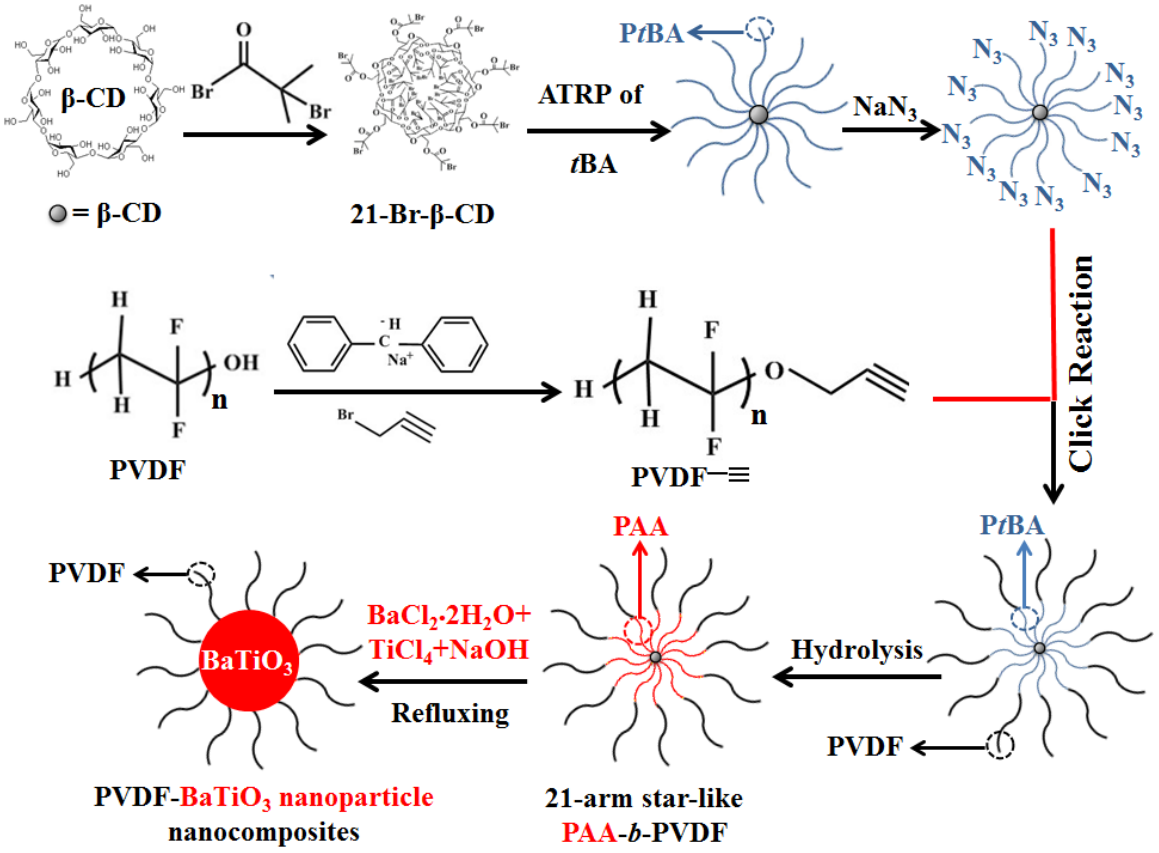

Figure 4.3 Synthetic Route to amphiphilic 21-Arm, star-like PAA-*b*-PVDF diblock copolymer and subsequent conversion into PVDF-Functionalized $BaTiO_3$ Nanoparticles (i.e., PVDF-$BaTiO_3$ Nanocomposites).[18]Copyright © 2015 American Chemical Society

At the same time, alkyne-terminated PVDF (i.e., PVDF-propargyl; PVDF—≡) was obtained by the nucleophilic substitution of the hydroxyl group on hydroxyl-capped PVDF into the alkyne group (central right panel in **Figure 4.3**). Finally, the click reaction between star-like P*t*BA-N_3 and PVDF—≡ formed star-like P*t*BA-*b*-PVDF (lower right panel in **Figure 4.3**). The *t*ert-butyl substituents in star-like P*t*BA-*b*-PVDF block copolymers can be readily hydrolyzed, thereby yielding amphiphilic star-like PAA-*b*-PVDF consisting of inner hydrophilic PAA blocks and outer hydrophobic PVDF blocks with well-controlled molecular weight of each block and narrow molecular weight distribution (lower central panel in **Figure 4.3**). The proton NMR (^{1}H NMR) spectrum of a representative star-like PAA-*b*-PVDF is shown in **Figure 4.4**. The signal associated with the triazole ring appeared at δ = 7.8 ppm, suggesting the success in coupling P*t*BA-N_3 with PVDF—≡.

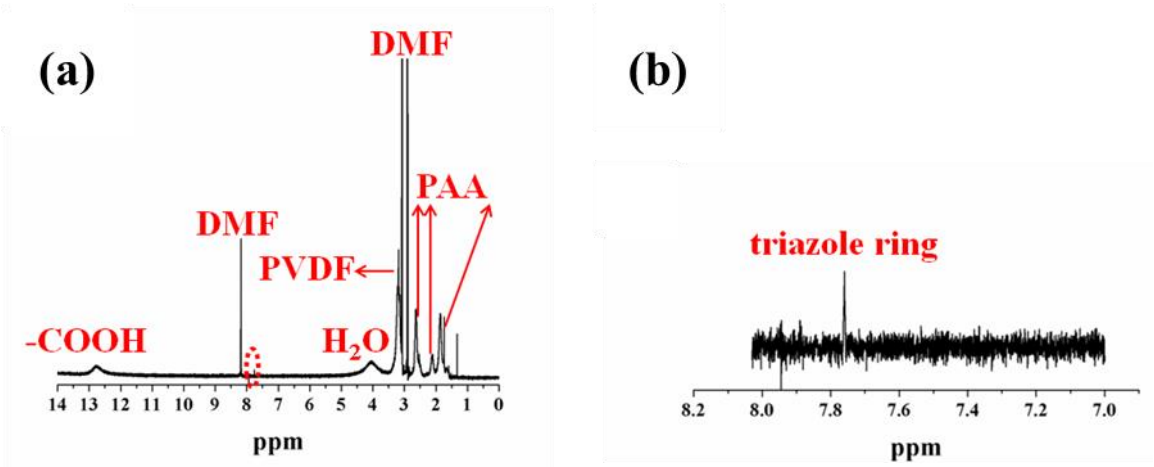

Figure 4.4 ^{1}H NMR spectrum of star-like PAA-*b*-PVDF diblock copolymer. The signal associated with the triazole ring appeared at δ = 7.8 ppm in (b) (i.e., a close-up of red dashed circle in (a)), indicating the success in coupling P*t*BA-N_3 with PVDF—≡. [18] Copyright © 2015 American Chemical Society

4.2.2 *In-situ* synthesis of $BaTiO_3$-PVDF nanocomposites by star-like PAA-b-PVDF template

PVDF-functionalized $BaTiO_3$ nanoparticles were then crafted by capitalizing on PAA-*b*-PVDF diblock copolymers as nanoreactors (i.e., templates). The hydrophilic inner PAA blocks in star-like PAA-*b*-PVDF rendered a strong coordination interaction between the carboxylic groups (-COOH) of PAA and the metal moieties of $BaTiO_3$ (Ba^{2+} and Ti^{4+}), while the outer hydrophobic PVDF blocks did not possess such coordinating functional groups [14] (lower left panel in **Figure 4.3**). Thus, it is not surprising that the precursors were selectively incorporated into the space occupied by inner PAA blocks and converted into $BaTiO_3$ nanoparticles *in-situ*, *intimately* and *stably* capped with PVDF chains. Remarkably, the diameter of these PVDF-functionalized $BaTiO_3$ nanoparticles can be precisely tuned by varying the molecular weight of inner PAA blocks during the ATRP of *t*BA. Accordingly, the volume ratio of $BaTiO_3$ to PVDF can be readily altered. In this study, we synthesized star-like PAA-*b*-PVDF block copolymers with two different molecular weights of PAA. **Table 4.1** summaries the molecular weight of each block in star-like PAA-*b*-PVDF and the corresponding diameter of PVDF-functionalized $BaTiO_3$ nanoparticles derived from them.

Table 4.1. Molecular weights of amphiphilic multi-arm, star-like PAA-*b*-PVDF diblock copolymers and the corresponding size of PVDF-functionalized $BaTiO_3$ nanoparticles

Sample	MW of PAA block	MW of PVDF block	Diameter of PVDF-capped $BaTiO_3$ nanoparticles
Sample-1	8,400	8,600	10.2 ± 0.6 nm
Sample-2	16,800	8,600	16.1 ± 0.8 nm

Figure 4.5 compares the size of two PVDF-capped $BaTiO_3$ nanoparticles (i.e., PVDF-$BaTiO_3$ nanocomposites) measured by transmission electron microscope (TEM). The diameters of $BaTiO_3$ nanoparticles are approximately 10.2±0.6 nm (**Figure 4.5a**) and 16.1±0.8 nm (**Figure 4.5b**), respectively. Representative high-resolution transmission electron microscopy (HRTEM) images are shown in the insets demonstrating that they had continuous crystalline lattices. A good uniformity of nanoparticles is clearly evident. This is in stark contrast to the limited report on *in-situ* synthesis of $BaTiO_3$ nanoparticles in the presence of PVDF-based polymer possessing functional groups (e.g., hydroxyl) for direct coupling with the precursors[8] but often yielding poorly controlled size, as noted above. Notably, the ability to precisely tune the size of $BaTiO_3$ nanoparticles by varying the molecular weights of inner PAA block (i.e., 10.2±0.6 nm and 16.1±0.8 nm in this work) is of practical interest for investigating the size effect on ferroelectric properties for the future research.

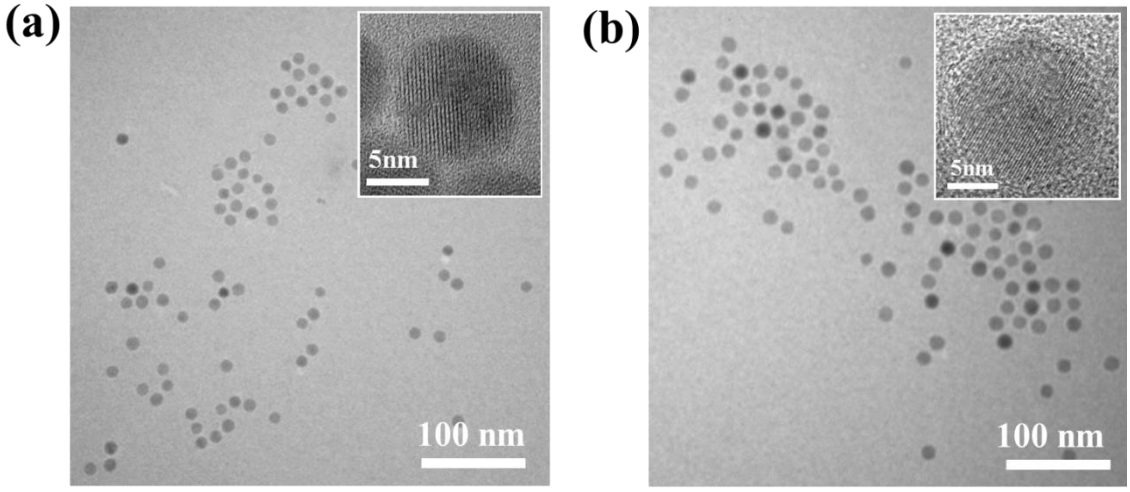

Figure 4.5 TEM images of PVDF-$BaTiO_3$ nanocomposites synthesized by capitalizing on star-like PAA-*b*-PVDF diblock copolymers with different molecular weights of PAA blocks as nanoreactors. (a) Diameter, D = 10.2 ± 0.6 nm; and (b) D = 16.1 ± 0.8 nm. Insets: the crystalline lattices of each nanoparticle are clearly evident in HRTEM images.[18] Copyright © 2015 American Chemical Society

It is worth noting that the choice of mixed solvents of DMF and BA afforded the tailorablitiy of the solubility of each block in DMF and BA for a better encapsulation of inorganic precursors, representing a key to monodisperse PVDF-functionalized $BaTiO_3$ nanoparticles. The star-like PAA-*b*-PVDF can be readily dissolved in pure DMF, forming unimolecular micellar structure (i.e., fully expanded chain conformation) as DMF is a good solvent for both PAA and PVDF blocks. The addition of BA triggers the outer PVDF blocks to contract owing to unfavorable interaction between BA and PVDF as BA is a good solvent for PAA yet a non-solvent for PVDF, while the inner PAA blocks maintain a coil-like conformation. Interestingly, $BaTiO_3$ nanoparticles had relatively irregular shapes when the volume ratio of DMF to BA was $V_{DMF} : V_{BA} = 9 : 1$ (**Figure 4.6a**) as well as $V_{DMF} : V_{BA} = 3 : 7$ (**Figure 4.6c**). However, at $V_{DMF} : V_{BA} = 5 : 5$, $BaTiO_3$ nanoparticles with the best uniformity were produced (**Figure 4.6b**). This can be

rationalized as follows. At the high volume ratio of DMF to BA (9 : 1), the outer PVDF blocks contract slightly. Thus, the star-like PAA-*b*-PVDF diblock copolymer adopts a spherical macromolecular structure with loosely collapsed PVDF chains outside. On the other hand, at the low DMF to BA volume ratio (3 : 7), the outer PVDF chains contract significantly, producing densely collapsed PVDF chains outside. The incorporation of precursors in both cases is limited, thereby yielding relatively non-uniform $BaTiO_3$ nanoparticles. In contrast, the $V_{DMF} : V_{BA} = 5 : 5$ imparts the formation of well-defined spherical macromolecules composed of outer more compact PVDF chains and inner coil-like PAA chains, which promotes the optimal loading of precursors and thus yields uniform $BaTiO_3$ nanoparticles.

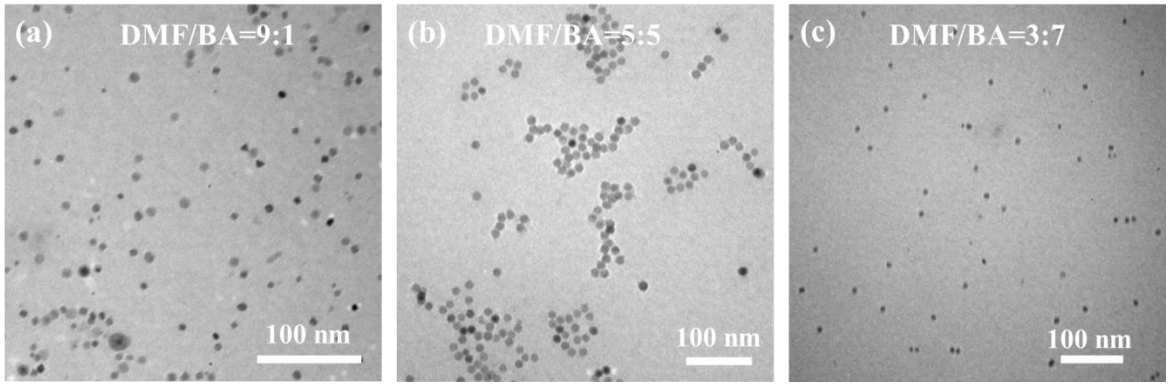

Figure 4.6 TEM images of PVDF-$BaTiO_3$ nanocomposites formed in the mixed solvents of DMF and benzyl alcohol (BA). (a) VDMF: VBA= 9 : 1 (by volume), (b) VDMF: VBA = 5 : 5, (c) VDMF: VBA= 3 : 7.[18] Copyright © 2015 American Chemical Society

The energy dispersive spectroscopy (EDS) measurement detected the elements of F, Ba, and Ti, which may suggest the successful formation of $BaTiO_3$-PVDF nanocomposites(**Figure 4.7**).

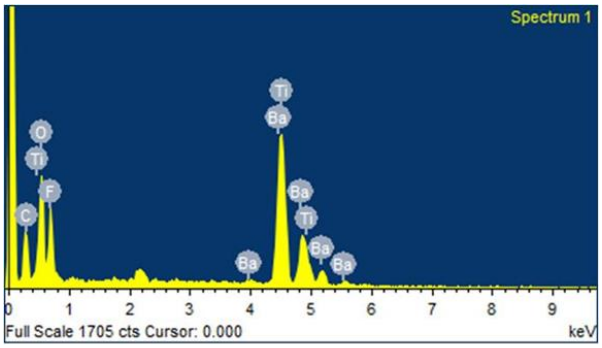

Element	Weight%	Atomic%
C K	26.22	26.47
O K	39.56	29.97
F K	38.11	24.32
Ba L	120.60	10.64
Ti K	33.97	8.60
Totals	258.46	100

Figure 4.7 EDS spectrum of PVDF-$BaTiO_3$ nanoparticle nanocomposites. The emergence of high Ba and Ti contents suggests the presence of $BaTiO_3$. Moreover, the existence of F element indicates the presence of PVDF chains in nanocomposites.[18] Copyright © 2015 American Chemical Society

Raman spectroscopy is well-suited for detecting the ferroelectric (tetragonal) phase of $BaTiO_3$ as some bands that are active in the tetragonal $BaTiO_3$ become inactive in the cubic $BaTiO_3$.[243] **Figure 4.8** shows the Raman spectra of PVDF-$BaTiO_3$ nanocomposites containing different size of $BaTiO_3$ nanoparticles. Notably, the presence of the sharp band at around 305 cm^{-1} and the broad band at around 720 cm^{-1} was indicative of the ferroelectric (tetragonal) phase of $BaTiO_3$.[243]

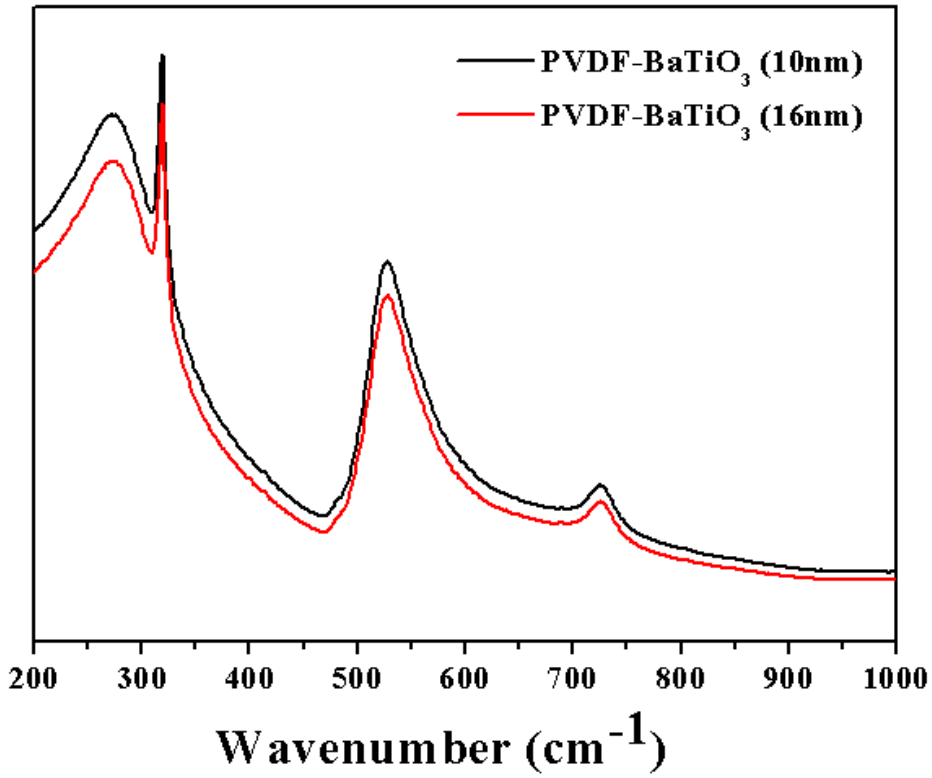

Figure 4.8 Raman spectra from PVDF-$BaTiO_3$ nanocomposites of two different sizes (i.e., 10.2 nm and 16.1 nm). The sharp band at 305 cm^{-1} and the broad band at 720 cm^{-1} signified the tetragonal phase of $BaTiO_3$. [18] Copyright © 2015 American Chemical Society

Figure 4.9a,b depicts the X-ray diffraction (XRD) pattern for PVDF-$BaTiO_3$ nanocomposites with the size of 10.2 nm and 16.1nm, respectively. Similar XRD patters were obtained for the two different sizes. The inset shows the splitting of the (200) peak at $2\theta = 45°$ into two peaks, corresponding to the (002) and (200) planes.[244] The emergence of these two diffraction peaks in this region can be attributed to the distortion of unit cell, suggesting that $BaTiO_3$ nanoparticle possessed the tetragonal structure (i.e., ferroelectric behavior), which correlated well with the Raman results discussed above.[244] Due to the high crystallinity and strong diffraction peaks of $BaTiO_3$ part in the

nanocomposites, the peaks at 19-20 degree assignable to PVDF part are much weaker and less evident.

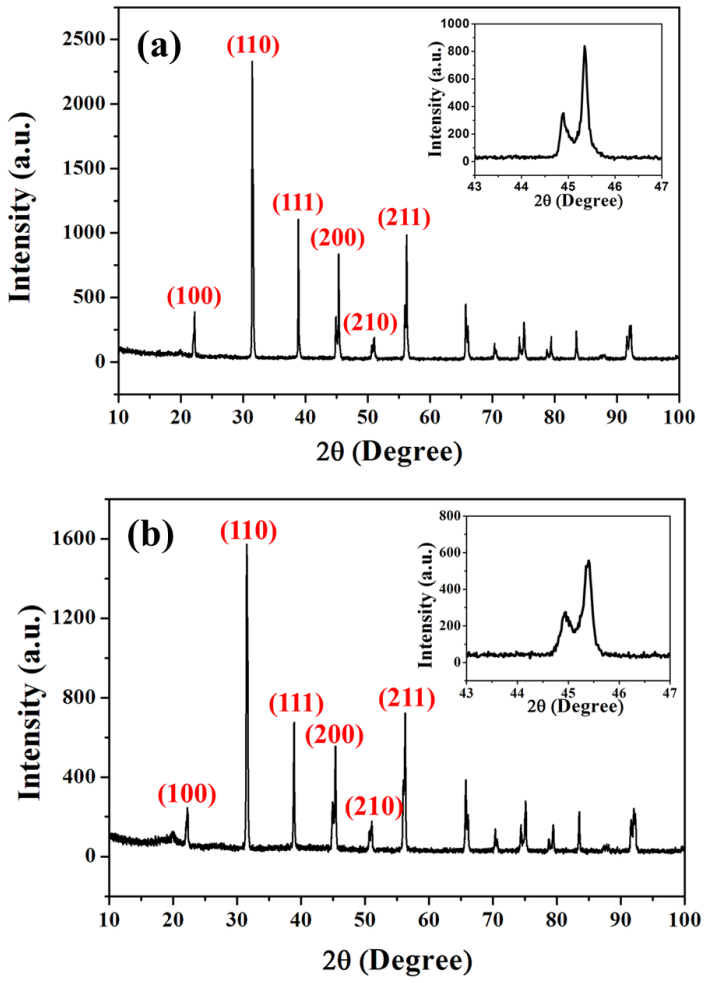

Figure 4.9 Powder X-ray diffraction (XRD) patterns of $BaTiO_3$-PVDF nanocomposites at 2θ of 10-100 degrees for (a) 10.2 nm and (b) 16.1nm. Insets are the zoom in XRD pattern for the peak at 45 degree for (200) plane. [18] Copyright © 2015 American Chemical Society

We note that among the five crystalline phases of PVDF, β phase contains the largest spontaneous polarization which can be attributed to the closer packing of polymer chains in a unit cell.[197] Fourier transform infrared spectroscopy (FTIR) has been widely utilized to detect the existence of β phase PVDF.[197, 245] **Figure 4.10** shows the FTIR

spectra of star-like PAA-*b*-PVDF diblock copolymers. Clearly, the peaks corresponding to both α phase (i.e., the absorption bands at 530 cm^{-1} (CF_2 bending), 615 cm^{-1} and 765 cm^{-1} (CF_2 bending and skeletal bending), and 795 cm^{-1} (CF_2 rocking)[197]) and β phase (i.e., the absorption bands at 510 cm^{-1} (CF_2 bending) and 840 cm^{-1} (CH_2 rocking)[197]) were seen, suggesting the coexistence of both α phase and β phase in the resulting star-like PAA-*b*-PVDF diblock copolymers.

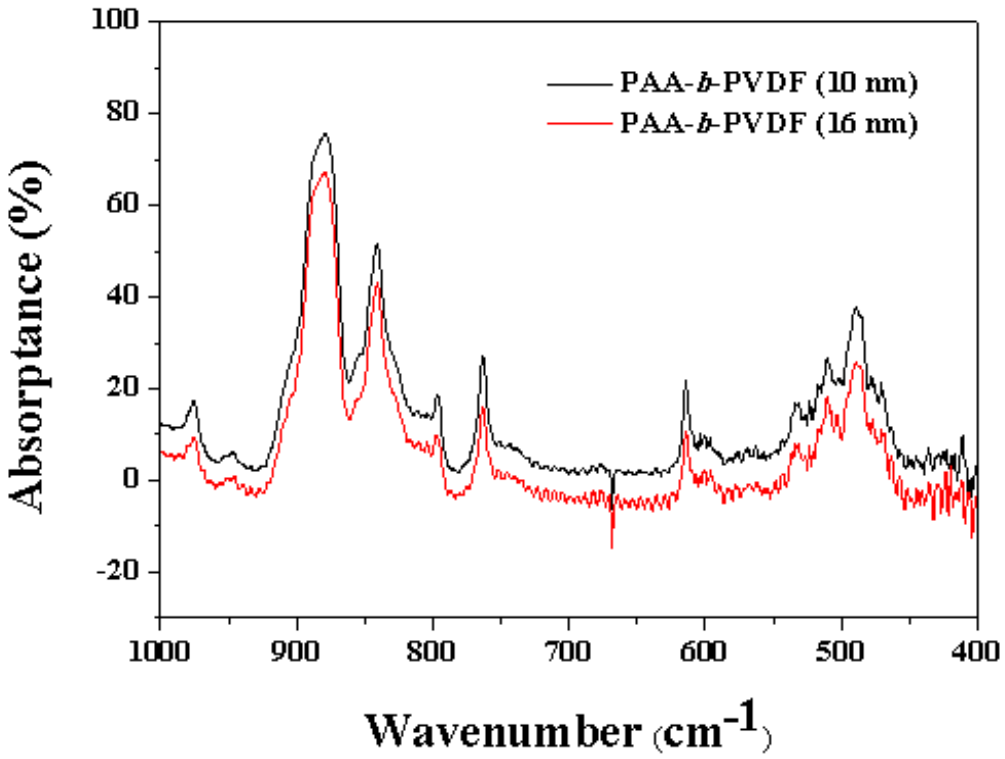

Figure 4.10 FTIR spectra of star-like PAA-*b*-PVDF diblock copolymers. The vibrational bands at 510 cm^{-1} and 840 cm^{-1} are the characteristic peaks of the β phase PVDF. [18] Copyright © 2015 American Chemical Society

4.2.3 Dielectric and ferroelectric properties of $BaTiO_3$-PVDF nanocomposites

The dielectric properties of PVDF-$BaTiO_3$ nanocomposites were obtained by measuring the capacitance and dissipation factor of parallel-plate capacitors prepared by

hot-pressing the nanocomposites powder under high temperature (T = 150 °C, below the melting temperature of PVDF, T_m = 177 °C) and high pressure (16.71N/cm^2) (**Figure 4.11**). Thin layers of Au were evaporated on both surfaces of hot-pressed film as electrodes. The volume fractions of $BaTiO_3$ nanoparticles in nanocompsites can be calculated based on the density of $BaTiO_3$ and PVDF from the thermogravimetric analysis (TGA) measurements (**Figure 4.12**), which are 74% for 10.2±0.6 nm and 84.7% for 16.1±0.8 nm nanoparticles, respectively.

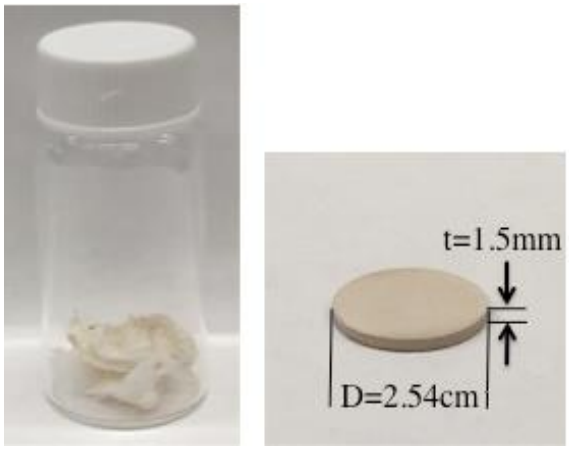

Figure 4.11 Digital images of PVDF-$BaTiO_3$ nanocomposites powder after purification (left), and PVDF-$BaTiO_3$ nanoparticle nanocomposites plate after hot-pressing nanocomposites powder (right).[18] Copyright © 2015 American Chemical Society

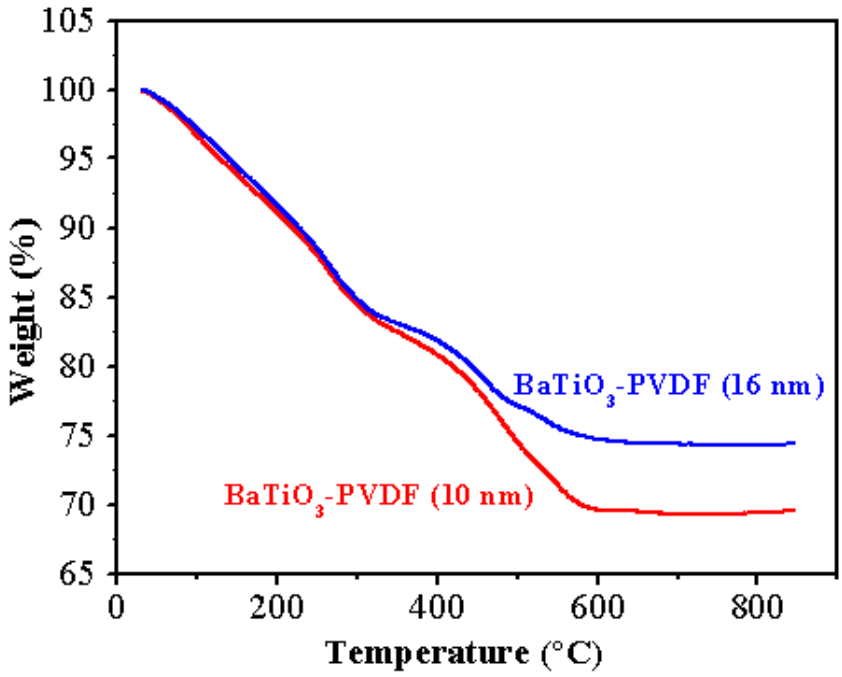

Figure 4.12 Thermogravimetric analysis (TGA) of PVDF-BaTiO3 nanocomposites. The weight fraction of the $BaTiO_3$ nanoparticle was 69.5% for D = 10.2 ± 0.6 nm, and 74.4% for D =16.1 ± 0.8 nm, respectively. [18] Copyright © 2015 American Chemical Society

Figure 4.13 compares the dielectric properties of two different nanocomposites (i.e., *D* = 10.2±0.6 nm and *D* =16.1±0.8 nm) and pure PVDF over a frequency range from 100Hz to 2MHz. Obviously, the dielectric constant of PVDF-$BaTiO_3$ nanocomposites decreased with the increase of frequency (**Figure 4.13a**). This can be ascribed to the dipole relaxation of nanocomposites as the dipole movement of nanocomposites fell behind the applied electric field.[246] In addition, the loss tangent of nanocomposites, tanδ = ε''/ε' (where ε' and ε'' are the real and imaginary parts of permittivity, respectively), also known as the dissipation factor, first decreased and then gradually increased at high frequency. More importantly, compared to pure PVDF, PVDF-$BaTiO_3$ nanocomposites exhibited a lower tanδ, and this reduction was much more significant in the high frequency region (**Figure 4.13b**). This can be ascribed to the large interfacial areas in the

PVDF-$BaTiO_3$ nanocomposites which promote the interfacial exchange coupling through a dipolar interface layer, thereby leading to the enhanced polarization, dielectric response and breakdown strength.[81, 247] In addition, the tethered multi-arm PVDF chains can contribute even higher breakdown strength than its bulk counterpart by avoiding avalanche effects.[53, 247] The rapid increase in tanδ of pure PVDF in the high frequency range was resulted from the α relaxation, which was associated with the glass transition of PVDF. [248-249] It is clear that in comparison to pure PVDF at $2x10^6$ Hz, the tanδ was 0.020 for PVDF-$BaTiO_3$ nanocomposites (D = 10.2±0.6 nm), and 0.028 for PVDF-$BaTiO_3$ nanocomposites (D = 16.1±0.8 nm), respectively, implying that the loss of PVDF-functionalized $BaTiO_3$ nanoparticles was relatively low (**Figure 4.13b**).

The nanocomposites plates prepared for dielectric properties measurements described above are microscopically homogeneous, as clearly evidenced by SEM imaging on the freeze-fractured cross sections of nanocomposite plates (**Figure 4.14**). There was limited amount of porosity and the nanocomposites possessed good homogeneity, signifying that *intimate* PVDF-$BaTiO_3$ nanocompsites afforded favorable structure for achieving uniform morphology.

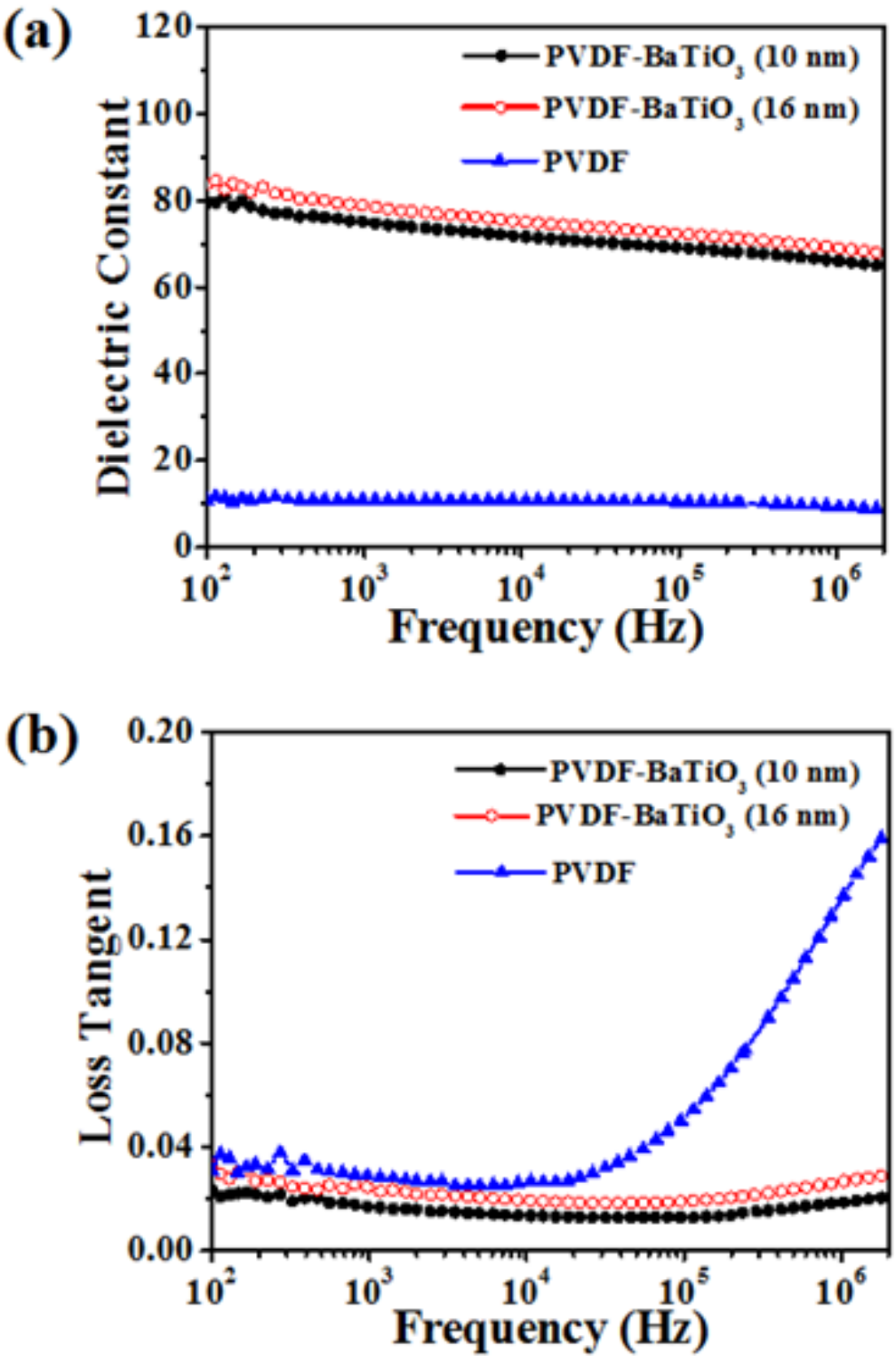

Figure 4.13 Dielectric constants and loss tangents of PVDF and PVDF-BaTiO3 nanocomposites with different diameters of $BaTiO_3$ nanoparticles (i.e., D = 10.2 ± 0.6 nm and D = 16.1 ± 0.8 nm). [18] Copyright © 2015 American Chemical Society

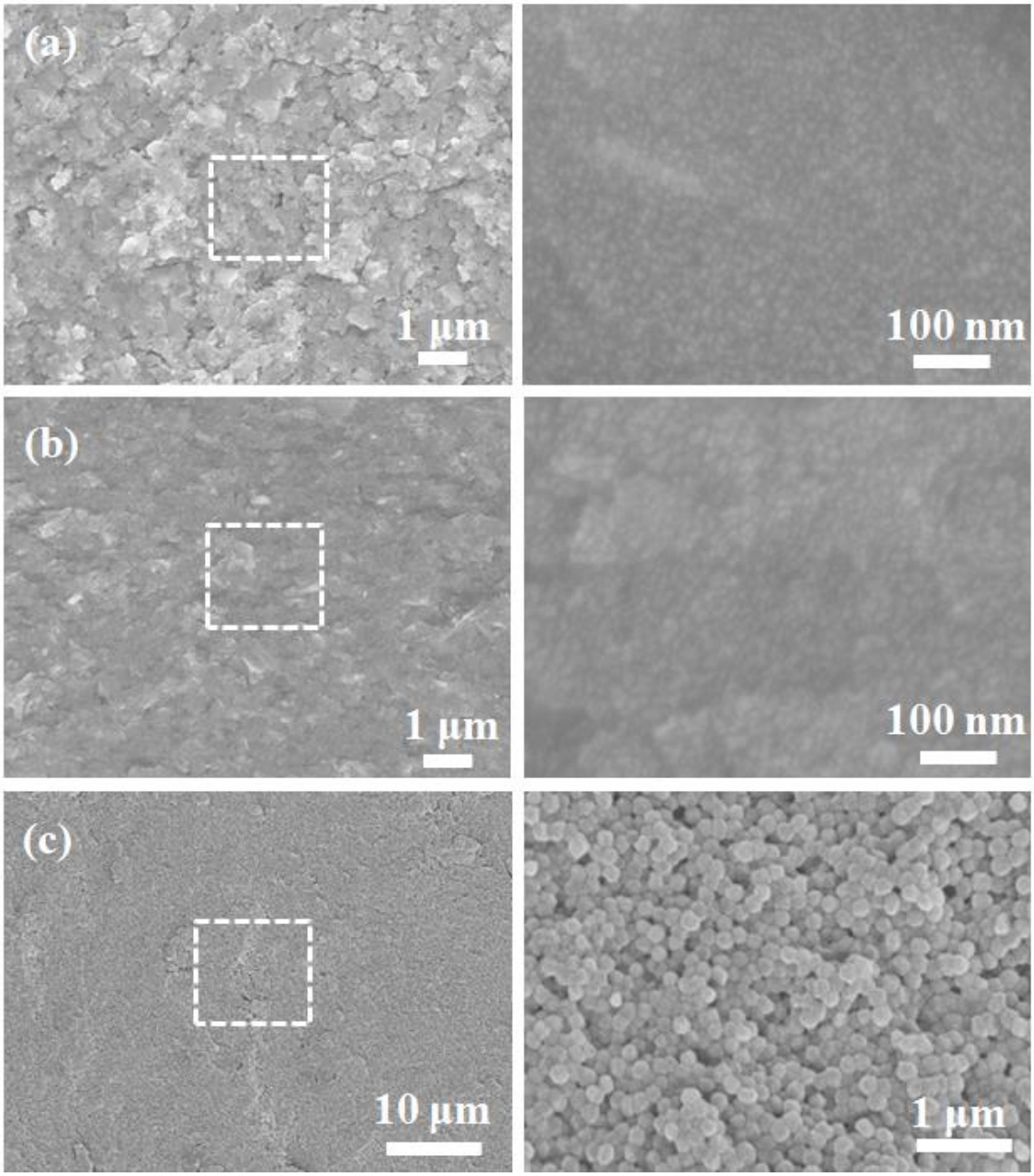

Figure 4.14 SEM images of PVDF-$BaTiO_3$ nanocomposites and pure PVDF (i.e., freeze-fractured cross sections of nanocomposites plates prepared for dielectric properties measurements). (a) PVDF-$BaTiO_3$, D = 10.2 ± 0.6 nm; (b) PVDF-$BaTiO_3$, D =16.1 ± 0.8 nm; and (c) pure PVDF. The right panels are the close-ups of dash-boxed regions in the left panels. [18] Copyright © 2015 American Chemical Society

The effective dielectric constant of $BaTiO_3$ nanoparticle solely can be extracted from the dielectric properties measurements of PVDF-$BaTiO_3$ nanocomposites. As the PVDF chains intimately cover the $BaTiO_3$ nanoparticles,[250] the Landauer-Bruggeman effective approximation is more appropriate than other models and is employed for calculating the effective dielectric constant of $BaTiO_3$ nanoparticles calculation. The model is given by: [251]

$$\gamma \frac{\varepsilon_{BTO} - \varepsilon_{eff}}{\varepsilon_{BTO} + 2\varepsilon_{eff}} + (1-\gamma) \frac{\varepsilon_{PVDF} - \varepsilon_{eff}}{\varepsilon_{PVDF} + 2\varepsilon_{eff}} = 0 \qquad (1)$$

where γ is the volume ratio of $BaTiO_3$ nanoparticle, which can be calculated based on the TGA measurement, and ε_{eff}, ε_{BTO} and ε_{PVDF} (ε_{PVDF} = 10) are the dielectric constants of PVDF-$BaTiO_3$ nanocomposites, $BaTiO_3$ nanoparticle and PVDF, respectively. **Figure 4.15** shows the calculated dielectric constants of $BaTiO_3$ nanoparticles with two different sizes, suggesting that larger-sized nanoparticle had higher dielectric constant.

We observed that the calculated effective dielectric constant is much larger than the reported calculated ones for the same sizes shown in **Figure 4.2**. We deduce that the much larger dielectric constant may come from the contribution of the domain-wall, as many previous reports have confirmed that most of the dielectric and piezoelectric responses at room temperature are from the domain-wall contribution. [252-254] As the PVDF-$BaTiO_3$ nanoparticles were synthesized using star-like diblock copolymer PAA-*b*-PVDF templates, the resulting $BaTiO_3$ nanoparticles still contain PAA in them, which, may lead to the formation of domain walls, and hence cause the larger effective dielectric constant of $BaTiO_3$ nanoparticles.

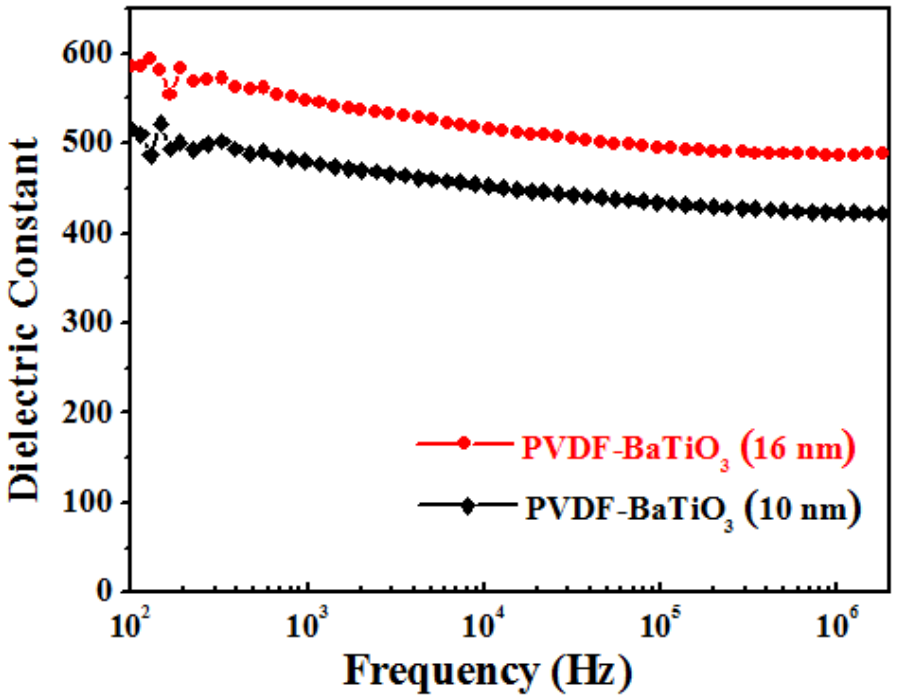

Figure 4.15 Calculated dielectric constants of BaTiO3 nanoparticles in PVDF-BaTiO3 nanocomposites based on the Landauer-Bruggeman effective approximation model. [18] Copyright © 2015 American Chemical Society

The physical properties of nanocomposites are fundamentally related to the chemical compositions, size, crystal structure, and surface chemistry of organic and inorganic constituents. Piezoresponse force microscopy (PFM) measurements were performed on the spots occupied by the individual PVDF-functionalized $BaTiO_3$ nanoparticle (D = 10.2 ± 0.6 nm) as well as the spots on the same substrate but with no presence of PVDF- $BaTiO_3$ nanocomposites to probe the ferroelectric property of the synthesized PVDF-$BaTiO_3$ nanocomposites. The piezoresponse hysteresis loops were collected by imposing a DC bias from -10V to 10V, while the piezoresponse amplitude (A) and phase (Φ) of the induced piezoresponse were simultaneously monitored (**Figure 4.16**). The piezoresponse amplitude (A; in nm) was calculated by dividing the measured amplitude (A; in mV) with the cantilever sensitivity (0.00853V/nm for the tip). For the

spot occupied by the individual PVDF-$BaTiO_3$ nanoparticle, the piezoresponse displayed a square-shaped hysteresis loop of the phase loop with 180° phase change (**Figure 4.16a**) and a classic butterfly-shaped amplitude loop (**Figure 4.16b**). On the contrary, the empty spot on the same substrate but with no presence of PVDF- $BaTiO_3$ nanocomposites showed a clear "V" shaped response for the amplitude signal and a 180° phase change without any hysteresis for both the amplitude and phase signals. The comparison of the PFM signals for the two spots with or without PVDF-$BaTiO_3$ nanoparticle, together with the fact that both components in the PVDF-$BaTiO_3$ nanocomposites are of ferroelectric phase as confirmed by Raman and XRD results, suggest that the synthesized PVDF-$BaTiO_3$ nanocomposites may have well-defined spontaneous polarization that can be switched by external electric field. (*i.e.*, the ferroelectric property). We note that the lateral size of single $BaTiO_3$ nanoparticle measured by PFM is much larger than 10.2±0.6 nm obtained by TEM, and this may be due to the PFM tip artifact (the radius of curvature of PFM tip used is 20 nm), while the height (approximately 12.5 nm, including the PVDF chains situated on the surface of 10.2±0.6-nm nanoparticle) is in good agreement with the TEM measurement.

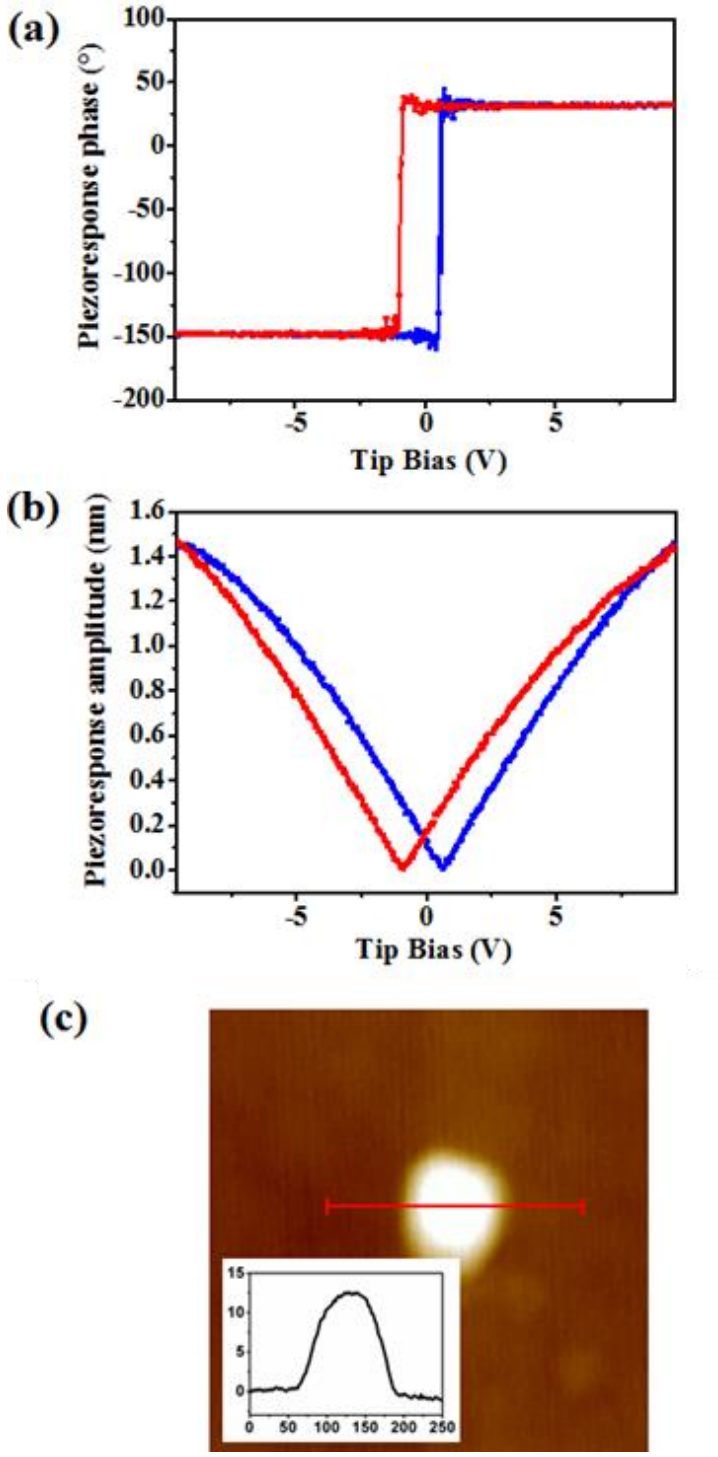

Figure 4.16 Piezoresponse of a single PVDF-functionalized $BaTiO_3$ nanoparticle (D = 10.2 ± 0.6 nm) on the TEM grid. (a) phase, and (b) amplitude of the first harmonic signal as a function of Vdc to the tip while a 2V peak-to-peak ac voltage is applied to the bottom electrode. (c) AFM height image of a single PVDF-functionalized $BaTiO_3$ nanoparticle and its corresponding profile. [18] Copyright © 2015 American Chemical Society

4.3 Conclusions

In summary, we have developed, for the first time, a viable and robust *in-situ* synthesis of intimate ferroelectric organic−inorganic nanocomposites with well-controlled dimensions and compositions by exploiting both the ability to synthesizing amphiphilic star-like PAA-*b*-PVDF diblock copolymers with well-defined molecular weight of each block as nanoreactors, and the strong coordination interaction between the precursors and hydrophilic PAA blocks. The PAA-*b*-PVDF nanoreactors were prepared by a combination of ATRP and click reaction, followed by hydrolysis. PVDF-$BaTiO_3$ nanocomposites are composed of uniform $BaTiO_3$ nanoparticles with tunable size stably connected with PVDF. By judiciously tune the molecular weight of inner PAA blocks, $BaTiO_3$ nanoparticles with different sizes intimately and permanently linked with PVDF chains can be created.

Notably, the unimolecular nanoreactor strategy we have described renders the crafting of functional nanocomposites with a well-defined size and shape, precisely controllable PVDF/$BaTiO_3$ ratio, and superior long-term stability. PVDF-$BaTiO_3$ nanocomposites displayed high dielectric constant and low dielectric loss. As such, they offer promising potential for applications in energy storage, such as high-energy density capacitors. In addition, these PVDF-functionalized $BaTiO_3$ nanoparticles exhibited the ferroelectric tetragonal structure, and the capped semicrystalline PVDF contains the ferroelectric β phase in it. By extension, this amphiphilic star-like diblock copolymer nanoreactor strategy has the capacity to yield a myriad of intimate organic-inorganic nanocomposites with functional organic and inorganic constituents, for example all semiconducting conjugated polymer-quantum dot nanocomposites by utilizing

amphiphilic star-like PAA-*b*-conjugated polymer diblock copolymer as nanoreactors, for future generations of complex nanoscale materials and devices.

Chapter 5 Polymer-templated $ZnFe_2O_4$-carbon nanocomposites as advanced electrodes for LIBs

Related publication: B. Jiang, C. Han, B. Li, Y. He, and Z. Lin, "*In-situ* Crafting of $ZnFe_2O_4$ Nanoparticles Impregnated within Continuous Carbon Network as Advanced Anode Materials", ***ACS Nano***. **10**, 2728 (2016)

5.1 Introduction

To date, a wide variety of anode materials with much higher lithium storage capacity are under extensively investigation for replacing the graphite anode material. For example, silicon, which electrochemically form alloys with Li, has emerged as one of the most promising high-energy electrode materials, as it offers an appropriate low voltage as an anode and a high theoretical specific capacity of ~4200 mAh g^{-1}, ten times higher than that of traditional graphite anode.[98] Transition metal oxides (M_xO_y, where M is Fe, Co, Ni, Cu, Sn, Mn, etc.) are also widely studied as promising alternatives to graphite owing to their attractive higher theoretical capacities ($>$ 600 mAh g^{-1}), low cost, environmental friendliness and wide availability containing earth-abundant elements.[11, 97, 106] Lithium storage within transition metal oxides is mainly achieved through the reversible conversion reaction between lithium ions and metal oxides, which form metal nanocrystals dispersed in the Li_2O matrix, *i.e.*, $M_xO_y + 2yLi \leftrightarrow xM + yLi_2O$.[11, 143] For example, Fe_3O_4 has attracted lots of interest due to their advantages of natural abundance, environmentally friendly, and biocompatible. It offers a theoretical capacity of 926 mA h

g^{-1} by reacting with eight lithium ions completely per formula unit. [110, 255] However, the reduced iron is not electrochemically active, by replacing one iron atom with zinc, the resulting ternary oxide (*i.e.*, $ZnFe_2O_4$) contributes an extra lithium uptake by forming LiZn alloy, leading to an enhanced theoretical capacity of 1000.5 mAh g^{-1}.[143] SnO_2 is converted into Sn nanoparticles dispersed in Li_2O matrix by reacting with 4 moles of Li ions, and the resulting Sn nanoparticles continuously form alloys with Li ions, leading to a theoretical capacity of around 1494 mA h g^{-1} by uptaking 8.4 moles of lithium ions. Other transition metal oxides also deliever much higher capacity than graphite, such as MnO_2 (1233 mA h g^{-1}), SnO_2 (790 mA h g^{-1}), Fe_2O_3 (1005 mA h g^{-1}) [107], CoO (715 mA h g^{-1}), Co_3O_4 (mA h g^{-1}), to name but a few[108], making them attractive anode materials for high energy density application.

Despite the intriguing features described above, these high-capacity metal oxides have not yet been implemented for practical applications. This is due to their capacity decay over cycling which originates primarily from the electrode pulverization and the subsequent loss of electrical contacts between the active materials and the current collectors caused by the volume change induced stress during the repeated insertion and extraction of lithium ions.[109-110] Another challenging issue is the poor electrical conductivity of transition metal oxides, which limits the attainable Li storage capacity at high charge/discharge rate.[11, 112-113] Fe_3O_4 has a higher conductivity of 10^2 S cm^{-1} than other metal oxide active materials (e.g. TiO_2 (10^{-10} S cm^{-1}) and SnO_2 (10^{-3} S cm^{-1})) [114-115], still cannot satisfy the requirement of high power density for future large-scale applications in electric or hybrid vehicles.

Two main strategies have been widely recognized as effective methods in alleviating these issues. The first strategy is to reduce the active electrode materials to nanometer scale, which provide multiply advantageous functions as introduced in **Chapter 1**, such as (i) a better accommodation of mechanical stress; (ii) the shortened transport length for electrons and lithium ions and thus rendering fast discharging/charging; and (iii) a higher electrode/electrolyte contact area favorable for improving the lithium reaction rate. Another main strategy for improving the electrochemical performance of LIBs is to construct hierarchically structured nanocomposites by integrating nanostructured active materials with those more electrically conductive carbon materials (e.g., porous carbon, carbon nanotubes, nanofibers, graphene/graphite, etc.).

Clearly, the synergy of the two strategies noted above, that is, nanostructure engineering of active materials and its hybridization with conductive carbonaceous material, would impart a better electrochemical performance. However, it remains challenging to achieve this synergy. In this study, the integration of carbons with active materials will be realized by the polymer-templated approach. Active materials, including Fe_3O_4, $ZnFe_2O_4$, and SnO_2, will be illustrated as examples to demonstrate the versatility of the polymer-templated approach. In this chapter, the focus is on the $ZnFe_2O_4$-carbon nanocomposites composed of $ZnFe_2O_4$ nanoparticles with an average diameter of 16±5 nm impregnated within the continuous carbon network via the pyrolysis of $ZnFe_2O_4$ precursors-containing polystyrene@poly(acrylic acid) (PS@PAA) core@shell nanospheres. The PS@PAA nanospheres were synthesized in one-step by emulsion polymerization, followed by thermal annealing of $ZnFe_2O_4$ precursor-containing

PS@PAA nanospheres, leading to the formation of $ZnFe_2O_4$ nanoparticles embedded in the continuous carbon network due to the carbonization of PS@PAA nanospheres.

5.2 Experiments, results and discussion

5.2.1 Synthesis of core-shell structured PS@PAA nanospheres and construction of $ZnFe_2O_4$-carbon nanocomposites

The PS@PAA nanospheres were synthesized in one-step by emulsion polymerization of the mixture of styrene and acrylic acid in aqueous solution as shown in **Figure 5.1**. In the beginning of forming PS@PAA core@shell nanospheres, hydrophobic monomers of styrene and hydrophilic monomers of acrylic acid were first dispersed in water, forming uniform oil-in-water droplets. The polymerization of oil-in-water droplets of styrene and the creation of free radical of acrylic acid was initiated by the initiator $K_2S_2O_8$. The resulting PS formed the core of the core@shell nanospheres (upper left panel in **Figure 5.1**). Interestingly, on the other hand, a small portion of hydrophilic acrylic acid monomers and their resulting oligomers acted as surfactant to stabilize the oil-in-water droplets noted above (upper left panel in **Figure 5.1**).[256] In the meantime, a great portion of hydrophilic acrylic acid monomers were dissolved in water and further polymerized to yield oligomers. As the polymerization continues, the molecular weight of the formed acrylic acid oligomers increased, leading to the decrease in hydrophilicity of acrylic acid oligomers and the formation of PAA. The coagulation of PAA on the PS core produced the PAA shell, and thus PS@PAA core@shell nanospheres (upper right panel in **Figure 5.1**).[256]

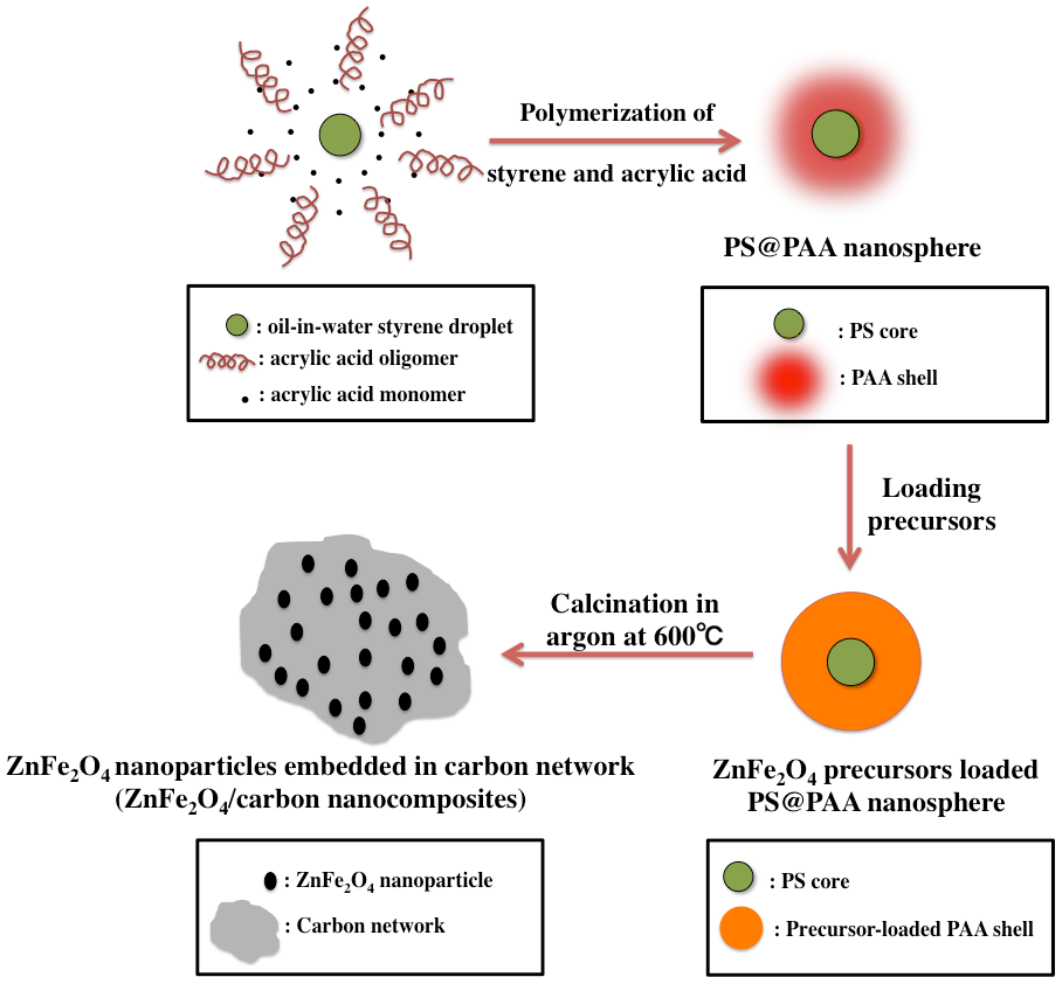

Figure 5.1 Schematic illustration of the formation of PS@PAA nanospheres and the resulting $ZnFe_2O_4$/carbon nanocomposites comprising $ZnFe_2O_4$ nanoparticles impregnated within the carbon network.[19] Copyright © 2016 American Chemical Society

Fourier transform infrared spectroscopy (FTIR) spectra of PS@PAA nanospheres before and after the introduction of $ZnFe_2O_4$ precursors were also measured to further confirm the loading of precursors. As shown in **Figure 5.2**, the characteristic absorption at 3023, 2921, 1600, 1493, 1452, 1025, 757 and 697 cm^{-1} corresponding to benzene rings[257] in the PS core and the characteristic peak at 1709 cm^{-1} attributed to the carboxylic acid group of PAA are clearly evident in as-prepared PS@PAA nanospheres.[258] After the loading of $ZnFe_2O_4$ precursors, a strong peak at 1385 cm^{-1}

corresponding to the NO_3^- ions[259] emerged, signifying that the precursors (*i.e.*, $Zn(NO_3)_2 \cdot 6H_2O$ and $Fe(NO_3)_3 \cdot 9H_2O$) were successfully incorporated within the space occupied by the PAA shell of PS@PAA core/shell nanospheres. Notably, the peaks corresponding to PS core and PAA shell became weaker after the loading of precursors.

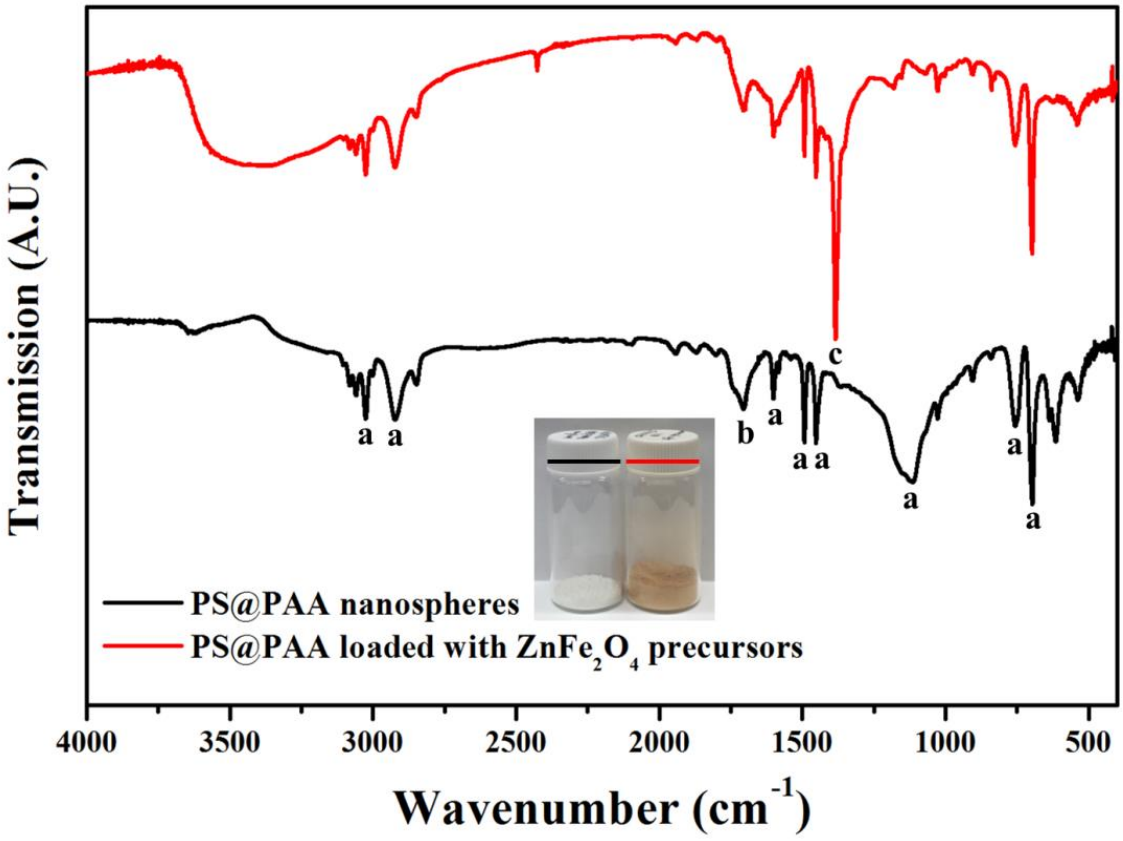

Figure 5.2 FTIR spectra of PS@PAA nanospheres before and after loading the $ZnFe_2O_4$ precursors. The inset shows the digital images of the PS@PAA nanospheres before and after loading the $ZnFe_2O_4$ precursors.[19] Copyright © 2016 American Chemical Society

The TEM image for the PS@PAA nanospheres clearly showed their core@shell structure with an average diameter of approximately 260 nm (**Figure 5.3a**). After the polymerization was complete by reacting at 80 °C for 24 h, the precursors solution (*i.e.*, $Zn(NO_3)_2 \cdot 6H_2O$ and $Fe(NO_3)_3 \cdot 9H_2O$ dissolved in water) with controlled amount and pH

value was added dropwise to the PS@PAA nanospheres solution at 80 °C under vigorous stirring. As the carboxyl group of PAA has a strong coordination interaction with Fe^{3+} and Zn^{2+} ions,[14, 18, 260] the PS@PAA nanospheres functioned as templates by incorporating $ZnFe_2O_4$ precursors, yielding the $ZnFe_2O_4$ precursors-loaded PS@PAA nanospheres (**Figure 5.3b**). In comparison with pure PS@PAA nanospheres, the edges of PAA shell was blurred by the precursors, suggesting the success in loading $ZnFe_2O_4$ precursors.

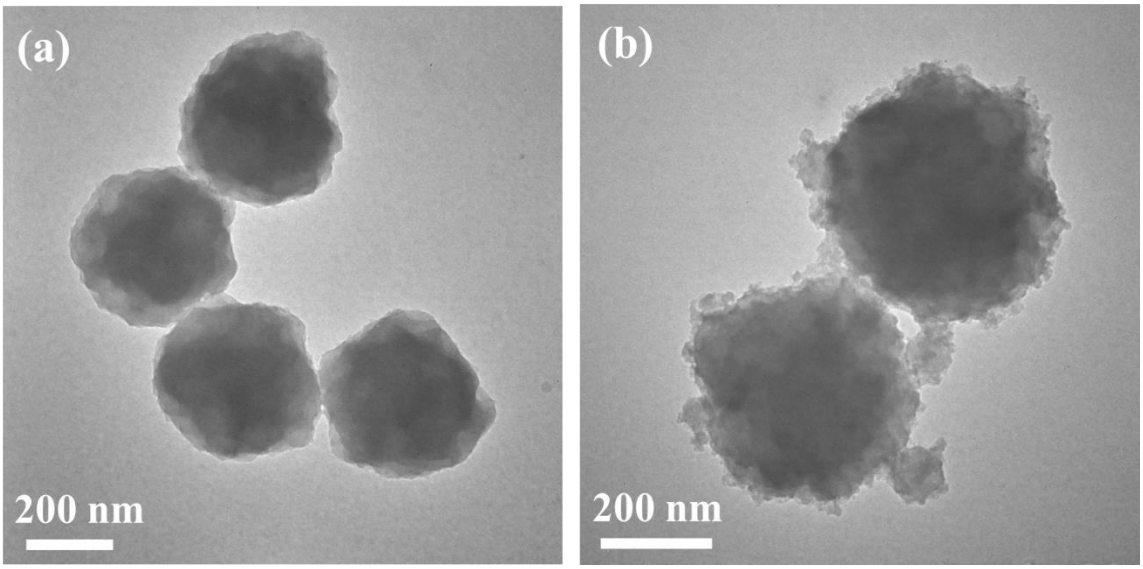

Figure 5.3 Sample characterizations. TEM images of (a) PS@PAA core@shell nanospheres, (b) $ZnFe_2O_4$ precursors-loaded PS@PAA nanospheres.[19] Copyright © 2016 American Chemical Society

The $ZnFe_2O_4$ precursors-containing PS@PAA nanospheres provided a good source for the formation of $ZnFe_2O_4$ nanoparticles (from precursors) and the creation of carbon network (from PS@PAA nanospheres). The thermogravimetric analysis (TGA) of the $ZnFe_2O_4$ precursors-loaded PS@PAA nanospheres in nitrogen atmosphere showed a significant weight loss at around 400 °C due to the degradation of PS and PAA; the weight loss was then slowed over a temperature range of 400-600 °C (**Figure 5.4**). After

600 °C, the weight remained nearly constant, implying that the thermal decomposition process was complete. Thus, 600 °C was chosen as the temperature for the calcination treatment as higher temperature may result in the reduction of $ZnFe_2O_4$ by the formed carbon.[261]

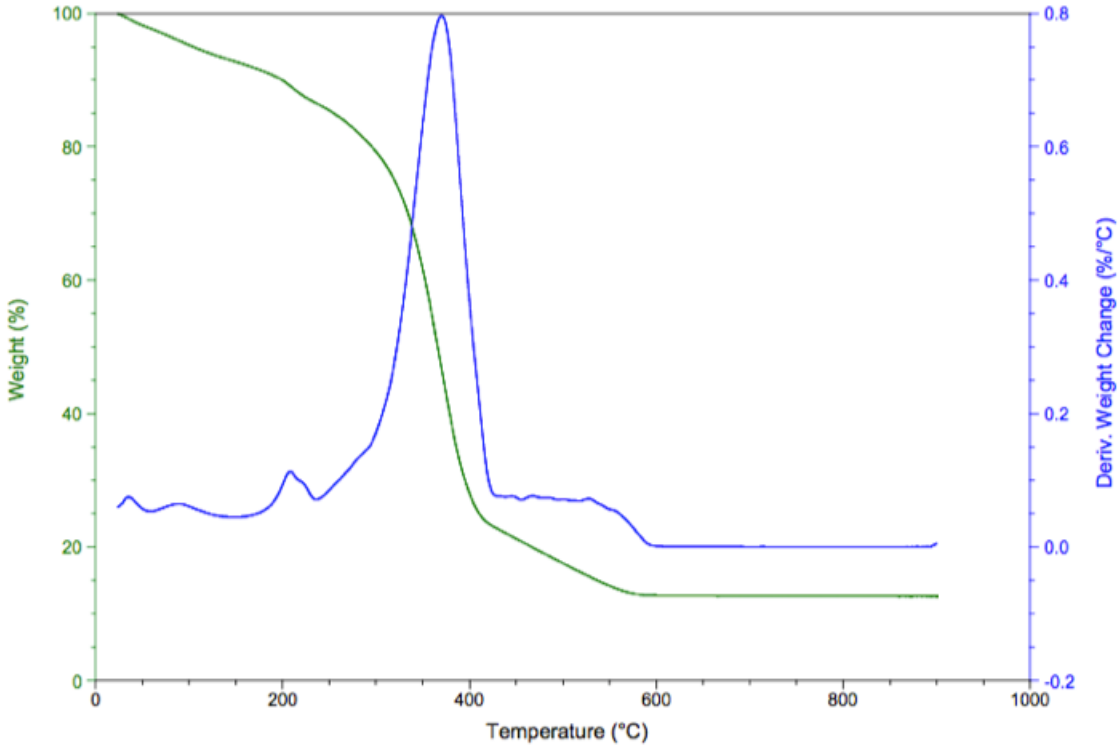

Figure 5.4 TGA plot of the $ZnFe_2O_4$ precursors-loaded PS@PAA nanospheres under nitrogen flow with a temperature ramp of 10 °C/min.[19] Copyright © 2016 American Chemical Society

The calcination of the precursors-loaded PS@PAA nanospheres under argon atmosphere at a ramping rate of 1 °C/min for 2 h led to the thermal decomposition of both the PS@PAA nanospheres and the loaded precursors, converting the precursors into $ZnFe_2O_4$ nanoparticles in conjunction with the collapse and shrinkage of PS@PAA nanospheres and their final transformation into carbon. It is noteworthy that the loading of precursors within the PAA core of PS@PAA nanospheres restricted the aggregation

and coarsening of $ZnFe_2O_4$ nanoparticles during the high-temperature treatment, thereby rendering the formation of $ZnFe_2O_4$ nanoparticles with an average diameter of 16±5 nm dispersed in the continuous carbon network (*i.e.*, $ZnFe_2O_4$/carbon nanocomposites) TEM images of the $ZnFe_2O_4$/carbon nanocomposites shown in **Figure 5.5a**,**b** clearly shows the presence of continuous carbon network encapsulating $ZnFe_2O_4$ nanoparticles. The selected area electron diffraction (SAED) pattern (inset in **Figure 5.5b**) exhibited a series of concentric rings, signifying the polycrystalline characteristics of the resulting $ZnFe_2O_4$ nanoparticles.

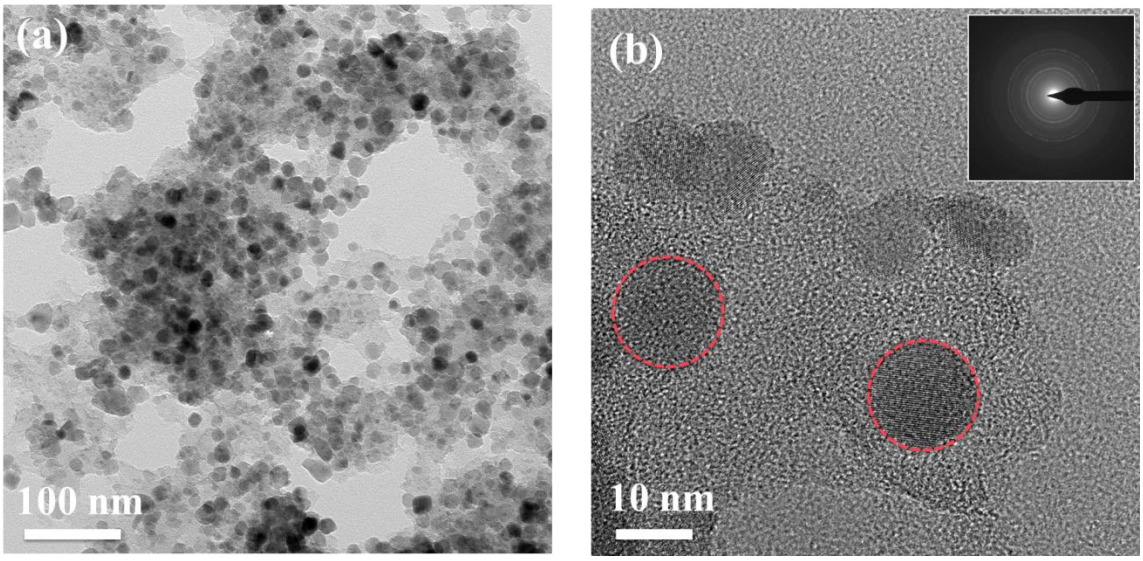

Figure 5.5 (a). TEM images of the $ZnFe_2O_4$(79.28wt%)/carbon nanocomposites formed after calcination in argon at 600 ℃ with $ZnFe_2O_4$ nanoparticles embedded within the continuous carbon network (the average diameter of $ZnFe_2O_4$ nanoparticles is 16±5 nm); (b) The corresponding HRTEM image of (a), where the $ZnFe_2O_4$ nanoparticles are marked in red circles. The inset in (b) is the SAED pattern of $ZnFe_2O_4$/carbon nanocomposites.[19] Copyright © 2016 American Chemical Society

The chemical composition of $ZnFe_2O_4$/carbon nanocomposites was analyzed by energy-dispersive X-ray spectroscopy (EDX). As shown in **Figure 5.6a**, the elements of both Zn and Fe were observed, indicating the existence of $ZnFe_2O_4$. The formation of

$ZnFe_2O_4$ phase was further corroborated by the X-ray diffraction (XRD) measurement (**Figure 5.6b**). The XRD peaks at 30°, 35.5°, 38.0°, 43.5°, 53.2°, 56.7° and 62.3° can be assigned to the [220], [311], [222], [400], [422], [511] and [440] planes of $ZnFe_2O_4$ in cubic spinel structure with F*d*-3*m* space group (JCPDS Card No. 022-1012), which matched very well with the previously reported results.[143, 262] The absence of peaks assignable to the crystalline phase of carbon suggested the carbon network was likely in amorphous state.

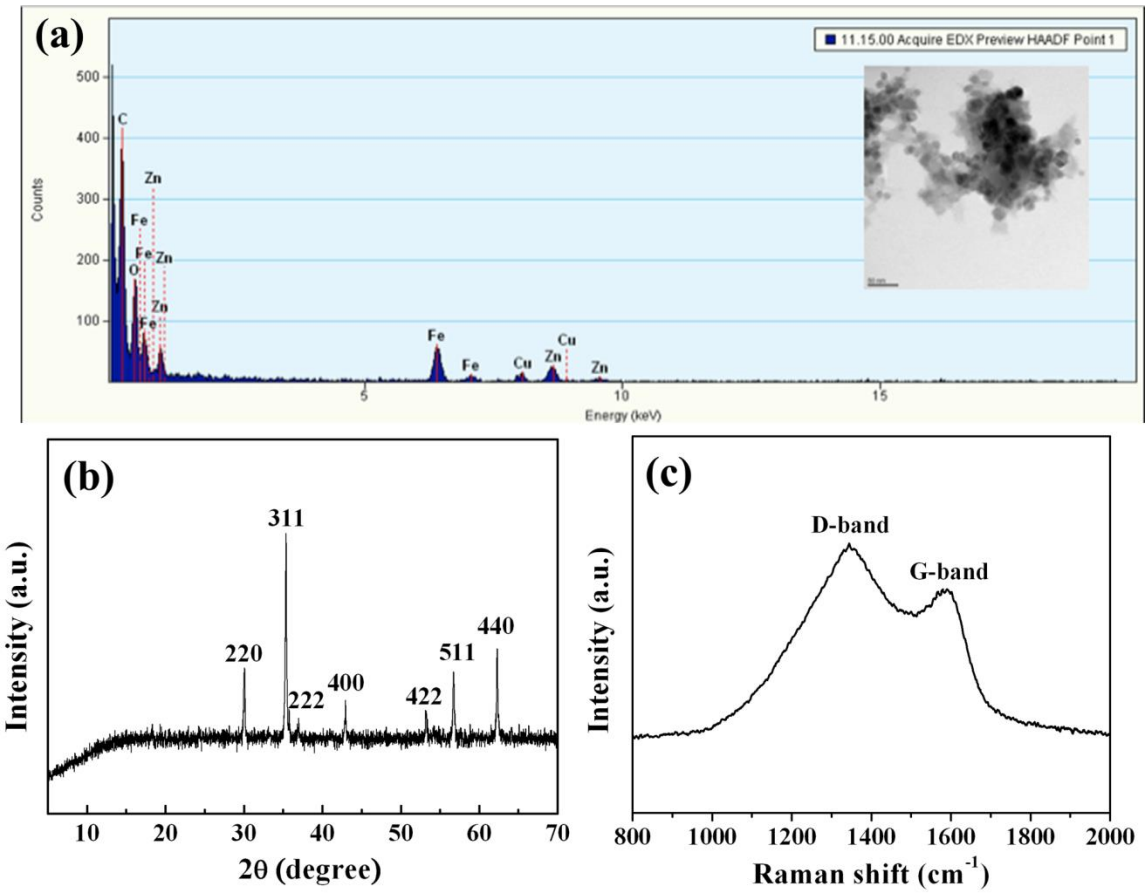

Figure 5.6 (a) EDX spectrum of the $ZnFe_2O_4$ (79.3wt%)/carbon nanocomposites. The inset is the corresponding TEM image for the region examined. (b) XRD pattern of $ZnFe_2O_4$(79.3wt%)/carbon nanocomposites. (c) Raman spectra of $ZnFe_2O_4$ (79.3wt%)/carbon nanocomposites. The excitation wavelength is 785 nm.[19] Copyright © 2016 American Chemical Society

Raman spectroscopy measurement on $ZnFe_2O_4$/carbon nanocomposites was performed with an excitation wavelength of 785 nm. The peaks at around 1340 cm^{-1} and 1590 cm^{-1} correspond to D band (disordered graphitic structure) and G band (graphitic structure) of carbon, respectively (**Figure 5.6c**). The large intensity ratio of I_D/I_G for the $ZnFe_2O_4$/carbon nanocomposites verified the amorphous nature of carbon,[263] correlating well with the XRD result.

It is well-known that the amount of carbon is a crucial parameter in determining the electrochemical performance of the nanocomposites electrode.[264-265] To optimize the electrochemical performance, we scrutinized $ZnFe_2O_4$/carbon nanocomposites at different $ZnFe_2O_4$ to carbon ratios by varying the molar ratio of $ZnFe_2O_4$ precursors to PS@PAA nanospheres. Based on the TGA results shown in **Figure 5.7**, the $ZnFe_2O_4$ contents in these $ZnFe_2O_4$/carbon nanocomposites were determined to be 61.4 wt%, 67.4 wt%, 74.5 wt%, 79.3 wt% and 83.5 wt%, respectively. We note that the TEM, XRD, and Raman results described above are all from the $ZnFe_2O_4$/carbon nanocomposites containing 79.3 wt% $ZnFe_2O_4$ (hereafter referred to as $ZnFe_2O_4$(79.3wt%)/carbon); and the other four nanocomposites samples showed similar results from these characterizations.

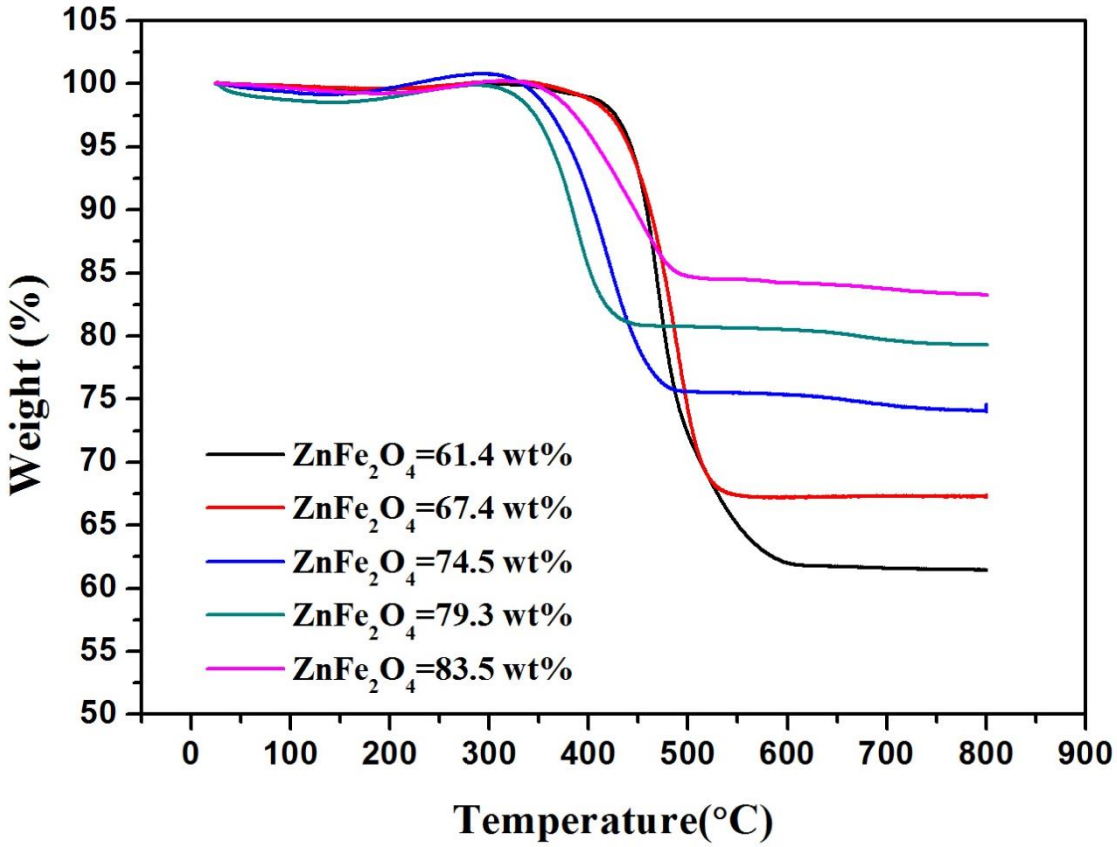

Figure 5.7. TGA plots of the $ZnFe_2O_4$/carbon nanocomposites under the air flow with a temperature ramp of 10°C/min. The $ZnFe_2O_4$ contents in these $ZnFe_2O_4$/crabon nanocomposites are 61.4 wt%, 67.4 wt%, 74.5 wt%, 79.3 wt%, and 83.5 wt%, respectively.[19] Copyright © 2016 American Chemical Society

5.2.2 Electrochemical performance of $ZnFe_2O_4$-carbon nanocomposites electrodes

To scrutinize the lithiation and delithiation behavior of $ZnFe_2O_4$/carbon nanocomposites electrode, the cyclic voltammetry (CV) measurement on the $ZnFe_2O_4$(79.3wt%)/carbon electrode was performed at a scan rate of 0.1 mVs^{-1} over a potential range from 0.005 V to 3 V. **Figure 5.8a** shows the CVs for the first seven cycles. In the first cathodic scan, a broad peak at around 0.8 V was observed, which can be attributed to the reduction of Fe^{3+} and Zn^{2+} to their metallic states, the formation of Li-Zn

alloys, and an irreversible reaction related to the decomposition of electrolyte.[266] The cathodic peak shifts to around 0.95 V in the subsequent scans, differentiating the later reduction mechanism from the one in the first scan. For the anodic scans, a broad peak centered at around 1.75 V was seen due to the oxidation of metallic Fe and Zn to Fe^{3+} and Zn^{2+}, respectively.[267] Moreover, the cathodic and anodic peaks did not shift in the subsequent cycles, confirming a highly reversible reaction with lithium once the initial structural changes were completed.

Figure 5.8b presents the galvanostatic discharge/charge profiles of $ZnFe_2O_4$(79.3wt%)/carbon nanocomposites electrode over a voltage range from 0.005 V to 3 V at specific current of 100 mA g^{-1} for the first ten cycles. The initial discharge profile showed a voltage plateau at around 0.8 V. It was then shifted to approximately 0.95 V for the subsequent cycles, consistent with the CV results discussed above. The charge profiles displayed a voltage plateau at about 1.75 V for the first ten cycles, indicating high reversibility. The initial discharge and charge capacities for $ZnFe_2O_4$ (79.3wt%)/carbon nanocomposites anode are 1626 mA h g^{-1} and 1206 mA h g^{-1}, respectively, with the initial coulombic efficiency of 74.2% (all specific capacities are calculated based on the net weight of $ZnFe_2O_4$ nanoparticles). The initial irreversible capacity loss was owing probably to the initial lithiation of $ZnFe_2O_4$ which irreversibly consumed extra lithium and the formation of solid electrolyte interface (SEI) layer at the electrode/electrolyte interface caused by the reduction of electrolyte.[148] For the subsequent cycles, the discharge and charge capacities were stabilized at around 1200 mAh g^{-1} with coulombic efficiencies approaching 100%, signifying a high reversibility of lithium uptake and release.

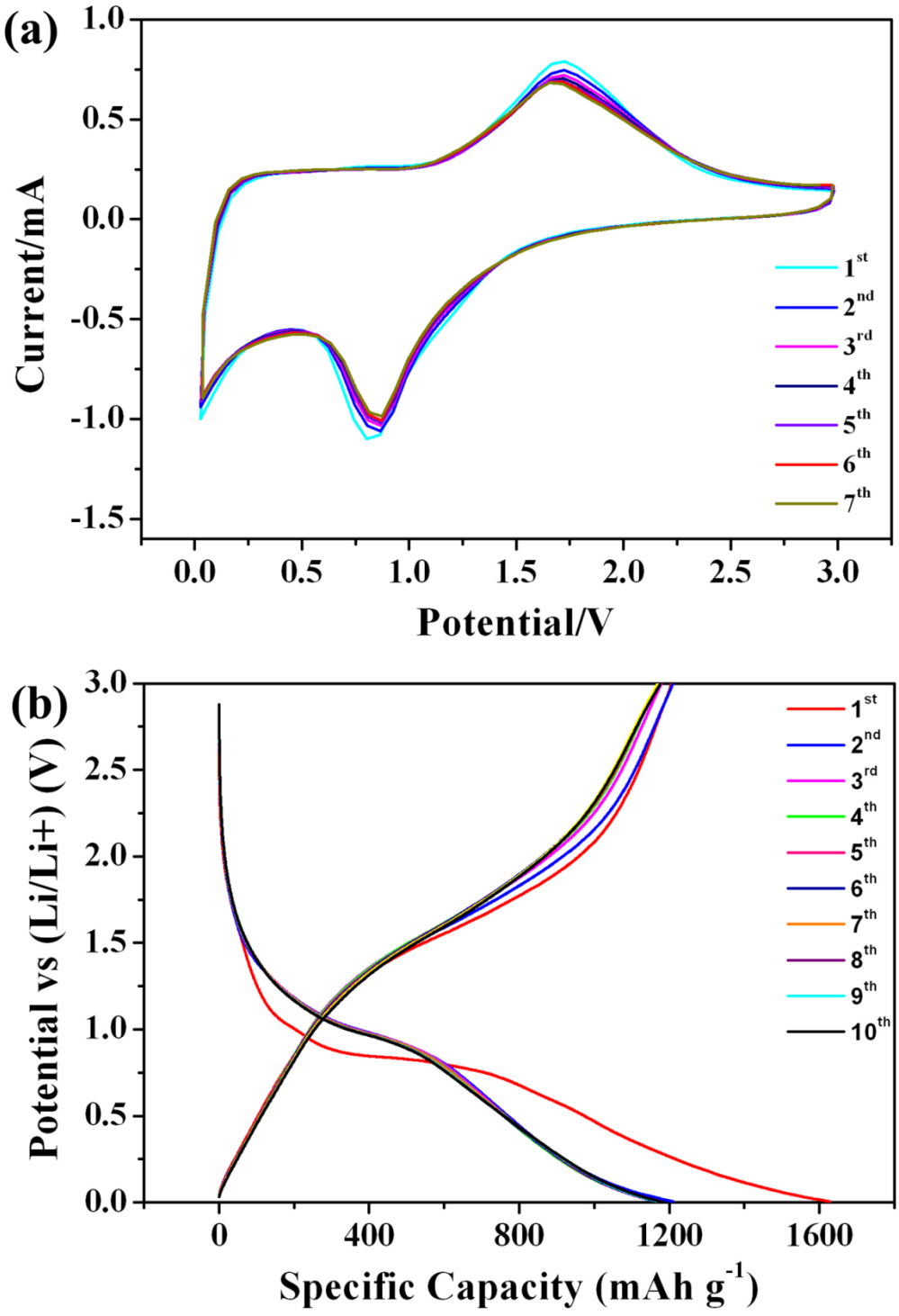

Figure 5.8 (a) Cyclic voltammetry profiles of $ZnFe_2O_4$/carbon nanocomposites for the first seven cycles between 0.005 V and 3 V at a scan rate of 0.1 mV s^{-1}; (b) Charge/discharge profiles of the $ZnFe_2O_4$/C nanocomposites electrode for the first ten cycles between 0.005 V and 3 V at specific current of 100 mA g^{-1}. [19] Copyright © 2016 American Chemical Society

The rate performance of $ZnFe_2O_4$/carbon nanocomposites electrode was investigated by increasing the applied specific current every 10 cycles from 0.1C (1C = 1000 mA g^{-1}), 0.2C, 0.5C, 1C, 2C to 5C and then back to 0.1C. The rate performances of the five $ZnFe_2O_4$/carbon nanocomposites electrodes with different $ZnFe_2O_4$ contents were compared (**Figure 5.9a**). The best rate performance was achieved in $ZnFe_2O_4$ (79.3wt%)/carbon nanocomposites. Clearly, the specific capacity for $ZnFe_2O_4$ (79.3wt%)/carbon nanocomposites electrode decreased with the increase in specific current. Interestingly, the attractive capacities of 1238 mA h g^{-1}, 1198 mA h g^{-1}, 1136 mA h g^{-1}, 1052 mA h g^{-1}, 926 mA h g^{-1}, and 521 mA h g^{-1} were achieved at specific currents of 100 mA g^{-1} (0.1C), 200 mA g^{-1} (0.2C), 500 mA g^{-1} (0.5C), 1000 mA g^{-1} (1C), 2000 mA g^{-1} (2C) and 5000 mA g^{-1} (5C), respectively. When the specific current returned to 0.1C, the capacities not only rebounded back to high value but also showed a continuous increase and reached a higher value of approximately 1500 mA h g^{-1} due to the gradual activation process. [105] Such outstanding rate performance can be ascribed to the synergistic effect of the presence of nanosized $ZnFe_2O_4$ particles and the continuous carbon network. The carbon network with good electrical conductivity served as the conductive medium between $ZnFe_2O_4$ nanoparticles and the current collectors, therefore, the fast charge-discharge can be realized.[149] In addition, the $ZnFe_2O_4$ nanoparticles with such a small size increased the interfacial area for Li reaction and shortened the transport length for ions and electrons, leading to high reversible capacities even at high specific currents.[262] The pure $ZnFe_2O_4$ nanoparticles (*i.e.*, in the absence of continuous carbon network) obtained by calcination in air were compared with the $ZnFe_2O_4$/C nanocomposites calcinated under argon.

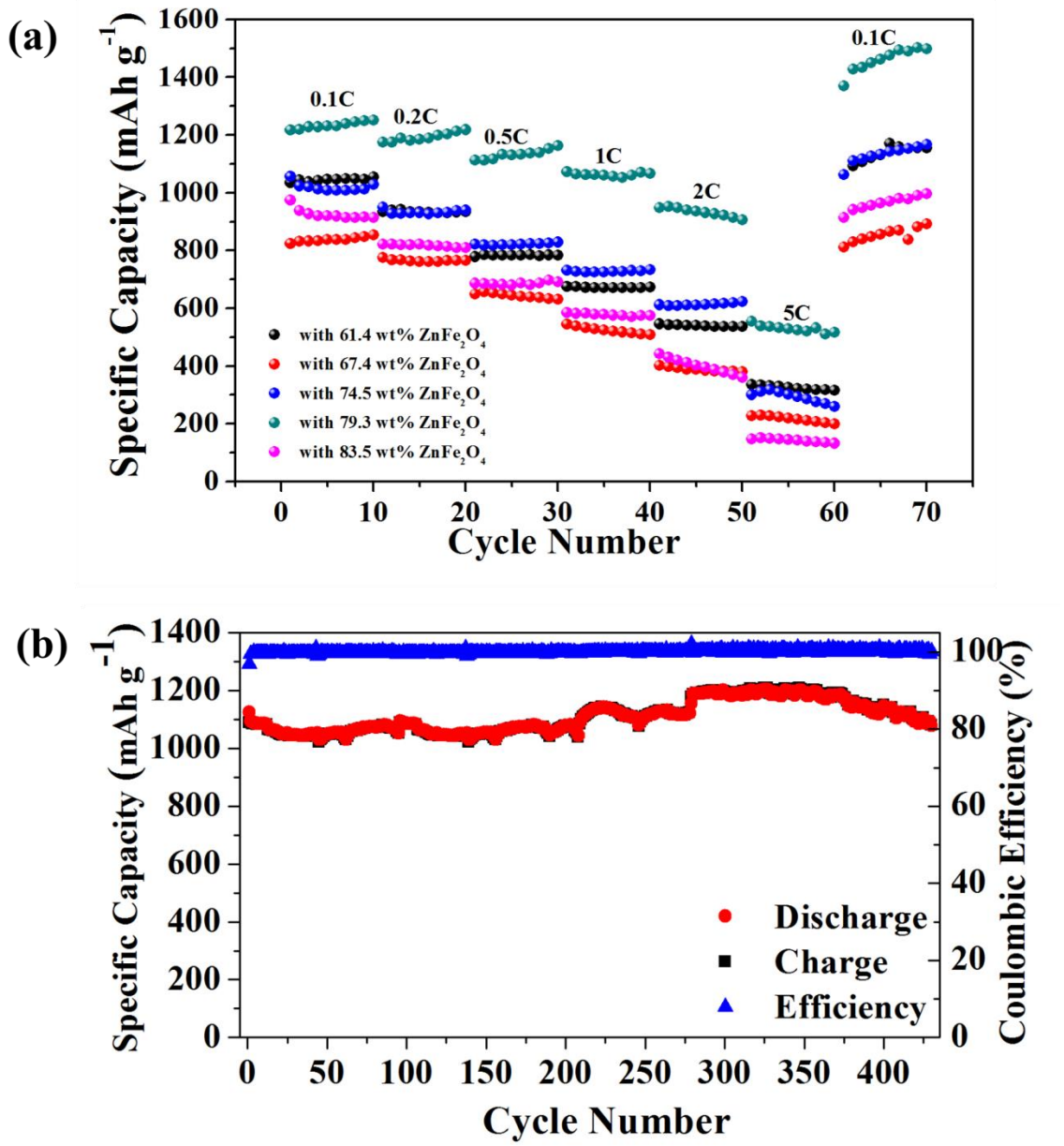

Figure 5.9 (a) Rate capabilities of the five $ZnFe_2O_4$/carbon nanocomposites electrodes with different $ZnFe_2O_4$ contents at various current densities from 0.1C (1C = 1000 mA g-1) to 5C as indicated. The $ZnFe_2O_4$/carbon nanocomposites containing 79.3wt% $ZnFe_2O_4$ exhibited the best rate performance; (b) Cycling performance of $ZnFe_2O_4$ (79.3wt%)/carbon nanocomposites tested at specific current of 200 mA g-1 (0.2C) for 430 cycles. [19] Copyright © 2016 American Chemical Society

Figure 5.9b shows the galvanostatic cycling performance of the $ZnFe_2O_4$(79.3wt%)/carbon nanocomposites electrode tested under specific current density of 200 mA g^{-1} over a voltage window between 0.005 V and 3 V for 430 cycles. Prior to the leveling off, the discharge capacity gradually increased from initial value of 1090 mA h g^{-1} to around 1190 mA h g^{-1} for the first 280 cycles and reached a stable value around 1090 mAh g^{-1} from 280 to 370 cycles. The rapid capacity decay was then observed after 370 cycles and the capacity decreased to about 1078 mA h g^{-1} after the cycling finished at 430 cycles, yielding a capacity retention of 98%. The observed capacity increase during cycling was commonly observed for graphene/carbon-based metal oxide composites, and was attributed largely to the improved Li-diffusion kinetics due to the gradual activation process and reversible reaction between metal particles and electrolytes.[105] Such long-term cyclic stability demonstrated the excellent structural stability for the $ZnFe_2O_4$/carbon nanocomposites with $ZnFe_2O_4$ nanoparticles encapsulated in the carbon matrix.

It is notable that the precursors-loaded PS@PAA nanospheres were also calcinated in air, and the pure $ZnFe_2O_4$ nanoparticles without the carbon network encapsulation was obtained and used as control. **Figures 5.10a** and **5.10b** show the TEM image and the rate performance of pure $ZnFe_2O_4$ nanoparticles. Clearly, comparing with pure $ZnFe_2O_4$ nanoparticles, due to the presence of continuous and conductive carbon network in $ZnFe_2O_4$/carbon nanocomposites, their rate performance was markedly improved.

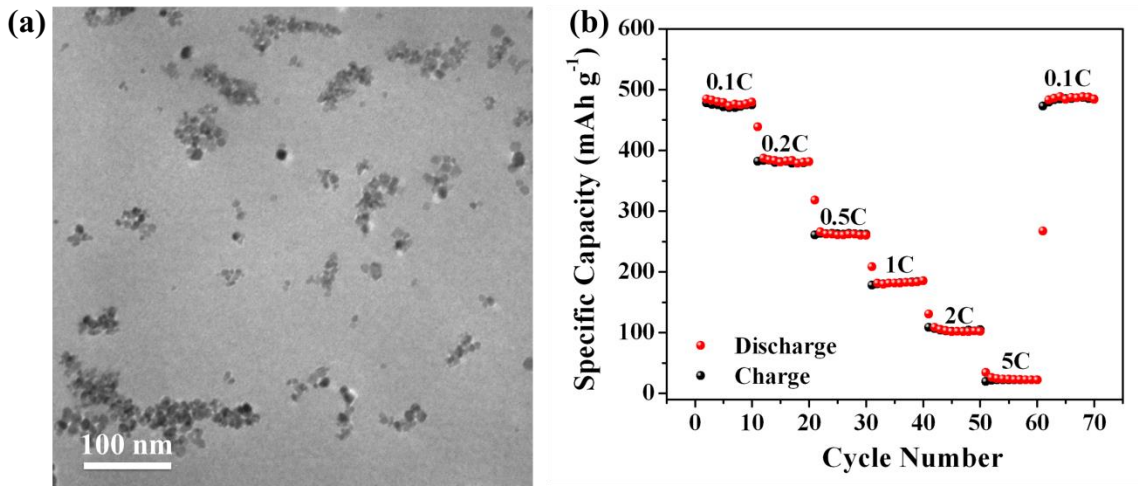

Figure 5.10 (a) TEM image of pure $ZnFe_2O_4$ nanoparticles obtained by calcinating the $ZnFe_2O_4$ precursors-loaded PS@PAA nanospheres in air. (b) Rate capability of pure $ZnFe_2O_4$ nanoparticles electrode tested under different current rates (1C = 1000 mA g^{-1}). [19] Copyright © 2016 American Chemical Society

The Nyquist electrochemical impedance spectra (EIS) of ZnFe2O4 (79.3wt%)/carbon nanocomposites electrode in the fresh state as well as after cycling (in the charged state) at 0.2C for 430 cycles are shown in **Figure 5.11**. The EIS spectra showed a quasi-semicircle from the high to intermediate frequency range and a straight slopping line in the low frequency range. The inset in **Figure 5.11** illustrates the corresponding equivalent circuit model, where Rohm is the ohmic resistance, reflecting a combined resistance of the electrolyte, separator and electrodes. The semicircle in the high frequency range can be attributed to the resistance Rsei and the capacitance Csei of the formation of SEI layer. The semicircle in the intermediate frequency is associated with the charge-transfer resistance Rct and its relative double-layer capacitance Cdl. The sloping line in the low frequency region is related to the Warburg impedance W, representing the lithium ion diffusion resistance in bulk electrode. From the EIS plots, it is clear that the radii of the quasi-semicircle after cycling is much smaller than that of

fresh cell, which can be ascribed to the formation of SEI film and the activation process during cycling.[268]

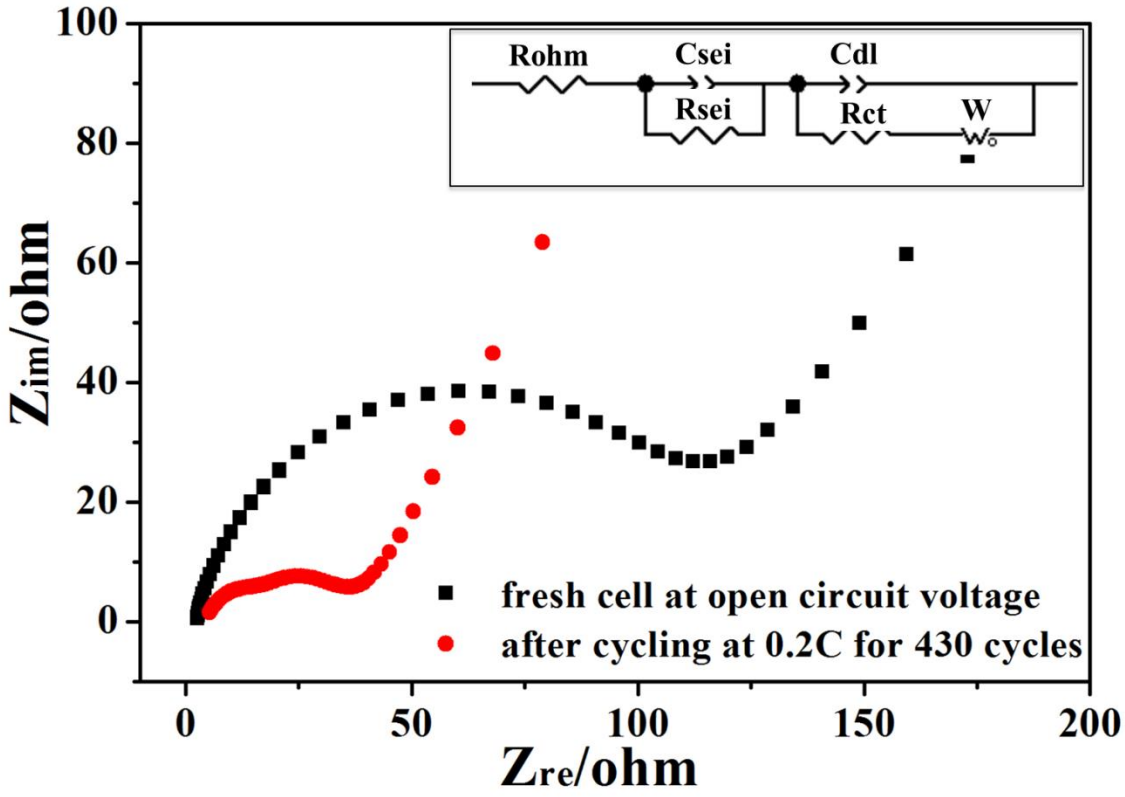

Figure 5.11. Electrochemical impedance spectra (Nyquist plot) of fresh and cycled $ZnFe_2O_4$(79.3wt%)/carbon nanocomposites electrodes. The electrical equivalent circuit is shown as an inset.[19] Copyright © 2016 American Chemical Society

After the cycling finished, the battery was dissembled inside the glove box and the electrode was washed with dimethyl carbonate (DMC) rigorously for structural analysis. **Figures 5.12a** and **5.12b** show the TEM images of the $ZnFe_2O_4$(79.3wt%)/carbon nanocomposites after cycling. The structure of nanocomposites was seen to be retained after cycling with the continuous carbon network encapsulating the nanoparticles, except the nanoparticles turning into much smaller size after the repeated lithiation/delithiation. Such good structural stability rendered the prolonged cycling stability.

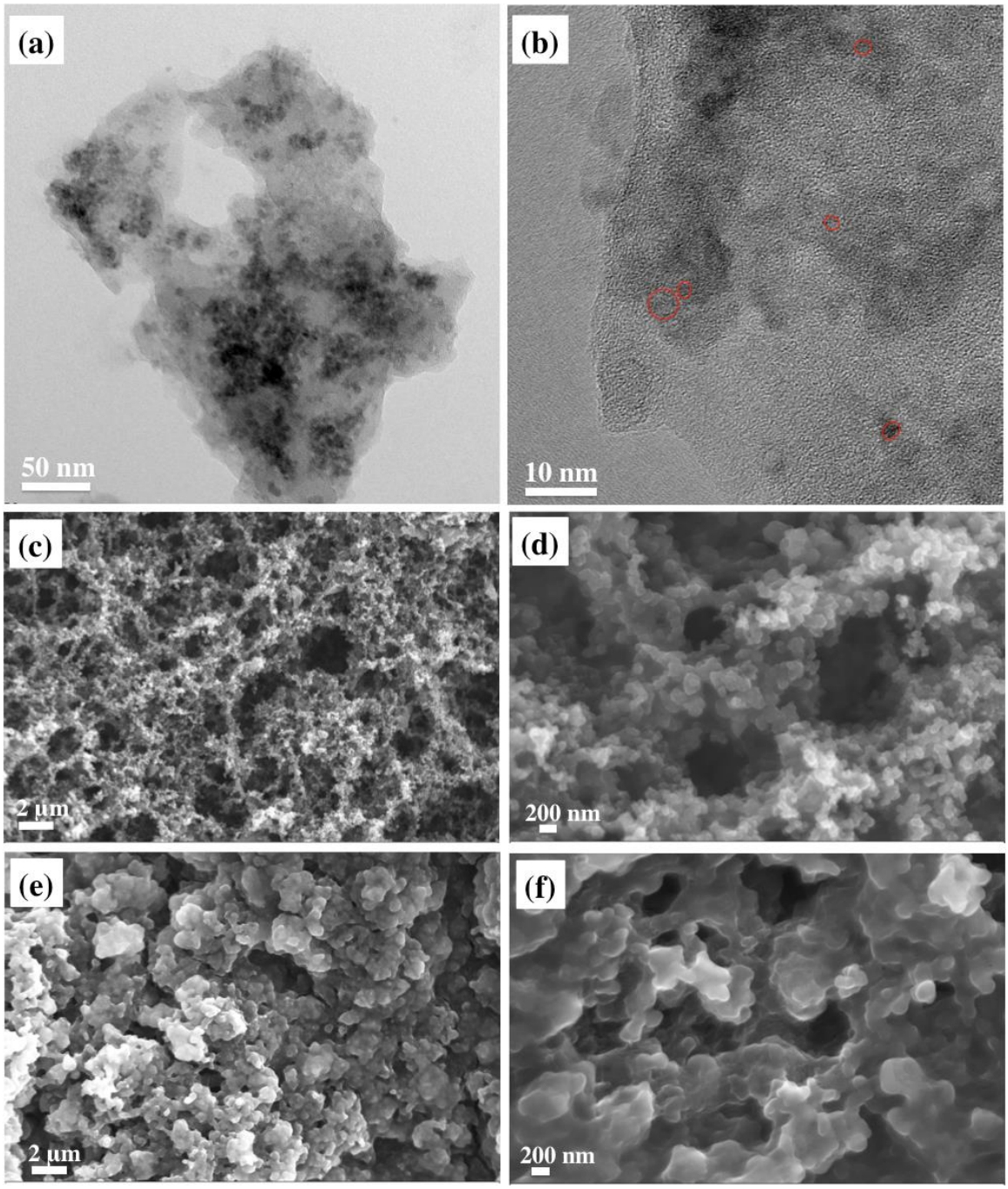

Figure 5.12. HRTEM images of $ZnFe_2O_4$ (79.3wt%)/carbon nanocomposites electrodes after cycling at 0.2C for over 400 cycles. (c) and (d) SEM images of freshly prepared $ZnFe_2O_4$ (79.3wt%)/carbon nanocomposites electrodes. (e) and (f) SEM images of $ZnFe_2O_4$ (79.3wt%)/carbon nanocomposites after cycling at 0.2C for over 400 cycles.[19] Copyright © 2016 American Chemical Society

Figures 5.12c-5.12f display the SEM images of the $ZnFe_2O_4$(79.3wt%)/carbon nanocomposites electrode that was freshly prepared **(Figures 5.12c-5.12d)** and after cycling **(Figures 5.12e-5.12f)**. No significant morphological change was observed after cycling, suggesting the good structural stability of the nanocomposites electrode. The SEM images (**Figures 5.12e-5.12f**) for the electrode after cycling revealed that a uniform SEI layer resulting from the catalytically enhanced electrolyte reduction at low potential was formed on the $ZnFe_2O_4$/carbon nanocomposites surface. As a result, the morphology was changed from loose powder-like **(Figures 5.12c-5.12d)** to self-holding appearance **(Figures 5.12e-5.12f)**,[98] thereby reducing the contact area between the active materials and the electrolyte by blocking some holes, which may be responsible for the capacity decay after 370 cycles.

5.3 Conclusion

In summary, we developed a facile and effective strategy for *in-situ* crafting $ZnFe_2O_4$/carbon nanocomposites electrode comprising 16±5nm $ZnFe_2O_4$ nanoparticles embedded within the continuous carbon network through the pyrolysis of $ZnFe_2O_4$ precursors-containing PS@PAA core@shell nanospheres. The advantages of this strategy are threefold. First, the PS@PAA nanosphere template is synthesized by emulsion polymerization in *one-step.* Second, the pyrolysis leads to the formation of $ZnFe_2O_4$ nanoparticles. Third, in the meantime the pyrolysis also induced the carbonization of PS@PAA, forming continuous carbon network that encapsulates the formed $ZnFe_2O_4$ nanoparticles. Notably, the carbon network offers a continuous conductive pathway for electron transport, improves the mechanical flexibility of active materials, and more

importantly maintains the structural integrity of $ZnFe_2O_4$/carbon nanocomposites during the repeated lithiation/delithiation. As anode materials for lithium ion batteries, the $ZnFe_2O_4$/C nanocomposites containing 79.3 wt% $ZnFe_2O_4$ exhibited the best electrochemical performance, delivering excellent rate performance with high capacities of 1238 mA h g^{-1}, 1198 mA h g^{-1}, 1136 mA h g^{-1}, 1052 mA h g^{-1}, 926 mA h g^{-1}, and 521 mA h g^{-1} at specific currents of 100 mA g^{-1}, 200 mA g^{-1}, 500 mA g^{-1}, 1000 mA g^{-1}, 2000 mA g^{-1} and 5000 mA g^{-1}, respectively, and prolonged cycling stability over several hundred cycles. Such outstanding electrochemical performance of $ZnFe_2O_4$/carbon nanocomposites electrode is a direct consequence of the synergy of nanoscopic $ZnFe_2O_4$ particles and their hybridization with a continuous conductive carbon network. We envision that this synthetic strategy is simple and robust, and can be readily extended for the preparation of other carbon hybridized electrode materials for high-performance lithium ion batteries.

Chapter 6 Polymer-templated formation of Corn-on-the cob-like SnO_2 nanocrystals coated with polydopamine as anodes for LIBs with superior cyclability

Related publication: Polymer-templated Formation of Corn-on-the-Cob-like SnO_2 Nanocrystals Coated with Polydopamine as Anodes for Lithium Ion Battery with Superior Cyclability, submitted (2016)

6.1 Instroduction

The past several decades have witnessed remarkable progress in developing anode materials with higher reversible lithium storage capacity and rate capability for replacing the commercialized graphite anode due to its low specific capacity of 372 mA h g^{-1}.[269] As one of the most intensively investigated anode materials, SnO_2-based nanomaterials show great potential for substituting graphite anode because of their numerous appealing features including low cost, abundance, environmental benignity, safe working potential (a few hundreds of millivolts higher than Li^+/Li), and high theoretical capacity (two times higher than that of graphite).[270-272] The electrochemical interaction between lithium and SnO_2 can be described in two steps.[269, 273-275] During the initial lithiation process, the SnO_2 anode electrochemically reacts with Li ions, resulting in the formation of Sn and lithium oxide (Li_2O), as described by equation 1. Subsequently, the Sn phase reacts with Li ions, forming Li_xSn alloys according to the Li-Sn alloying/dealloying reaction, as depicted by equation 2.

$$SnO_2 + 4Li^+ + 4e^- \rightarrow Sn + 2Li_2O \quad (1)$$

$$Sn + xLi^+ + xe^- \leftrightarrow Li_xSn\ (0 \leq x \leq 4.4) \quad (2)$$

It is widely recognized that the conversion from Sn to SnO_2 (equation 1) is irreversible for bulk SnO_2 but can become reversible for nanostructured SnO_2.[273-274, 276] In contrast, the reaction of forming Li_xSn alloys (equation 2) is reversible, in which Li ions can be repeatedly alloyed and dealloyed with Sn formed *in-situ*, with a maximum uptake of 4.4 moles of Li ions per unit of Sn. Assuming equation 1 to be fully irreversible, the commonly reported theoretical capacity calculated based on 4.4 moles of Li ions uptake per unit of SnO_2 is 782 mA h g^{-1}.[152, 271, 277-282] On the other hand, when considering both reactions to be completely reversible, the theoretical capacity of 1494 mA h g^{-1} can be obtained (i.e., 8.4 moles of Li ions uptake per unit of SnO_2).[272] However, there are still limited reports on reversible conversion between Sn and SnO_2 for SnO_2-based electrodes.[272-273, 283] Clearly, reversible SnO_2 nanomaterials with specific capacities approaching 1494 mA h g^{-1} are highly desirable for producing high-performance lithium ion batteries (LIBs) with high energy density and long cycle life.

It is notable that the rapid capacity fading for SnO_2-based electrode hinders its practical applications. SnO_2 anode experiences approximately a 358% volume change after lithiation between Sn and $Li_{4.4}Sn$.[284] Such large volume change during the repetitive charging-discharging process leads to the mechanical failure of electrode and the loss of electrical contact between active materials and the conductive additive or the current collectors.[271, 274] In addition, the formed active Sn nanoparticles have a strong tendency to aggregate into big and inactive Sn clusters even at room temperature,[273, 285-286] leaving behind the electrochemically inactive Li_2O due to the irreversible conversion

from Sn to SnO_2 (equation 1). Moreover, the large volume change can easily break the SEI layer formed in the lithiated expanded state and repeatedly expose the fresh surface of active materials to electrolyte, leading to the continuous growth of SEI layer and gradual depletion of electrolyte over cycling. Taken together, the severe capacity fading in SnO_2-based electrodes is often observed. [272] Obviously, the SnO_2-based electrodes need to be rationally designed to address the issues noted above in order to further improve the cyclability for practical application.

In this context, much effort has been directed toward constructing nanostructured SnO_2 to enhance the cyclability of SnO_2-based electrodes.[152, 278, 287] Nanostructured materials can better accommodate the volume change and the induced stress than bulk materials, as the absolute volume changes in the local environment for nanostructured materials are very small.[98, 288] In addition, nanostructured materials carry additional advantages over conventional bulk materials, such as fast charging/discharging due to the shortened transport lengths for Li ions and electrons, the high electrode/electrolyte contact area favorable for improving the lithium reaction rate, and the large volume fraction of Sn/Li_2O interfaces beneficial for enhancing the reversibility from Sn to SnO_2 (equation 1).[19, 273] However, it is noteworthy that the use of nanostructured SnO_2 alone is not sufficient to significantly enhance the cycling stability of SnO_2-based electrodes, as SnO_2 nanomaterials and the produced Sn nanoparticles are still easily aggregated.[289] It has been demonstrated that by confining SnO_2 nanoparticles within the electronically conductive matrix is effective in preventing the aggregation of active Sn nanoparticles.[152, 290] However, it usually requires the matrix to be highly porous that would otherwise penalize the rate capability due to the limited Li ions transport within the matrix. On the

other hand, the ability to form a stable and passivating SEI layer at the active material/electrolyte interface is critical for realizing high reversibility and long-term cycling stability.[291-292] Thus, nanostructured SnO_2 with a high $Sn \rightarrow SnO_2$ reversibility, the suppressed Sn aggregation, and a stable SEI layer over cycling would be the ideal material choice for achieving high-performance LIBs. This has yet to be realized.

6.2 Experiments, results and discussion

Herein, corn-on-the-cob-like SnO_2 nanocrystals (thereafter referred to as corn-like SnO_2) comprising small-sized SnO_2 nanoparticles decorated along the cob were crafted and exploited as electrode for high-performance LIBs. In addition, a protective thin layer of polydopamine (PDA) was coated on the surface of corn-like SnO_2 for further enhancing the performance, forming PDA-coated corn-like SnO_2. Specifically, the corn-like SnO_2 were created by employing judiciously designed hydrophilic bottlebrush-like hydroxypropyl cellulose-*graft*-poly (acrylic acid) (denoted HPC-*g*-PAA) as template. The strong coordination bonding between the carboxylic acid groups (-COOH) of PAA blocks and SnO_2 nanoparticles effectively hindered the aggregation of Sn nanoparticles and retaining a high fraction of Sn/Li_2O interfaces, thus promoting the reversible reaction between Li_2O and Sn to form SnO_2 (equation 1).

Figure 6.1 depicts the synthetic scheme for crafting PDA-coated corn-like SnO_2. Hydroxypropyl cellulose (HPC) is first converted into HPC-based macroinitiator (i.e., HPC-Br) through homogeneous esterification. The poly(*tert*-butyl acrylate) (P*t*BA) blocks are then grafted onto HPC-Br by atom transfer radical polymerization (ATRP) technique, yielding bottlebrush-like HPC-*g*-P*t*BA (upper middle panel in **Figure 6.1**).

The hydrolysis of P*t*BA into PAA blocks produces hydrophilic bottlebrush-like HPC-*g*-PAA (upper right panel in **Figure 6.1**), which serves as the template for the growth of corn-like SnO_2 nanocrystals. At the early stage of creating corn-like SnO_2, tiny SnO_2 nanoparticles are instantly formed under the hydrothermal condition (lower right panel in **Figure 6.1**). Instead of self-aggregation, these small-sized SnO_2 nanoparticles are quickly bonded to PAA blocks of HPC-*g*-PAA due to a strong coordination interaction between the –COOH groups of PAA blocks and SnO_2 nanoparticles.[18, 293] Consequently, the bottlebrush-like HPC-*g*-PAA is decorated by SnO_2 nanoparticles, yielding the nanostructure resembling the corn-on-the-cob-like architecture, except that such corn-like SnO_2 nanocrystals are composed of multilayers of SnO_2 nanocorns (i.e., small-sized nanoparticles) which are not closely packed along the polymer backbone due to the slight difference in size and shape (i.e., having voids between nanoparticles) (lower central panel in **Figure 6.1**). Finally, each SnO_2 nanoparticle on the corn-like SnO_2 is coated with a thin layer of PDA by a simple polymerization of dopamine, forming PDA-coated corn-like SnO_2 nanocrystals (lower left panel in **Figure 6.1**).

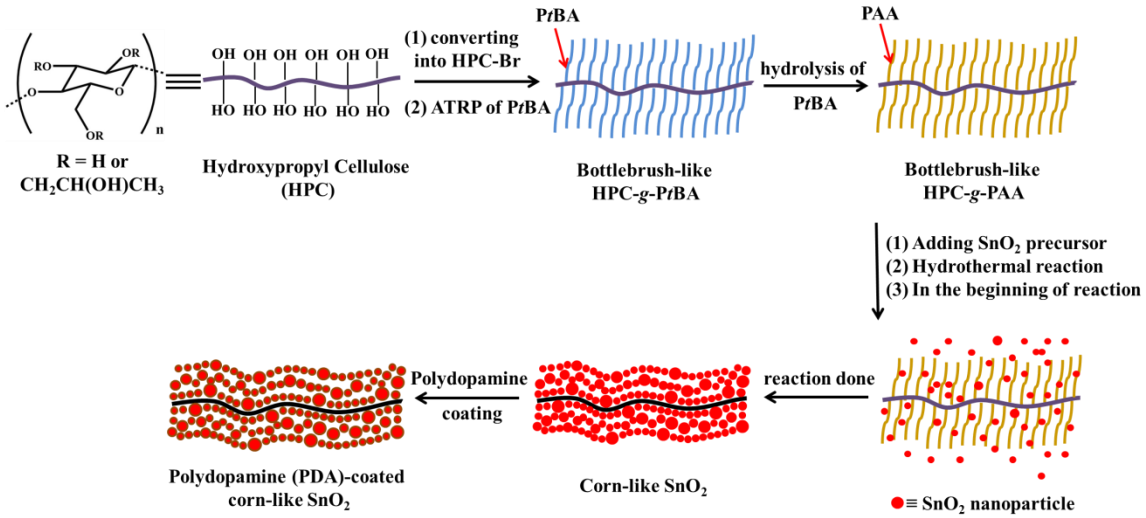

Figure 6.1 Schematic representation of the synthesis of the polymer template, that is, hydrophilic bottlebrush-like HPC-*g*-PAA (upper right panel), and the templated growth of PDA-coated corn-like SnO_2 nanocrystals comprising hundreds of small-sized SnO_2 nanoparticles decorated along the backbone of HPC-*g*-PAA template (lower left panel).

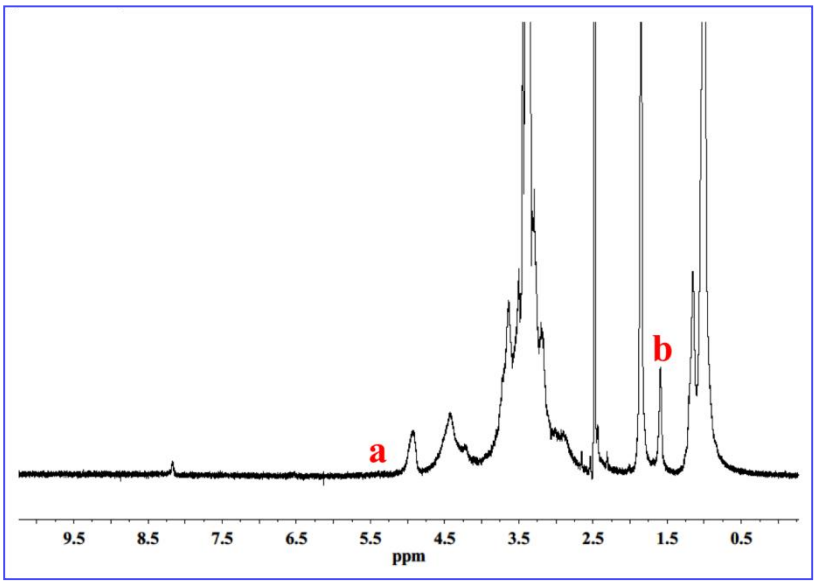

Figure 6.2. ^{1}H-NMR spectrum of hydroxypropyl cellulose (HPC)-based macroinitiator (i.e., HPC-Br) using dimethyl sulfoxide (DMSO)-d_6 as solvent. The esterification efficiency of hydroxyl groups of HPC was calculated according to the equation: $E_T = \frac{A_b}{18A_a}$, where E_T is the esterification efficiency of hydroxyl groups of HPC; and A_b and A_a are the integral areas of the methyl protons of HPC-Br and protons of HPC from the ^{1}H NMP spectrum, respectively.

The grafting density of PAA chains in the bottlebrush-like HPC-*g*-PAA is directly dictated by the number of available initiating sites in the HPC-Br macroinitiator (three hydroxyl groups per HPC allows for the esterification (i.e., forming HPC-Br) and the grafting of three PAA chains (i.e., the growth of P*t*BA by ATRP followed by the hydrolysis to yield PAA)) (**Figure 6.1**). The high grafting density of PAA chains per HPC backbone leads to the high loading of active SnO_2 in the final corn-like SnO_2 nanocrystals via the coordination interaction between the –COOH groups of PAA blocks and SnO_2 nanoparticles as noted above. According to the NMR spectrum of HPC-Br (**Figure 6.2**), the esterification efficiency of hydroxyl groups on HPC was calculated to be approximately 100%, indicating that nearly all hydroxyl groups on HPC were converted into active Br-terminated groups for initiating the ATRP of P*t*BA blocks.

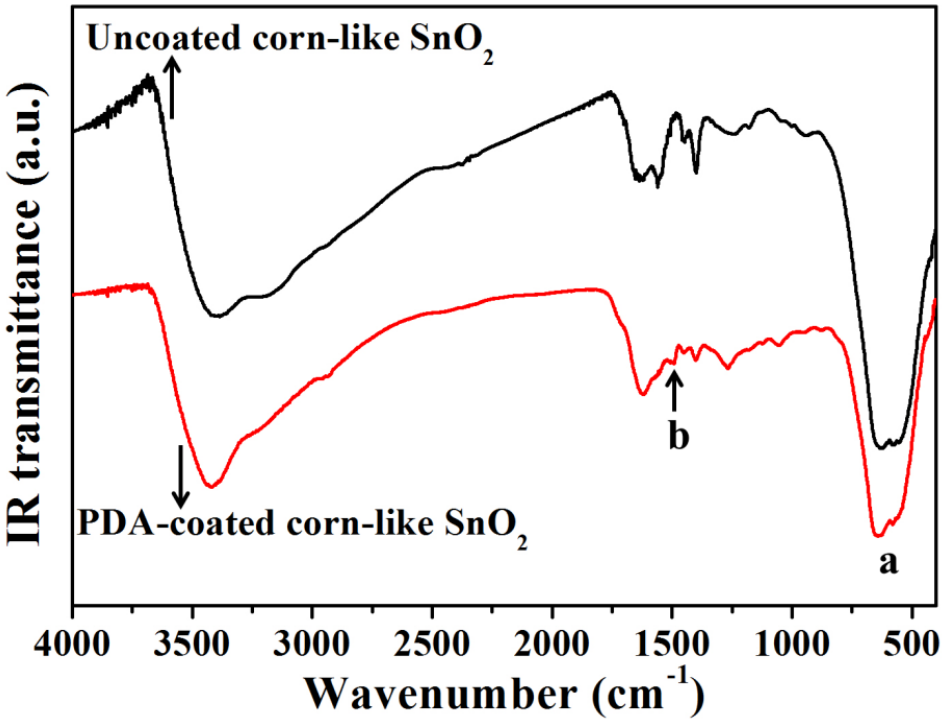

Figure 6.3 FTIR spectra of PDA-coated and uncoated corn-like SnO_2 nanocrystals. The brands marked as "**a**" at low wavenumber (800-500 cm^{-1}) on both spectra are assigned to the antisymmetric and symmetric Sn-O-Sn stretches, and the brand marked as "**b**" at 1500 cm^{-1} (C=O region) confirmed the PDA coating on SnO_2 nanocrystals.

PDA is a catechol-containing polymer commonly found in mussel adhesive proteins. [294] PDA can be applied to coat various materials offered by the catechol groups including metals, metal oxides, nonmetal oxides, silica, ceramics, polymers, and nanomaterials.[13] It has been demonstrated that thin PDA coating exhibits elastic and porous properties and does not disrupt the ionic transport though it.[295-296] In this study, the PDA coating on the corn-like SnO_2 was obtained by the polymerization of dopamine in basic buffer solution at pH = 8.5.[294] The Fourier transform infrared spectroscopy (FTIR) of corn-like SnO_2 before and after the PDA coating (i.e., uncoated corn-like SnO_2 and PDA-coated corn-like SnO_2, respectively) was conducted and confirmed the success in coating PDA. As shown in **Figure 6.3**, the brands marked as "a" at low wavenumber (800-500 cm^{-1}) on both spectra can be assigned to the antisymmetric and symmetric Sn-O-Sn stretches,[297] and the brand marked as "b" at 1500 cm^{-1} (C=O region) verifies the PDA coating on SnO_2 nanoparticles.[298] In addition, the product turned black after coating, further substantiating the successful coating of PDA on the surface of SnO_2 nanocrystals.

Figure 6.4a-6.4d shows the transmission electron microscopy (TEM) images of the corn-like structure for PDA-coated SnO_2 nanocrystals at different magnifications. Small SnO_2 nanoparticles (marked by solid circles) with an average size of ~5 nm are bonded along the bottlebrush-like HPC-*g*-PAA template, forming the corn-like structure (**Figure 6.4c-6.4d**). The voids of approximately 3~5 nm between SnO_2 nanoparticles were clearly seen (marked by the dashed circles in **Figure 6.4d)**, indicating the corn-like structure was porous. In addition, a thin layer of PDA coating (~1 nm in thickness) is also evident (marked by the arrow in **Figure 6.4c-6.4d**).

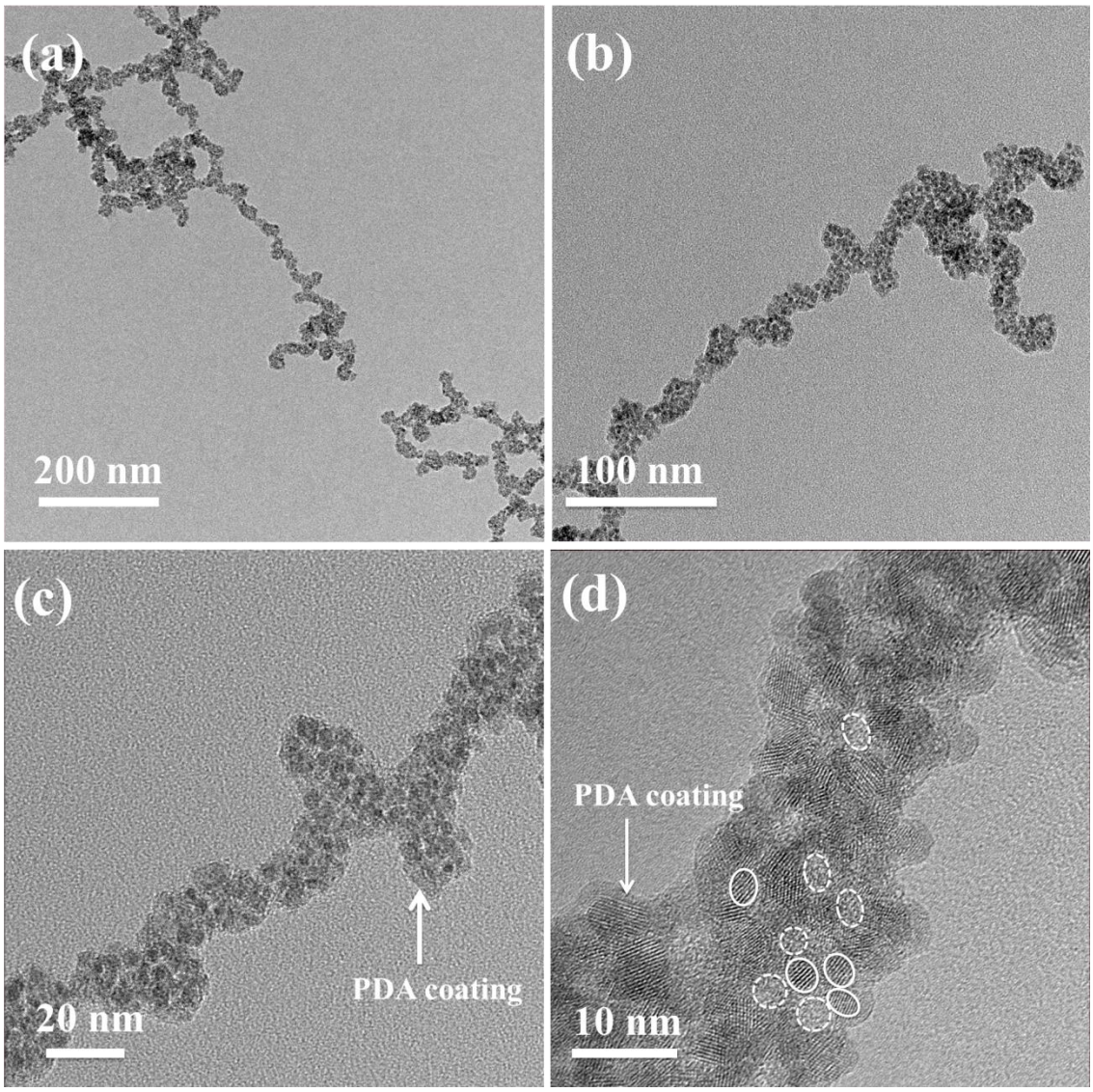

Figure 6.4 (a)-(b) Lower magnification, and (c)-(d) higher magnification TEM images of PDA-coated corn-like SnO_2 enabled by capitalizing on bottlebrush-like HPC-*g*-PAA as template. The solid circles in (d) mark the crystalline SnO_2 nanoparticles, and the dash circles indicate the existence of porosity between SnO_2 nanoparticles. The PDA coating is clearly evident and labeled by the arrow.

To corroborate the role of bottlebrush-like HPC-*g*-PAA in guiding the formation of corn-like SnO_2, three control experiments were performed where each experiment was slightly different in the choice of polymer template and the addition of SnO_2 precursors, as summarized in **Table 6.1**. TEM images of these control samples labeled as CS1-CS3

are shown in **Figure 6.5**. For the CS1 sample, carbonaceous nanospheres were obtained under the hydrothermal reaction when HPC-*g*-PAA template was added solely in the system (**Figure 6.5a**). For the CS2 sample, when precursors were added in the absence of HPC-*g*-PAA template, SnO_2 microspheres due to the aggregation of small SnO_2 nanoparticles were seen (**Figure 6.5b**). On the other hand, when linear PAA was employed as template, similar corn-like structures but with a much smaller thickness were observed (**Figure 6.5c**) when compared to the corn-like SnO_2 templated by bottlebrush-like HPC-*g*-PAA (**Figure 6.4a-6.4d**). This may be due to less –COOH groups on linear PAA, thus much less SnO_2 nanoparticles are bonded per chain of linear PAA.

Table 6.1 Reaction parameters of the three control samples. For each control sample, the parameter differed from that of corn-like SnO_2 is highlighted in bold

	polymer template	SnO_2 precursors	Other parameters
Corn-like SnO_2	HPC-*g*-PAA	Na_2SnO_4	see experiments
Control sample 1 (denoted CS1; template only)	HPC-*g*-PAA	**None**	Same as making corn-like SnO_2
Control sample 2 (denoted CS2; precursors only)	**None**	Na_2SnO_4	Same as making corn-like SnO_2
Control sample 3 (denoted CS3; linear PAA as template)	**Linear PAA**	Na_2SnO_4	Same as making corn-like SnO_2

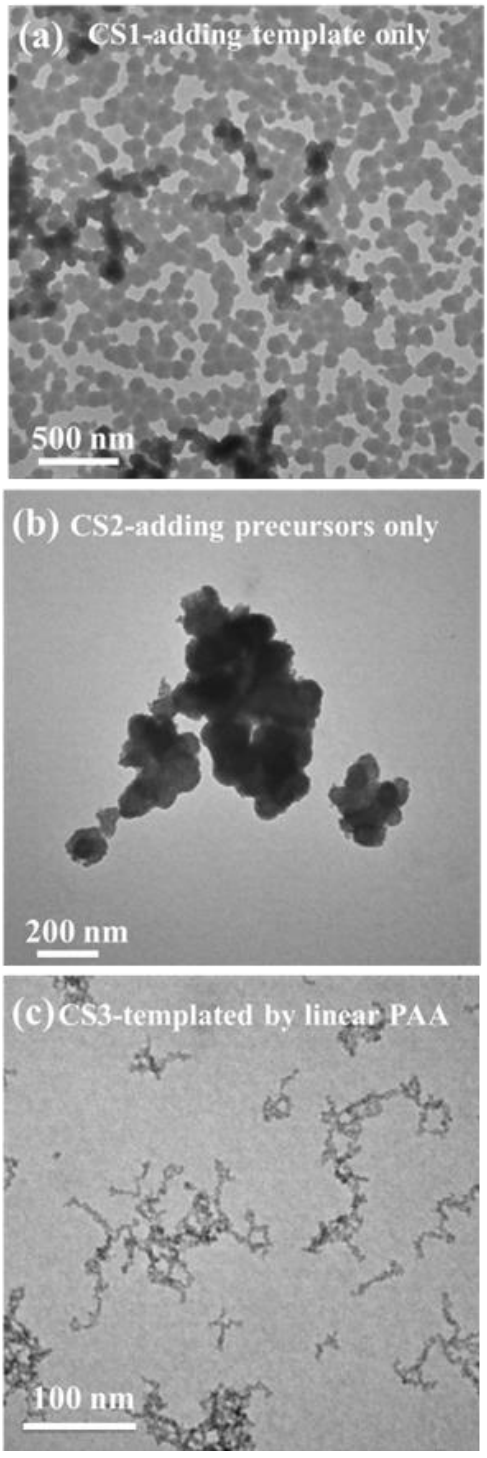

Figure 6.5 TEM images of three control samples: (a) CS1 obtained by adding polymer template bottlebrush-like HPC-*g*-PAA only (no precursors added); (b) CS2 by adding precursors only (no polymer template bottlebrush-like HPC-*g*-PAA added); and (c) CS3 templated by linear PAA (the viscosity average molecular weight, Mv, of linear PAA is 450,000 according to *Sigma-Aldrich*)

Figure 6.6 shows X-ray powder diffraction (XRD) profiles for corn-like SnO_2 before and after the PDA coating, and PDA-coated CS2 and CS3 samples. All peaks can be assigned to the tetragonal rutile-like SnO_2 (JCPDS card no. 41-1445).[272] No additional peaks are found after the PDA coating. The crystal sizes of SnO_2 nanoparticles for these samples are summarized in **Table 6.2**. They are calculated from the (110) diffraction peak according to Scherrer's equation ($d = k\lambda\beta^{-1}cos\theta^{-1}$; where k = 0.89, λ is the X-ray wavelength, θ is the Bragg angle, and β is the real half-peak width in radians after corrections for the instrument broadening). The crystal size of SnO_2 nanoparticles for PDA-coated corn-like SnO_2 is 5.4 nm, in accordance with that measured by HRTEM (**Figure 6.4c-6.4d**).

Table 6.2. The calculated crystal sizes of SnO_2 nanoparticle, the BET surface areas, and the average pore sizes of PDA-coated corn-like SnO_2 (enabled by HPC-*g*-PAA), CS2 (obtained by adding precursors only), and CS3 (yielding by adding linear PAA)

	SnO_2 crystal size (nm)	BET surface area ($m^2\ g^{-1}$)	pore size (nm)
PDA-coated corn-like SnO_2	5.4	132	3.3
PDA-coated CS2	9.9	111.5	7.1
PDA-coated CS3	5.1	156.6	2.9

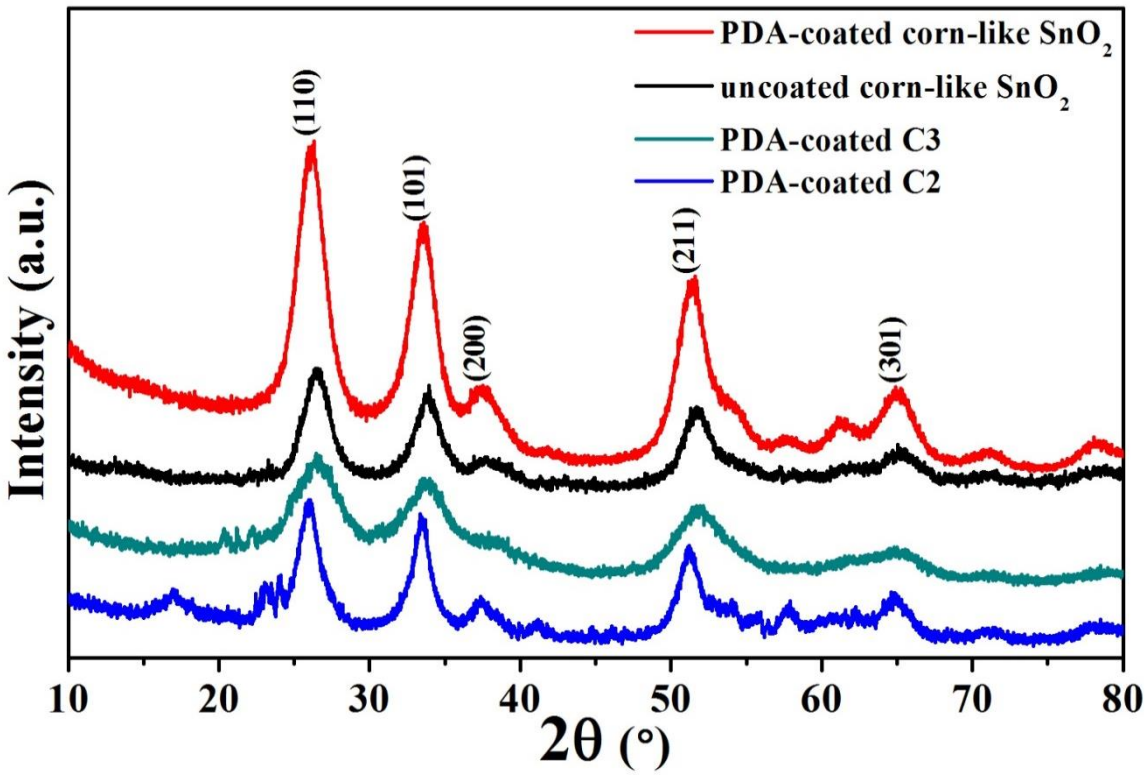

Figure 6.6 XRD patterns for PDA-coated and uncoated corn-like SnO_2 templated by bottlebrush-like HPC-*g*-PAA, and control samples: PDA-coated CS2 (obtained by adding SnO_2 precursors only), and PDA-coated CS3 (templated by linear PAA). All peaks can be identified as tetragonal rutile-like SnO_2. The sizes of SnO_2 crystals calculated according to Scherrer's equation are 5.4 nm for both PDA-coated and uncoated samples, in accordance with that measured by HRTEM (**Figure 6.4c-6.4d**).

In order to investigate the surface structure and porosity derived from the voids between SnO_2 nanoparticles, the N_2-sorption measurement was carried out on PDA-coated corn-like SnO_2 and PDA-coated CS2 - adding precursors only and CS3 - templated by linear PAA samples. As shown in **Figure 6.7a-6.7c**, all samples exhibited a type IV isotherm curve with a small hysteresis loop, suggesting the presence of mesoporous structure. The PDA-coated corn-like SnO_2 nanocrystals have a high Brunauer-Emmett-Teller (BET) surface area of 132 m^2/g and a Barrett-Joyner-Halenda (BJH) desorption average pore size of 3.3 nm, which agree well with the pores shown in

Figure 6.4d. The BET surface areas and the average pore size for all control samples are summarized in **Table 6.2**.

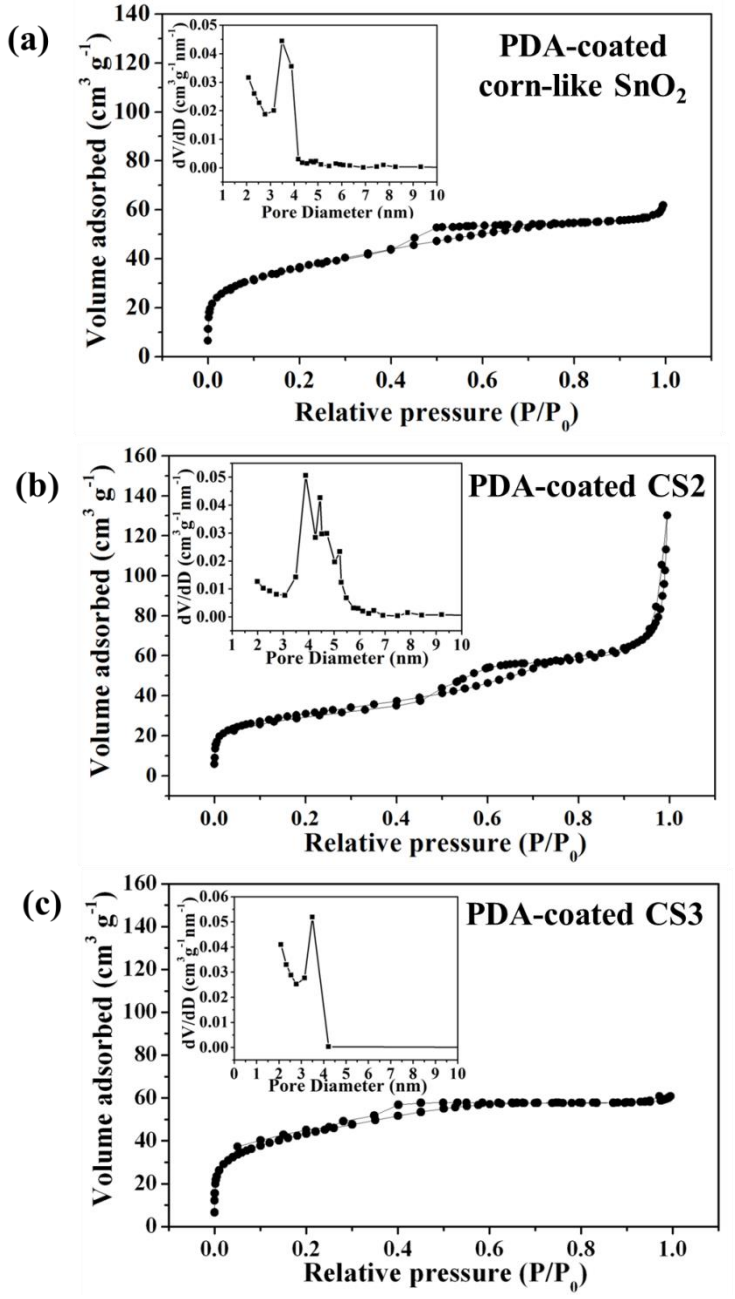

Figure 6.7 N_2 adsorption-desorption isotherms of (a) PDA-coated corn-like SnO_2, (b) PDA-coated CS2 (obtained by adding precursors only), and (c) PDA-coated CS3 (templated by linear PAA). The insets show the pore-size distribution calculated by the Barrett-Joyner-Halenda (BJH) method from the desorption branch.

To scrutinize the lithium storage mechanism, the LIBs assembled using PDA-coated corn-like SnO_2 as anodes were tested. **Figure 6.8a** shows the cyclic voltammetry (CV) characteristics for the first seven cycles of the fresh cell over a voltage window of 0.005-3 V vs. Li/Li^+ at the scan rate of 0.1mV s^{-1}. In the initial discharge process, a broad reduction peak was observed in the range of 0.8 to 1.2 V due to the formation of SEI layers and the conversion of SnO_2 to Sn and Li_2O (equation 1).[272, 282-283] A weak peak at approximately 0.2 V can be assigned to the alloying reaction between Sn and Li ions, forming Li_xSn (equation 2).[283, 299] During the first charging process, two obvious anodic peaks at 0.58 V and 1.27 V are present, similar to the results reported in literature.[299-300] The sharp oxidation peak at 0.58 V corresponds to the reversible Li-Sn dealloying reaction (equation 2), and the relatively weaker and broader peak located at 1.27 V is attributed to the conversion from Sn to SnO_2 (equation 1).[272-273, 299] For the following cycles, the two anodic peaks stay at the same position as the first charging process, while the cathodic peak positions are slightly different. The broad cathodic peaks in the range of 0.8 to 1.2 V shift to the lower voltage with cycling. The peak shifts to 0.87 V at the 7^{th} discharge cycle, which can be assigned to the conversion of $SnO_2 \rightarrow SnO \rightarrow Sn$.[282] Moreover, the cathodic peak at around 0.2 V becomes more significant than the first discharging process over cycling. Additionally, it is worth noting that all the peak currents (also capacities in mA h) for later cycles are higher than the previous cycles, suggesting an activated electrochemical process involving active materials not only near the surface but also within the anode over cycling, as well as the enhanced reversibility from Sn to SnO_2 (equation 1) for the later cycles.[273, 301-302] This phenomenon of gradual

activation process was also observed for some other cells assembled for cycling tests as discussed later.

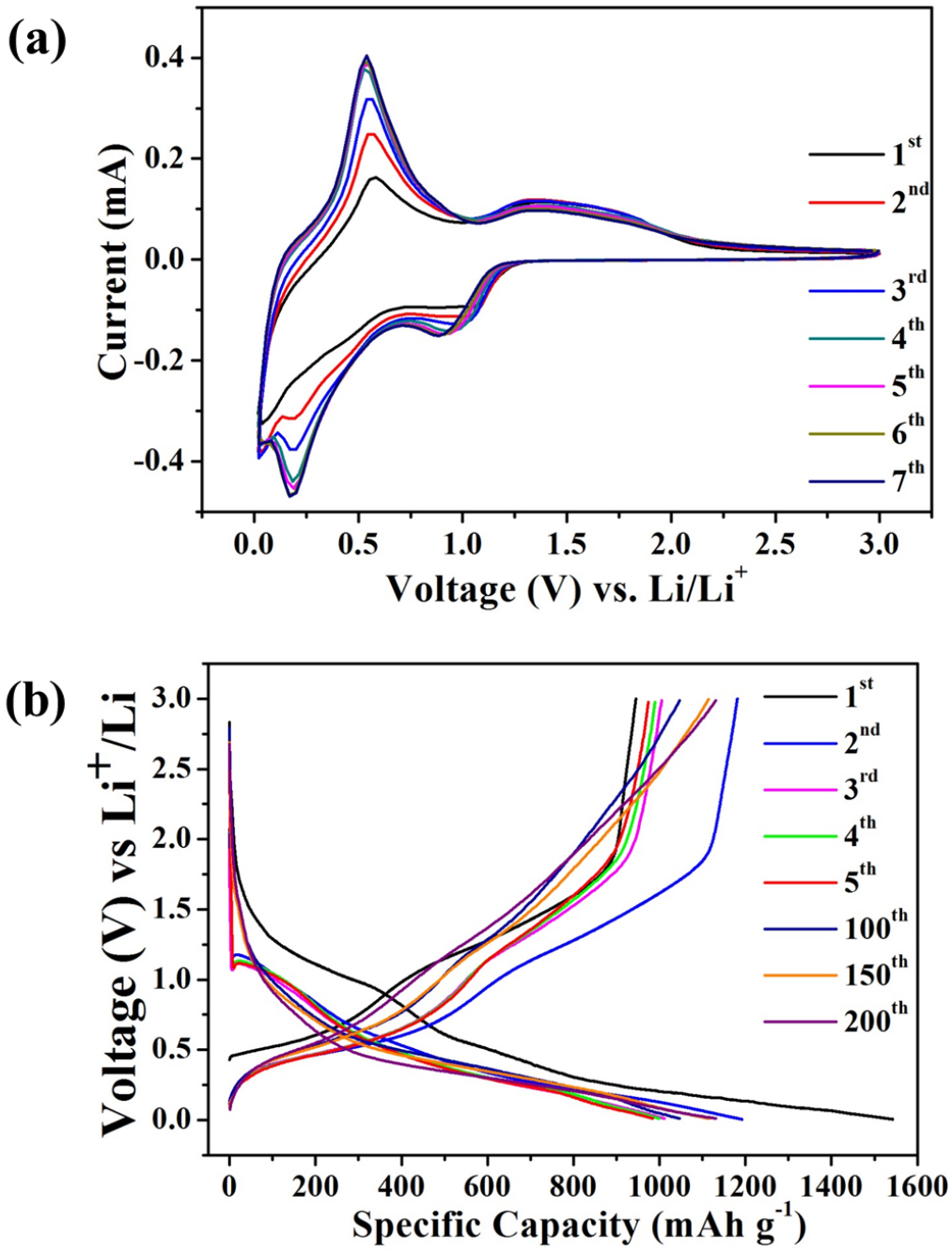

Figure 6.8 (a) CV curves of the first seven cycles for the fresh cell based on PDA-coated corn-like SnO_2 electrode tested at 0.1mV s^{-1} in the voltage range of 0.005-3 V. (b) Galvanostatic charge-discharge voltage profiles for the first five cycles, 100^{th}, 150^{th}, and 200^{th} cycles of the PDA-coated corn-like SnO_2 electrode tested at the current density of 160 mA g^{-1} in the voltage range of 0.01-3.0V vs. Li/Li^+.

Figure 6.8b depicts the galvanostatic charge-discharge profiles for the first five cycles, 100th, 150th, and 200th cycles of the PDA-coated corn-like SnO_2 electrode tested at the current density of 160 mA g^{-1} over the voltage range of 0.01-3.0 V vs. Li/Li^+. The initial discharge and charge capacities are 1542 and 945 mA h g^{-1}, respectively, with a low Coulombic efficiency of approximately 61.3% for the first cycle. The large irreversible capacity loss during the first cycle is due primarily to the irreversibility of the conversion from Sn to SnO_2 (equation 1) and the formation of the SEI layer owing to the reductive decomposition of electrolyte. It is important to note, however, this value is still larger than 52.3 % (782/1494=52.3%), which is the largest Coulombic efficiency calculated for the first cycle if assuming equation 1 to be completely irreversible after initial discharge, signifying that the widely assumed irreversible conversion from Sn to SnO_2 during the charging process is at least partially reversible for this PDA-coated corn-like SnO_2 electrode. The discharge/charge capacities for the 2nd, 3rd, 4th, 5th, 150th, 200th cycles are 1191.4/1180.9, 1011.3/1004.6, 999.9/989.8, 984.3/974.4, 1046.7/1046.4, 1114.9/1114.2, and 1131.5/1131.1, respectively. The poorly defined plateaus for the first five cycles are in good agreement with the CV measurements, and the curves after the 2nd cycle are nearly overlapped with one another with small variations, suggesting high reversibility and stability.

The cycling performance at 160 mA g^{-1} for batteries based on PDA-coated and uncoated corn-like SnO_2 is shown in **Figure 6.9**. The two cycling tests show the same trend of capacity decreases for the first 25 cycles and then gradual increases. For the uncoated corn-like SnO_2 electrode, the capacity displays a good cyclability for the first 150 cycles and reaches the highest value of approximately 856 mA h g^{-1} at the 150th cycle.

This can be ascribed to the corn-like nanostructures that impart good structural stability due to the small dimension and the presence of sufficient voids between SnO_2 nanoparticles to accommodate the volume change and release the stress, as well as the limited aggregation of the produced Sn nanoparticles because of the strong interaction between SnO_2/Sn and the polymer template. However, a continuous capacity fading was observed after 150 cycles for the uncoated corn-like SnO_2 electrode, yielding low capacity retention of 56% at the 290th cycle. In sharp contrast, the cycling for the PDA-coated corn-like SnO_2 exhibited significantly improved prolonged cycling stability. The capacity gradually increases to a high value of 1187 mA h g^{-1} at the 120th cycle before leveling off after 140th cycle and stabilizes at about 1130 mA h g^{-1} for the following cycles. In addition, the PDA-coated corn-like SnO_2 demonstrates a much higher capacity than the uncoated counterpart for the entire cycle life, which may be attributed to the synergistic effect of the corn-like nanostructures and the PDA coating.

The same cycling tests at 160 mA g^{-1} for batteries based on the control samples (PDA-coated CS2 and CS3) were also conducted. As shown in **Figure 6.9**, the PDA-coated CS2 anode has a high initial specific capacity. However, the capacity continues decreasing during the following cycles and remains only 28% of its initial capacity after stopped at the 240th cycle. The PDA-coated CS3 anode that was templated by linear PAA and possessed a corn-like structure displays a good cycling stability, substantiating the synergistic effect of the corn-like nanostructure and the PDA coating layer in improving the cycling stability. However, it is notable that the specific capacity of 400 mA h g^{-1} for the PDA-coated CS3 anode is much lower than that for the PDA-coated corn-like SnO_2. This is not surprising and can be attributed to the much lower mass loading of active

SnO_2 materials in the PDA-coated CS3, since the specific capacities for all samples are calculated based on the total mass of active SnO_2 materials and the inactive carbonaceous materials derived from the polymeric template under the hydrothermal condition. As shown in the thermogravimetric analysis (TGA) plots in **Figure 6.10**, the weight fraction of active SnO_2 in the PDA-coated CS3 sample is only 45%, while it is 84% in PDA-coated corn-like SnO_2, owing primarily to a large number of –COOH groups per bottlebrush-like HPC-*g*-PAA that render more SnO_2 nanoparticles to be bonded to PAA blocks in HPC-*b*-PAA. Nonetheless, the markedly improved cycling performance for corn-like SnO_2 electrodes over the control samples underpins the synergy of the nanostructured corn-like morphology and the protective PDA coating in promoting the reversible conversion from Sn to SnO_2 and imparting the long-term cycling stability for SnO_2-based anodes.

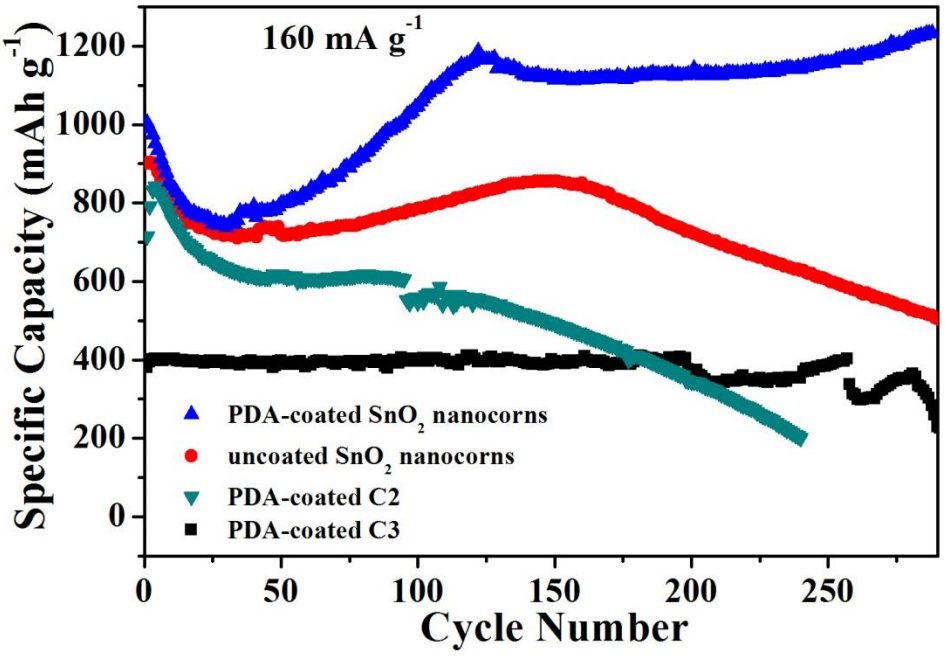

Figure 6.9 Cycling performance for PDA-coated and uncoated corn-like SnO_2 electrodes, and PDA-coated CS2 (obtained by adding precursors only) and PDA-coated CS3 (templated by linear PAA) tested at 160 mA g^{-1}.

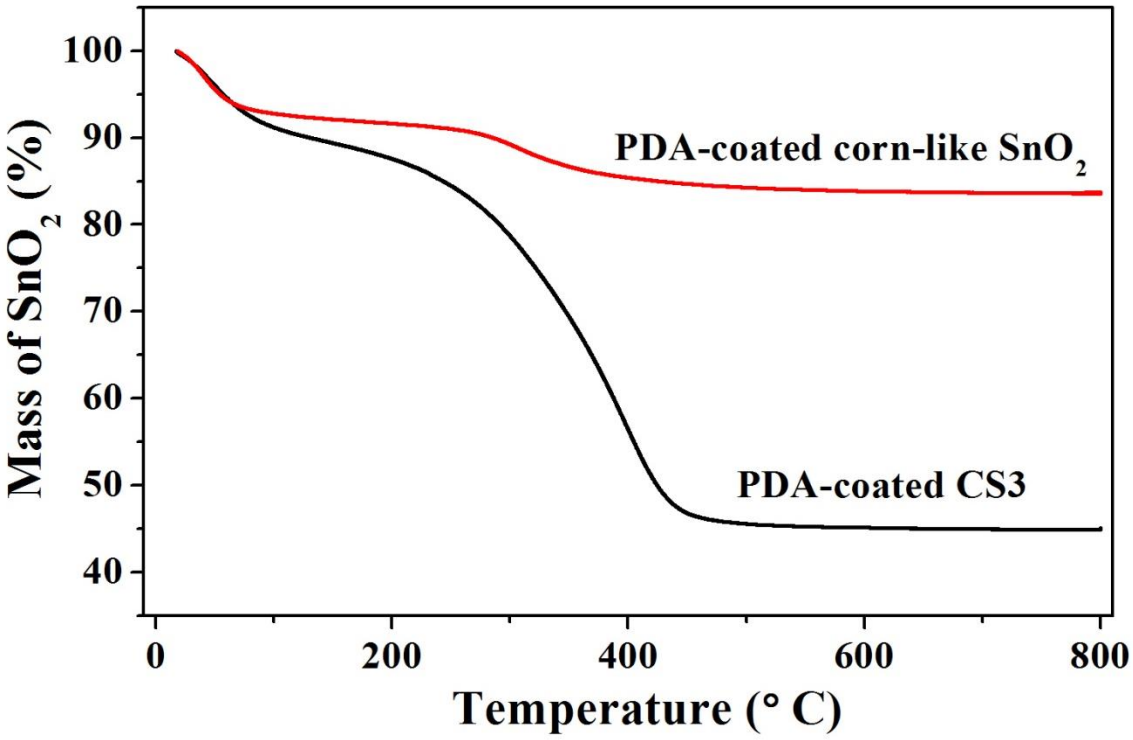

Figure 6.10 Thermogravimetric analysis (TGA) plots for PDA-coated corn-like SnO_2 and PDA-coated CS3. The weight fractions of SnO_2 are 84% for the PDA-coated corn-like SnO_2 and 45% for the PDA-coated CS3, respectively.

Figure 6.11a-6.11b compares the rate performance of PDA-coated and uncoated corn-like SnO_2 electrodes. The LIBs assembled using these electrodes were first cycled at a low current density of 160 mA g^{-1}, followed by testing at various current densities of 400, 780, 1000, 2000, 1000, and 780 mA g^{-1} for 10 cycles at each current density. After that, the batteries were cycled at a small test current of 160 mA g^{-1} to investigate any structural changes caused by previous rate testing. The close-ups of the rate performance with 10 cycles at each test current are shown in **6.12a-6.12b**. Obviously, the specific capacity of the PDA-coated corn-like SnO_2 anode first decreases and then gradually increases (**Figure 6.11a**), similar to the trends observed in **Figure 6.9**, and the specific capacity reaches a high value of 1057 mA h g^{-1} at 160 mA g^{-1} at the 105th cycle. The

capacity starts to decline when gradually increasing the test current to 2000 mA g^{-1}, and the average specific capacities are 921, 851, 835, 667 mA h g^{-1} at specific currents of 400, 780, 1000, and 2000 mA g^{-1}, respectively (**Figure 6.12a**). When the current density returns to 160 mA g^{-1}, the high capacity is resumed and continues to rise over cycling and positioned at 1502 mA h g^{-1} at the 300th cycling, implying an activated electrochemical process involving more active materials over cycling and carrying highly reversible conversion from Sn to SnO_2.[273, 301-304] For the uncoated corn-like SnO_2 (**Figure 6.11b**), however, the capacity fails to return to previously high values when the test current switches back to 1000 and 780 mA g^{-1} after the test at 2000 mA g^{-1}, showing a trend of decrease during the 10 cycles. In addition, when the battery is back-cycled at 160 mA g^{-1}, the capacity decays quickly over cycling and drops to 413 mA h g^{-1} when stopped at the 300th cycle, indicating that the cycling stability and reversibility for the uncoated corn-like SnO_2 is largely disrupted by the rate testing. It is worth noting that the greatly improved cycling performance and rate performance for the PDA-coated corn-like SnO_2 further support that the PDA coating is beneficial to maintain the prolonged cycling stability and achieve high reversibility for the Sn→SnO_2 conversion for corn-like SnO_2 electrodes. This is probably because the PDA coating can effectively suppress the coarsening of the produced Sn nanoparticles and retain a large Sn/Li_2O interface that facilitate the reversible reaction between Sn and Li_2O in forming SnO_2.

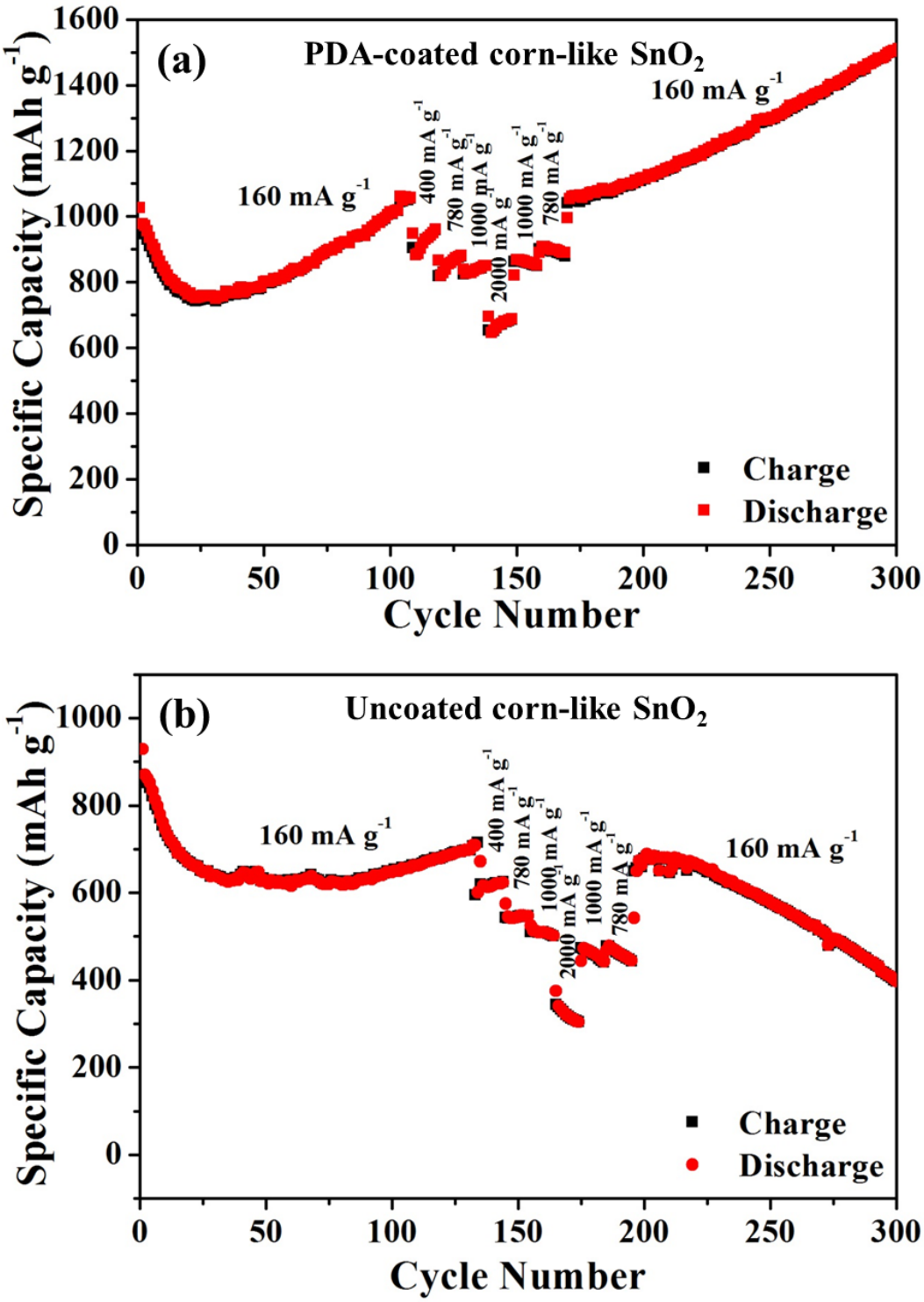

Figure 6.11 Rate performance for (a) PDA-coated corn-like SnO_2 electrode, and (b) uncoated corn-like SnO_2 electrode. They were first cycled at 160 mA g^{-1} and then tested at various current densities of 400, 780, 1000, 2000, 1000, and 780 mA g^{-1} for 10 cycles, and finally cycled at 160 mA g^{-1}.

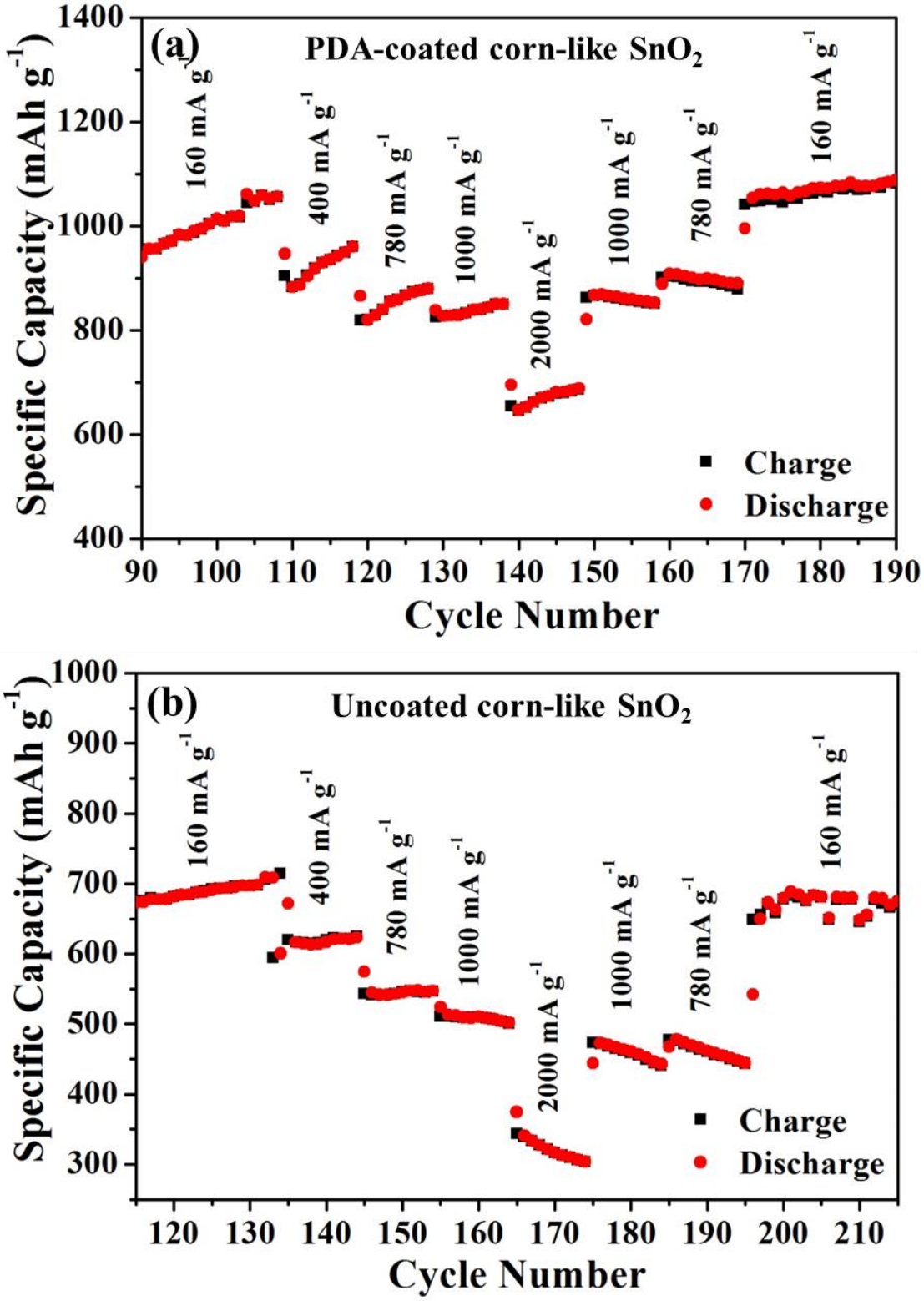

Figure 6.12 Close-ups of the rate performance for (a) PDA-coated corn-like SnO_2 electrode, and (b) uncoated corn-like SnO_2 electrode tested at current densities of 160, 400, 780, 1000, 2000, 1000, 780 and 160 mA g^{-1}.

The superior cyclability for the PDA-coated corn-like SnO_2 electrode is further manifested in the cycling performance at various current densities of 200, 400, 780, 1500 mA g^{-1} as shown in **Figure 6.13a-6.13d**. The batteries were first tested at a small current density of 160 mA g^{-1} for 5 cycles to activate the battery, followed by cycling at high current densities for over 300 cycles. These cycling tests all demonstrate the superior cyclability for over 300 cycles, with the trend of a decrease for the first couple of cycles, followed by a continuous increase and gradually being stabilized. The specific capacities at the 300^{th} cycle are 600, 450, and 354 mA h g^{-1} at the test current densities of 400, 780, and 1500 mA g^{-1}, respectively. The cycling at 200 mA g^{-1} after the 300^{th} cycle shown in **Figure 6.13a** displays a similar increased trend due to the activation process as observed in the cycling at 160mA g^{-1} in **Figure 6.9**. All these cycling results further reveal the superior cyclability for the PDA-coated corn-like SnO_2 electrode. Notably, the specific capacities (e.g., 600 and 450 mA h g^{-1} at the testing currents of 400 and 780 mA g^{-1}, respectively) are much lower than the corresponding values seen in the rate testing in **Figure 6.11a** (e.g., 921 and 851 mA h g^{-1} at the testing currents of 400 and 780 mA g^{-1}, respectively). This can be attributed to the cycling history for the cell in **Figure 6.11a**, which involves a long cycling at 160 mA g^{-1} and the activation process starts to promote the reversibility of the $Sn \rightarrow SnO_2$ conversion. Moreover, we note that some cells are not electrochemically activated for the first two cycles and deliver a lower initial specific capacity, as evidenced in **Figure 6.13a** and **6.13c** and the CV results in **Figure 6.8a**. This is due largely to the electrochemically inactive PDA coating, which is in direct contact with the electrolyte and may affect the initial lithiation/delithiation process. However, as

Li ions quickly penetrate through the outer thin PDA coating and react with inner active materials during the following cycles, much higher specific capacity is then obtained.

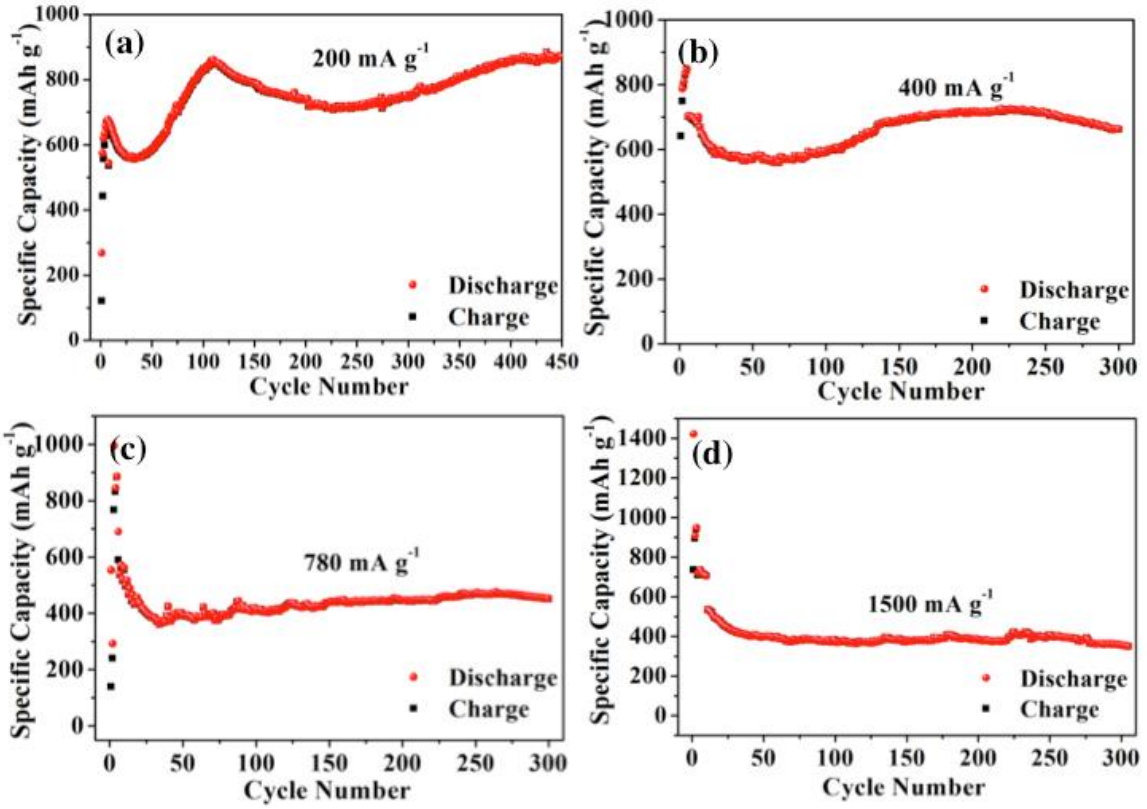

Figure 6.13. Cycling performance of PDA-coated corn-like SnO_2 electrodes tested at current densities of (a) 200 mA g^{-1}, (b) 400 mA g^{-1}, (c) 780 mA g^{-1}, and (d) 1500 mA g^{-1}, respectively. The batteries were first tested at 160 mA g^{-1} for the five cycles prior to being further tested at higher current densities for (b), (c) and (d).

To further elucidate the electrochemical characteristics of corn-like SnO_2 electrodes, electrochemical impedance spectroscopy (EIS) measurements were performed. **Figure 6.14a-6.14b** compares the Nyquist plots for batteries based on PDA-coated and uncoated corn-like SnO_2 electrodes after freshly assembled and after the 1st, 2nd, 100th, and 300th cycles in the charging state. **Figure 6.14c** shows the equivalent circuit model, where R_{ohm} is the combined ohmic resistance of the electrolyte, separator, and electrodes. The high-frequency semicircle can be attributed to the constant phase

element of the SEI film and the contact resistance. The depressed semicircle in the medium-frequency region is associated with the charge-transfer resistance R_{ct} and the constant phase element of the electrode/electrolyte interface. The sloping line at low-frequency region is related to the Warburg impedance, *W*, representing the Li ion diffusion resistance in the electrode.[19, 283] From the Nyquist plots, it is clear that the radii of the quasi-semicircle after the 100th and 300th cycles are much smaller than that of fresh cells for both PDA-coated and uncoated corn-like SnO_2 samples, reflecting that the charge transfer is facilitated due to the activation process.[305] The R_{ohm} at the high-frequency intercept on the real axis after the 100th and 300th cycles for both batteries are higher than those of fresh cells, which is mainly because of the consumption of electrolyte due to the formation of the SEI layer over cycling.[306-307] For the PDA-coated corn-like SnO_2 electrode (**Figure 6.14a**), the R_{ohm} after the 300th cycle is similar to that after the 100th cycle. However, for the uncoated corn-like SnO_2 electrode (**Figure 6.14b**), the resistance after the 300th cycle increases significantly compared with that after the 100th cycle, which is indicative of large consumption of electrolyte by forming a thick SEI film over cycling. Clearly, the PDA coating is advantageous to prevent the continuous depletion of electrolyte and maintain the long-term stability of the SEI film, probably because the PDA coating provides an elastic buffer for accommodating the volume change of active materials and prevents the direct contact between active materials and electrolyte. Such a good passivating SEI film contributes to the greatly improved cycling stability for the PDA-coated corn-like SnO_2 electrode.

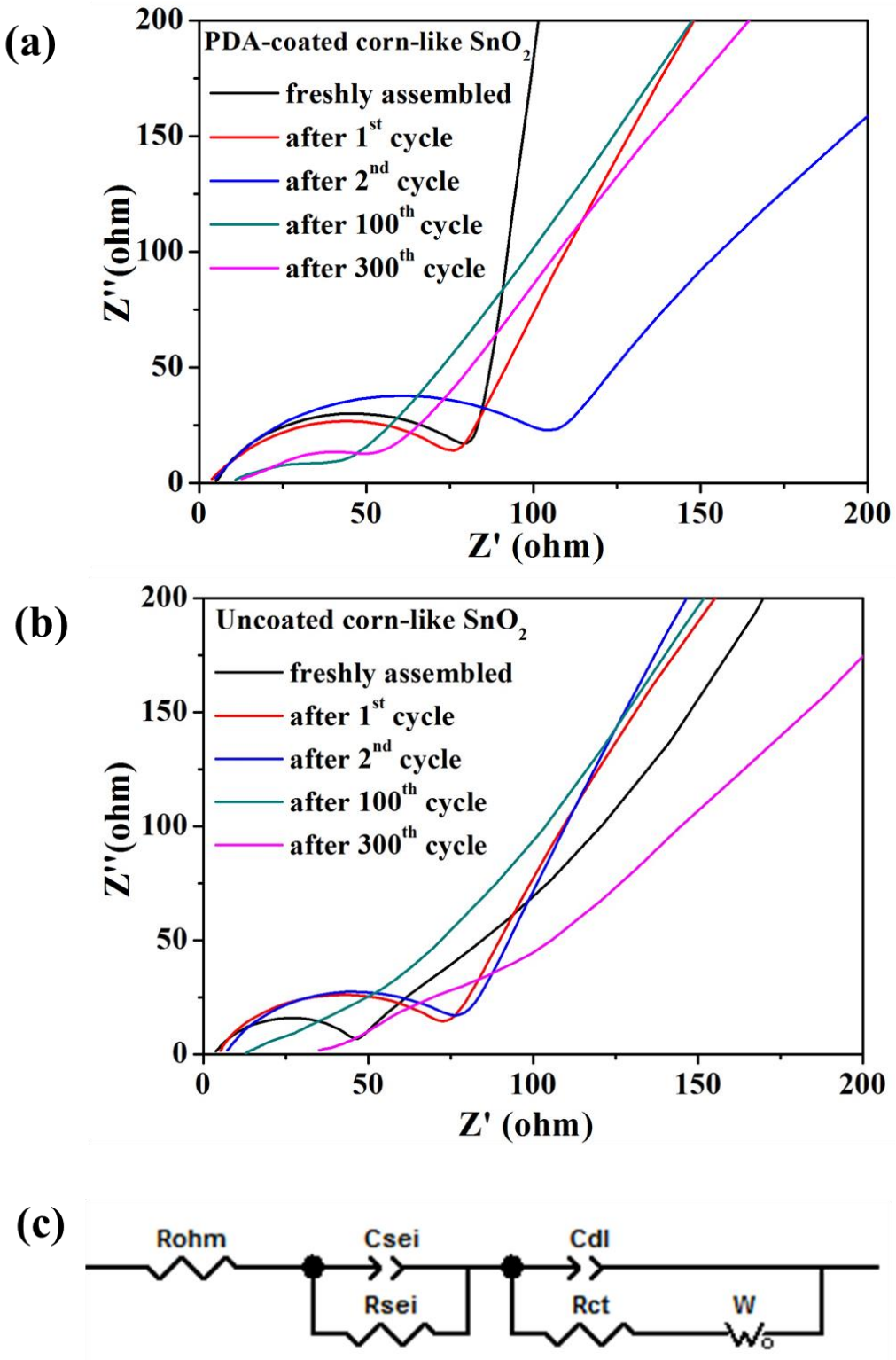

Figure 6.14 Electrochemical impedance spectroscopy (EIS) results for (a) PDA-coated corn-like SnO_2 electrode, (b) uncoated corn-like SnO_2 electrode of freshly assembled, after the 1st, 2nd, 100th, and 300th cycles in the charged state over a frequency range of 100 kHz to 10 mHz at an amplitude of 5mV, and (c) equivalent circuit model for the battery.

Intrigued by the attractive cycling stability of the PDA-coated corn-like SnO_2 electrode, we set out to investigate the electrode morphology after cycling. The batteries after cycling at 160 mA g^{-1} for 300 cycles (in charging state) were dissembled in glove box and characterized by *ex-situ* scanning electron microscopy (SEM) and X-ray photoelectron spectroscopy (XPS). The morphologies of fresh electrode prior to cycling, the uncoated corn-like SnO_2 electrode after cycling, and the PDA-coated corn-like SnO_2 electrode after cycling are shown in **Figure 6.15**(**a**, **d**, **g**), **Figure 6.15(b**, **e**, **h**), and **Figure 6.15**(**c**, **f**, **i**), respectively. Thick SEI films are clearly evident for the uncoated corn-like SnO_2 electrode (**Figure 6.15(b, e, h**)). Notably, thick SEI films, covering the surface of active materials, block the holes existed in the electrode and make the electrolyte inaccessible to active materials, and thus leading to a poor cycling stability for the uncoated corn-like SnO_2 electrode. In stark contrast, for the PDA-coated corn-like SnO_2 electrode (**Figure 6.15**(**c, f, i**)), the SEI film is much thinner and the morphology remains almost unchanged compared with the fresh electrode, signifying that the layer of PDA coating on the corn-like SnO_2 indeed acts as a protective layer for accommodating the volume change for active materials and suppresses the formation of thick SEI. Such protective PDA layer together with the corn-like nanostructures account for the observed superior cyclability for the PDA-coated corn-like SnO_2 electrode.

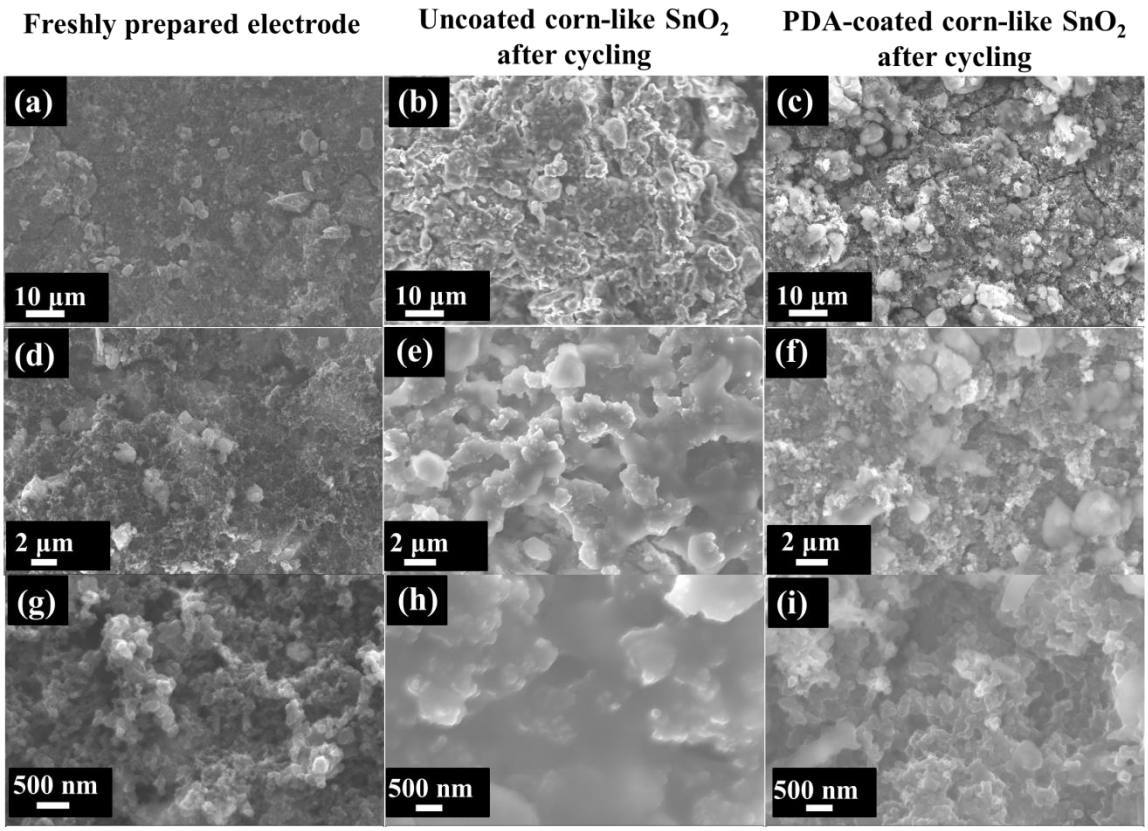

Figure 6.15 SEM images of (a, d, g) freshly prepared electrode at different magnifications; (b, e, h) uncoated corn-like SnO_2 electrode after cycling at 160mA g^{-1} for 300 cycles, and (c, f, i) PDA-coated corn-like SnO_2 electrode after cycling at 160mA g^{-1} for 300 cycles.

X-ray photoelectron spectroscopy (XPS) measurement was also carried out to examine the surface electronic state of Sn after cycling. The high-resolution spectrum of the Sn 3d XPS spectra of freshly prepared electrode, the PDA-coated and uncoated corn-like SnO_2 electrodes after cycling are shown in **Figure 6.16**. The XPS spectrum for the PDA-coated corn-like SnO_2 electrode exhibits the same binding energy as the as-prepared electrode with two broad peaks centered at 495.6 and 487.2 eV. These two peaks can be assigned to Sn $3d_{3/2}$ and Sn $3d_{5/2}$, respectively, corresponding to Sn^{4+} in SnO_2,[281, 289] indicating that the conversion from Sn to SnO_2 (equation 1) is reversible for

the PDA-coated corn-like SnO_2. However, for the uncoated corn-like SnO_2, the obvious shifts to lower binding energies of 494.9 and 486.5 eV was observed, which can be attributed to the formation of SnO,[289, 308] implying that the conversion from Sn to SnO_2 (equation 1) is not fully reversible and instead SnO is formed during this conversion. Such comparison demonstrated that the PDA coating is helpful for the reversible conversion from Sn to SnO_2 (equation 1), largely because the PDA coating can suppress the coarsening of Sn nanoparticles and retain a high fraction of Sn/Li_2O interface for promoting the reversible reaction between Sn and Li_2O in forming SnO_2.

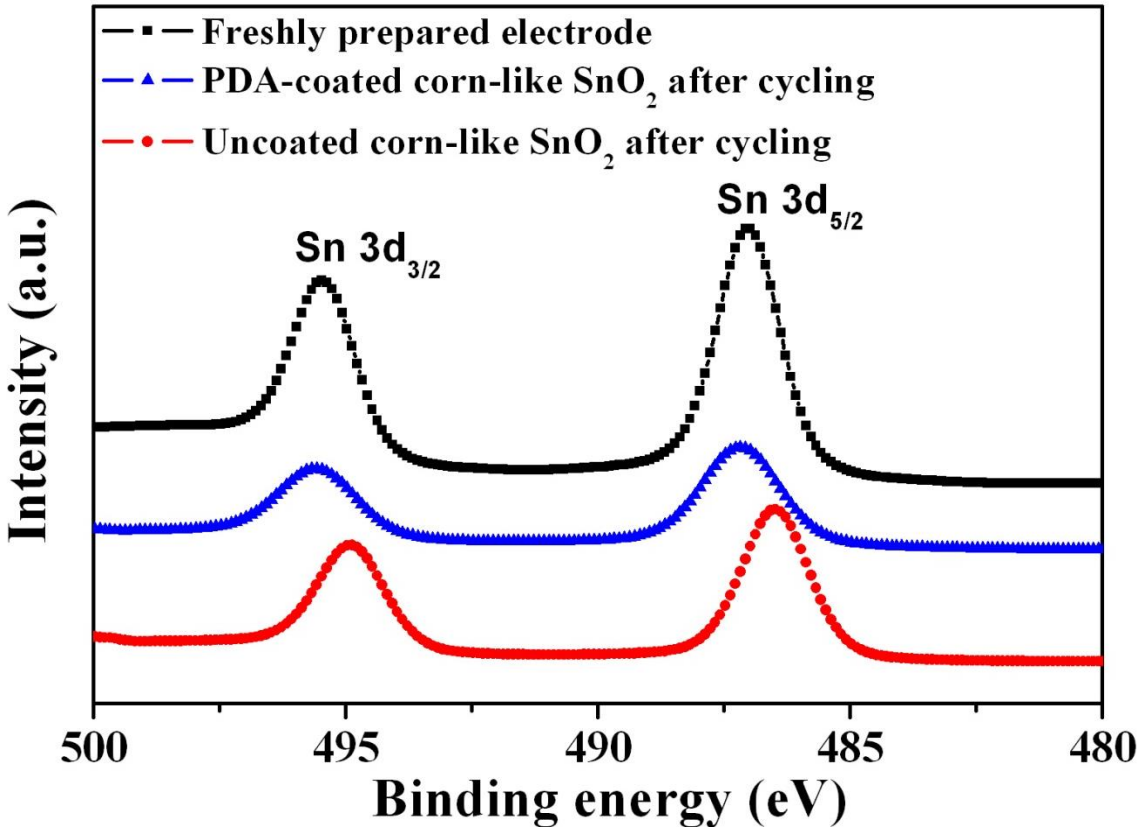

Figure 6.16 High-resolution Sn 3d XPS spectra for freshly prepared electrode, PDA-coated and uncoated corn-like SnO_2 electrodes after cycling at 160 mA g^{-1} for 300 cycles (in charged state).

6.3 Conclusions

In summary, we crafted corn-like SnO_2 nanocrystals using judiciously designed bottlebrush-like HPC-*g*-PAA as template and coated the corn-like SnO_2 with a thin layer of protective PDA for enhancing the electrochemical performance of SnO_2-based electrodes. The batteries based on the uncoated corn-like SnO_2 demonstrated a good short-term cycling stability for 150 cycles and a good rate performance, which can be attributed to the shortened ionic and electronic transport length, the good structural stability enabled by the reduced dimension of active SnO_2 nanoparticles in the corn-like nanostructures, the high porosity favorable for accommodating the volume change and liberating the stress, and the limited aggregation of Sn nanoparticles due to the strong interaction between SnO_2/Sn nanoparticles and the HPC-*g*-PAA template.

More importantly, the introduction of PDA coating to the corn-like SnO_2 provided a protective layer for active SnO_2 nanoparticles and carried several distinct advantages over the non-PDA coated corn-like SnO_2 counterpart. The PDA coating offered an elastic buffer to accommodate the volume change of active materials during the lithiation/delithiation process, thus further suppressing the coarsening of Sn nanoparticles and enhancing the reversible conversion from Sn back to SnO_2 due to the large fraction of the Sn/Li_2O interfaces. Moreover, the PDA coating also prevented the direct contact of active materials with electrolyte, thereby avoiding the depletion of electrolyte for forming think SEI and finally resulting in a good passivating SEI layer with a superior long-term stability. The synergy of the corn-like nanostructures and the protective PDA coating enabled the excellent electrochemical performance for the PDA-coated corn-like SnO_2

electrode, including the superior long-term cycling stability for over 300 cycles at 200, 400, 780, and 1500 mA g^{-1}, the high $Sn \rightarrow SnO_2$ reversibility with capacities approaching the theoretical value of 1494 mA h g^{-1} at low current density of 160 mA g^{-1}, and the excellent rate capability. We envisage that the bottlebrush-like polymer templating strategy is facile and robust, and can be readily extended to create a rich variety of other functional metal oxides and metal sulfides for high-performance LIBs as a diversity of materials are amenable to such templating growth reaction.

Chapter 7 General Discussion and Broader Impacts

7.1 General conclusions and discussion

We rationally designed and exploited amphiphilic multi-arm star-like poly(acrylic acid)-block-poly(vinylidene fluoride) (PAA-*b*-PVDF) diblock copolymers consisting of hydrophilic PAA and hydrophobic PVDF blocks that are covalently linked to a small core as nanoreactors to craft *in-situ* monodisperse $BaTiO_3$ nanoparticles with tunable sizes that are intimately and permanently connected to PVDF chains (i.e., intimate PVDF-$BaTiO_3$ nanocomposites possessing a well-defined interface between PVDF/$BaTiO_3$ nanoparticles and preventing direct particle/particle contact). The hydrophilic inner PAA blocks in star-like PAA-*b*-PVDF rendered a strong coordination interaction between the carboxylic groups (-COOH) of PAA and the metal moieties of $BaTiO_3$ (Ba^{2+} and Ti^{4+}), while the outer hydrophobic PVDF blocks did not possess such coordinating functional groups, therefore the precursors were selectively incorporated into the space occupied by inner PAA blocks and converted into $BaTiO_3$ nanoparticles intimately and stably capped with PVDF chains. Remarkably, the diameter of these PVDF-functionalized $BaTiO_3$ nanoparticles can be precisely tuned by varying the molecular weight of inner PAA blocks, and accordingly, the volume ratio of $BaTiO_3$ to PVDF can be readily altered.

In addition, we also judiciously designed amphiphilic bottlebrush-like PAA-*b*-PVDF diblock copolymers comprising hydrophilic PAA and hydrophobic PVDF blocks that are covalently linked to a one dimensional backbone and used it as nanoreactors to produce *in-situ* monodisperse $BaTiO_3$ nanorods with tunable diameter and length. The $BaTiO_3$ nanorods are *intimately* and *permanently* capped by PVDF chains thorough a well-defined interface between PVDF/$BaTiO_3$ nanorods. The aggregation of nanorods is prevented due to their limited direct contact. The diameter and length of the PVDF-capped $BaTiO_3$ nanorods can be controlled by the molecular weight (i.e. length) of inner PAA block and the molecular weight (i.e. length) of the initiator (cellulose-Br), respectively. In addition, the uniformity of PVDF-capped $BaTiO_3$ nanorods can be well controlled through tailoring the polydispersity of the molecular weight of cellulose-Br initiator and inner PAA block of the bottlebrush-like PAA-*b*-PVDF.

On the other hand, we reported a robust *in-situ* crafting of $ZnFe_2O_4$/carbon nanocomposites electrode composed of $ZnFe_2O_4$ nanoparticles with an average diameter of 16±5 nm impregnated within the continuous carbon network *via* the pyrolysis of $ZnFe_2O_4$ precursors-containing polystyrene@poly(acrylic acid) (PS@PAA) core@shell nanospheres. The PS@PAA nanospheres were synthesized in *one-step* by emulsion polymerization, followed by thermal annealing of $ZnFe_2O_4$ precursor-containing PS@PAA nanospheres, leading to the formation of $ZnFe_2O_4$ nanoparticles embedded in the continuous carbon network due to the carbonization of PS@PAA nanospheres. Intriguingly, the PS@PAA nanospheres not only functioned as templates by incorporating $ZnFe_2O_4$ precursors in the region occupied by the PAA shell owing to a strong coordination bonding between the carboxyl groups of PAA and the metal moieties

of precursors, but also acted as the polymeric source for the creation of carbon network. The mass content of $ZnFe_2O_4$ nanoparticles in $ZnFe_2O_4$/C nanocomposites can be systematically varied to find the optimum mass loading of $ZnFe_2O_4$ nanoparticles for the best electrochemical performance. It is noteworthy that the carbon network provides a continuous and conductive pathway for electron transport, resulting in excellent rate capability when $ZnFe_2O_4$/carbon nanocomposites containing 79.3 wt% $ZnFe_2O_4$ were evaluated as potential anode materials. In addition, the carbon network renders the mechanical flexibility of active materials, as well as retains the structural integrity of $ZnFe_2O_4$/Carbon nanocomposites during the repeated lithiation/delithiation, thereby leading to a prolonged cyclic life of the $ZnFe_2O_4$/carbon electrode.

Moreover, we crafted corn-like SnO_2 nanocrystals using judiciously designed bottlebrush-like HPC-*g*-PAA as template and coated the corn-like SnO_2 with a thin layer of protective PDA for enhancing the electrochemical performance of SnO_2-based electrodes. The batteries based on the uncoated corn-like SnO_2 demonstrated a good short-term cycling stability for 150 cycles and a good rate performance, which can be attributed to the shortened ionic and electronic transport length, the good structural stability enabled by the reduced dimension of active SnO_2 nanoparticles in the corn-like nanostructures, the high porosity favorable for accommodating the volume change and liberating the stress, and the limited aggregation of Sn nanoparticles due to the strong interaction between SnO_2/Sn nanoparticles and the HPC-*g*-PAA template. More importantly, the introduction of PDA coating to the corn-like SnO_2 provided a protective layer for active SnO_2 nanoparticles and carried several distinct advantages over the non-PDA coated corn-like SnO_2 counterpart. The PDA coating offered an elastic buffer to

accommodate the volume change of active materials during the lithiation/delithiation process, thus further suppressing the coarsening of Sn nanoparticles and enhancing the reversible conversion from Sn back to SnO_2 due to the large fraction of the Sn/Li_2O interfaces. Moreover, the PDA coating also prevented the direct contact of active materials with electrolyte, thereby avoiding the depletion of electrolyte for forming think SEI and finally resulting in a good passivating SEI layer with a superior long-term stability. The synergy of the corn-like nanostructures and the protective PDA coating enabled the excellent electrochemical performance for the PDA-coated corn-like SnO_2 electrode, including the superior long-term cycling stability for over 300 cycles at 200, 400, 780, and 1500 mA g^{-1}, the high $Sn \rightarrow SnO_2$ reversibility with capacities approaching the theoretical value of 1494 mA h g^{-1} at low current density of 160 mA g^{-1}, and the excellent rate capability. We envisage that the bottlebrush-like polymer templating strategy is facile and robust, and can be readily extended to create a rich variety of other functional metal oxides and metal sulfides for high-performance LIBs as a diversity of materials are amenable to such templating growth reaction.

7.2 Significance and broader impacts

7.2.1 Precisely controlling the size, shape, and uniformity of nanocrystals

A precise control over the size and shape of ferroelectric perovskite oxide nanocrystals renders the systematic investigation of the size effect and shape effect on

both dielectric and ferroelectric properties of ferroelectric perovskite oxide-based nanocomposites. We demonstrated, for the first time, that the size of monodispersed $BaTiO_3$ nanoparticles can be precisely controlled ranging from a few nanometers to tens of nanometers by changing the molecular weight of the polymer template. The capability of synthesizing uniform $BaTiO_3$ nanoparticles with different sizes enables the systematic study of the size effect on the dielectric properties of $BaTiO_3$ nanoparticles, which will provide guidance in designing $BaTiO_3$-polymer nanocomposite materials with controlled dielectric permittivity and maximized energy storage density. In addition, the systematic variation of the size of $BaTiO_3$ nanoparticles allows the probing of the critical size of $BaTiO_3$ nanoparticles, below which the ferroelectric property of $BaTiO_3$ nanoparticles disappears. Such information of the size-dependent ferroelectricity will be helpful when $BaTiO_3$ nanoparticles and related nanocomposites are used in nanoscale ferroelectric memory devices.

On the other hand, the delicate control on the diameter and length of $BaTiO_3$ nanorods enables the systematic investigation of the dependence of dielectric and ferroelectric properties on the aspect ratio (the ratio of the diameter to the length) of $BaTiO_3$ nanorods. The fundamental study of the size and shape effect of $BaTiO_3$ nanomaterials will provide useful information when designing nanostructured $BaTiO_3$ for practical applications in capacitors and memory devices.

7.2.2 Improving the organic/inorganic interface

We demonstrated, for the first time, the surface modification of $BaTiO_3$ nanocrystals by *in-situ* synthesis of $BaTiO_3$ nanocrystals in the presence of polymer matrix, yielding $BaTiO_3$ nanocrystals intimately and permanently tethered with ferroelectric polymer. Such *in-situ* synthesis approach enables an elegantly defined organic/inorganic interface, which allows the homogeneous dispersion of PVDF-functionalized $BaTiO_3$ nanoparticles in the polymer matrix without phase separation. In addition, the capped PVDF arm with tunable length can serve as the polymer matrix for constructing the $BaTiO_3$-PVDF nanocomposites. Such well-defined interface between organic and inorganic components is of great importance to the homogeneity of the resulting organic-inorganic nanocomposites, as well as their dielectric properties. Such bottom-up crafting of intimate organic-inorganic nanocomposites offers new levels of tailorability to nanostructured materials and promises new opportunities for achieving exquisite control over the surface chemistry and properties of nanocomposites with engineered functionality for diverse applications in energy conversion and storage, catalysis, electronics, nanotechnology, and biotechnology.

7.2.3 Enabling complex architecture and compositions for active-inactive nanocomposites in one-step

We demonstrated, for the first time, the construction of complex nanostructures such as corn-on-the-cob-like structure and carbon-network encapsulated nanoparticles, by a simple one-step polymer-templated approach. The nanostructured morphology is

directly enabled and reflected by the rationally designed polymer template, which itself, is in the nanometer scale, therefore, the thermodynamically unstable nanostructured inorganic materials can be easily obtained, which is in stark contrast to the commonly reported method for preparing nanostructured materials but often encounters lot of difficulty in obtaining stable and rationally controlled nanostructured architectures. This approach also allows the flexible design of complex compositions involving multiply elements and can precisely vary the stoichiometry ratio of each element for realizing unique properties, such as up-conversion materials NaYF4:Yb/Er (18%/2%). This method, compared to traditional method, is more cost-effective and versatile in designing complex architecture and multi-composition materials with much enhanced stability.

Dissemination of work

This work has been distributed to the research community by the following publications and presentations.

Publications

1. **B. Jiang**, X. Pang, B. Li and Z. Lin, "Organic-Inorganic Nanocomposites via Placing Monodisperse Ferroelectric Nanocrystals in Direct and Permanent Contact with Ferroelectric Polymer", *Journal of the American Chemical Society*, 137, 11760 (2015)

2. **B. Jiang**, C. Han, B. Li, Y. He and Z. Lin, "In-situ Crafting of $ZnFe_2O_4$ Nanoparticles Impregnated within Continuous Carbon Network as Advanced Anode Materials", *ACS Nano*, 10, 2728 (2016)

3. **B. Jiang**, L. Zhao, and Z. Lin*, "Barium Titanate at Nanoscale: Controlled Synthesis and Properties", *Chemical Reviews* (under review)

4. **B. Jiang**, B. Li and Z. Lin, "Polymer-templated Formation of Corn-on-the-Cob-like SnO_2 Nanocrystals Coated with Polydopamine as Anodes for Lithium Ion Battery with Superior Cyclability"(submitted)

5. **B. Jiang**, X. Pang, B. Li and Z. Lin, "PVDF-$BaTiO_3$ nanorods via placing monodisperse $BaTiO_3$ nanorods in direct and permanent contact with PVDF", in preparation

6. M. He, X. Pang, X. Liu, **B. Jiang**, Y. He, H. Snaith, and Z. Lin*, "Monodisperse Dual-Functional Upconversion Nanoparticles-Enabled Near-Infrared Organolead Halide Perovskite Solar Cells", *Angewandte Chemie International Edition*, 128, 4352 (2016)

7. Y. Yang, C. Han, **B. Jiang**, J. Iocozzia, and Z. Lin*, "Graphene-based Materials with Tailored Nanostructures for Energy Conversion and Storage", *Materials Science and Engineering* R: Reports. 102, 1(2016)

8. B. Li, C. Zhang, **B. Jiang**, and Z. Lin*, "Flow-Enabled Self-Assembly of Large-Scale Aligned Nanowires", *Angewandte Chemie International Edition*. 54, 4250 (2015) (Selected as Very Important Paper (VIP))

9. S. Wu, R. Xu, M. Lu, R. Ge, J. Iocozzia, C. Han, **B. Jiang**, and Z. Lin*, "Graphene-Containing Nanocomposites for Lithium Ion Battery", *Advanced Energy Materials*, 1500400 (2015)

10. B. Li, **B. Jiang**, H. Tang, and Z. Lin*, "Unconventional Seed-Mediated Growth of Ultrathin Au Nanowires in Aqueous Solution", *Chemical Science*, 6, 6349 (2015)

11. C. Han, D. Yang, Y. Yang, **B. Jiang**, Y. He, and Z. Lin*, "Hollow Titanium Dioxide Spheres as Anode Material for Lithium Ion Battery with Largely Improved Rate Stability and Cycle Performance by Suppressing the Formation of SEI Layer", Journal of Materials Chemistry A. 3, 13340 (2015)

12. B. Li, W. Han, **B. Jiang**, and Z. Lin*, "Crafting threads of diblock copolymer micelles via flow-enabled self-ssembly", *ACS Nano*, 8, 2936 (2014)

13. X. Pang, Y. He, **B. Jiang**, J. Iocozzia, L. Zhao, H. Guo, J. Liu, M. Akinc, X. Tan, N. Bowler, and Z. Lin*, "Block copolymer/ferroelectric nanoparticle nanocomposites", *Nanoscale*. 5, 8695 (2013)

Selected Presentations

1. "Carbon-Coated $ZnFe_2O_4$ Nanocrystals for Advanced Lithium-Ion Anodes", Oral presentation, MRS Spring Meeting & Exhibit, San Francisco, 2015

2. "Polymer-templated carbon hybridized nanostructured transition metal oxide as Advanced Lithium-Ion Anodes", 229th ECS meeting, San Diego, 2016

3. "Organic-Inorganic Nanocomposites via Direct Growth of Ferroelectric Nanocrystals Intimately Connected with Ferroelectric Polymers", Oral Presentation, MRSEC EAB meeting, Georgia Tech, 2013 & 2014

Awards

Center of Organic Photonics and Electronics Fellowship, Georgia Tech 2016

References

[1]. Sanchez, C.; Julian, B.; Belleville, P.; Popall, M., "Applications of hybrid organic-inorganic nanocomposites". *J. Mater. Chem.* ***15,*** 3559-3592.(2005).

[2]. Dang, Z.M., et al., "Fundamentals, processes and applications of high-permittivity polymer–matrix composites". *Prog. Mater. Sci.* ***57,*** 660-723.(2012).

[3]. Kango, S., et al., "Surface modification of inorganic nanoparticles for development of organic–inorganic nanocomposites—A review". *Prog. Polym. Sci.* ***38,*** 1232-1261.(2013).

[4]. Kickelbick, G., "Concepts for the incorporation of inorganic building blocks into organic polymers on a nanoscale". *Prog. Polym. Sci.* ***28,*** 83-114.(2003).

[5]. Jung, H. M.; Kang, J.-H.; Yang, S. Y.; Won, J. C.; Kim, Y. S., "Barium titanate nanoparticles with diblock copolymer shielding layers for high-energy density nanocomposites". *Chem. Mater.* ***22,*** 450-456.(2009).

[6]. Yang, K.; Huang, X.; Huang, Y.; Xie, L.; Jiang, P., "Fluoro-polymer@ $BaTiO_3$ hybrid nanoparticles prepared via RAFT polymerization: toward ferroelectric polymer nanocomposites with high dielectric constant and low dielectric loss for energy storage application". *Chem. Mater.* ***25,*** 2327-2338.(2013).

[7]. Xie, L.; Huang, X.; Wu, C.; Jiang, P., "Core-shell structured poly(methyl methacrylate)/$BaTiO_3$ nanocomposites prepared by in situ atom transfer radical polymerization: a route to high dielectric constant materials with the inherent low loss of the base polymer". *J. Mater. Chem.* ***21,*** 5897-5906.(2011).

[8]. Lin, M.F.; Lee, P. S., "Formation of PVDF-*g*-HEMA/$BaTiO_3$ nanocomposites via in situ nanoparticle synthesis for high performance capacitor applications". *Journal of Materials Chemistry A* ***1,*** 14455-14459.(2013).

[9]. Liu, R.; Duay, J.; Lee, S. B., "Heterogeneous nanostructured electrode materials for electrochemical energy storage". *Chem. Commun.* ***47,*** 1384-1404.(2011).

[10]. Su , D. S.; Schlögl, R., "Nanostructured Carbon and Carbon Nanocomposites for Electrochemical Energy Storage Applications". *ChemSusChem* ***3,*** 136-168.(2010).

[11]. He, C., et al., "Carbon-Encapsulated Fe_3O_4 Nanoparticles as a High-Rate Lithium Ion Battery Anode Material". *ACS Nano* ***7,*** 4459-4469.(2013).

[12]. Wu, H., et al., "Stable Li-ion battery anodes by in-situ polymerization of conducting hydrogel to conformally coat silicon nanoparticles". *Nat Commun* ***4,*** (2013).

[13]. Kong, J., et al., "Highly electrically conductive layered carbon derived from polydopamine and its functions in SnO_2-based lithium ion battery anodes". *Chem. Commun.* ***48,*** 10316-10318.(2012).

[14]. Pang, X.; Zhao, L.; Han, W.; Xin, X.; Lin, Z., "A general and robust strategy for the synthesis of nearly monodisperse colloidal nanocrystals". *Nat Nano* ***8,*** 426-431.(2013).

[15]. Kwei, G. H.; Lawson, A. C.; Billinge, S. J. L.; Cheong, S. W., "Structures of the Ferroelectric Phases of Barium-Titanate". *J. Phys. Chem.* ***97,*** 2368-2377.(1993).

[16]. Shaw, T. M.; Trolier-McKinstry, S.; McIntyre, P. C., "The properties of ferroelectric films at small dimensions". *Annu. Rev. Mater. Sci.* ***30,*** 263-298.(2000).
[17]. Tsurumi, T.; Hoshina, T.; Takeda, H.; Mizuno, Y.; Chazono, H., "Size Effect of Barium Titanate and Computer-Aided Design of Multilayered Ceramic Capacitors". *IEEE Trans. Ultrason. Ferroelectr. Freq. Control* ***56,*** 1513-1522.(2009).
[18]. Jiang, B.; Pang, X.; Li, B.; Lin, Z., "Organic–Inorganic Nanocomposites via Placing Monodisperse Ferroelectric Nanocrystals in Direct and Permanent Contact with Ferroelectric Polymers". *J. Am. Chem. Soc.* ***137,*** 11760-11767.(2015).
[19]. Jiang, B.; Han, C.; Li, B.; He, Y.; Lin, Z., "In-Situ Crafting of $ZnFe_2O_4$ Nanoparticles Impregnated within Continuous Carbon Network as Advanced Anode Materials". *ACS Nano* ***10,*** 2728-2735.(2016).
[20]. Bai, Y.; Cheng, Z.Y.; Bharti, V.; Xu, H. S.; Zhang, Q. M., "High-dielectric-constant ceramic-powder polymer composites". *Appl. Phys. Lett.* ***76,*** 3804-3806.(2000).
[21]. Seger, B.; Kamat, P. V., "Electrocatalytically active graphene-platinum nanocomposites. Role of 2-D carbon support in PEM fuel cells". *The Journal of Physical Chemistry C* ***113,*** 7990-7995.(2009).
[22]. Tian, Z. Q.; Jiang, S. P.; Liang, Y. M.; Shen, P. K., "Synthesis and characterization of platinum catalysts on multiwalled carbon nanotubes by intermittent microwave irradiation for fuel cell applications". *The Journal of Physical Chemistry B* ***110,*** 5343-5350.(2006).
[23]. Wang, P., et al., "One-step, solvothermal synthesis of graphene-CdS and graphene-ZnS quantum dot nanocomposites and their interesting photovoltaic properties". *Nano Research* ***3,*** 794-799.(2010).
[24]. Scher, E., et al., Nanostructure and nanocomposite based compositions and photovoltaic devices. Google Patents: 2005.
[25]. Godovsky, D. Y., Device applications of polymer-nanocomposites. In *Biopolymers· PVA Hydrogels, Anionic Polymerisation Nanocomposites*, Springer: 2000; pp 163-205.
[26]. Huang, Q., et al., "Structure and interaction of organic/inorganic hybrid nanocomposites for microelectronic applications. 1. MSSQ/P (MMA-co-DMAEMA) nanocomposites". *Chem. Mater.* ***14,*** 3676-3685.(2002).
[27]. Ng, S. H., et al., "Highly Reversible Lithium Storage in Spheroidal Carbon-Coated Silicon Nanocomposites as Anodes for Lithium-Ion Batteries". *Angewandte Chemie International Edition* ***45,*** 6896-6899.(2006).
[28]. Mao, O., et al., "Active/Inactive nanocomposites as anodes for Li-Ion batteries". *Electrochemical and Solid-State Letters* ***2,*** 3-5.(1999).
[29]. Kim, P., et al., "High energy density nanocomposites based on surface-modified $BaTiO_3$ and a ferroelectric polymer". *ACS Nano* ***3,*** 2581-2592.(2009).
[30]. Yang, K.; Huang, X.; Huang, Y.; Xie, L.; Jiang, P., "Fluoro-Polymer@$BaTiO_3$ Hybrid Nanoparticles Prepared via RAFT Polymerization: Toward Ferroelectric Polymer Nanocomposites with High Dielectric Constant and Low Dielectric Loss for Energy Storage Application". *Chem. Mater.* ***25,*** 2327-2338.(2013).
[31]. Sanchez, C.; Ribot, F., "Design of hybrid organic-inorganic materials synthesized via sol-gel chemistry". *New J. Chem.* ***18,*** 1007-1047.(1994).
[32]. Boury, B.; Corriu, R. J. P., "Auto-organisation of hybrid organic-inorganic materials prepared by sol-gel chemistry". *Chem. Commun.* 795-802.(2002).

[33]. Bantignies, J. L., et al., "Hydrogen bonding in self organized lamellar hybrid silica". *J. Non-cryst. Solids.* ***345–346,*** 605-609.(2004).
[34]. Moreau, J. J. E.; Pichon, B. P.; Arrachart, G.; Wong Chi Man, M.; Bied, C., "Nanostructuring organo-silicas: combination of intermolecular interactions and molecular recognition properties to generate self-assembled hybrids with phenylene or adenine[three dots, centered]thymine bridging units". *New J. Chem.* ***29,*** 653-658.(2005).
[35]. Moreau, J. J. E.; Vellutini, L.; Bied, C.; Man, M. W. C., "New Approach for the Organisation and the Shaping of Organo-Bridged Silicas: An Overview". *J. Sol-gel. Sci. Techn.* ***31,*** 151-156.(2004).
[36]. Moreau, J. J. E., et al., "Lamellar Bridged Silsesquioxanes: Self-Assembly through a Combination of Hydrogen Bonding and Hydrophobic Interactions". *Chemistry – A European Journal* ***11,*** 1527-1537.(2005).
[37]. Li, H.; Eddaoudi, M.; O'Keeffe, M.; Yaghi, O. M., "Design and synthesis of an exceptionally stable and highly porous metal-organic framework". *Nature* ***402,*** 276-279.(1999).
[38]. Chae, H. K., et al., "A route to high surface area, porosity and inclusion of large molecules in crystals". *Nature* ***427,*** 523-527.(2004).
[39]. Millange, F., et al., "Synthesis, structure and properties of a three-dimensional porous rare-earth carboxylate MIL-83(Eu): $Eu_2(O_2C\text{-}C_{10}H_{14}\text{-}CO_2)_3$". *J. Mater. Chem.* ***14,*** 642-645.(2004).
[40]. Yaghi, O. M., et al., "Reticular synthesis and the design of new materials". *Nature* ***423,*** 705-714.(2003).
[41]. Sanchez, C., et al., "Designed Hybrid Organic−Inorganic Nanocomposites from Functional Nanobuilding Blocks". *Chem. Mater.* ***13,*** 3061-3083.(2001).
[42]. Kresge, C. T.; Leonowicz, M. E.; Roth, W. J.; Vartuli, J. C.; Beck, J. S., "Ordered mesoporous molecular sieves synthesized by a liquid-crystal template mechanism". *Nature* ***359,*** 710-712.(1992).
[43]. Corriu, R. J. P.; Mehdi, A.; Reye, C.; Thieuleux, C., "Control of coordination chemistry in both the framework and the pore channels of mesoporous hybrid materials". *New J. Chem.* ***27,*** 905-908.(2003).
[44]. Steunou, N.; Forster, S.; Florian, P.; Sanchez, C.; Antonietti, M., "Synthesis of nanostructured polymer-titanium oxide composites through the assembly of titanium-oxo clusters and amphiphilic block copolymers micelles". *J. Mater. Chem.* ***12,*** 3426-3430.(2002).
[45]. Fornasieri, G., et al., "Reactivity of Titanium Oxo Ethoxo Cluster $[Ti_{16}O_{16}(OEt)_{32}]$. Versatile Precursor of Nanobuilding Block-Based Hybrid Materials". *J. Am. Chem. Soc.* ***127,*** 4869-4878.(2005).
[46]. Bruce, P. G.; Scrosati, B.; Tarascon, J.-M., "Nanomaterials for Rechargeable Lithium Batteries". *Angewandte Chemie International Edition* ***47,*** 2930-2946.(2008).
[47]. Ogihara, H.; Randall, C. A.; Trolier-McKinstry, S., "High-Energy Density Capacitors Utilizing 0.7 $BaTiO_3$-0.3 $BiScO_3$ Ceramics". *J. Am. Ceram. Soc.* ***92,*** 1719-1724.(2009).
[48]. Li, J. Y.; Zhang, L.; Ducharme, S., "Electric energy density of dielectric nanocomposites". *Appl. Phys. Lett.* ***90,***.(2007).

[49]. Rao, Y.; Ogitani, S.; Kohl, P.; Wong, C. P., "Novel polymer–ceramic nanocomposite based on high dielectric constant epoxy formula for embedded capacitor application". *J. Appl. Polym. Sci.* ***83,*** 1084-1090.(2002).
[50]. Dang, Z. M.; Lin, Y. H.; Nan, C. W., "Novel Ferroelectric Polymer Composites with High Dielectric Constants". *Adv. Mater.* ***15,*** 1625-1629.(2003).
[51]. Zhang, Q. M., et al., "An all-organic composite actuator material with a high dielectric constant". *Nature* ***419,*** 284-287.(2002).
[52]. Chen, G.; Zhao, J.; Li, S.; Zhong, L., "Origin of thickness dependent dc electrical breakdown in dielectrics". *Appl. Phys. Lett.* ***100,*** 222904.(2012).
[53]. Bune, A. V., et al., "Two-dimensional ferroelectric films". *Nature* ***391,*** 874-877.(1998).
[54]. Dahn, J. R.; Zheng, T.; Liu, Y.; Xue, J., "Mechanisms for lithium insertion in carbonaceous materials". *Science* ***270,*** 590.(1995).
[55]. Ng, S.H., et al., "Highly Reversible Lithium Storage in Spheroidal Carbon-Coated Silicon Nanocomposites as Anodes for Lithium-Ion Batteries". *Angewandte Chemie International Edition* ***45,*** 6896-6899.(2006).
[56]. Sebastian, M. T.; Jantunen, H., "Polymer-Ceramic Composites of 0-3 Connectivity for Circuits in Electronics: A Review". *International Journal of Applied Ceramic Technology* ***7,*** 415-434.(2010).
[57]. Newnham, R. E., "Composite electroceramics". *Ferroelectrics* ***68,*** 1-32.(1986).
[58]. Ryu, J.; Carazo, A. V.; Uchino, K.; Kim, H.-E., "Piezoelectric and magnetoelectric properties of lead zirconate titanate/Ni-ferrite particulate composites". *J. Electroceram.* ***7,*** 17-24.(2001).
[59]. Bhimasankaram, T.; Suryanarayana, S.; Prasad, G., "Piezoelectric polymer composite materials". *CURRENT SCIENCE-BANGALORE-* ***74,*** 967-976.(1998).
[60]. Newnham, R. E.; Skinner, D. P.; Cross, L. E., "Connectivity and piezoelectric-pyroelectric composites". *Mater. Res. Bull.* ***13,*** 525-536.(1978).
[61]. Dang, Z. M.; Wang, H. Y.; Zhang, Y. H.; Qi, J. Q., "Morphology and dielectric property of homogenous $BaTiO_3$/PVDF nanocomposites prepared via the natural adsorption action of nanosized BaTiO3". *Macromol. Rapid. Comm.* ***26,*** 1185-1189.(2005).
[62]. Tsangaris, G.; Psarras, G.; Kouloumbi, N., "Electric modulus and interfacial polarization in composite polymeric systems". *J. Mater. Sci.* ***33,*** 2027-2037.(1998).
[63]. Tuncer, E.; Gubański, S. M.; Nettelblad, B., "Dielectric relaxation in dielectric mixtures: Application of the finite element method and its comparison with dielectric mixture formulas". *J. Appl. Phys.* ***89,*** 8092-8100.(2001).
[64]. Dang, Z.-M.; Shen, Y.; Nan, C.-W., "Dielectric behavior of three-phase percolative Ni–BaTiO3/polyvinylidene fluoride composites". *Appl. Phys. Lett.* ***81,*** 4814-4816.(2002).
[65]. Lü, W.; Dong, J.; Li, Z.-Y., "Optical properties of aligned carbon nanotube systems studied by the effective-medium approximation method". *Phys. Rev. B* ***63,*** 033401.(2000).
[66]. Yu, K.; Niu, Y.; Zhou, Y.; Bai, Y.; Wang, H., "Nanocomposites of Surface-Modified $BaTiO_3$ Nanoparticles Filled Ferroelectric Polymer with Enhanced Energy Density". *J. Am. Ceram. Soc.* ***96,*** 2519-2524.(2013).

[67]. Shay, D. P.; Podraza, N. J.; Donnelly, N. J.; Randall, C. A., "High Energy Density, High Temperature Capacitors Utilizing Mn-Doped $0.8CaTiO_3$–$0.2CaHfO_3$ Ceramics". *J. Am. Ceram. Soc.* ***95,*** 1348-1355.(2012).
[68]. Kim, P., et al., "Solution-processible high-permittivity nanocomposite gate insulators for organic field-effect transistors". *Appl. Phys. Lett.* ***93,*** 013302.(2008).
[69]. Ramesh, S.; Shutzberg, B. A.; Huang, C.; Jie, G.; Giannelis, E. P., "Dielectric nanocomposites for integral thin film capacitors: materials design, fabrication and integration issues". *IEEE. T. Adv. Packaging* ***26,*** 17-24.(2003).
[70]. Kim, P., et al., "Phosphonic Acid-Modified Barium Titanate Polymer Nanocomposites with High Permittivity and Dielectric Strength". *Adv. Mater.* ***19,*** 1001-1005.(2007).
[71]. Laine, R. M.; Choi, J.; Lee, I., "Organic–Inorganic Nanocomposites with Completely Defined Interfacial Interactions". *Adv. Mater.* ***13,*** 800-803.(2001).
[72]. Rong, M. Z., et al., "Structure–property relationships of irradiation grafted nano-inorganic particle filled polypropylene composites". *Polymer* ***42,*** 167-183.(2001).
[73]. Yu, K., et al., "Enhanced electric breakdown strength and high energy density of barium titanate filled polymer nanocomposites". *J. Appl. Phys.* ***114,*** 174107.(2013).
[74]. Dou, X., et al., "Improved dielectric strength of barium titanate-polyvinylidene fluoride nanocomposite". *Appl. Phys. Lett.* ***95,*** (2009).
[75]. Li, Z., et al., "In Situ Catalytic Encapsulation of Core-Shell Nanoparticles Having Variable Shell Thickness: Dielectric and Energy Storage Properties of High-Permittivity Metal Oxide Nanocomposites". *Chem. Mater.* ***22,*** 5154-5164.(2010).
[76]. Yu, K.; Niu, Y.; Zhou, Y.; Bai, Y.; Wang, H., "Nanocomposites of Surface-Modified $BaTiO_3$ Nanoparticles Filled Ferroelectric Polymer with Enhanced Energy Density". *J. Am. Ceram. Soc.* ***96,*** 2519-2524.(2013).
[77]. Kobayashi, Y.; Kosuge, A.; Konno, M., "Fabrication of high concentration barium titanate/polyvinylpyrrolidone nano-composite thin films and their dielectric properties". *Appl. Surf. Sci.* ***255,*** 2723-2729.(2008).
[78]. El Achaby, M., et al., "Nanocomposite films of poly(vinylidene fluoride) filled with polyvinylpyrrolidone-coated multiwalled carbon nanotubes: Enhancement of β-polymorph formation and tensile properties". *Polymer Engineering & Science* ***53,*** 34-43.(2013).
[79]. Kumar, S. K.; Jouault, N.; Benicewicz, B.; Neely, T., "Nanocomposites with Polymer Grafted Nanoparticles". *Macromolecules* ***46,*** 3199-3214.(2013).
[80]. Wu, J.; Ling, L.; Ma, G.; Wang, B., "A comparative study of grafting steps on the preparation and properties of modified nanosilica for UV-curable coatings". *Journal of Coatings Technology Research* ***11,*** 717-725.(2014).
[81]. Guo, N., et al., "Supported Metallocene Catalysis for In Situ Synthesis of High Energy Density Metal Oxide Nanocomposites". *J. Am. Chem. Soc.* ***129,*** 766-767.(2007).
[82]. Ohno, K.; Morinaga, T.; Koh, K.; Tsujii, Y.; Fukuda, T., "Synthesis of Monodisperse Silica Particles Coated with Well-Defined, High-Density Polymer Brushes by Surface-Initiated Atom Transfer Radical Polymerization". *Macromolecules* ***38,*** 2137-2142.(2005).
[83]. Ramakrishnan, A.; Dhamodharan, R.; Rühe, J., "Growth of poly(methyl methacrylate) brushes on silicon surfaces by atom transfer radical polymerization". *Journal of Polymer Science Part A: Polymer Chemistry* ***44,*** 1758-1769.(2006).

[84]. Rakhmatullina, E., et al., "Functionalization of Gold and Silicon Surfaces by Copolymer Brushes Using Surface-Initiated ATRP". *Macromol. Chem. Phys.* ***208,*** 1283-1293.(2007).
[85]. Yuan, G.; Xueping, G.; Yongfeng, Z.; Deyue, Y., "Preparation of poly(methyl methacrylate) grafted titanate nanotubes by in situ atom transfer radical polymerization". *Nanotechnology* ***19,*** 495604.(2008).
[86]. Kong, H.; Gao, C.; Yan, D., "Controlled Functionalization of Multiwalled Carbon Nanotubes by in Situ Atom Transfer Radical Polymerization". *J. Am. Chem. Soc.* ***126,*** 412-413.(2004).
[87]. Goncalves, G., et al., "Graphene oxide modified with PMMA via ATRP as a reinforcement filler". *J. Mater. Chem.* ***20,*** 9927-9934.(2010).
[88]. Zhao, B.; Brittain, W. J., "Polymer brushes: surface-immobilized macromolecules". *Prog. Polym. Sci.* ***25,*** 677-710.(2000).
[89]. Paniagua, S. A., et al., "Surface-Initiated Polymerization from Barium Titanate Nanoparticles for Hybrid Dielectric Capacitors". *ACS Applied Materials & Interfaces* ***6,*** 3477-3482.(2014).
[90]. Krysiak, E., et al., "Core–shell system based on titanium dioxide with elevated value of dielectric permittivity: Synthesis and characterization". *Synthetic Metals* ***209,*** 150-157.(2015).
[91]. Bartholome, C.; Beyou, E.; Bourgeat-Lami, E.; Chaumont, P.; Zydowicz, N., "Nitroxide-Mediated Polymerizations from Silica Nanoparticle Surfaces: "Graft from" Polymerization of Styrene Using a Triethoxysilyl-Terminated Alkoxyamine Initiator". *Macromolecules* ***36,*** 7946-7952.(2003).
[92]. Shirai, Y.; Kawatsura, K.; Tsubokawa, N., "Graft polymerization of vinyl monomers from initiating groups introduced onto polymethylsiloxane-coated titanium dioxide modified with alcoholic hydroxyl groups". *Prog. Org. Coat.* ***36,*** 217-224.(1999).
[93]. Bockstaller, M. R.; Mickiewicz, R. A.; Thomas, E. L., "Block Copolymer Nanocomposites: Perspectives for Tailored Functional Materials". *Adv. Mater.* ***17,*** 1331-1349.(2005).
[94]. Li, B.; Han, W.; Jiang, B.; Lin, Z., "Crafting threads of diblock copolymer micelles via flow-enabled self-assembly". *ACS Nano* ***8,*** 2936-2942.(2014).
[95]. Li, B., et al., "Macroscopic highly aligned DNA nanowires created by controlled evaporative self-assembly". *ACS Nano* ***7,*** 4326-4333.(2013).
[96]. Chen, Y.; Du, N.; Zhang, H.; Yang, D., "Facile synthesis of uniform MWCNT@Si nanocomposites as high-performance anode materials for lithium-ion batteries". *J. Alloy. Compd.*
[97]. Hou, L., et al., "Self-Sacrifice Template Fabrication of Hierarchical Mesoporous Bi-Component-Active ZnO/ZnFe2O4 Sub-Microcubes as Superior Anode Towards High-Performance Lithium-Ion Battery". *Adv. Funct. Mater.* ***25,*** 238-246.(2015).
[98]. Wu, H., et al., "Stable cycling of double-walled silicon nanotube battery anodes through solid-electrolyte interphase control". *Nat Nano* ***7,*** 310-315.(2012).
[99]. Yu, Y., et al., "Reversible Storage of Lithium in Silver-Coated Three-Dimensional Macroporous Silicon". *Adv. Mater.* ***22,*** 2247-2250.(2010).
[100]. Song, T., et al., "Arrays of Sealed Silicon Nanotubes As Anodes for Lithium Ion Batteries". *Nano Lett.* ***10,*** 1710-1716.(2010).

[101]. Wang, Y.; Cao, G., "Developments in Nanostructured Cathode Materials for High-Performance Lithium-Ion Batteries". *Adv. Mater.* ***20,*** 2251-2269.(2008).
[102]. Li, N.; Patrissi, C. J.; Che, G.; Martin, C. R., "Rate Capabilities of Nanostructured LiMn2 O 4 Electrodes in Aqueous Electrolyte". *J. Electrochem. Soc.* ***147,*** 2044-2049.(2000).
[103]. Amatucci, G.; Tarascon, J.-M., "Optimization of Insertion Compounds Such as $LiMn_2O_4$ for Li-Ion Batteries". *J. Electrochem. Soc.* ***149,*** K31-K46.(2002).
[104]. Kang, B.; Ceder, G., "Battery materials for ultrafast charging and discharging". *Nature* ***458,*** 190-193.(2009).
[105]. Wu, R., et al., "In-Situ Formation of Hollow Hybrids Composed of Cobalt Sulfides Embedded within Porous Carbon Polyhedra/Carbon Nanotubes for High-Performance Lithium-Ion Batteries". *Adv. Mater.* ***27,*** 3038-3044.(2015).
[106]. Poizot, P.; Laruelle, S.; Grugeon, S.; Dupont, L.; Tarascon, J. M., "Nano-sized transition-metal oxides as negative-electrode materials for lithium-ion batteries". *Nature* ***407,*** 496-499.(2000).
[107]. Zhu, X.; Zhu, Y.; Murali, S.; Stoller, M. D.; Ruoff, R. S., "Nanostructured Reduced Graphene Oxide/Fe_2O_3 Composite As a High-Performance Anode Material for Lithium Ion Batteries". *ACS Nano* ***5,*** 3333-3338.(2011).
[108]. Cabana, J.; Monconduit, L.; Larcher, D.; Palacín, M. R., "Beyond Intercalation-Based Li-Ion Batteries: The State of the Art and Challenges of Electrode Materials Reacting Through Conversion Reactions". *Adv. Mater.* ***22,*** E170-E192.(2010).
[109]. Xiong, S.; Chen, J. S.; Lou, X. W.; Zeng, H. C., "Mesoporous Co_3O_4 and CoO@C Topotactically Transformed from Chrysanthemum-like $Co(CO_3)_{0.5}(OH)\cdot_{0.11}H_2O$ and Their Lithium-Storage Properties". *Adv. Funct. Mater.* ***22,*** 861-871.(2012).
[110]. Zhou, G., et al., "Graphene-Wrapped Fe3O4 Anode Material with Improved Reversible Capacity and Cyclic Stability for Lithium Ion Batteries". *Chem. Mater.* ***22,*** 5306-5313.(2010).
[111]. Lou, X. W.; Deng, D.; Lee, J. Y.; Feng, J.; Archer, L. A., "Self-Supported Formation of Needlelike Co_3O_4 Nanotubes and Their Application as Lithium-Ion Battery Electrodes". *Adv. Mater.* ***20,*** 258-262.(2008).
[112]. Bazin, L., et al., "High rate capability pure Sn-based nano-architectured electrode assembly for rechargeable lithium batteries". *J. Power Sources* ***188,*** 578-582.(2009).
[113]. Li, N.; Martin, C. R., "A High-Rate, High-Capacity, Nanostructured Sn-Based Anode Prepared Using Sol-Gel Template Synthesis". *J. Electrochem. Soc.* ***148,*** A164-A170.(2001).
[114]. Liu, J., et al., "Hydrothermal Fabrication of Three-Dimensional Secondary Battery Anodes". *Adv. Mater.* ***26,*** 7096-7101.(2014).
[115]. Han, C., et al., "Hollow titanium dioxide spheres as anode material for lithium ion battery with largely improved rate stability and cycle performance by suppressing the formation of solid electrolyte interface layer". *Journal of Materials Chemistry A* ***3,*** 13340-13349.(2015).
[116]. Arico, A. S.; Bruce, P.; Scrosati, B.; Tarascon, J.M.; van Schalkwijk, W., "Nanostructured materials for advanced energy conversion and storage devices". *Nat Mater* ***4,*** 366-377.(2005).
[117]. Yu, D., et al., "Mica-like vanadium pentoxide-nanostructured thin film as high-performance cathode for lithium-ion batteries". *J. Power Sources* ***266,*** 1-6.(2014).

[118]. Yao, X., et al., "Mesoporous zinc ferrite/graphene composites: Towards ultra-fast and stable anode for lithium-ion batteries". *Carbon* ***79,*** 493-499.(2014).
[119]. Jiang, C.; Ichihara, M.; Honma, I.; Zhou, H., "Effect of particle dispersion on high rate performance of nano-sized $Li_4Ti_5O_{12}$ anode". *Electrochim. Acta* ***52,*** 6470-6475.(2007).
[120]. Hu, Y. S.; Kienle, L.; Guo, Y. G.; Maier, J., "High Lithium Electroactivity of Nanometer-Sized Rutile TiO_2". *Adv. Mater.* ***18,*** 1421-1426.(2006).
[121]. Jamnik, J.; Maier, J., "Nanocrystallinity effects in lithium battery materials Aspects of nano-ionics. Part IV". *Phys. Chem. Chem. Phys.* ***5,*** 5215-5220.(2003).
[122]. Larcher, D., et al., "Effect of Particle Size on Lithium Intercalation into α Fe_2O_3". *J. Electrochem. Soc.* ***150,*** A133-A139.(2003).
[123]. Morales, J.; Sánchez, L.; Martín, F.; Berry, F.; Ren, X., "Synthesis and Characterization of Nanometric Iron and Iron-Titanium Oxides by Mechanical Milling:: Electrochemical Properties as Anodic Materials in Lithium Cells". *J. Electrochem. Soc.* ***152,*** A1748-A1754.(2005).
[124]. Chen, J.; Xu, L.; Li, W.; Gou, X., "α-Fe_2O_3 Nanotubes in Gas Sensor and Lithium-Ion Battery Applications". *Adv. Mater.* ***17,*** 582-586.(2005).
[125]. Shaju, K. M.; Jiao, F.; Debart, A.; Bruce, P. G., "Mesoporous and nanowire Co_3O_4 as negative electrodes for rechargeable lithium batteries". *Phys. Chem. Chem. Phys.* ***9,*** 1837-1842.(2007).
[126]. Li, J.; Claude, J.; Norena-Franco, L. E.; Seok, S. I.; Wang, Q., "Electrical Energy Storage in Ferroelectric Polymer Nanocomposites Containing Surface-Functionalized $BaTiO_3$ Nanoparticles". *Chem. Mater.* ***20,*** 6304-6306.(2008).
[127]. Li, J.; Zeng, H. C., "Size Tuning, Functionalization, and Reactivation of Au in TiO_2 Nanoreactors". *Angewandte Chemie International Edition* ***44,*** 4342-4345.(2005).
[128]. Zhang, W.M.; Wu, X.L.; Hu, J.S.; Guo, Y.G.; Wan, L.J., "Carbon Coated Fe_3O_4 Nanospindles as a Superior Anode Material for Lithium-Ion Batteries". *Adv. Funct. Mater.* ***18,*** 3941-3946.(2008).
[129]. Zhan, F.; Geng, B.; Guo, Y., "Porous Co_3O_4 Nanosheets with Extraordinarily High Discharge Capacity for Lithium Batteries". *Chemistry – A European Journal* ***15,*** 6169-6174.(2009).
[130]. Park, M.H., et al., "Silicon Nanotube Battery Anodes". *Nano Lett.* ***9,*** 3844-3847.(2009).
[131]. Wang, G.; Shen, X.; Yao, J.; Park, J., "Graphene nanosheets for enhanced lithium storage in lithium ion batteries". *Carbon* ***47,*** 2049-2053.(2009).
[132]. Yoo, E., et al., "Large Reversible Li Storage of Graphene Nanosheet Families for Use in Rechargeable Lithium Ion Batteries". *Nano Lett.* ***8,*** 2277-2282.(2008).
[133]. Zhou, H.; Zhu, S.; Hibino, M.; Honma, I.; Ichihara, M., "Lithium Storage in Ordered Mesoporous Carbon (CMK-3) with High Reversible Specific Energy Capacity and Good Cycling Performance". *Adv. Mater.* ***15,*** 2107-2111.(2003).
[134]. Tessonnier, J.P., et al., "Analysis of the structure and chemical properties of some commercial carbon nanostructures". *Carbon* ***47,*** 1779-1798.(2009).
[135]. Frackowiak, E.; Gautier, S.; Gaucher, H.; Bonnamy, S.; Beguin, F., "Electrochemical storage of lithium in multiwalled carbon nanotubes". *Carbon* ***37,*** 61-69.(1999).

[136]. Mukhopadhyay, I., et al., "Electrochemical Li Insertion in B-Doped Multiwall Carbon Nanotubes". *J. Electrochem. Soc.* ***149,*** A39-A44.(2002).
[137]. Endo, M., et al., "Vapor-grown carbon fibers (VGCFs): Basic properties and their battery applications". *Carbon* ***39,*** 1287-1297.(2001).
[138]. Liwen, J.; Xiangwu, Z., "Fabrication of porous carbon nanofibers and their application as anode materials for rechargeable lithium-ion batteries". *Nanotechnology* ***20,*** 155705.(2009).
[139]. Tang, K., et al., "Hollow Carbon Nanospheres with Superior Rate Capability for Sodium-Based Batteries". *Adv. Energy Mater.* ***2,*** 873-877.(2012).
[140]. Wu, S., et al., "Graphene-Containing Nanomaterials for Lithium-Ion Batteries". *Adv. Energy Mater.* ***5,*** n/a-n/a.(2015).
[141]. Ji, L.; Lin, Z.; Alcoutlabi, M.; Zhang, X., "Recent developments in nanostructured anode materials for rechargeable lithium-ion batteries". *Energy Environ. Sci.* ***4,*** 2682-2699.(2011).
[142]. Yu, Y.; Gu, L.; Zhu, C.; van Aken, P. A.; Maier, J., "Tin Nanoparticles Encapsulated in Porous Multichannel Carbon Microtubes: Preparation by Single-Nozzle Electrospinning and Application as Anode Material for High-Performance Li-Based Batteries". *J. Am. Chem. Soc.* ***131,*** 15984-15985.(2009).
[143]. Bresser, D., et al., "Carbon Coated $ZnFe_2O_4$ Nanoparticles for Advanced Lithium-Ion Anodes". *Adv. Energy Mater.* ***3,*** 513-523.(2013).
[144]. Wang, Y.; Wang, Y.; Hosono, E.; Wang, K.; Zhou, H., "The Design of a $LiFePO_4$/Carbon Nanocomposite With a Core–Shell Structure and Its Synthesis by an In Situ Polymerization Restriction Method". *Angewandte Chemie International Edition* ***47,*** 7461-7465.(2008).
[145]. Liu, X.m., et al., "Synthesis of superior fast charging-discharging nano-$LiFePO_4$/C from nano-$FePO_4$ generated using a confined area impinging jet reactor approach". *Chem. Commun.* ***49,*** 5396-5398.(2013).
[146]. Cheng, L., et al., "General synthesis of carbon-coated nanostructure $Li_4Ti_5O_{12}$ as a high rate electrode material for Li-ion intercalation". *J. Mater. Chem.* ***20,*** 595-602.(2010).
[147]. Yao, L., et al., "An excellent performance anode of $ZnFe_2O_4$/flake graphite composite for lithium ion battery". *J. Alloy. Compd.* ***585,*** 398-403.(2014).
[148]. Xia, H.; Qian, Y.; Fu, Y.; Wang, X., "Graphene anchored with $ZnFe_2O_4$ nanoparticles as a high-capacity anode material for lithium-ion batteries". *Solid State Sci.* ***17,*** 67-71.(2013).
[149]. Kong, J., et al., "Polydopamine-derived porous nanofibers as host of $ZnFe_2O_4$ nanoneedles: towards high-performance anodes for lithium-ion batteries". *RSC Advances* ***5,*** 13315-13323.(2015).
[150]. Wang, H., et al., "Mn_3O_4−Graphene Hybrid as a High-Capacity Anode Material for Lithium Ion Batteries". *J. Am. Chem. Soc.* ***132,*** 13978-13980.(2010).
[151]. Zhou, J., et al., "Carbon-Encapsulated Metal Oxide Hollow Nanoparticles and Metal Oxide Hollow Nanoparticles: A General Synthesis Strategy and Its Application to Lithium-Ion Batteries". *Chem. Mater.* ***21,*** 2935-2940.(2009).
[152]. Paek, S. M.; Yoo, E.; Honma, I., "Enhanced cyclic performance and lithium storage capacity of SnO_2/graphene nanoporous electrodes with three-dimensionally delaminated flexible structure". *Nano Lett.* ***9,*** 72-75.(2009).

[153]. Luo, Y., et al., "Controlled synthesis of hierarchical graphene-wrapped TiO_2@Co_3O_4 coaxial nanobelt arrays for high-performance lithium storage". *Journal of Materials Chemistry A* ***1,*** 273-281.(2013).
[154]. Heidari, E. K.; Zhang, B.; Sohi, M. H.; Ataie, A.; Kim, J.K., "Sandwich-structured graphene-$NiFe_2O_4$-carbon nanocomposite anodes with exceptional electrochemical performance for Li ion batteries". *Journal of Materials Chemistry A* ***2,*** 8314-8322.(2014).
[155]. Chang, J., et al., "Multilayered Si Nanoparticle/Reduced Graphene Oxide Hybrid as a High-Performance Lithium-Ion Battery Anode". *Adv. Mater.* ***26,*** 758-764.(2014).
[156]. Wu, Z.S., et al., "Graphene Anchored with Co_3O_4 Nanoparticles as Anode of Lithium Ion Batteries with Enhanced Reversible Capacity and Cyclic Performance". *ACS Nano* ***4,*** 3187-3194.(2010).
[157]. Qin, J., et al., "Graphene Networks Anchored with Sn@Graphene as Lithium Ion Battery Anode". *ACS Nano* ***8,*** 1728-1738.(2014).
[158]. Zhang, J., et al., "Sulfur nanocrystals anchored graphene composite with highly improved electrochemical performance for lithium–sulfur batteries". *J. Power Sources* ***270,*** 1-8.(2014).
[159]. Veeraraghavan, B.; Paul, J.; Haran, B.; Popov, B., "Study of polypyrrole graphite composite as anode material for secondary lithium-ion batteries". *J. Power Sources* ***109,*** 377-387.(2002).
[160]. Wang, G. X., et al., "An investigation of polypyrrole-$LiFePO_4$ composite cathode materials for lithium-ion batteries". *Electrochim. Acta* ***50,*** 4649-4654.(2005).
[161]. Cui, L.; Shen, J.; Cheng, F.; Tao, Z.; Chen, J., "SnO_2 nanoparticles@polypyrrole nanowires composite as anode materials for rechargeable lithium-ion batteries". *J. Power Sources* ***196,*** 2195-2201.(2011).
[162]. P. Wong, H., et al., "Synthesis and characterization of polypyrrole/vanadium pentoxide nanocomposite aerogels". *J. Mater. Chem.* ***8,*** 1019-1027.(1998).
[163]. Liu, T., et al., "Polyaniline and Polypyrrole Pseudocapacitor Electrodes with Excellent Cycling Stability". *Nano Lett.* ***14,*** 2522-2527.(2014).
[164]. Guo, Z. P.; Wang, J. Z.; Liu, H. K.; Dou, S. X., "Study of silicon/polypyrrole composite as anode materials for Li-ion batteries". *J. Power Sources* ***146,*** 448-451.(2005).
[165]. Chew, S. Y., et al., "Novel nano-silicon/polypyrrole composites for lithium storage". *Electrochem. Commun.* ***9,*** 941-946.(2007).
[166]. Cai, J.J.; Zuo, P.J.; Cheng, X.-Q.; Xu, Y.-H.; Yin, G.-P., "Nano-silicon/polyaniline composite for lithium storage". *Electrochem. Commun.* ***12,*** 1572-1575.(2010).
[167]. Naoi, K.; Lien, M.; Smyrl, W. H., "Quartz Crystal Microbalance Study: Ionic Motion Across Conducting Polymers". *J. Electrochem. Soc.* ***138,*** 440-445.(1991).
[168]. Nam, D.H.; Lim, S.J.; Kim, M.J.; Kwon, H.S., "Facile synthesis of SnO_2-polypyrrole hybrid nanowires by cathodic electrodeposition and their application to Li-ion battery anodes". *RSC Advances* ***3,*** 16102-16108.(2013).
[169]. Liu, R., et al., "Core–shell structured hollow SnO_2–polypyrrole nanocomposite anodes with enhanced cyclic performance for lithium-ion batteries". *Nano Energy* ***6,*** 73-81.(2014).
[170]. Wu, Y. P.; Fang, S.; Jiang, Y.; Holze, R., "Effects of doped sulfur on electrochemical performance of carbon anode". *J. Power Sources* ***108,*** 245-249.(2002).

[171]. Hasegawa, G., et al., "Monolithic electrode for electric double-layer capacitors based on macro/meso/microporous S-Containing activated carbon with high surface area". *J. Mater. Chem.* ***21,*** 2060-2063.(2011).
[172]. Paraknowitsch, J. P.; Thomas, A.; Schmidt, J., "Microporous sulfur-doped carbon from thienyl-based polymer network precursors". *Chem. Commun.* ***47,*** 8283-8285.(2011).
[173]. Zhang, X.-W., et al., "Electrochemical performance of lithium ion battery, nano-silicon-based, disordered carbon composite anodes with different microstructures". *J. Power Sources* ***125,*** 206-213.(2004).
[174]. Yue, L.; Wang, S.; Zhao, X.; Zhang, L., "Nano-silicon composites using poly(3,4-ethylenedioxythiophene):poly(styrenesulfonate) as elastic polymer matrix and carbon source for lithium-ion battery anode". *J. Mater. Chem.* ***22,*** 1094-1099.(2012).
[175]. Liu, R., et al., "Dopamine as a Carbon Source: The Controlled Synthesis of Hollow Carbon Spheres and Yolk-Structured Carbon Nanocomposites". *Angewandte Chemie International Edition* ***50,*** 6799-6802.(2011).
[176]. Raymundo-Piñero, E.; Leroux, F.; Béguin, F., "A High-Performance Carbon for Supercapacitors Obtained by Carbonization of a Seaweed Biopolymer". *Adv. Mater.* ***18,*** 1877-1882.(2006).
[177]. Liu, N., et al., "A Yolk-Shell Design for Stabilized and Scalable Li-Ion Battery Alloy Anodes". *Nano Lett.* ***12,*** 3315-3321.(2012).
[178]. Alexandridis, P.; Tsianou, M., "Block copolymer-directed metal nanoparticle morphogenesis and organization". *Eur. Polym. J.* ***47,*** 569-583.(2011).
[179]. Rozenberg, B. A.; Tenne, R., "Polymer-assisted fabrication of nanoparticles and nanocomposites". *Prog. Polym. Sci.* ***33,*** 40-112.(2008).
[180]. Bao, C.; Jin, M.; Lu, R.; Zhang, T.; Zhao, Y. Y., "Preparation of Au nanoparticles in the presence of low generational poly(amidoamine) dendrimer with surface hydroxyl groups". *Mater. Chem. Phys.* ***81,*** 160-165.(2003).
[181]. Sakai, T.; Alexandridis, P., "Single-Step Synthesis and Stabilization of Metal Nanoparticles in Aqueous Pluronic Block Copolymer Solutions at Ambient Temperature". *Langmuir* ***20,*** 8426-8430.(2004).
[182]. Sakai, T.; Alexandridis, P., "Mechanism of Gold Metal Ion Reduction, Nanoparticle Growth and Size Control in Aqueous Amphiphilic Block Copolymer Solutions at Ambient Conditions". *The Journal of Physical Chemistry B* ***109,*** 7766-7777.(2005).
[183]. Longenberger, L.; Mills, G., "Formation of Metal Particles in Aqueous Solutions by Reactions of Metal Complexes with Polymers". *The Journal of Physical Chemistry* ***99,*** 475-478.(1995).
[184]. Alexandridis, P.; Sakai, T. In *Amphiphilic block copolymer solutions as media for the facile synthesis and colloidal stabilization of metal nanoparticles*, ABSTRACTS OF PAPERS OF THE AMERICAN CHEMICAL SOCIETY, AMER CHEMICAL SOC 1155 16TH ST, NW, WASHINGTON, DC 20036 USA: 2004; pp U507-U507.
[185]. Ishii, T.; Otsuka, H.; Kataoka, K.; Nagasaki, Y., "Preparation of Functionally PEGylated Gold Nanoparticles with Narrow Distribution through Autoreduction of Auric Cation by α-Biotinyl-PEG-block-[poly(2-(N,N-dimethylamino)ethyl methacrylate)]". *Langmuir* ***20,*** 561-564.(2004).
[186]. Mayer, A. B. R.; Mark, J. E., "Colloidal gold nanoparticles protected by water-soluble homopolymers and random copolymers". *Eur. Polym. J.* ***34,*** 103-108.(1998).

[187]. Bronstein, L. M., et al., "Interaction of metal compounds with 'double-hydrophilic' block copolymers in aqueous medium and metal colloid formation". *Inorg. Chim. Acta* ***280,*** 348-354.(1998).
[188]. Shaikh, J. S.; Pawar, R. C.; Moholkar, A. V.; Kim, J. H.; Patil, P. S., "CuO–PAA hybrid films: Chemical synthesis and supercapacitor behavior". *Appl. Surf. Sci.* ***257,*** 4389-4397.(2011).
[189]. Chegel, V. I., et al., "Redox-Switching of Electrorefractive, Electrochromic, and Conductivity Functions of Cu^{2+}/Polyacrylic Acid Films Associated with Electrodes". *Adv. Mater.* ***14,*** 1549-1553.(2002).
[190]. Pang, X.; Zhao, L.; Akinc, M.; Kim, J. K.; Lin, Z., "Novel Amphiphilic Multi-Arm, Star-Like Block Copolymers as Unimolecular Micelles". *Macromolecules* ***44,*** 3746-3752.(2011).
[191]. Pang, X.; Zhao, L.; Feng, C.; Lin, Z., "Novel Amphiphilic Multiarm, Starlike Coil–Rod Diblock Copolymers via a Combination of Click Chemistry with Living Polymerization". *Macromolecules* ***44,*** 7176-7183.(2011).
[192]. Jiang, B.; Pang, X.; Li, B.; Lin, Z., "Organic–Inorganic Nanocomposites via Placing Monodisperse Ferroelectric Nanocrystals in Direct and Permanent Contact with Ferroelectric Polymers". *J. Am. Chem. Soc.* (2015).
[193]. Rao, Y.; Wong, C. P., "Material characterization of a high-dielectric-constant polymer–ceramic composite for embedded capacitor for RF applications". *J. Appl. Polym. Sci.* ***92,*** 2228-2231.(2004).
[194]. Schroeder, R.; Majewski, L. A.; Grell, M., "High-Performance Organic Transistors Using Solution-Processed Nanoparticle-Filled High-k Polymer Gate Insulators". *Adv. Mater.* ***17,*** 1535-1539.(2005).
[195]. Kim, H.; Han, B.; Choo, J.; Cho, J., "Three-Dimensional Porous Silicon Particles for Use in High-Performance Lithium Secondary Batteries". *Angewandte Chemie International Edition* ***47,*** 10151-10154.(2008).
[196]. Mao, Y. P.; Mao, S. Y.; Ye, Z.G.; Xie, Z. X.; Zheng, L. S., "Size-dependences of the dielectric and ferroelectric properties of $BaTiO_3$/polyvinylidene fluoride nanocomposites". *J. Appl. Phys.* ***108,*** -.(2010).
[197]. Salimi, A.; Yousefi, A. A., "Analysis Method: FTIR studies of β-phase crystal formation in stretched PVDF films". *Polym. Test.* ***22,*** 699-704.(2003).
[198]. Yu, S., et al., "Formation Mechanism of β-Phase in PVDF/CNT Composite Prepared by the Sonication Method". *Macromolecules* ***42,*** 8870-8874.(2009).
[199]. Donahoe, D. N.; Pecht, M.; Lloyd, I. K.; Ganesan, S., "Moisture induced degradation of multilayer ceramic capacitors". *Microelectron. Reliab.* ***46,*** 400-408.(2006).
[200]. Sakabe, Y.; Takeshima, Y.; Tanaka, K., "Multilayer ceramic capacitors with thin $(Ba,Sr)TiO_3$ layers by MOCVD". *J. Electroceram.* ***3,*** 115-121.(1999).
[201]. Azough, F.; Al-Saffar, R.; Freer, R., "A transmission electron microscope study of commercial X7R-type multilayer ceramic capacitors". *J. Eur. Ceram. Soc.* ***18,*** 751-758.(1998).
[202]. McSkimin, H. J., "Performance of High Frequency Barium Titanate Transducers for Generating Ultrasonic Waves in Liquids". *J. Acoust. Soc. Am.* ***31,*** 1519-1522.(1959).

[203]. Kim, H. U.; Lee, W. H.; Dias, H. V. R.; Priya, S., "Piezoelectric Microgenerators-Current Status and Challenges". *IEEE Trans. Ultrason. Ferroelectr. Freq. Control* ***56,*** 1555-1568.(2009).
[204]. Haertling, G. H., "Ferroelectric ceramics: History and technology". *J. Am. Ceram. Soc.* ***82,*** 797-818.(1999).
[205]. Hueter, T. F.; Dozois, E., "The Frequency Response of Barium Titanate Transducers". *J. Am. Ceram. Soc.* ***24,*** 85-86.(1952).
[206]. Meyer, R. J.; Newnham, R. E.; Amin, A.; Kulwicki, B. M., "Flextensional barium strontium titanate actuators". *J. Am. Ceram. Soc.* ***86,*** 934-938.(2003).
[207]. Dent, A. C.; Bowen, C. R.; Stevens, R.; Cain, M. G.; Stewart, M., "Effective elastic properties for unpoled barium titanate". *J. Eur. Ceram. Soc.* ***27,*** 3739-3743.(2007).
[208]. Landis, C. M.; McMeeking, R. M., "A self-consistent constitutive model for switching in polycrystalline barium titanate". *Ferroelectrics* ***255,*** 13-34.(2001).
[209]. Liu, J.; Shen, Z. J.; Yao, W. L.; Zhao, Y. H.; Mukherjee, A. K., "Visible and infrared transparency in lead-free bulk BaTiO3 and SrTiO3 nanoceramics". *Nanotechnology* ***21,*** (2010).
[210]. Lin, P. T.; Liu, Z.; Wessels, B. W., "Ferroelectric thin film photonic crystal waveguide and its electro-optic properties". *J. Opt. A: Pure Appl. Opt.* ***11,*** (2009).
[211]. Marx, J. M.; Eknoyan, O.; Taylor, H. F.; Tang, Z.; Neurgaonkar, R. R., "Electrooptic Modulation and Self-Poling in Strain-Induced Wave-Guides in Barium Strontium-Titanate Niobate". *Appl. Phys. Lett.* ***67,*** 1381-1383.(1995).
[212]. Takenaka, T.; Nagata, H.; Hiruma, Y.; Yoshii, Y.; Matumoto, K., "Lead-free piezoelectric ceramics based on perovskite structures". *J. Electroceram.* ***19,*** 259-265.(2007).
[213]. Liu, D.; Li, J. Y., "The enhanced and optimal piezoelectric coefficients in single crystalline barium titanate with engineered domain configurations". *Appl. Phys. Lett.* ***83,*** 1193-1195.(2003).
[214]. Maranganti, R.; Sharma, P., "Atomistic determination of flexoelectric properties of crystalline dielectrics". *Phys. Rev. B* ***80,*** (2009).
[215]. Ruglovsky, J. L.; Li, J. Y.; Bhattacharya, K.; Atwater, H. A., "The effect of biaxial texture on the effective electromechanical constants of polycrystalline barium titanate and lead titanate thin films". *Acta Mater.r.* ***54,*** 3657-3663.(2006).
[216]. Jin, H. Z.; Zhu, J., "Size effect and fatigue mechanism in ferroelectric thin films". *J. Appl. Phys.* ***92,*** 4594-4598.(2002).
[217]. Ezhilvalavan, S.; Tseng, T. Y., "Progress in the developments of (Ba,Sr)TiO_3 (BST) thin films for Gigabit era DRAMs". *Mater. Chem. Phys.* ***65,*** 227-248.(2000).
[218]. Yeh, M. H., et al., "Electrical Characteristics of Barium-Titanate Films Prepared by Laser-Ablation". *J. Appl. Phys.* ***74,*** 2143-2145.(1993).
[219]. Kotecki, D. E., et al., "(Ba,Sr)TiO3 dielectrics for future stacked-capacitor DRAM". *IBM J. Res. Dev.* ***43,*** 367-382.(1999).
[220]. Rasul, A.; Zhang, J.; Gamota, D.; Singh, M.; Takoudis, C., "Flexible high capacitance nanocomposite gate insulator for printed organic field-effect transistors". *Solid State Ionics* ***518,*** 7024-7028.(2010).
[221]. Jang, Y., et al., "High field-effect mobility pentacene thin-film transistors with nanoparticle polymer composite/polymer bilayer insulators". *Appl. Phys. Lett.* ***94,*** (2009).

[222]. Cai, Q. J., et al., "Solution-Processable Barium Titanate and Strontium Titanate Nanoparticle Dielectrics for Low-Voltage Organic Thin-Film Transistors". *Chem. Mater.* ***21,*** 3153-3161.(2009).
[223]. Salaoru, I.; Paul, S., "Non-volatile memory device- using a blend of polymer and ferroelectric nanoparticles". *J. Optoelectron. Adv. Mater.* ***10,*** 3461-3464.(2008).
[224]. Shut, V. N.; Kostomarov, S. V.; Gavrilov, A. V., "PTCR ceramics produced from oxalate-derived barium titanate". *Inorg. Chem.* ***44,*** 905-910.(2008).
[225]. Preis, W.; Sitte, W., "Electronic conductivity and chemical diffusion in n-conducting barium titanate ceramics at high temperatures". *Solid State Ionics* ***177,*** 3093-3098.(2006).
[226]. Ahmad, G., et al., "Rapid bioenabled formation of ferroelectric $BaTiO_3$ at room temperature from an aqueous salt solution at near neutral pH". *J. Am. Ceram. Soc.* ***130,*** 4-+.(2008).
[227]. Smith, D. S., et al., "Transient thermal gradients in barium titanate positive temperature coefficient (PTC) thermistors". *J. Am. Ceram. Soc.* ***81,*** 1789-1796.(1998).
[228]. Frey, M. H.; Payne, D. A., "Grain-size effect on structure and phase transformations for barium titanate". *Phys. Rev. B* ***54,*** 3158-3168.(1996).
[229]. Zhao, Z., et al., "Grain-size effects on the ferroelectric behavior of dense nanocrystalline $BaTiO_3$ ceramics". *Phys. Rev. B* ***70,*** (2004).
[230]. McNeal, M. P.; Jang, S. J.; Newnham, R. E., "The effect of grain and particle size on the microwave properties of barium titanate ($BaTiO_3$)". *J. Appl. Phys.* ***83,*** 3288-3297.(1998).
[231]. Heywang, W., "Semiconducting Barium Titanate". *J. Mater. Sci.* ***6,*** 1214-&.(1971).
[232]. Heywang, W., "Resistivity Anomaly in Doped Barium Titanate". *J. Am. Ceram. Soc.* ***47,*** 484-490.(1964).
[233]. McCauley, D.; Newnham, R. E.; Randall, C. A., "Intrinsic size effects in a barium titanate glass-ceramic". *J. Am. Ceram. Soc.* ***81,*** 979-987.(1998).
[234]. Aikawa, Y.; Iwazaki, Y.; Suzuki, T., "Theoretical analysis of surface effect of crystal and its application to $BaTiO_3$ fine particle". *J. Ceram. Soc. Jpn.* ***118,*** 1057-1061.(2010).
[235]. Yang, Y.; Wang, X. H.; Sun, C. K.; Li, L. T., "Structure study of single crystal $BaTiO_3$ nanotube arrays produced by the hydrothermal method". *Nanotechnology* ***20,*** -.(2009).
[236]. Mehta, R. R.; Silverman, B. D.; Jacobs, J. T., "Depolarization fields in thin ferroelectric films". *Journal of Applied Physics* ***44,*** 3379-3385.(1973).
[237]. Kalinin, S. V.; Johnson, C. Y.; Bonnell, D. A., "Domain polarity and temperature induced potential inversion on the $BaTiO_3$(100) surface". *Journal of Applied Physics* ***91,*** 3816-3823.(2002).
[238]. Popescu, D. G., et al., "Spectro-microscopic photoemission evidence of charge uncompensated areas in $Pb(Zr,Ti)O_3$(001) layers". *Physical Chemistry Chemical Physics* ***17,*** 509-520.(2015).
[239]. Beier, C. W.; Cuevas, M. A.; Brutchey, R. L., "Effect of Surface Modification on the Dielectric Properties of $BaTiO_3$ Nanocrystals". *Langmuir* ***26,*** 5067-5071.(2010).
[240]. Spanier, J. E., et al., "Ferroelectric phase transition in individual single-crystalline $BaTiO_3$ nanowires". *Nano Lett.* ***6,*** 735-739.(2006).

[241]. Kim, C.; Noh, M.; Choi, M.; Cho, J.; Park, B., "Critical Size of a Nano SnO_2 Electrode for Li-Secondary Battery". *Chem. Mater.* ***17,*** 3297-3301.(2005).
[242]. Hoshina, T.; Wada, S.; Kuroiwa, Y.; Tsurumi, T., "Composite structure and size effect of barium titanate nanoparticles". *Appl. Phys. Lett.* ***93,*** 192914.(2008).
[243]. Begg, B. D.; Finnie, K. S.; Vance, E. R., "Raman Study of the Relationship between Room-Temperature Tetragonality and the Curie Point of Barium Titanate". *J. Am. Ceram. Soc.* ***79,*** 2666-2672.(1996).
[244]. Hsiang, H.I.; Yen, F.-S., "Effect of Crystallite Size on the Ferroelectric Domain Growth of Ultrafine $BaTiO_3$ Powders". *J. Am. Ceram. Soc.* ***79,*** 1053-1060.(1996).
[245]. Lanceros-Méndez, S.; Mano, J. F.; Costa, A. M.; Schmidt, V. H., "FTIR AND DSC STUDIES OF MECHANICALLY DEFORMED β-PVDF FILMS". *Journal of Macromolecular Science, Part B* ***40,*** 517-527.(2001).
[246]. Upadhyay, R. H.; Deshmukh, R. R., "Investigation of dielectric properties of newly prepared β-phase polyvinylidene fluoride–barium titanate nanocomposite films". *J. Electrostat.* ***71,*** 945-950.(2013).
[247]. Li, J. Y.; Zhang, L.; Ducharme, S., "Electric energy density of dielectric nanocomposites". *Appl. Phys. Lett.* ***90,*** 132901.(2007).
[248]. Yu, K., et al., "Nanocomposites of Surface-Modified $BaTiO_3$Nanoparticles Filled Ferroelectric Polymer with Enhanced Energy Density". *J. Am. Ceram. Soc.* ***96,*** 2519-2524.(2013).
[249]. Chanmal, C. V., "Dielectric relaxations in PVDF/$BaTiO_3$ nanocomposites". *eXPRESS Polymer Letters* ***2,*** 294-301.(2008).
[250]. Landauer, R., "The Electrical Resistance of Binary Metallic Mixtures". *J. Appl. Phys.* ***23,*** 779-784.(1952).
[251]. Guo, H. Z., et al., "Structure evolution and dielectric behavior of polystyrene-capped barium titanate nanoparticles". *Journal of Materials Chemistry* (2012).
[252]. Zhang, Q. M.; Wang, H.; Kim, N.; Cross, L. E., "Direct evaluation of domain‐wall and intrinsic contributions to the dielectric and piezoelectric response and their temperature dependence on lead zirconate‐titanate ceramics". *J. Appl. Phys.* ***75,*** 454-459.(1994).
[253]. Xu, F., et al., "Domain wall motion and its contribution to the dielectric and piezoelectric properties of lead zirconate titanate films". *J. Appl. Phys.* ***89,*** 1336-1348.(2001).
[254]. Arlt, G.; Hennings, D., "Dielectric properties of fine‐grained barium titanate ceramics". *J. Appl. Phys.* ***58,*** 1619-1625.(1985).
[255]. Ban, C., et al., "Nanostructured Fe_3O_4/SWNT Electrode: Binder-Free and High-Rate Li-Ion Anode". *Adv. Mater.* ***22,*** E145-E149.(2010).
[256]. Wen, F., et al., "One-stage synthesis of narrowly dispersed polymeric core-shell microspheres". *Journal of Polymer Science Part A: Polymer Chemistry* ***46,*** 1192-1202.(2008).
[257]. Chen, C.; Li, R.; Xu, L.; Yan, D., "Three-dimensional superhydrophobic porous hybrid monoliths for effective removal of oil droplets from the surface of water". *RSC Advances* ***4,*** 17393-17400.(2014).
[258]. Zhang, W.; Zhang, A.; Guan, Y.; Zhang, Y.; Zhu, X. X., "Silver-loading in uncrosslinked hydrogen-bonded LBL films: structure change and improved stability". *J. Mater. Chem.* ***21,*** 548-555.(2011).

[259]. Huang, H., et al., "Preparation, characterization, and application of magnetic Fe-SBA-15 mesoporous silica molecular sieves". *Journal of Analytical Methods in Chemistry* ***2010,*** (2010).
[260]. Xu, H., et al., A general route to nanocrystal kebabs periodically assembled on stretched flexible polymer shish. 2015; Vol. 1.
[261]. Illán-Gómez, M. J.; Raymundo-Piñero, E.; García-García, A.; Linares-Solano, A.; Salinas-Martínez de Lecea, C., "Catalytic NOx reduction by carbon supporting metals". *Applied Catalysis B: Environmental* ***20,*** 267-275.(1999).
[262]. Yao, L., et al., "Green synthesis of mesoporous $ZnFe_2O_4$/C composite microspheres as superior anode materials for lithium-ion batteries". *J. Power Sources* ***258,*** 305-313.(2014).
[263]. Xu, J., et al., "Edge-Selectively Halogenated Graphene Nanoplatelets (XGnPs, X = Cl, Br, or I) Prepared by Ball-Milling and Used as Anode Materials for Lithium-Ion Batteries". *Adv. Mater.* ***26,*** 7317-7323.(2014).
[264]. Hu, X.; Lin, Z.; Yang, K.; Huai, Y.; Deng, Z., "Effects of carbon source and carbon content on electrochemical performances of $Li_4Ti_5O_{12}$/C prepared by one-step solid-state reaction". *Electrochim. Acta* ***56,*** 5046-5053.(2011).
[265]. Cho, Y.D.; Fey, G. T.-K.; Kao, H.-M., "The effect of carbon coating thickness on the capacity of $LiFePO_4$/C composite cathodes". *J. Power Sources* ***189,*** 256-262.(2009).
[266]. Deng, Y., et al., "One-pot synthesis of $ZnFe_2O_4$/C hollow spheres as superior anode materials for lithium ion batteries". *Chem. Commun.* ***47,*** 6828-6830.(2011).
[267]. Ding, Y.; Yang, Y.; Shao, H., "High capacity $ZnFe_2O_4$ anode material for lithium ion batteries". *Electrochim. Acta* ***56,*** 9433-9438.(2011).
[268]. Hou, X., et al., "One-step synthesis of SnOx nanocrystalline aggregates encapsulated by amorphous TiO_2 as an anode in Li-ion battery". *Journal of Materials Chemistry A* ***3,*** 9982-9988.(2015).
[269]. Li, X., et al., "Tin Oxide with Controlled Morphology and Crystallinity by Atomic Layer Deposition onto Graphene Nanosheets for Enhanced Lithium Storage". *Adv. Funct. Mater.* ***22,*** 1647-1654.(2012).
[270]. Lou, X. W.; Wang, Y.; Yuan, C.; Lee, J. Y.; Archer, L. A., "Template-Free Synthesis of SnO_2 Hollow Nanostructures with High Lithium Storage Capacity". *Adv. Mater.* ***18,*** 2325-2329.(2006).
[271]. Yu, Y.; Chen, C. H.; Shi, Y., "A Tin-Based Amorphous Oxide Composite with a Porous, Spherical, Multideck-Cage Morphology as a Highly Reversible Anode Material for Lithium-Ion Batteries". *Adv. Mater.* ***19,*** 993-997.(2007).
[272]. Zhou, X.; Wan, L.J.; Guo, Y.-G., "Binding SnO_2 Nanocrystals in Nitrogen-Doped Graphene Sheets as Anode Materials for Lithium-Ion Batteries". *Adv. Mater.* ***25,*** 2152-2157.(2013).
[273]. Hu, R., et al., "Dramatically enhanced reversibility of Li_2O in SnO_2-based electrodes: the effect of nanostructure on high initial reversible capacity". *Energy Environ. Sci.* ***9,*** 595-603.(2016).
[274]. Wang, C.M., et al., "In Situ Transmission Electron Microscopy Observation of Microstructure and Phase Evolution in a SnO_2 Nanowire during Lithium Intercalation". *Nano Lett.* ***11,*** 1874-1880.(2011).

[275]. Retoux, R.; Brousse, T.; Schleich, D. M., "High‐Resolution Electron Microscopy Investigation of Capacity Fade in SnO_2 Electrodes for Lithium‐Ion Batteries". *J. Electrochem. Soc.* ***146,*** 2472-2476.(1999).
[276]. Lou, X. W.; Chen, J. S.; Chen, P.; Archer, L. A., "One-Pot Synthesis of Carbon-Coated SnO_2 Nanocolloids with Improved Reversible Lithium Storage Properties". *Chem. Mater.* ***21,*** 2868-2874.(2009).
[277]. Yue; Zhou, "Synthesis of Porous Single Crystals of Metal Oxides via a Solid−Liquid Route". *Chem. Mater.* ***19,*** 2359-2363.(2007).
[278]. Deng, D.; Lee, J. Y., "Hollow Core–Shell Mesospheres of Crystalline SnO_2 Nanoparticle Aggregates for High Capacity Li+ Ion Storage". *Chem. Mater.* ***20,*** 1841-1846.(2008).
[279]. Wang, Y.; Su, F.; Lee, J. Y.; Zhao, X. S., "Crystalline Carbon Hollow Spheres, Crystalline Carbon−SnO_2 Hollow Spheres, and Crystalline SnO_2 Hollow Spheres: Synthesis and Performance in Reversible Li-Ion Storage". *Chem. Mater.* ***18,*** 1347-1353.(2006).
[280]. Wang, C., et al., "Large-Scale Synthesis of SnO_2 Nanosheets with High Lithium Storage Capacity". *J. Am. Chem. Soc.* ***132,*** 46-47.(2010).
[281]. Wang, X., et al., "N-Doped Graphene-SnO_2 Sandwich Paper for High‐Performance Lithium-Ion Batteries". *Adv. Funct. Mater.* ***22,*** 2682-2690.(2012).
[282]. Shiva, K.; Rajendra, H.; Subrahmanyam, K.; Bhattacharyya, A. J.; Rao, C., "Improved lithium cyclability and storage in mesoporous SnO2 electronically wired with very low concentrations (⩽ 1%) of reduced graphene oxide". *Chemistry–A European Journal* ***18,*** 4489-4494.(2012).
[283]. Liu, L.; An, M.; Yang, P.; Zhang, J., "Superior cycle performance and high reversible capacity of SnO_2/graphene composite as an anode material for lithium-ion batteries". *Sci. Rep.* ***5,*** 9055.(2015).
[284]. Beaulieu, L. Y.; Eberman, K. W.; Turner, R. L.; Krause, L. J.; Dahn, J. R., "Colossal Reversible Volume Changes in Lithium Alloys". *Electrochemical and Solid-State Letters* ***4,*** A137-A140.(2001).
[285]. Courtney, I. A.; McKinnon, W. R.; Dahn, J. R., "On the Aggregation of Tin in SnO Composite Glasses Caused by the Reversible Reaction with Lithium". *J. Electrochem. Soc.* ***146,*** 59-68.(1999).
[286]. Wang, Y.; Lee, J. Y.; Zeng, H. C., "Polycrystalline SnO_2 Nanotubes Prepared via Infiltration Casting of Nanocrystallites and Their Electrochemical Application". *Chem. Mater.* ***17,*** 3899-3903.(2005).
[287]. Zhao, N., et al., "Preparation of Nanowire Arrays of Amorphous Carbon Nanotube-Coated Single Crystal SnO_2". *Chem. Mater.* ***20,*** 2612-2614.(2008).
[288]. Besenhard, J. O.; Yang, J.; Winter, M., "Will advanced lithium-alloy anodes have a chance in lithium-ion batteries?". *J. Power Sources* ***68,*** 87-90.(1997).
[289]. He, M., et al., "A SnO_2@carbon nanocluster anode material with superior cyclability and rate capability for lithium-ion batteries". *Nanoscale* ***5,*** 3298-3305.(2013).
[290]. Shao, Q.G., et al., "SnO_2-based composite coaxial nanocables with multi-walled carbon nanotube and polypyrrole as anode materials for lithium-ion batteries". *Electrochem. Commun.* ***13,*** 1431-1434.(2011).

[291]. Deng, D.; Kim, M. G.; Lee, J. Y.; Cho, J., "Green energy storage materials: Nanostructured TiO2 and Sn-based anodes for lithium-ion batteries". *Energy Environ. Sci.* ***2,*** 818-837.(2009).
[292]. Marom, R.; Amalraj, S. F.; Leifer, N.; Jacob, D.; Aurbach, D., "A review of advanced and practical lithium battery materials". *J. Mater. Chem.* ***21,*** 9938-9954.(2011).
[293]. Zhang, L.; Zhang, G.; Wu, H. B.; Yu, L.; Lou, X. W., "Hierarchical Tubular Structures Constructed by Carbon-Coated SnO_2 Nanoplates for Highly Reversible Lithium Storage". *Adv. Mater.* ***25,*** 2589-2593.(2013).
[294]. Liebscher, J., et al., "Structure of Polydopamine: A Never-Ending Story?". *Langmuir* ***29,*** 10539-10548.(2013).
[295]. Nirasay, S.; Badia, A.; Leclair, G.; Claverie, J. P.; Marcotte, I., "Polydopamine-supported lipid bilayers". *Materials* ***5,*** 2621-2636.(2012).
[296]. Pérez-Mitta, G., et al., "Polydopamine Meets Solid-State Nanopores: A Bioinspired Integrative Surface Chemistry Approach To Tailor the Functional Properties of Nanofluidic Diodes". *J. Am. Chem. Soc.* ***137,*** 6011-6017.(2015).
[297]. Miao, Z., et al., "Large-scale production of self-assembled SnO_2 nanospheres and their application in high-performance chemiluminescence sensors for hydrogen sulfide gas". *J. Mater. Chem.* ***17,*** 1791-1796.(2007).
[298]. Iqbal, Z.; Lai, E. P. C.; Avis, T. J., "Development of polymer-modified magnetic nanoparticles and quantum dots for Escherichia coli binding test". *Microchimica Acta* ***176,*** 193-200.(2012).
[299]. Demir-Cakan, R.; Hu, Y.S.; Antonietti, M.; Maier, J.; Titirici, M.M., "Facile One-Pot Synthesis of Mesoporous SnO_2 Microspheres via Nanoparticles Assembly and Lithium Storage Properties". *Chem. Mater.* ***20,*** 1227-1229.(2008).
[300]. Zhou, X.; Yu, L.; Lou, X. W., "Nanowire-templated formation of SnO_2/carbon nanotubes with enhanced lithium storage properties". *Nanoscale* ***8,*** 8384-8389.(2016).
[301]. Guan, C., et al., "Highly Stable and Reversible Lithium Storage in SnO_2 Nanowires Surface Coated with a Uniform Hollow Shell by Atomic Layer Deposition". *Nano Lett.* ***14,*** 4852-4858.(2014).
[302]. Wang, Y., et al., "Designed hybrid nanostructure with catalytic effect: beyond the theoretical capacity of SnO_2 anode material for lithium ion batteries". *Sci. Rep.* ***5,*** 9164.(2015).
[303]. Lian, P., et al., "High reversible capacity of SnO_2/graphene nanocomposite as an anode material for lithium-ion batteries". *Electrochim. Acta* ***56,*** 4532-4539.(2011).
[304]. Noerochim, L.; Wang, J.Z.; Chou, S.L.; Li, H.J.; Liu, H.K., "SnO_2-coated multiwall carbon nanotube composite anode materials for rechargeable lithium-ion batteries". *Electrochim. Acta* ***56,*** 314-320.(2010).
[305]. Liu, H.; Wang, G.; Wang, J.; Wexler, D., "Magnetite/carbon core-shell nanorods as anode materials for lithium-ion batteries". *Electrochem. Commun.* ***10,*** 1879-1882.(2008).
[306]. Li, J.; Murphy, E.; Winnick, J.; Kohl, P. A., "Studies on the cycle life of commercial lithium ion batteries during rapid charge–discharge cycling". *J. Power Sources* ***102,*** 294-301.(2001).
[307]. Li, J., et al., "Study of the storage performance of a Li-ion cell at elevated temperature". *Electrochim. Acta* ***55,*** 927-934.(2010).

[308]. Jung, J.Y.; Lee, S.B.; Lee, H.Y.; Joo, Y.C.; Park, Y.B., "Electrochemical Migration Characteristics of Eutectic Sn-Pb Solder Alloy in NaCl and Na_2SO_4 Solutions". *J. Electron. Mater.* ***38,*** 691-699.(2009).